A STUDY OF SnO_2

A mio padre e mia madre

A STUDY OF SnO_2: PREPARATION, CHARACTERIZATION AND RESPONSE TO ION-IMPACT

By

ENRICO GIANI, Dottore in Physics, M.Sc.

A Thesis

Submitted to the School of Graduate Studies

in Partial Fulfilment of the Requirements

for the Degree

Doctor of Philosophy

McMaster University

December 1975

DOCTOR OF PHILOSOPHY (1975)
(Metallurgy and Materials Science)

McMASTER UNIVERSITY
Hamilton, Ontario

TITLE: A Study of SnO_2: Preparation, Characterization and Response to Ion-impact

AUTHOR: Enrico Giani, Dottore in Physics (Università degli Studi di Milano, Italy)
M.Sc. (McMaster University)

SUPERVISOR: Professor Roger Kelly

NUMBER OF PAGES: xx, 210

ABSTRACT

SnO_2 films have been prepared by reactive sputtering in an oxygen-containing glow discharge, by ion-beam sputtering in an accelerator, and by anodizing with an ethylen-glycol-based electrolyte. Preparation of SnO_2 films by bombarding metallic tin with oxygen ions has also been attempted. The sputter-deposited films were amorphous if deposited on KCl or Ta at temperatures from -100° to +200°C, though they were crystalline if deposited on SnO_2 at 200°C. The anodic films were variously crystalline or microcrystalline, though clearly not amorphous. Films formed by bombarding metallic tin with oxygen ions turned out to be crystalline α-SnO at all doses from 1×10^{15} to 3×10^{17} ions/cm^2. The crystallization temperatures ranged from <200°C for crystalline SnO_2 substrates, to 250°-300°C for KCl substrates, to 400°-450°C for Ta substrates, to 475°-550°C for unsupported films. The crystallization product was consistently cassiterite, i.e., normal SnO_2. Once crystallinity was attained in unsupported sputtered films, the grain size remained in the vicinity of 400 Å to a temperature of about 1000°C. This is in good agreement with the behaviour of anodic films, which retained their microcrystalline structure in heat treatment again until a temperature of about 1000°C was reached. The thickness of the reactively sputtered films was estimated from the observation of their interference colours when deposited on a Ta substrate, while the thickness of the anodic films was estimated by sputtering the films with 20-keV Kr ions until metal was exposed and noting the weight change.

The anodization of Sn has a rather low efficiency (4-21%), and this could be shown to be due to electronic conduction rather than dissolution. Kr-ion bombardment of SnO_2 thin films has shown that this oxide presents a very high value of the sputtering coefficient (21.5 ± 1.5 atoms/ion for 10-keV Kr impact), a result which can be attributed to thermal sputtering (i.e., bombardment induced vaporization). As far as the structure of the target material after bombardment is concerned, the experimental evidence was that SnO_2 undergoes amorphization. The effects of ion bombardment of bulk samples (either SnO_2 sintered powder or natural cassiterite) were investigated using the following techniques: (I) reflection electron diffraction, (II) marker-release spectrometry, (III) dissolution measurements, and (IV) resistivity measurements. Through the use of techniques I and II we have established that the annealing (to the original single-crystalline phase) of bombardment induced amorphousness occurs in two stages: (i) a homogeneous transformation to a polycrystalline phase showing the normal cassiterite structure; (ii) epitaxial recrystallization to single-crystal cassiterite. Dissolution measurements have established the depth of amorphization due to ion bombardment, while resistivity measurements have indicated that bombardment does not cause SnO_2 to change its stoichiometry. Finally the various results allowed us to expand the formalism on which marker-release spectrometry is based, namely we have identified a previously overlooked release process (Stage IC) due to epitaxial crystallization.

ACKNOWLEDGMENTS

I would like to express my gratitude to my supervisor, Professor R. Kelly, for continuously assisting me with his knowledge, talent and friendship.

I am also grateful to my friend, Dr. M. R. Arora, for his help and concern.

I would finally like to remember all my friends in the Department.

This project was supported by grants from the National Research Council and the Defence Research Board to Professor R. Kelly and from the Ontario Government and McMaster University to the author.

TABLE OF CONTENTS

		PAGE
PART 1	PREPARATION, CHARACTERIZATION AND ION-BOMBARDMENT OF SnO_2 THIN FILMS	
CHAPTER 1	INTRODUCTION AND REVIEW OF THE LITERATURE	1
	1.1 Introduction	1
	1.2 Review of the literature	3
	1.2.1 Chemical vapour deposition (CVD)	3
	1.2.2 Vacuum deposition	9
	1.2.3 Sputtering	10
	1.2.4 Anodizing	11
	1.2.5 Gas-oxidation of metallic tin	15
	1.2.6 Growing of single-crystals	16
	1.2.7 Ion-bombardment of SnO_2	18
	1.3 Conclusions drawn from the literature survey	22
	REFERENCES	26
CHAPTER 2	SPUTTERED FILMS	30
	2.1 Introduction	30
	2.2 Experimental	32
	2.2.1 Reactive sputtering	32
	2.2.2 Ion-beam sputtering	32
	2.3 Results	33
	2.3.1 Film continuity and crystal form	33
	2.3.2 Crystallization behaviour	36

PAGE

2.3.3 Abruptness of crystallization 48

2.3.4 Thickness of reactively sputtered films 54

2.4 Discussion 54

REFERENCES 60

CHAPTER 3 ANODIC FILMS 62

3.1 Introduction 62

3.1.1 The electrolyte 62

3.1.2 The growth of the film 63

3.2 Experimental 65

3.3 Results 67

3.3.1 Crystal form 67

3.3.2 Crystallization behaviour 71

3.3.3 Thickness 71

3.3.4 Anodizing efficiency 77

3.4 Discussion 79

REFERENCES 85

CHAPTER 4 OXYGEN-BOMBARDMENT OF Sn 87

4.1 General 87

4.2 Sn metal thin films 87

4.2.1 Preparation and thin-film analysis 87

4.2.2 Oxygen-ion bombardment of Sn 88

4.2.3 Sputtering coefficient of Sn due to O_2^+ impact 97

4.3 Discussion 97

4.4 Conclusions 102

		PAGE
	REFERENCES	103
CHAPTER 5	ION-IMPACT EFFECTS WITH SnO_2 FILMS	104
	5.1 Introduction	104
	5.2 Sputtering coefficient of SnO_2	104
	5.2.1 General	104
	5.2.2 Experimental and Results	105
	5.2.3 Discussion	109
	5.3 Bombardment-induced structure changes of SnO_2	122
	REFERENCES	124
PART 2	ION-IMPACT EFFECTS IN BULK SnO_2	
CHAPTER 6	INTRODUCTION AND THEORETICAL	126
	6.1 Introduction	126
	6.2 Criteria to predict the structural stability of solids under ion-impact	127
	6.2.1 Criterion based on a physical model involving thermal spikes	127
	6.2.2 Criterion based on ionicity	128
	6.2.3 Criterion for oxygen loss	129
	6.2.4 Other criteria	132
	6.3 Gas-release spectrometry as a means of studying ion-implanted specimens	135
	6.4 Electrical conductivity measurements as a means of studying bombardment-induced stoichiometry changes	146
	6.5 Dissolution experiments as a means of determining the thickness of amorphized layers	149

		PAGE
	REFERENCES	151
CHAPTER 7	EXPERIMENTAL	154
	7.1 Specimens	154
	7.2 Techniques	155
	REFERENCES	159
CHAPTER 8	RESULTS	160
	8.1 Marker-release measurements	160
	8.2 Reflection electron diffraction	160
	8.3 Dissolution and F-vs-dose curves	167
	8.4 Electrical conductivity measurements	176
	REFERENCES	180
CHAPTER 9	DISCUSSION	181
	9.1 Low-temperature process	181
	9.2 High-temperature process	184
	9.3 Marker-release stages	187
	9.4 Dissolution and F-vs-dose data	189
	9.5 Electrical conductivity measurements	189
	9.6 Other observations	192
	REFERENCES	193
CHAPTER 10	SUGGESTIONS FOR FUTURE WORK AND SUMMARY	195
	10.1 Suggestions for future work	195
	10.1.1 A possible thickness effect	195
	10.1.2 Thickness-vs-anodizing voltage	195

		PAGE
10.1.3	Preparation of SnO_2 by oxygen-bombardment of metallic tin	195
10.1.4	Formation of oxygen bubbles in O_2-implanted metallic tin	197
10.1.5	Stage IIA and melting point	199
10.2	Summary	200
REFERENCES		210

LIST OF TABLES

TABLE NO.		PAGE
1.I	Preparation of tin oxide films	6
1.II	Formation of tin oxide by sputtering	12
1.III	Temperature-ratio criterion and the structural stability of crystalline solids under ion-impact (from Ref. 74)	19
1.IV	The ratio Tc/Tm or Tc/Tp for various multiple-oxide minerals (from Ref. 75)	21
2.I	Grain size in heat treated SnO_2 films	52
2.II	Temperature interval for crystallization of unsupported SnO_2 films	53
2.III	Thickness of reactively sputtered SnO_2 films	55
2.IV	The product separation x pressure for reactive sputtering of SnO_2	57
2.V	The crystallization products of amorphous oxides	59
3.I	Thickness of anodic SnO_2 films	76
3.II	Anodizing efficiency	78
3.III	Structure of anodic oxides and of oxides subject to ion-bombardment (from Ref. 22)	82
3.IV	Comparison of fields and efficiencies for anodizing various metals (from Ref. 13)	84
4.I	Analysis of as-deposited evaporated Sn thin film	91
4.II	Diffraction data for the Sn-O system	94
4.III	Analysis of oxygen implanted metallic tin	96

TABLE NO.		PAGE
4.IV	Comparing the ASTM d-spacings for α-SnO with experimental (normalized) d-spacings obtained from Fig. 4.4	99
5.I	Sputtering yield at room temperature for Kr-impact on SnO_2	106
5.II	S at 20-keV for Kr-impact on SnO_2 as a function of temperature	112
5.III	Comparison of sputtering behaviour of oxides for 10-keV Kr-impact	115
5.IV	Comparison of surface binding energies	116
5.V	Effect of temperature on S for oxides (10-keV Kr-impact)	118
6.I	Experimental values for the width at half-height during crystallization	144
8.Ia	Analysis of marker-release spectra (He-flow) in SnO_2 pellets bombarded with 35-keV Kr	164
8.Ib	Analysis of marker-release spectra (O_2-flow) in SnO_2 pellets bombarded with 35-keV Kr	164
8.Ic	Analysis of marker-release spectra (O_2-flow) in natural cassiterite bombarded with 35-keV Kr	164
8.II	Comparison of experimental $\Delta T/T$ with expected values	165
8.III	Activity retained after dissolution of SnO_2 samples (pellets and natural cassiterite) has gone to completion	170
8.IV	Activity retained after heating to $T \geq 1100°C$	171
8.V	Activity retained after heating to $T < 1100°C$	173
8.VI	Released fractional activity after annealing (∿1030 K) and subsequent dissolution	177
8.VII	Retained fractional activity after annealing to $T \geq 1350$ K and after combined annealing (∿1030 K) and dissolution	178

TABLE NO.		PAGE
9.I	The intermediate and stable phase in the crystallization of amorphous oxides	183
9.II	The annealing of bombardment-induced amorphousness in oxides, as monitored using marker-release spectrometry and diffraction	188
9.III	Thickness of amorphized layer as a function of bombardment dose	190
9.IV	Thickness of amorphized layer in various substances	191

LIST OF ILLUSTRATIONS

FIGURE NO.		PAGE
1.1	Log resistivity versus reciprocal temperature for crystalline and amorphous V_2O_3 and V_2O_4. (from Ref. 13)	2
2.1	Micrographs with mag. 22,000 of SnO_2 films formed by reactive sputtering onto KCl at -100°C. The examples are amorphous (obvious from diffraction pattern) and show in (a) an island structure, though in other instances (b) the films were continuous.	34
2.2	Micrographs with mag. 22,000 of SnO_2 films formed by reactive sputtering onto KCl at ∿200°C (a) or by ion-beam sputtering of anodized tin (b). Films were always amorphous (again obvious from diffraction pattern) and continuous.	37
2.3	Reflection electron diffraction patterns of (a) SnO_2 single-crystal, (b) SnO_2 film deposited on SnO_2 single-crystal, (c) SnO_2 sintered pellet, (d) SnO_2 film deposited on SnO_2 sintered pellet.	39
2.4	Effect of heat treatment in air on crystallization of reactively sputtered (refrigerated substrates) unsupported SnO_2 films. The crystallization temperature is shown to be ∿550°C.	40
2.5	Effect of heat treatment in air on crystallization of reactively sputtered (heated substrates) unsupported SnO_2 films. Separate specimens were used for each treatment (6 min hold times in furnace). The crystallization temperature is shown to be ∿475°C.	42
2.6	Effect of heat treatment in air on crystallization of SnO_2 films prepared by ion-beam sputtering of anodized tin. Separate specimens were used for each treatment (6 min	44

FIGURE NO.		PAGE
	hold times in furnace).. The crystallization temperature is shown to be ~550°C. Crystallized films show as usual very fine grain size.	
2.7	Same sample which gives transmission and diffraction pattern of Fig. 2.2(a) (hence deposited by reactive sputtering on heated substrates) heat treated inside the microscope. Transmission, diffraction and dark-field images at 420° and 600°C respectively. Results at 500° and 550°C were very similar.	47
2.8	Reactive sputtering on Ta at ~50°C. (a) 5 min at 410°C in air. (b) 5 min at 440°C in air.	49
2.9	The effect on progressive crystallization of heating the films directly on KCl substrates. Air heating with hold times of 6 min. (b), (d) and (f) are diffraction micrographs of (a), (c) and (e) respectively. (a) mag. 17,000-100 keV, (c) mag. 22,000-80 keV, (e) mag. 22,000-80 keV.	50
2.10	Transmission, diffraction and dark-field micrographs of SnO_2 film deposited by reactive sputtering on KCl substrate. Then heated, on KCl itself, for 6 min at 550°-600°C in air. Showing a grain size as high as 600 Å.	51
3.1	Cell-voltage transient of aluminium anodizing in 0.1 M Na_2SO_4 at 50 mA/cm^2. (from Ref. 2)	64
3.2	Voltage-time curves for anodizing Sn at 10 mA/cm^2 in electrolytes consisting of ethylene glycol, 330 g/liter of ammonium pentaborate, and varying amounts (indicated in ml/liter) of water. "Old" refers to an electrolyte containing 300 ml/liter water which had aged owing to use. The upper voltage limit is due to presetting in all cases except "Δ" and "■", where it is a true upper limit.	66
3.3	Current-time curves for anodizing Sn when both current and voltage are preset. The	68

FIGURE NO.		PAGE
	anodizings are the same as in Fig. 3.2 in all cases except "Δ" and "■", where the preset voltages are 50 and 40. Note that, to avoid crowding, only one set of points "Δ" has been joined.	
3.4	Micrographs with mag. 22,000 of SnO_2 films formed by anodizing Sn using electrolyte (c). The film has a cellular structure on a scale of ∿500 Å but consists of crystallites on a much smaller scale. The diffraction pattern was judged to be more nearly indicative of crystallinity than amorphousness.	69
3.5	Micrograph with mag. 22,000 of SnO_2 film formed by anodizing Sn using electrolyte (c'). The film consists in part of thin regions and in part of thick regions, the latter appearing as large black areas. Such films had better defined crystallinity than those of Fig. 3.4 and the diffraction pattern could be readily shown to be that of cassiterite.	70
3.6	Coloured anodic film which has been stripped and heat treated in air, using a series of hold times in furnace of 6 min each, at increasing temperatures. Each row of pictures shows, from left to right, transmission, diffraction and dark-field micrographs. Mag. 27,000-80 keV.	72
3.7	(a,left) Bright-field micrograph with mag. 54,000 of SnO_2 film formed by anodizing Sn using electrolyte (c). The film was stripped and then heated for 6 min in air at 1000°C in an unsupported state. The diffraction pattern is still best described as consisting of rings. (b,right) As in (a) but dark-field and heated at 1100°C. The diffraction pattern now shows a tendency to be spotty.	75
3.8	Integral depth distribution of 30-keV Kr in Sn according to Eq. (3.3). The range parameters $\langle x \rangle$ and Δx in Eq. (3.3) were assigned values as for CdTe (12), which has a mean mass similar to that of Sn.	80

FIGURE NO.		PAGE
4.1(a)	Transmission micrograph (mag. 54,000) of Sn film.	89
4.1(b)	Diffraction micrograph of Sn film.	90
4.2	RED of evaporated metallic tin.	92
4.3	Diffraction pattern of oxygen-implanted metallic tin--Dose: 3×10^{15} ions/cm^2 - 35 keV.	93
4.4	Diffraction patterns of eight O_2-implanted Sn samples - 35 keV - Doses: (a) 1×10^{15} (b) 1×10^{15} (c) 1×10^{15} (d) 3×10^{15} (e) 3×10^{15} (f) 3×10^{15} (g) 3×10^{17} (h) 3×10^{17} ions/cm^2.	98
5.1	The sputtering yield for Kr-impact on SnO_2 as a function of the krypton energy. Vertical bars represent the standard deviation of the arithmetic mean. The arithmetic mean is obtained from Table 5.I, where, for each energy, the highest and the lowest value of the sputtering coefficient are neglected.	110
5.2	Variation of sputtering coefficient with dose for 20-keV bombardment of SnO_2. Data are taken from Table 5.I, where, again, the highest and the lowest value of the sputtering coefficient are neglected.	111
5.3	S at 20-keV for Kr-impact on SnO_2, as a function of temperature. Vertical bars represent the standard deviation of the arithmetic mean. The arithmetic mean is obtained from Table 5.I and 5.II, where, for each temperature, the highest and the lowest value of the sputtering coefficient are neglected.	113
5.4	Erosion depth of SiO_2 as caused by the impact of 12-keV Ar ions as a function of temperature. (from Ref. 21)	119
5.5	Arrhenius plot of vapour pressure of dominant species for the oxides as indicated. The cross-hatched box encloses the pressures and temperatures which are argued to be	121

FIGURE NO.		PAGE
	critical values for thermal-spike vaporization. The references are: ZrO_2(27), Al_2O_3(28), MgO(29), TiO_2(30), UO_2(31), SiO_2(20), WO_3(32), VO_2(33,34), MoO_3(35), and SnO_2(36). Dashed lines constitute extrapolations.	
5.6	RED of anodized tin (a) before bombardment (b) amorphization due to ion-impact in sample bombarded with 20-keV Kr-ions. Dose: 2.8×10^{16} ions/cm^2 (c) amorphization due to ion-impact in sample bombarded with 20-keV Kr-ions. Dose: 5.6×10^{16} ions/cm^2.	123
6.1	Arrhenius plot of vapour pressure for the reactions: $SnO_2(s) \rightarrow Sn(l) + O_2(g)$, $SnO_2(s) \rightarrow Sn(l) + 2.0(g)$, $SnO_2(s) \rightarrow SnO(g) + 1/2\ O_2(g)$, $SnO_2(s) \rightarrow SnO(g) + O(g)$, $SnO_2(s) \rightarrow Sn(g) + O_2(g)$, $SnO_2(s) \rightarrow Sn(g) + 2.O(g)$.	131
6.2	The temperature-versus-time relations to be expected for an initial energy distribution which is concentrated either just beneath the surface (T versus t appropriate to the use of Eq. (3) of Ref. 3) or else at the surface ($T \propto t^{-3/2}$ as for a point source). (from Ref. 3)	134
6.3	Systematic representation of the System of Stages in gas-release studies for the case of a linear temperature increase (dF/dt vs temperature). T_{sd} refers to the temperatures for self-diffusion for the geometrical conditions of ion-bombardment. In compound materials, the temperature range for self-diffusion of the less mobile lattice species is relevant. (from Ref. 21)	136
6.4	Activity-versus-time curves for 65 V WO_3 films which had been heated as indicated, bombarded with 10-keV Kr to doses as indicated, and then exposed to 0.1 g/l KOH. (from Ref. 25)	139
6.5	Typical differential gas-release spectra for Bi_2O_3 specimens which have been	143

FIGURE NO.		PAGE
	bombardment-labeled with 10-keV Kr^{85} and then heated at 25 K/min in flowing oxygen. Two processes are clearly re-resolved. (from Ref. 27)	
6.6	Typical differential gas-release spectra for TeO_2 and V_2O_5 specimens which have been bombardment-labeled with 10-keV Kr^{85} and then heated at 25 K/min in flowing oxygen. Two processes are clearly resolved with TeO_2, but only one, owing to the volatility, with V_2O_5. (from Ref. 27)	143
6.7	Schematic of conductivity measurement method; S_1, S_2, S_3 are the inter-probe spacings; W is the conducting thickness; a, b, and l are the specimen dimensions where generally W << S. (after Valdes, Ref. 54)	148
6.8	Integral depth distribution of 35-keV Kr in SnO_2 according to Eq. (6.9). The range parameters <x> and Δx in Eq. (6.9) were assigned values as for ZnS, which has a mean mass similar to that of SnO_2.	150
7.1	(a) from Section 6.5. (b) from Fig. 8.5. A retained fractional activity of (e.g.) 32% corresponds to a dissolved layer of 8.5 $\mu g/cm^2$ of SnO_2. 8.5 $\mu g/cm^2$ is about 13 nm.	157
8.1	Typical differential gas-release spectrum for SnO_2 pellets which have been bombardment-labeled with 35-keV Kr^{85} and then heated at 25 K/min in flowing helium. In this specific example the dose used was 4.7×10^{15} ions/cm^2; the release processes maximize at temperatures as indicated.	161
8.2	Typical differential gas-release spectrum for SnO_2 pellets which have been bombardment-labeled with 35-keV Kr^{85} and then heated at 25 K/min in flowing oxygen. In this specific example the dose used was 4.6×10^{15} ions/cm^2; the release processes maximize at temperatures as indicated.	162

FIGURE NO.		PAGE
8.3	Typical differential gas-release spectrum for natural cassiterite specimens which have been bombardment-labeled with 35-keV Kr^{85} and then heated at 25 K/min in flowing oxygen. In this specific example the dose used was 4.6×10^{15} ions/cm^2; the release processes maximize at temperatures as indicated.	163
8.4	RED at 80-keV of natural cassiterite. (a) before bombardment, (b) after bombardment to $\sim 10^{17}$ ions/cm^2 with 35-keV Kr, (c) after annealing in air to 650°C, (d) after annealing in air to 1100°C.	166
8.5	Dissolution curves for Kr-implanted (35-keV) SnO_2 pellets. Doses as indicated on curves. Solvent: 10% HF.	168
8.6	Dissolution curves for Kr-implanted (35-keV) natural cassiterite. Doses as indicated on curves.	169
8.7	Fractional release of implanted ions in SnO_2, due to dissolution and annealing, ▲ dissolution, o annealing to T $\gtrsim$ 1100°C, □ annealing to T < 1100°C (helium flow), ● annealing to T < 1100°C (oxygen flow).	175
9.1	dF/dt vs. T curves for Cr_2O_3 and MgO which have been ion-bombardment labeled with 10-keV Kr. The doses are given in units of μ Amin/cm^2, written "μ Am". The percentage refers to the amount of gas remaining at the highest temperature reached. (from Ref. 16)	186
10.1	SnO_2 reactively sputtered on Ta substrate. All thicknesses deduced gravimetrically, i.e. weighing Ta before and after deposition.	196
10.2	Sn film on carbon-coated grid--Bombarded with oxygen: 3×10^{15} ions/cm^2 - 35-keV, mag. 53,000 - 100-keV.	198

PART 1

PREPARATION, CHARACTERIZATION AND

ION-BOMBARDMENT OF

SnO_2 THIN FILMS

CHAPTER 1

INTRODUCTION AND REVIEW OF THE LITERATURE

1.1 Introduction

SnO_2 is nearly unique among electronic materials in being a fairly good conductor when oxygen deficient yet in having a high degree of transparency to visible light (1,2). By contrast, oxides such as MoO_3, Nb_2O_5, Ta_2O_5, TiO_2, V_2O_5 or WO_3 are strongly absorbing when oxygen deficient and, therefore, conductive (3-7). This has led to a considerable amount of work on the electrical and optical properties of SnO_2 and has resulted in SnO_2 being proposed, among other things, for transparent heating elements (8,9), for transparent anti-static coatings (9,10), and for making transistors or other devices where transparency was required (9,11,12).

There has been an enormous amount of electronic and optical characterization in previous work, though notably lacking has been structural characterization. We regard the latter to be nearly as important as other aspects in view of the fact that, for example, both the magnitude of conductivity, as well as its temperature stability, are affected by crystallinity. Striking examples of this interdependence occur with V_2O_3 and VO_2 (13)(Fig. 1.1).

Also lacking has been virtually any degree of success in producing SnO_2 films by anodizing Sn at high voltages.

We would propose in Part 1 of the present work to explore the properties of 500-5000 Å SnO_2 films as formed by reactive sputtering, ion-

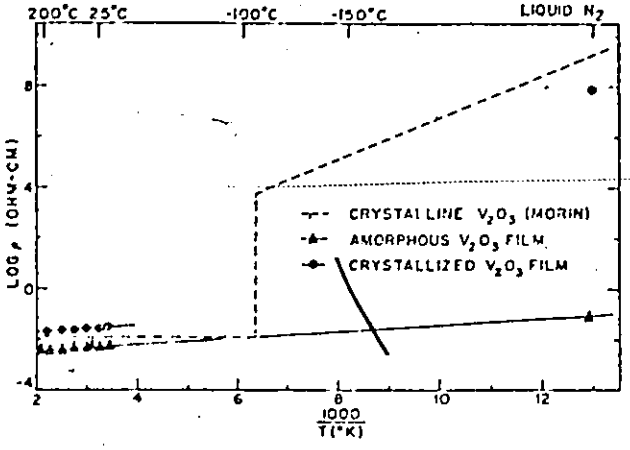

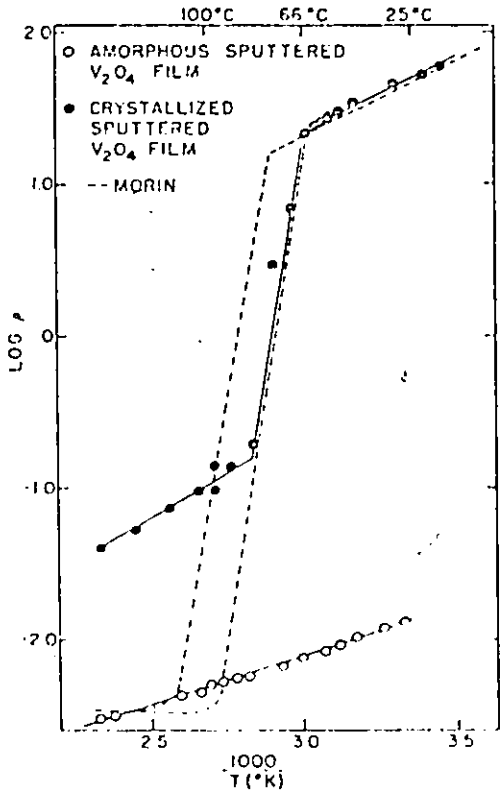

Fig. 1.1. Log resistivity versus reciprocal temperature for crystalline and amorphous V_2O_3 and V_2O_4. (from ref. 13)

beam sputtering and high-voltage anodizing. These properties will include the crystal form, crystallization behaviour, thickness and anodizing efficiency. Using the results of this work as a guide, we will undertake to investigate ion-impact effects with SnO_2 films, while in Part 2 we will deal with ion-impact effects in bulk SnO_2, especially bombardment-induced phase tranformations and stoichiometry changes.

1.2 Review of the literature

1.2.1 Chemical vapour deposition (CVD) - SnO_2 films are commonly prepared by hydrolyzing a volatile tin compound on a hot surface (normally a glass substrate), as for example according to the following reaction:

$$SnCl_4 + 2H_2O \xrightarrow{400°-800°C} SnO_2 + 4HCl$$

It should be noticed, incidentally, that stannic chloride vapour is not hydrolyzed by water vapour at temperatures below 350°C (14), and that CVD is thus an inherently high-temperature process. By contrast, vacuum deposition (Section 1.2.2) and sputtering (Section 1.2.3) are not restricted as to temperature. Since Littleton (15) was granted the first patent for producing tin oxide coatings on high voltage insulators in 1938, the patent literature has become rich on the subject of SnO_2 films prepared by CVD.

In most instances, the object was to obtain films doped in such a way as to have adequate conductivity. For example, Davies (16) in 1951 patented a process for obtaining doped tin oxide by spraying an aqueous solution of Sn chloride plus other metal (Sb, In, Mn, V, Co and Zn) chlorides, together with HCl, on a hot plate. Also issued in 1951 were six patents to Mochel (17) dealing with conductive coatings, most of them based on doped tin oxide. Coatings on glass were obtained by spraying for 10-20 s on heat-resistant

borosilicate glass, heated to about 700°C, a solution containing, e.g., $SnCl_4 \cdot 5H_2O$ 100g., H_2O 50cm^3, HCl 10cm^3 and $SbCl_3$. The quantity of $SbCl_3$ was chosen so as to yield films having between 0.001 and 38% Sb_2O_3.

A patent issued to McAuley (18) in 1954 dealt with the addition of tellurium or tungsten chlorides to the solutions to be sprayed in order to increase the electrical conductivity of the films without reducing the transparency. A solution of a Sn compound in a suitable organic vehicle to which has been added a soluble Te or W compound is sprayed on glass heated nearly to its softening point. For example, a solution of 10% $SnCl_4$ and 90% isopropanol by volume to which are added small amounts of $TeCl_4$ or WCl_6 is sprayed on a polished plate of glass of suitable size after the latter has been heated at 650°C for 2 1/2 min.

In other instances conductivity was achieved by virtue of the SnO_2 film being somewhat reduced. For example, Gomer (19) in 1953 prepared transparent, conducting films by evaporating $SnCl_2 \cdot 2H_2O$ crystals on a glass substrate at 400°C. The author does not mention what compound the deposited film consisted of, though we suspect that it may have been a mixture of SnO and SnO_2. Ladwig (20), in fact, states that "SnO-containing layers are precipitated from $SnCl_2$". Also Inokuchi and Tokuda (21) report that SnO films were formed by spraying on glass or quartz heated to 700°-750°C a 15% solution of $SnCl_2 \cdot 5H_2O$ in CH_3OH.

A more explicit example of a reduced film is found in work by Aitchison (22). He prepared transparent films of SnO_2 by spraying $SnCl_4$ in ethanol or acetic acid on to surfaces at 500°-800°C, the breakdown of the organic solvent producing reducing conditions and hence metal excess oxides. Measurements of reflectivity permitted calculation of the thick-

ness of the layers to be between 1000 and 4000 Å.

Since these early studies there have been at least 22 other major attempts to prepare SnO_2 films in pure, doped, or reduced form. These are summarized in Table 1.I.

In most cases the films were characterized only in terms of their transparency, conductivity, or thickness. In a few instances, however, electron optical techniques were used to get more precise structural information. This includes evidence by Ishiguro et al. (27), based on electron diffraction, that the "main pattern coincides with that of SnO_2 and the rings are fairly sharp, indicating that the film is composed of crystallites not so small as to be interpreted as an amorphous state". Kuznetsov (9) reports that "electrographic investigations" showed the films to have a crystalline structure, "with a unit cell completely identical to the SnO_2 cell". Also, the film was isolated from the base layer by dissolving the latter in water, and chemical analysis showed that the film is composed of 99.9% SnO_2 and a trace of monoxide (<0.1%). Besides, spectroscopical investigation revealed the presence of metal. Van der Maesen and Witmer (35) report that X-ray diagrams of sprayed layers show a crystalline structure. Tigane (36) studied film surfaces by electron microscopy, and observed that unheated layers on glass at room temperature had a uniform, fine-grained structure. "Tests on films heated to 550°-650°C showed considerable changes in the structure: irregular crystallites appeared on the surface of a uniform layer and the dimensions of these crystallites increased as the heating temperature increased." Heating to 650°-700°C or higher leads to the breakup of the continuous conducting film. Aboaf et al. (2) observed that films deposited between 300° and 600°C were polycrystal-

TABLE 1.I

Preparation of tin oxide films

Author	Ref.	Year	Substrate	Sn compound	Vehicle	Result
Ackerman	23	1954	glass at 200°C (!)	$SnCl_4$	phenylhydrazine - HCl + HF + H_2O + dioctyl Na sulfo-succinate + CH_3OH	transparent, conductive 25-800 mμ films
Fisher	24	1954	glass	$SnCl_4$	H_2O	150-700 nm transparent films
Kuznetsov	25, 26	1956, 1957	glass, ceramic at 450°-500°C	$SnCl_4$ or $SnCl_2$ vapour	warm alkaline solvent	conducting, transparent films which adhere well to glass, porcelain and other materials; films can only be removed by long polishing or by the action of HF, and are reduced by H_2
Ishiguro et al.	27	1958	glass, fused silica, NaCl cleavages at 500°-600°C	$SnCl_4 \cdot 5H_2O$ crystals or $SnCl_4$ liquid	H_2O or ethanol	transparent and conducting films

Preparation of tin oxide films (continued)

Kuznetsov et al.	28	1959	glass	$SnCl_2$	H_2O or H_2O + NH_4F	transparent 250 nm films
Miloslavskii	29	1959	glass, rock salt at 500°-600°C	$SnCl_4$ or $SnCl_2$	ethanol or H_2O	300 nm layers
Imai	30	1960	fused quartz at 500°-600°C	$SnCl_4$	H_2O or ethanol	transparent conducting films
Kuznetsov	9	1960	silica at 400°-500°C	$Sn(OC_2H_5)_4$ or $SnCl_2$ or $SnCl_4$	ether-alcohol or humid atmosphere or alcohol in presence of moisture	dielectric films or conducting films--thickness up to 3×10^3 nm
Miloslavskii and Lyashenko	31	1960	glass	$SnCl_4$		
Filimonov	32	1960	NaCl plates at 500°C	$SnCl_4$	ethanol	2-3 μ g/cm^2 films
Soleilhavoup and Dreyfus-Alain	33	1961	glass	$SnCl_4$ or $SnCl_2$	H_2O or H_2O + oxidation at 1000°C	
Groth et al.	1	1962	glass, quartz at 550°C	$SnCl_4$	butylacetate	130-300 nm

Preparation of tin oxide films (continued)

Koch	34	1963		$SnCl_4$	moist air	
Ladwig	20	1964	glass	$SnCl_4$ or $Sn(OAc)_4$ Dibutyltin diacetate		conducting layers or non-conducting layers
Van der Maesen and Witmer	35	1964	substrates at 550°C	$SnCl_4$ or Dibutyltin diacetate or Tetrabutyltin		50-500 nm films
Tigane	36	1965	glass, quartz			conducting films
Ganley	37	1965	glass at 400°C	$SnCl_2.2H_2O$	air or oxygen	conducting, almost transparent films
Golovcenco	38	1965		$SnCl_4.5H_2O$	$H_2O + B(OH)_3$	uniform, transparent films
Krogius and Vlasov	39	1966	glass	$SnCl_4$, $SnCl_4$ + $SbCl_3$, $SnCl_4$ + $FeCl_3$, $SnCl_4$ + $Co(OAc)_2$	aerosol	
Vorob'eva and Polurotova	40	1971		$Sn(OAc)_4$		transparent conducting films
Aboaf et al.	2	1973	oxidized Si at 380°-600°C	$SnCl_4$	H_2O vapour	

line. Low-angle X-ray diffraction (which gives informations on the bulk material) and reflection electron diffraction studies of the films indicated the presence of a second phase, most likely SnO, in the surface layer of the film. They report that the grain size of the film, for 380°C, was less than 1000 Å.

1.2.2 Vacuum deposition - As an alternative to chemical preparation of SnO_2 films, vacuum evaporation has been used occasionally. Basically there are two variants--evaporation of SnO_2 or of Sn.

Shiojiri et al. (41) prepared SnO_2 films by the first variant, evaporation of SnO_2 from a W basket onto the surface of NaCl cleavages at room temperature. In marked distinction to CVD films, the evaporated films showed structureless microscopic images and gave rise to an amorphous pattern in electron diffraction. Electron irradiations of the order of 0.01 to 0.10 amperes/cm^2 were made in the electron microscope by using a large condenser lens aperture or by removing it, in order to obtain a crystallized product. The amorphous tin oxide film was found to crystallize into fine granules as did TiO_2 (rutile) prepared in the same way, and did not grow into large grains.

Spence (42) obtained SnO_2 films by the second variant, namely by evaporation of tin (99.999%) from a tungsten boat under a 2×10^{-5} to 2×10^{-4} torr partial pressure of oxygen onto glass substrates at 300°C. Film thicknesses varied from 400 to 1600 Å.

The same technique was used by Van der Maesen and Witmer (35). They obtained SnO_2 films by evaporation of Sn in an O_2 atmosphere of 10^{-4} torr onto a substrate at 280°C. X-ray diagrams showed the films to have an amorphous structure.

1.2.3 Sputtering - Still a further alternative is sputtering. The first examples were remarkable for the lack of formal composition control. For example, it was found by Preston (43) that films deposited by sputtering of a tin cathode in argon were identifiable by reflection electron diffraction as tin oxide. The formation of the oxide was argued to be due either to a superficial oxide film initially on the cathode or due to reaction with traces of exygen present because the chamber was not thoroughly outgassed. Anonymous (sic) (11) prepared SnO_2 films in a similar way. He or she reports: "... a sputtered partially oxidized tin film on glass is subject to suitable heat treatment. The initial film must be amorphous, it seems, while the final product after heating gives the reflection electron diffraction pattern of stannic oxide". Holland and Siddal (10) have also prepared tin oxide films by reactive sputtering. Their technique involved reaction of the cathode with oxygen before film deposition and sputtering was then done in a 95% Ar-5% O_2 atmosphere. Preston (44), sputtering pure tin in argon followed by heating in air at 350°C for 5 min , produced transparent, conductive tin oxide films. Substrates were ordinary glass.

Secrist and Mackenzie (45) deposited non-crystalline films of Sn_xO_y on various substrates by decomposing suitable compounds in an oxygen plasma at approximately room temperature. The plasma was generated by a d.c. glow discharge or alternatively by a microwave induced discharge.

Sinclair and Peters (46) were among the first to use a more reproducible and currently acceptable approach to prepare SnO_2 films by sputtering. The method was, namely, that of reactive sputtering, such that a tin electrode is sputtered in oxygen. Films deposited on unheated

substrates were determined to be amorphous, as indicated by electron diffraction results on the unsupported films and by X-ray diffraction results on supported films. On heating the films to 400°C or higher, the writers found that films crystallized to the rutile-like structure of cassiterite with an average crystalline diameter of about 400 Å. Amorphousness of the as-deposited films and structure of thermally treated films were confirmed in a subsequent publication (47).

Lieberman and Medrud (48) prepared oxide films of eleven metals by reactive sputtering. The use of a liquid-nitrogen cooled glass substrate, to decrease the atomic mobility (especially that leading to surface diffusion), resulted in amorphous films in eight of the metal-oxide systems including Sn. Reactive sputtering was performed in a nominally 1:1 argon-oxygen mixture. Films of tin oxide were again confirmed to crystallize as the rutile analog of SnO_2. Specifically, amorphous SnO_2 heated for 1 hour at 250°C gave cassiterite-type SnO_2. Films were examined by X-ray diffraction. We would point out that Sarjeant and Roy (49) have examined the phases of metal oxides obtained from splat cooling and other rapid quenching techniques and were unable to prepare amorphous SnO_2. This suggests that sputtering is equivalent to a particularly rapid quench.

Other examples of the formation of SnO_2 by sputtering are summarized in Table 1.II.

1.2.4 Anodizing - Attempts to anodize tin so as to form a covering film of SnO_2 have remained remarkably unsuccesful from the first reported work in 1937 until the most recent in 1968. The results were invariably of two kinds: either the film was thick, badly adherent, and discoloured or it

TABLE 1.II

Formation of tin oxide by sputtering

Author	Ref.	Year	Cathode	Gas	Substrate	Result
Vainshtein	50	1965	metallic tin	Ar-O_2 mixture (40:60)	polished glass and silica at 300°C	polycrystalline, finely grained SnO_2 films
Jachimowski and Leja	51	1966	99.999% pure tin	Ar-O_2 mixture (80:20)	glass plates	200-300 nm films
Yamanaka and Oohashi	52	1969	SnO_2 disc sintered from SnO_2 powder	Ar or O_2 or N_2 or Air	glass slides	SnO_2 films composed of crystallites of approximately 10 nm in size
Vossen	53	1969				highly oriented [002] SnO_2 with some hydrated SnO
Hecq and Portier	54	1972			glass plates at 90°C	crystalline or amorphous films, depending on the product (anode-cathode separation) x (gas pressure)

was of negligible thickness and therefore undetectable except by inference.

An example of the first kind is work by Kerr and MacNaughtan (55), who obtained blue-black coatings on Sn in solutions containing high concentrations of Na_2HPO_4. Specifically, they used an aqueous solution containing 100 g/l $Na_2HPO_4.12H_2O$ and 20 cc/l H_3PO_4 (specific gravity 1.75). Over a wide range of current density the films were colourless below 60°C, various shades of gray between 60°C and 90°C and blue-black above 90°C. At 90°C a minimum current density of 11 mA/cm^2 was necessary to form a continuous film. Up to about 32 mA/cm^2 the current efficiency increased and above that remained constant. On the assumption that the film was SnO_2 (they thought that the film that forms was probably the hydrated oxide, $SnO_2 \cdot H_2O$) the thickness of the film formed in 4 min at 39 mA/cm^2 was 1.8×10^3 nm. The thickness increased with the time of treatment, with thicker films tending to flake off.

Kerr (56) prepared anodic films on tin in sodium hydroxide solutions. At 20°C a brown film was formed on the anode, regardless of other conditions. At 50°C a yellow film was formed and much more Sn went into solution, especially at low current densities. At high current density the brown film was formed and very little Sn went into solution. The yellow film was very thin and unstable, especially when removed from the Sn surface while moist, and could be shown to consist of SnO_2 68.5, SnO 12.4 and H_2O 19.1%. It was soluble in alkalies and acids. The brown film may become much thicker and more dense and was shown to consist of SnO_2 80.9, SnO 9.3 and H_2O 9.8%. The brown film was more stable than the yellow, but it was changed to a white powder by salt solutions or prolonged atmospheric exposure.

Bianchi (57) examined the conditions leading to passivation of a Sn

anode in an NaOH solution. Three different types of film were obtained depending on the current density, varying in appearance from dark to light brown. Addition to the alkaline bath of Na_2CO_3, $NaCH_3COO$, NaCl, K_2SiO_3 or gelatin influenced the current density at which passivation took place.

The above examples were all of the type where the films were thick, badly adherent, and discoloured. In other work the result was essentially the opposite, with the films having a negligible thickness.

For example, Shams el Din and Adb el Wahab (58) studied the anodic oxidation of Sn in NaOH solutions of different concentration. Primary passivity was obtained in all solutions when the metal was covered with a film inferred to consist of $Sn(OH)_2$ or SnO (voltage <2). Permanent passivity set in when supposed $Sn(OH)_4$ formed as a continuous layer on the electrode surface. They noted the competition between anodic formation and chemical dissolution of the supposed $Sn(OH)_4$.

Pugh et al. (59) made an assessment of the formation, composition and properties of protective films on electrodeposited Sn coatings. The alkaline electrolytes were variously 0.1N and N Na_2CO_3, 0.1N and N NaOH, 0.1M $Na_2B_2O_7.10H_2O$. Two steps were involved in the process, the first involving either $Sn(OH)_2$, as inferred from V vs I curves, or SnO or $2SnO.H_2O$, as deduced from electron diffraction patterns. In the second stage, oxidation to $Sn(OH)_4$ or SnO_2 was believed to take place.

Hampson and Larkin (60) determined the differential capacitance of polycrystalline Sn electrodes in a 0.1-0.0007 M $NaClO_4$ solution. They noticed "the formation of oxide or hydroxide films", with a typical thickness of perhaps 3 Å.

Hampson and Spencer (61) studied the anodic behaviour of tin in

potassium hydroxide solution. The structure of the film on passive anodes was assessed. They noted that discharge of OH^- on a passive electrode occurred when a 50-110 Å film of SnO_2 covered the anode.

1.2.5 Gas-oxidation of metallic tin - One of the first comprehensive and carefully carried out studies of oxide films formed on tin in air was by Britton and Bright (62). Films were detached from the metal substrate by the following method: "The metal specimen carrying its film and a coating of Formavar (a solution of 0.5-2% Formavar in chloroform or trichlorethylene), with the edges trimmed to expose bare tin, is placed in a glass vessel with one edge resting in a pool of mercury. The mercury amalgamates rapidly with the tin and soon rises up the specimen under the surface films. The film can then be peeled from the surface." The Formavar can then be dissolved in chloroform. The oxide formed on tin heated in air at 200°-220°C was identified as stannous oxide. At temperatures below 180°C the composition is uncertain and the film may be amorphous. This is of importance as tentatively establishing the amorphous-crystalline transition of SnO to occur at ~200°C.

The observation of SnO is in accordance with the information given by previous investigators (63,64). It differs from the findings of Kutzelnigg (65) who obtained stannic reactions from films removed from the metal with ferric chloride solutions.

Kuznetsov (9) prepared SnO_2 by means of oxidation of a metallic tin layer in air at high temperature. He describes the main results in these terms: "The oxidation reactions proceed in two stages: in the beginning at 200°C the metal was completely oxidized to SnO and then converted in bulk to SnO_2 by further heating in the range 400°-450°C. The small part of SnO that remained unoxidized decomposed spontaneously into the dioxide and metallic

tin at these temperatures. As a result of similar reactions, there arises on the base layer an SnO_2 film, which contains small impurities of SnO and Sn in its structure." He obtained transparent layers with thicknesses up to 200 mm.

Boggs et al. (66) examined, by means of electron microscopy and electron diffraction, oxide films on pure tin, under different conditions of time, temperature and oxygen pressure. Results show that only one crystalline oxide, α-SnO, is formed under all of the oxidation conditions investigated. As far as the thickness of the film is concerned, they suggested a value of about 10 nm for specimens oxidized at 190°C and 10^{0} torr oxygen for 100 min. They were able to identify crystalline α-SnO, down to temperatures as low as 75°C, in disagreement with Britton and Bright, who claim that the film is amorphous below 180°C.

The formation of SnO_2 was observed by Baird et al. (67) when metallic tin films were oxidized within the electron microscope. The electron beam was used as a source of heat. The Sn-films were single-crystals and SnO_2 formed below the melting point of tin.

1.2.6 Growing of single-crystals - We have seen that polycrystalline films of SnO_2 can be prepared by the hydrolysis of stannic chloride in substrates heated to 400°-800°C. On the other hand, SnO_2 single crystals can be grown by vapour-deposition techniques at temperatures exceeding 1000°C. We will refer to a few examples of the latter technique, though it is out of the context of this thesis. We are, in fact, interested in techniques where SnO_2 can be prepared in an amorphous state, thus permitting a study of its crystallization behaviour. The examples to be considered are chosen to represent basically different approaches, in which the species transported is respectively SnO_2, Sn, $SnCl_4$ or SnI_4.

Marley and MacAvoy (68) prepared single-crystals of stannic oxide by a high temperature vapour deposition. The method employed involved the high temperature vapour transport of SnO_2 powder, via a decomposition process to SnO and O_2, followed by subsequent reoxidation and deposition of SnO_2 crystals at lower temperatures. The temperature of the vaporization site was 1300°-1650°C.

Reed et al. (69) used a reaction between tin vapour and oxygen at 1350°C.

Nagasawa et al. (70) grew SnO_2 crystals using the vapour reaction of $SnCl_4$ with H_2O. Vapours of H_2O and $SnCl_4$ were transported by carrier gases (O_2 and N_2) into the growing zone, which was at a temperature between 1100° and 1300°C.

SnO_2 single-crystalline films, providing electrically conductive, transparent coatings, were prepared by Caslavska and Roy (71). Substrates were rutile single-crystals at 450°-650°C. SnI_4 was used for the hydrolysis reaction: $SnI_4 + 2H_2O = SnO_2 + 4HI$.

Besides the examples based on vapour transport we would point out that liquid phase procedures have also been used.

Kunkle and Kohnke (72) report an evaporation method in which SnO_2 crystals "are grown from a Cu_2O flux". It is of interest to note here that these authors mention having experienced some difficulty in "operating above 1250°C where there seems to be an increased tendency for the formation of small amounts of free copper and/or tin which react with platinum and destroy the crucible". We have experienced a similar effect ourselves when trying to evaporate SnO_2 powder. In fact, at 1250°C and at an oxygen partial pressure $<10^{-10}$ torr, SnO_2 dissociates according to the reaction, $SnO_2(s) \rightarrow Sn(\ell) + O_2(g)$ (cfr. Section 4.4.4).

Gruner (73) described a simplified method of growing SnO_2 crystals at 1300°C. Crystals were grown from pure Sn in corundum crucibles, the roughness of the crucible walls allowing access of the necessary oxygen for oxidation of the Sn to SnO_2.

1.2.7 Ion-bombardment of SnO_2 - Naguib and Kelly (74) have developed three criteria to predict the structural stability of solids under ion-impact, in particular to indicate the likelihood of crystalline-amorphous transitions, amorphous-crystalline transitions, or stoichiometry changes. The first criterion states that the ratio of crystallization temperature (Tc) to melting temperature (Tm) must be lower than 0.30 for crystallinity to be preserved. This temperature-ratio criterion worked for some 33 out of 34 substances for which information was available (74). (As a matter of fact, the success of this criterion is somewhat greater, as the article in question did not consider mixed oxides such as columbite, wolframite or zircon.) The above mentioned substances are tabulated in Table 1.III, while Table 1.IV gives all mixed oxides for which information is available.

The second criterion of Ref. (74) states that the ionicity must be greater than 0.59 for crystallinity to be preserved and less than 0.47 for amorphicity to be preserved. It was successful in 50 out of 53 cases for which information was given (74). Mixed oxides are here difficult to include, as it is not clear whether a material such as zircon should be regarded as having the ionicity of ZrO_2, or of SiO_2, or of the average. This criterion is basically empirical, without an explicit underlying physical model.

A third criterion for oxides stability under ion-impact is one concerned with oxygen loss. Oxides losing oxygen under ion-impact, namely undergoing a stoichiometry change, usually show a lower enthalpy change for

TABLE 1.III

Temperature-ratio criterion and the structural stability of crystalline solids under ion-impact (from Ref. 74)

Substance	Tc/Tm (K/ K)	Observed structure following ion-impact
Ge	0.61	am
Si	0.59	am
Bi_2Te_3	0.55	am
As_2Se_3	>0.47	am
SiC	≥0.33	am
MoS_2	∿0.39	am
GaSb	>0.64	am
Si_3N_4	0.31-0.41	am
AlAs	0.31	am
MoO_3	0.49	am
TeO_2	0.53	am
AlP	0.32	am
GaAs	>0.38	am
InSb	>0.78	am
WO_3	0.43	am
InAs	∿0.64	am
GaP	∿0.38-0.44	am
Bi_2O_3	0.49	am
GeO_2	0.65	am
Fe_2O_3	∿0.43	am
SiO_2	0.57	am
V_2O_5	0.61	am
Al_2O_3	0.59	am
Cr_2O_3	0.27	am
Nb_2O_5	0.42-0.49	am

Temperature-ratio criterion and the structural stability of crystalline solids under ion-impact (from Ref. 74)

(continued)

TiO_2	0.35	am
BeO	0.21	cr
Ta_2O_5	0.38-0.46	am
ThO_2	<0.20	cr
ZrO_2	0.27	cr
HfO_2	∿0.25	cr
UO_2	0.30	cr
MgO	∿0.15	cr
CaO	∿0.22	cr

TABLE 1.IV

The ratio Tc/Tm or Tc/Tp for various multiple-oxide minerals

(Tc = crystallization temp., Tm = melting temp., Tp = peritectoid temp.)(from Ref. 75)

Mineral	Formula	Tc(K)	Tm or Tp	Tc/Tm or Tc/Tp	Observed structure following ion-impact
apatite	$CaF_2 \cdot 3Ca_3(PO_4)_2$	865	1923	.35-.45	am
cobalt titanate	$CoO.TiO_2$	850	1743	.49	am
columbite	$(Fe,Mn)O.(Nb,Ta)_2O_5$	810-905	1673-1873	.43-.54	am
enstatite	$MgO.SiO_2$	875-1075	1823	.45-.59	am
fergusonite	$(Ce,Y)_2O_3 \cdot Nb_2O_5$	925-975	1673-1873	.49-.58	am
hardystonite	$2CaO.ZnO.2SiO_2$	725*	1698	.43	am
olivine	$2(Mg,Fe)O.SiO_2$	775*	1453-2163	.36-.53	am
samarskite	$Y(Fe,U)O_3.(Ta,Nb)_2O_5$	975	~2053	.47	am
thorite	$ThO_2.SiO_2$	990-1125	2248	.44-.50	am
zircon	$ZrO_2.SiO_2$	1035	1949	.50-.53	am

* Tc(K) for fission-track annealing.

partial atomization (leaving a residue of a lower oxide) than for complete atomization (leaving no residue). For example with TiO_2 we have the following:

partial atomization leaving residue of Ti_2O_3, ΔH_a = 5.1 eV

partial atomization leaving residue of TiO, ΔH_a = 6.4 eV

complete atomization leaving no residue, ΔH_a = 6.4 eV

A bombardment-induced change $TiO_2 \rightarrow Ti_2O_3$ is thus predicted. The oxygen loss can in turn be detected by the remarkable increase in the electrical conductivity that normally accompanies it. In fact, an increase in the concentration of oxygen vacancies in some cases implies an increase in conductivity, according to the following:

$$O_a + 2e^- + \frac{1}{2} O_2 \rightleftarrows \text{oxygen ion on lattice site}$$

In other cases, the oxygen loss leads to a completely different oxide having metallic properties.

These criteria are readily applied to SnO_2. The ratio Tc/Tm is here ~0.41 and the ionicity 0.43 (to be discussed in Chapter 5) both of which suggest easy amorphizability. The criterion relating to oxygen loss (to be discussed in Chapter 6) suggests that loss will not take place.

There is apparently no other information on ion-impact effects with SnO_2 to be considered, as this substance, in spite of its increasing electronic interest, has never been the object of an explicit ion-bombardment study.

1.3 Conclusions drawn from the literature survey

Basically four different approaches have been used to form SnO_2

films. (a) Most commonly the films have been formed by CVD, for example by passing $SnCl_4$ or $SnCl_4$ plus water vapour over a substrate held at 400°-800°C (2,20,24,27,29-31,33-35,38)or by a similar procedure involving other volatile tin compounds (1,9,16,22,23,25,27,28,32,35,71). (b) In other work vacuum evaporation of SnO_2 (41) has been used so as to take advantage of the unusually high vapour pressure (76). Closely related is the reactive evaporation of Sn (35,42). (c) SnO_2 films have been successfully prepared by reactive sputtering either of Sn cathodes (11,43,44,46-48,50, 51,54) or of SnO_2 itself (10,52). (d) Finally, gas oxidation of metallic tin has sometimes (9,65,67), though not always (62-64,66), produced SnO_2 films.

The present knowledge, as far as structural characterization is concerned, is largely confined to two results: chemically deposited layers are invariably crystalline (2,9,27,30,35) while evaporated or reactively sputtered layers are normally (11,35,41,45-48,54) though not always (43, 50,52-54) amorphous. Evidently the range of crystallization temperatures for supported SnO_2 films lies in the interval between the substrate temperatures used in chemical deposition and those used in evaporation or sputtering.

Concerning the possibility of obtaining SnO_2 films by anodizing Sn at high voltages, work with both acidic (55,60) and basic (56,58,59) electrolytes has generally involved low voltages (<5) and never values ($>>5$) characteristic of the growth of thick, uniform, protective films analogous to those formed on Si (77) and Ge (78). More specifically, Hampson and Larkin (60) showed that the capacitances of anodically polarized Sn had values appropriate to perhaps a monolayer of oxide when acidic electrolytes

were used. Kerr (56), by contrast, obtained thick films (up to 10^4 nm) with basic electrolytes but the films neither showed interference colours nor supported a significant voltage. Only Bianchi (57) appears to have succeded in polarizing Sn at a high voltage. Using an electrolyte of water with NaOH and potassium silicate he reached 100 V, though the film was described as a "thick, black crust" and this cannot, therefore, be considered as a meaningful way to prepare anodic SnO_2.

As far as ion-impact effects are concerned, there is, as already mentioned in Section 1.2.7, no previously published study in which SnO_2 was considered explicitly. We have therefore made use of the general criteria (74) and concluded that SnO_2 should amorphize but not lose oxygen.

Though the instability of a crystalline oxide under ion-impact, i.e. its amorphization, is not by itself an unusual result, it is known that amorphizability is often the precursor of bombardment-induced oxygen loss. If such loss were to occur with SnO_2 (in spite of our prediction that it will not), the result would be of fundamental importance in device fabrication owing to the semiconducting nature of sub-stoichiometric SnO_2. Its conductivity varies as much as 5 orders of magnitude due to stoichiometry changes (79). Besides, amorphizability infers the possibility of etching and this again is vital for device fabrication.

We will in the following two chapters describe experiments in which SnO_2 films have been prepared both by sputtering and by anodizing. The anodically-formed films are perhaps the most unique of the two types, as it was found possible (apparently for the first time) to anodize Sn in a "normal manner". For example, anodizing voltages up to 65 V were used and the growing films showed 6 orders of interference colours. Major emphasis

will be put in these two chapters into characterizing the films structurally. This will be seen to lead to explicit information on crystallization and on grain growth.

The fourth chapter will describe an attempt to prepare SnO_2 films by O_2^+ bombardment of Sn. The nominal objective failed in that the films had the stoichiometry SnO.

Ion-impact effects with SnO_2 films will be considered in Chapter 5, where results will be given concerning sputtering and amorphization.

This will end Part 1 of the thesis, devoted, as has been seen, to the preparation and properties of SnO_2 films.

REFERENCES

1. R. Groth, E. Kauer, and P. C. v.d. Linden, Z. Naturforschung. 17a, 789 (1962).

2. J. A. Aboaf, V. C. Marcotte and N. J. Chou, J. Electrochem. Soc. 120, 701 (1973).

3. H. M. Naguib and R. Kelly, J. Phys. Chem. Solids 33, 1751 (1972).

4. D. K. Murti and R. Kelly, Surface Science 47, 282, (1975).

5. D. R. Kudrak and M. J. Sienko, Inorg. Chem. 5, 880 (1967).

6. T. E. Parker and R. Kelly, Ion Implantation in Semiconductors and Other Materials, edited by Billy L. Crowder, p. 551.

7. T. E. Parker and R. Kelly, J. Phys. Chem. Solids 36, 377 (1975).

8. J. W. Ward, Applic. and Ind. 16, 408 (1955).

9. A. Ya. Kuznetsov, Soviet Physics--Solid State 2,30 (1960).

10. L. Holland and G. Siddal, Vacuum 3, 375 (1953).

11. Anonymous, Nature 169, 829 (1952).

12. H. A. Klasens and H. Koelmans, Solid-State Electron. 7, 701 (1964).

13. T. N. Kennedy and J. D. Mackenzie, J. Non-Cryst. Sol. 1, 326 (1969).

14. R. F. Hudson, Proc. Intern. Congr. Pure and Appl. Chem.(London) 11, 297 (1947).

15. J. S. Littleton, U.S. Patent 2, 118, 795 (1938).

16. J. K. Davies, U.S. Patent 2, 564, 677 (1951).

17. J. M. Mochel, U.S. Patent 2, 564, 707, U.S. 2, 564, 987, U.S. 2, 564, 709, U.S. 2, 564, 710 (1951).

18. J. W. McAuley, U.S. Patent 2, 692, 836 (1954).

19. R. Gomer, Rev. Sci. Instr. 24, 993 (1953).

20. H. Ladwig, Silikattechnik. 15 (6), 182 (1964).

21. H. Inokuchi and Y. Tokuda, Nippon Kagaku Zasshi 85, 201 (1964).

22. R. E. Aitchison, Australian J. Appl. Sci. 5, 10 (1954).

23. R. L. Ackerman, U.S. Patent 2. 689, 803 (1954).

24. A. Fisher, Z. Naturforsch. 9a, 508 (1954).

25. A. Ya Kuznetsov, A. V. Kruglova and B. P. Kryzhanovskiĭ, Zavodskaya Lab. 22, 993 (1956).

26. A. Ya. Kuznetsov, Zavodskaya Lab. 23, 90 (1957).

27. K. Ishiguro, T. Sasaki, T. Arai, and I. Imai, J. Phys. Soc. Japan 13, 296 (1958).

28. A. Ya. Kuznetsov, A. V. Kruglova and B. P. Kryzhanovskiĭ, J. Appl. Chem. of the U.S.S.R. 32,1186 (1959).

29. V. K. Miloslavskiĭ, Optics and Spectroscopy 7, 154 (1959).

30. I. Imai, J. Phys. Soc. Japan 15, 937 (1960).

31. V. K. Miloslavskiĭ and S. P. Lyashenko, Optics and Spectroscopy 8, 455 (1960).

32. V. N. Filimonov, Optics and Spectroscopy 8, 139 (1960).

33. I. Soleilhavoup and B. Dreyfus-Alain, Colloq. Intern. Dispositifs Semicond., Paris, 1, 718 (1961).

34. H. Koch, phys. stat. sol. 3, 1059 (1963).

35. F. v.d. Maesen and C. H. M. Witmer, Proc. 7th Intern. Conf. on the Phys. of Semiconductors, p. 1211, Paris (1964).

36. I. F. Tigane, Soviet Physics--Solid State 7, 212 (1965).

37. W. P. Ganley, J. Opt. Soc. Am. 55 (12), 1692 (1965).

38. I. Golovcenco, Gh. Ioan Rusu, V. Stefan and M. Rusu, Analele Stiint. Univ. "Al. I. Cuza", Iasi, Sect. Ib. Fiz. 11, 77 (1965).

39. E. A. Krogius and V. A. Vlasov, Steklo. Tr. Inst. Stekla. 1 (129), 79 (1966).

40. O. V. Vorob'eva and T. F. Polurotova, Izvestiya Akad. Nauk S.S.S.R. 7, 266 (1971).

41. M. Shiojiri, H. Morikawa, and E. Suito, Sixth Intern. Cong. for Electron Microscopy, p. 467, Kyoto (1966).

42. W. Spence, J. Appl. Phys. 38, 3767 (1967).

43. J. S. Preston, Proc. Roy. Soc. A 202, 449 (1950).

44. J. S. Preston, U.S. Patent 2, 769, 778 (1956).

45. D. R. Secrist and J. D. Mackenzie, Am. Ceram. Soc. Bull. 45(9), 784 (1966).

46. W. R. Sinclair and F. G. Peters, J. Am. Ceram. Soc. 46, 20 (1963).

47. W. R. Sinclair, F. G. Peters, D. W. Stillinger, and S. E. Koonce, J. Electrochem. Soc. 112, 1096 (1965).

48. M. L. Lieberman and R. C. Medrud, J. Electrochem. Soc. 116, 242 (1969).

49. P. T. Sarjeant and R. Roy, J. Am. Ceram. Soc. 50, 500 (1967).

50. V. M. Vainshtein, Simp. Protsessy Sin. Rosta Krist. Plenok Poluprov. Mater., Tezisy Dokl., p. 296, Novosibirsk (1965).

51. M. Jachimowski and E. Leja, Acta. Phys. Pol. 30(1), 45 (1966).

52. S. Yamanaka and T. Oohashi, Jap. J. Appl. Phys. 8, 1058 (1969).

53. J. L. Vossen, Symposium on Sputtering, Vacuum Society Meeting, Rochester, September 1969.

54. M. Hecq and E. Portier, Thin Sol. Films 9, 341 (1972).

55. R. Kerr and D. J. MacNaughtan, J. Electrodep. Tech. Soc. 12, 19 (1937).

56. R. Kerr, J. Soc. Chem. Ind. 57, 405 (1938).

57. G. Bianchi, Chim. Ind. 29, 295 (1947).

58. A. M. Shams El Din and F. M. Abd el Wahab, Electrochim. Acta. 9, 883 (1964).

59. M. Pugh, L. M. Warner, and D. R. Gabe, Corrosion Sci. 7, 807 (1967).

60. N. A. Hampson and D. Larkin, J. Electrochem. Soc. 115, 612 (1968).

61. N. A. Hampson and N. E. Spencer, Brit. Corros. J. 3(1), 1 (1968).

62. S. C. Britton and K. Bright, Metallurgia 56, 163 (1957).

63. M. Bound and D. A. Richards, Proc. Phys. Soc. 51, 256 (1939).

64. R. K. Hart, Proc. Phys. Soc. B. 65, 955 (1952).

65. A. Kutzelnigg, Zeitsch. Anorg. Chem. 202, 418 (1931).

66. W. E. Boggs, P. S. Trozzo and G. E. Pellissier, J. Electrochem. Soc. 108, 13 (1961).

67. T. Baird, J. R. Fryer and E. V. Riddel, Surface Science 28, 525 (1971).

68. J. A. Marley and T. C. MacAvoy, J. Appl. Phys. 32, 2504 (1961).

69. T. B. Reed, J. T. Roddy and A. T. Mariano, J. Appl. Phys. 33, 1014 (1962).

70. M. Nagasawa, S. Shionoya and S. Makishima, Jap. J. Appl. Phys. 4(3), 195 (1965).

71. V. Caslavska and R. Roy, J. Appl. Phys. 40, 3414 (1969).

72. H. F. Kunkle and E. E. Kohnke, J. Appl. Phys. 36, 1489 (1965).

73. H. Gruner, Naturwissenschaften 55, 132 (1968).

74. H. M. Naguib and R. Kelly, Radiation Effects 25, 1 (1975).

75. E. Giani, D. K. Murti, H. M. Naguib and R. Kelly, To be published.

76. R. Colin, J. Drowart, and G. Verhaegen, Trans. Faraday Soc. 61, 1364 (1965).

77. M. A. Wilkins, Harwell (U.K.) Report AERER5875 (1968).

78. S. Zwerdling and S. Sheff, J. Electrochem. Soc. 107, 338 (1960).

79. A. F. Peterson, Ph.D. thesis, 1968--University Microfilms, Inc., Ann Arbor, Michigan, U.S.A.

CHAPTER 2

SPUTTERED FILMS

2.1 Introduction*

Sputtering is the term describing the ejection of atoms from a solid surface due to the impact of high kinetic energy particles. The ejected atoms can be deposited on a substrate, providing a method of constructing thin films atom by atom. Since sputtering is a non-evaporative process, high-melting point materials like Ta and W, and even ceramics, can be deposited. This makes the technique useful in microelectronics and other areas where films of such materials are desired.

The phenomenon of sputtering was first observed as far back as 1852, when an Englishman named Grove noticed that in a normal glow discharge, cathode material was deposited on surrounding surfaces. In the 1920's sputtering was widely used for depositing metals, mainly gold and silver, on fabrics for decorative purposes. In the same period, sputtering got into electronics: the old Ediphone records required a mold that could be made from the wax master cut in the recording studio. Sputtering proved convenient because, being essentially a "cold" process,

---

* The material of this introduction is adapted from an article by G. Wehner, which appeared in the September 1968 issue of Science and Technology.

it could deposit a metal film directly onto the wax, yet reproduce faithfully every nuance of the surface.

Once the technology of high vacuum was mastered, sputtering pretty much went out of the picture in many applications because vacuum evaporation was the simpler and more straightforward method of depositing thin films. Then in the late 1950's, came the concept of microminiaturization of electronic circuits, and with it the need to deposit films of refracting metals like Nb, W and Mo, materials with melting points far too high for simple vacuum evaporation. Thus sputtering was rejuvenated.

Researchers have found that, in sputtering, the material is always transferred in the same composition, so that the deposited films have the same composition as the original target, even if the target is some complex alloy. This ability to deposit material without influencing its composition is one of the distinct advantages of sputtering, and one of the reasons it is now so popular. Another reason is that it has been learned recently how to sputter electrical insulating materials, as well as metals and alloys. This is done using the so-called rf-sputtering. In integrated circuitry, for example, one must be able to lay down dielectric films as efficiently as one does metals and alloys. These insulators range from quartz and the simpler glasses through aluminum oxide and, more recently sophisticated materials like silicon nitride. All these can be deposited by sputtering, as can Pyrex glass. Finally, it is an established fact that sputtered films adhere far more strongly to most substrates than films deposited by other techniques such as vacuum evaporation or plasma-spraying.

2.2 Experimental

2.2.1 Reactive sputtering - The preparation of SnO_2 films by reactive sputtering is an already well-understood process. In the present work the equipment was of the diode type (e.g., 1,2), with a 50 mm diameter Sn cathode. The substrates, consisting of pieces of chemically polished Al, Ta, or V, or of cleaved KCl, or of air-annealed SnO_2, were laid on a 42 mm diameter anode table placed 30 mm beneath the cathode. The dark-space region of the discharge usually extended about 20 mm away from the cathode when the gas pressure was about 1×10^{-2} torr. The gas was a 1:1 mixture of oxygen and argon which was purified by being passed through a liquid-nitrogen trap. Applied d-c voltages ranged from 1000 to 3000 and the discharge current was typically 10 mA. Those films which were deposited on KCl could be stripped using water.

2.2.2 Ion-beam sputtering - SnO_2 films were also prepared by sputtering Sn anodized to 50V with 10-30 keV Kr ions at doses ranging from 25 to 200 μ Amin/cm^2. The sputtering was performed using a high-current ion accelerator and collecting the deposit on unheated KCl (3). This method of film preparation involves a vacuum of 10^{-6} torr and the sputtered particles therefore reach the substrate with their full energy [1-60 eV (4)] and without contamination.

SnO_2 films were also prepared by ion-beam sputtering of pressed and sintered SnO_2 powder. SnO_2 being an insulating material, a tungsten filament emitting thermoelectrons was put close to the target. In this way we have been able to obtain ionic currents of 30-60 μ A (at an ion energy of 4 and 5 keV and background pressure of 1×10^{-6} torr).

Yamanaka and Oohashi (16) prepared SnO_2 films by ion-beam sput-

tering, the target material being SnO_2 pressed and sintered powder. They do not give details of the experimental technique, except for values of 4.5 kV for the applied voltage and gas pressure of 3×10^{-2} torr. They claim that films obtained were composed of crystallites with a rutile-like structure.

We obtained, in samples of the same sputtering, both amorphous as well as crystalline regions, possibly due to a temperature gradient in the supports where films were collected (gradient due to the hot tungsten filament).

The uncertainty on the structure of the as-deposited film, as well as the quite troublesome technique of sputtering an insulating material, were the reasons why we decided to build a reactive sputtering apparatus (at this time we had in fact not yet been successful in obtaining anodized SnO_2; in fact, chronologically, SnO_2 films were first sputter-deposited by ion-beam sputtering of SnO_2 pressed and sintered powder, then by reactive sputtering and finally by ion-beam sputtering of anodized tin).

2.3 Results

2.3.1 Film continuity and crystal form - The state of the films that were obtained was determined using transmission electron microscopy as well as electron diffraction. Some 400 specimens were examined, the main trends being as follows:

(i) Reactive sputtering onto KCl substrates at -100°C gave amorphous films, sometimes continuous and sometimes with an island structure (Fig. 2.1). Though the island structure is not understood, the amorphousness is a reasonable result given that most oxides deposit amorphously at low temper-

(a)

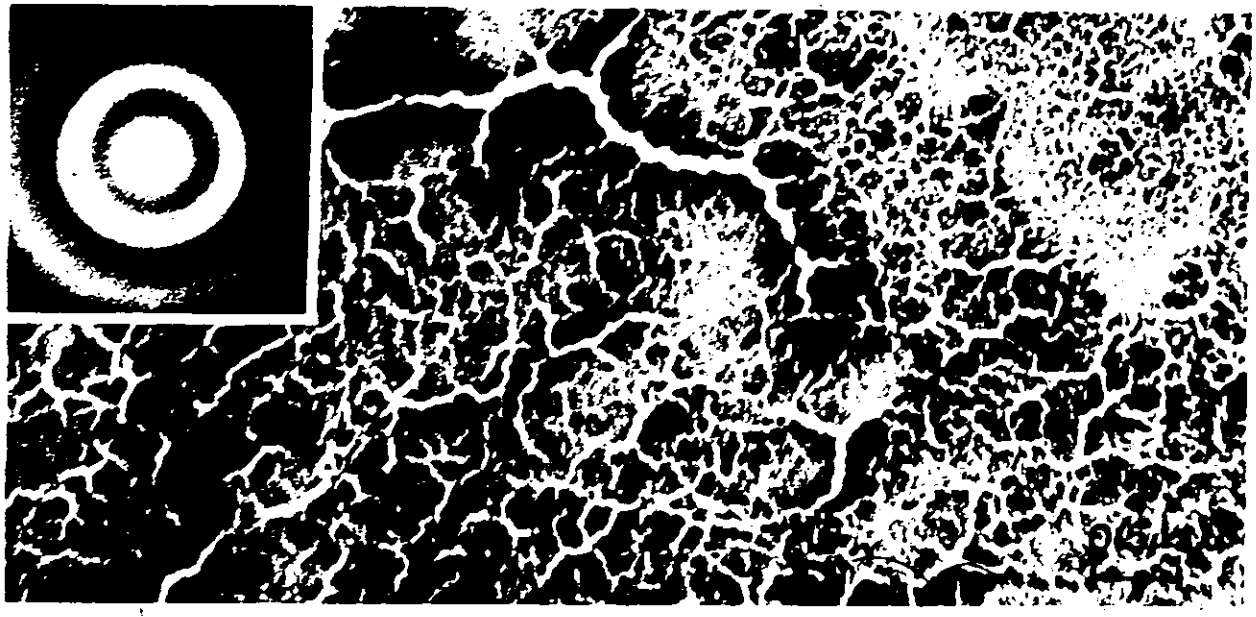

Fig. 2.1. Micrographs with mag. 22,000 of SnO_2 films formed by reactive sputtering onto KCl at -100°C. The examples are amorphous (obvious from diffraction pattern) and show in (a) an island structure, though in other instances (b) the films were continuous.

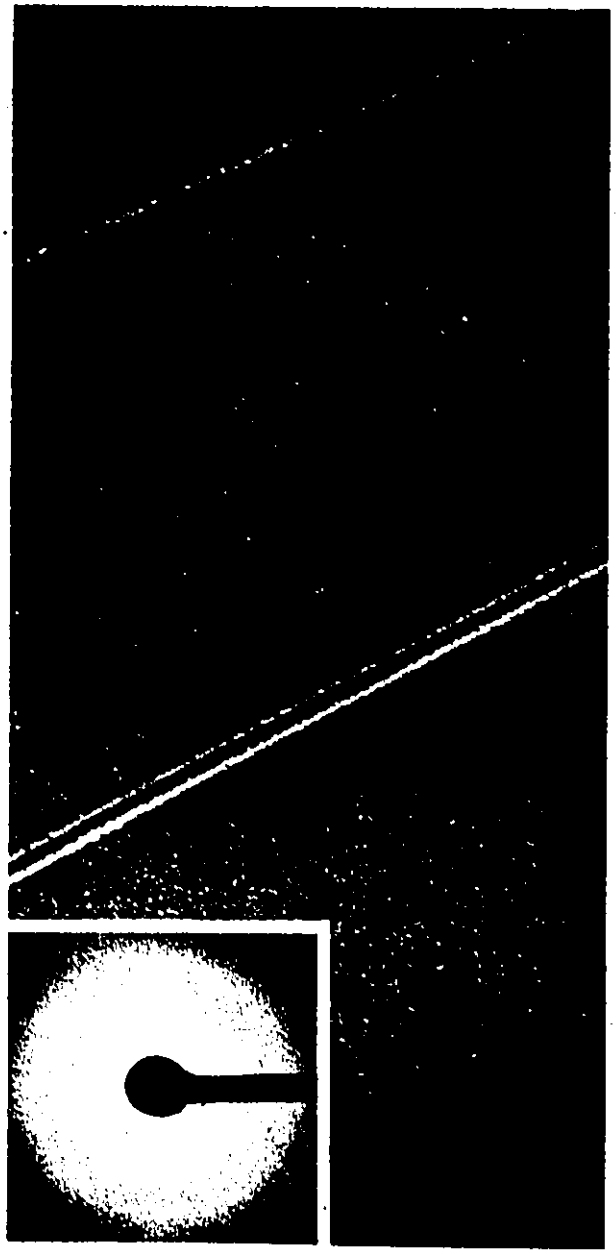

Fig. 2.1(b)

atures (3,5).

(ii) Reactive sputtering onto KCl or Ta at 25°-200°C as well as ion-beam sputtering onto KCl at 25°C, gave amorphous films which were continuous (Fig. 2.2). Apparently 25°-200°C also constitute "low" temperatures as far as SnO_2 is concerned.

(iii) Reactive sputtering onto SnO_2 single-crystals or sintered pellets at 200°C gave finely polycrystalline films with the structure of cassiterite (Fig. 2.3). This result is consistent with the ready availability of crystallization nuclei in spite of the temperature being "low".

2.3.2 Crystallization behaviour - The main trends resulted to be as follows:

(i) Unsupported films, whether formed by reactive or ion-beam sputtering (Fig. 2.4-2.6), crystallized in air at 475°-550°C, to yield grains having sizes ≤100 Å.

In Fig. 2.4 the effect of heat treatment (films stripped from KCl and then heated in air) on the crystallization of a reactively sputtered film (refrigerated substrates) is shown. The upper row of transmission micrographs illustrates the transition from an amorphous film on the left to a uniform and completely crystallized structure on the right. The corresponding electron diffraction patterns are shown in the lower row. The diffuse bands of an amorphous phase are seen in the diffraction pattern for the as-sputtered film before heat treatment (Fig. 2.4(b)). A stage just before the onset of crystallization is seen after 6 min at 450°C (Fig. 2.4(d)), the diffuse bands of the amorphous phase still being present. Crystallization is well underway at 550°C (Fig. 2.4(f)) and

(a)

Fig. 2.2. Micrographs with magnification 22,000 of SnO_2 films formed by reactive sputtering onto KCl at ∿200°C (a) or by ion-beam sputtering of anodized tin (b). Films were always amorphous (again obvious from diffraction pattern) and continuous.

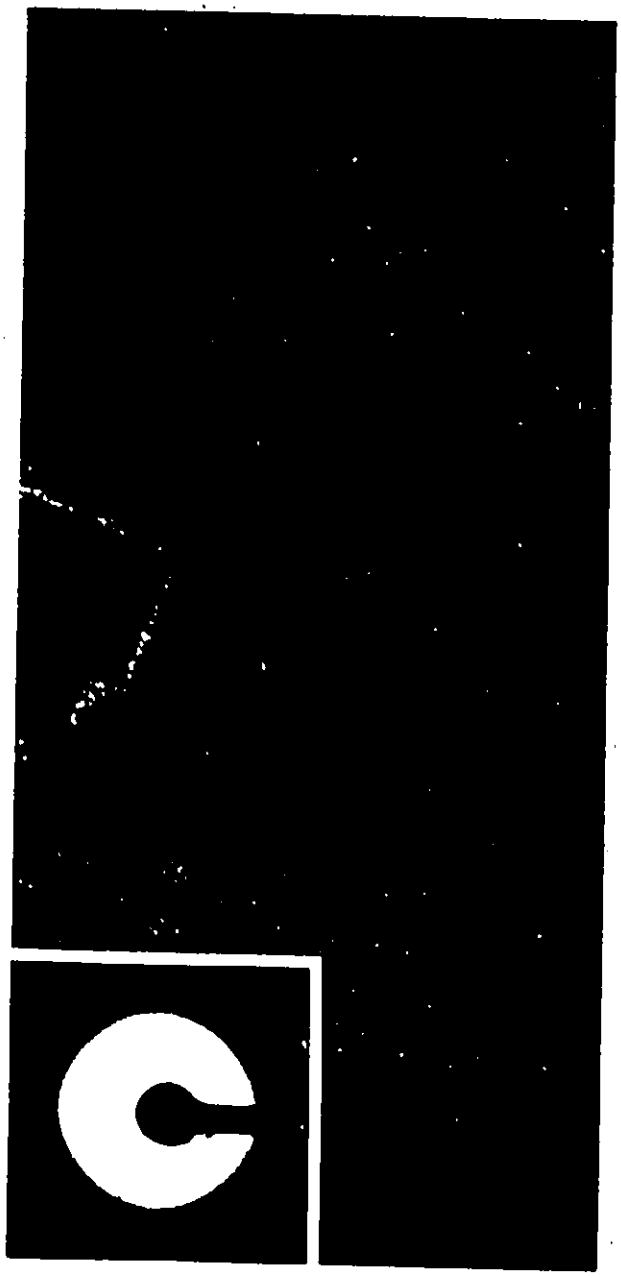

Fig. 2.2(b)

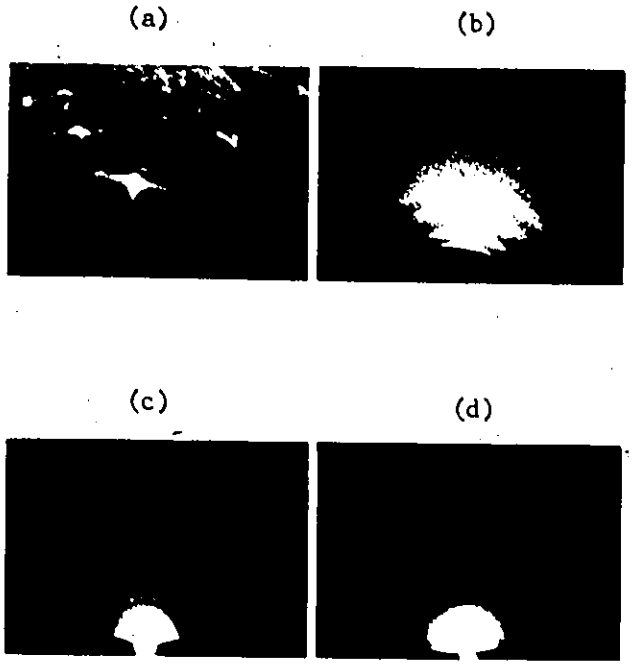

Fig. 2.3. Reflection electron diffraction patterns of (a) SnO_2 single crystal, (b) SnO_2 film deposited on SnO_2 single crystal, (c) SnO_2 sintered pellet, (d) SnO_2 film deposited on SnO_2 sintered pellet.

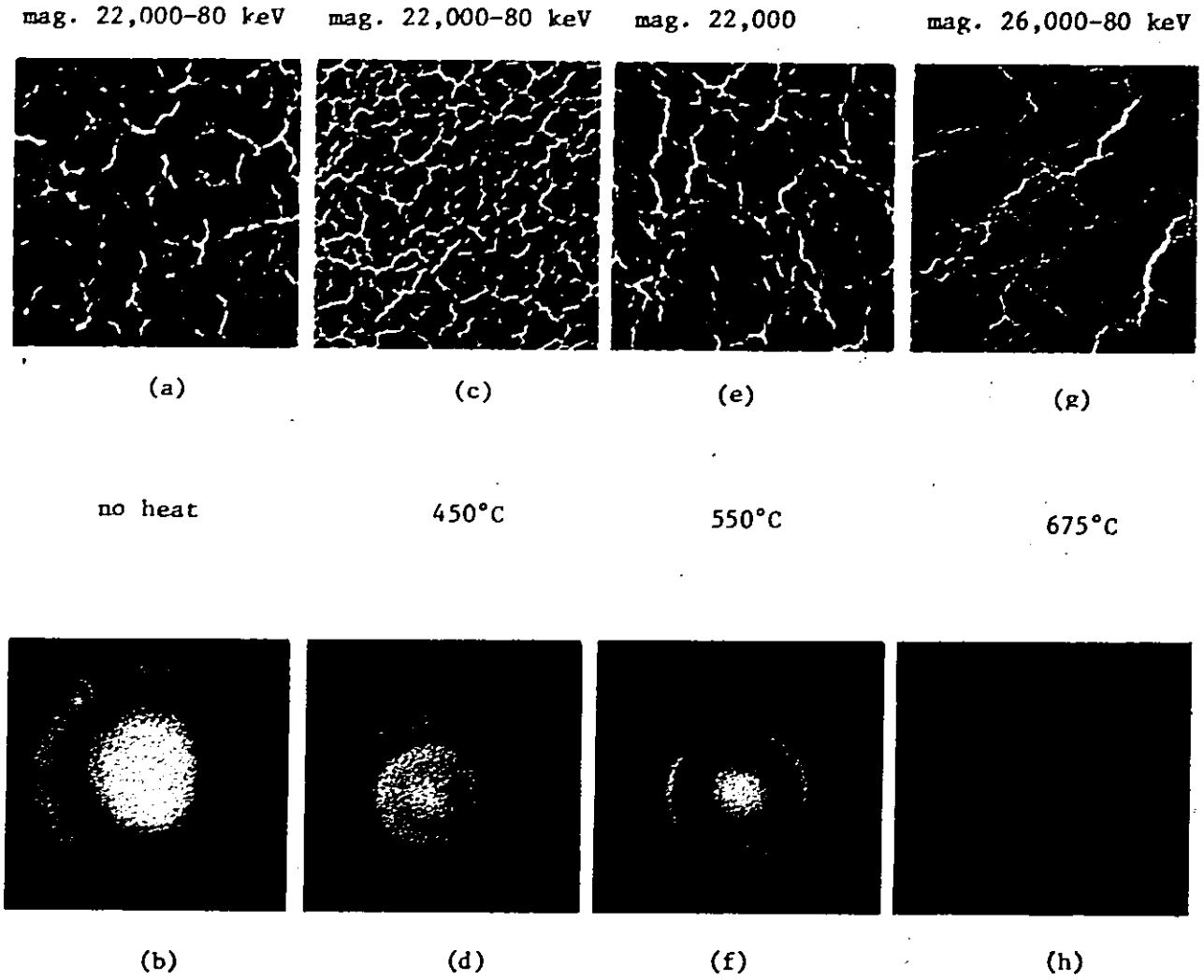

Fig. 2.4. Effect of heat treatment in air on crystallization of reactively sputtered (refrigerated substrates) unsupported SnO_2 films. The crystallization temperature is shown to be ~550°C.

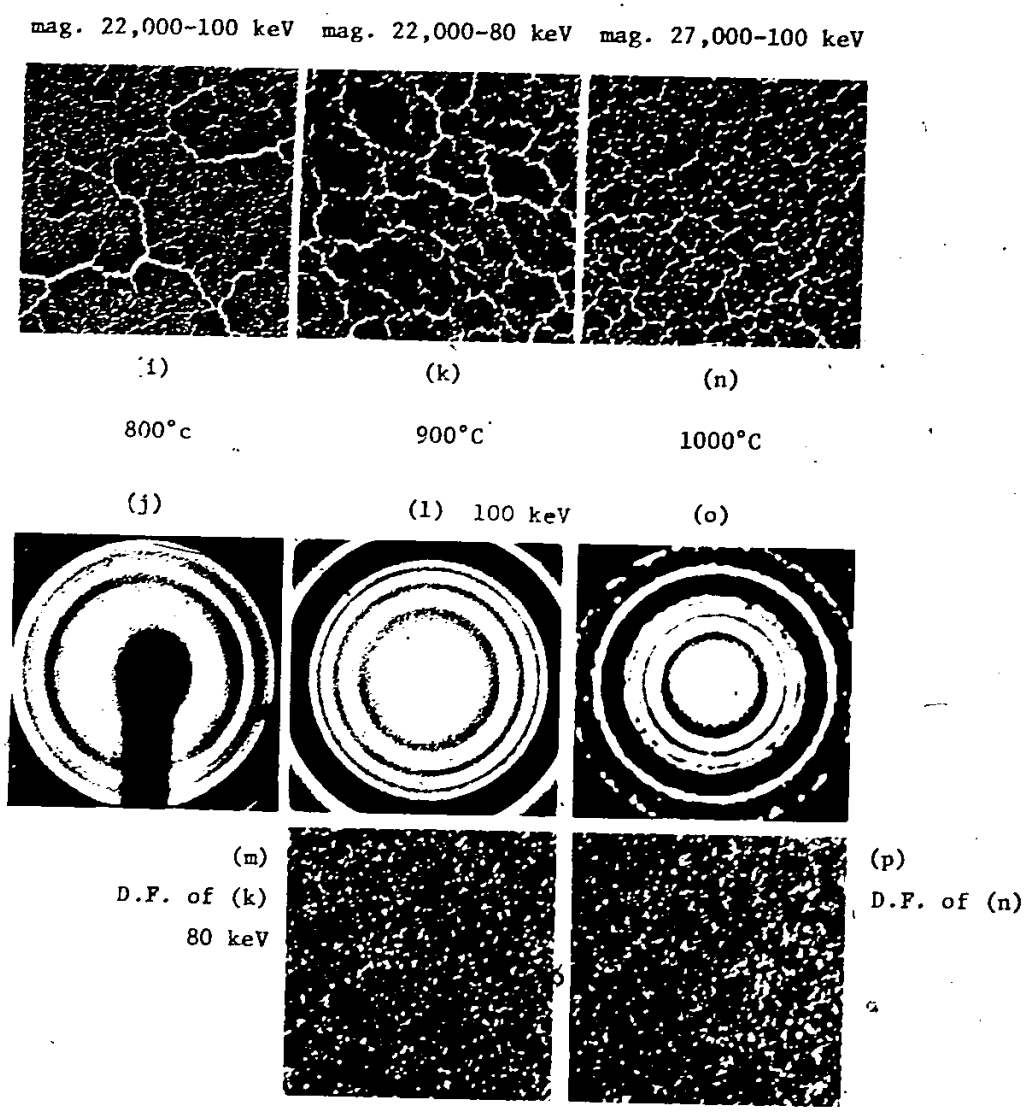

Fig. 2.4 (continued)

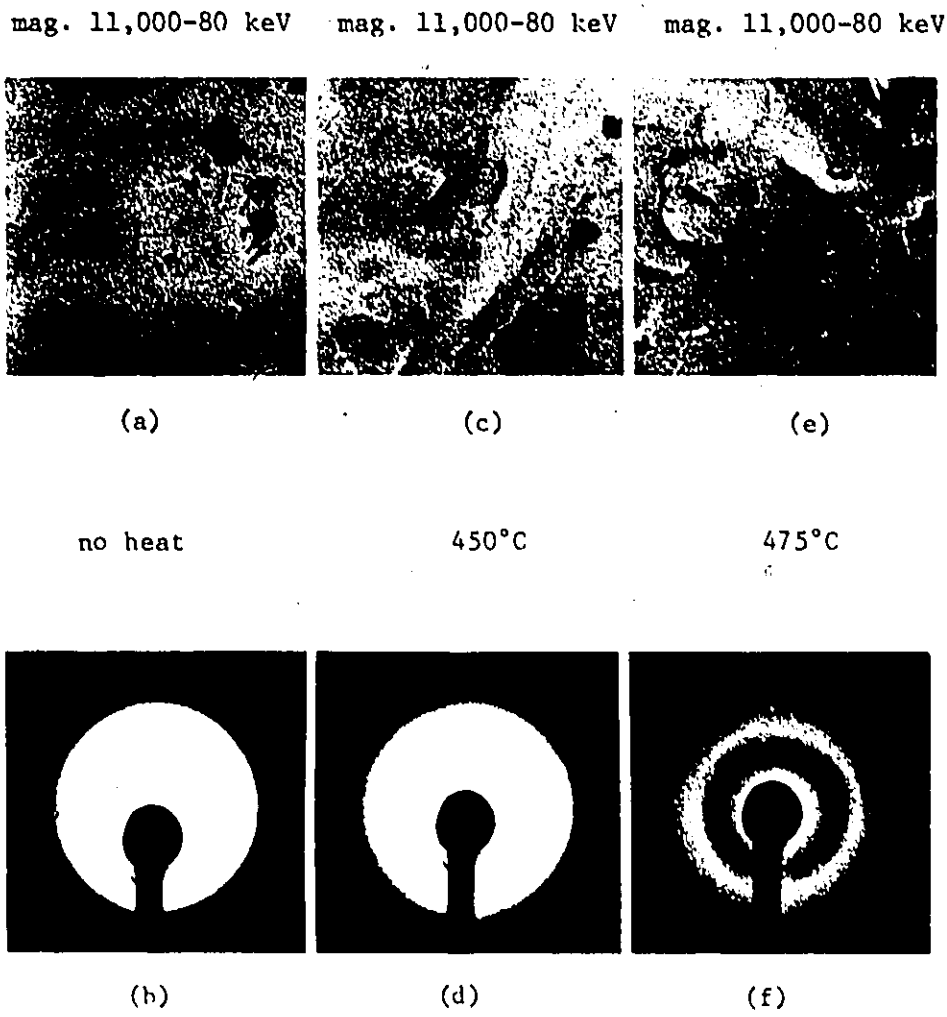

Fig. 2.5. Effect of heat treatment in air on crystallization of reactively sputtered (heated substrates) unsupported SnO_2 films. Separate specimens were used for each treatment (6 min hold times in furnace). The crystallization temperature is shown to be ~475°C.

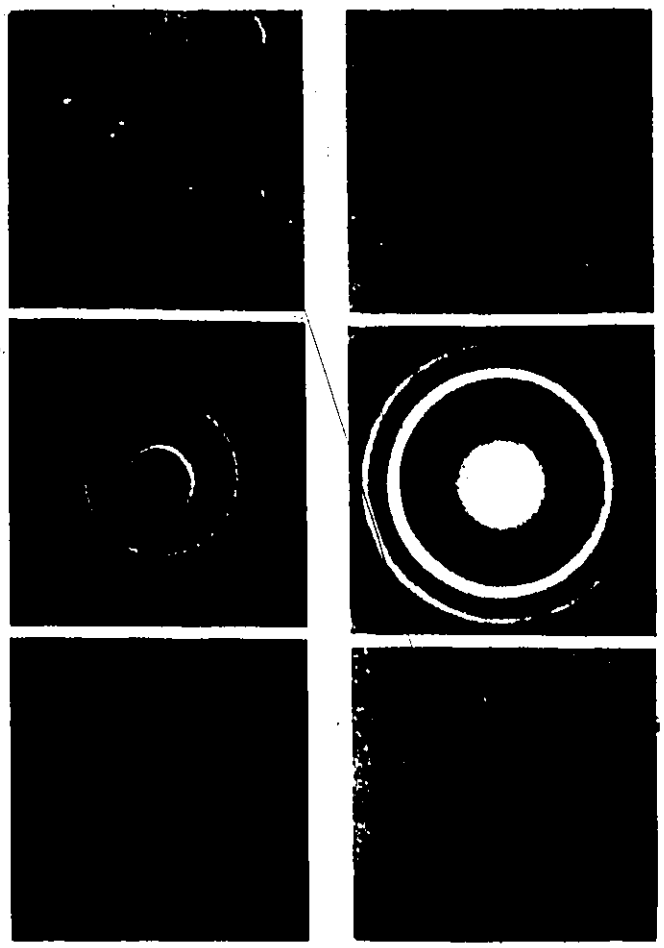

Fig. 2.5 (continued)

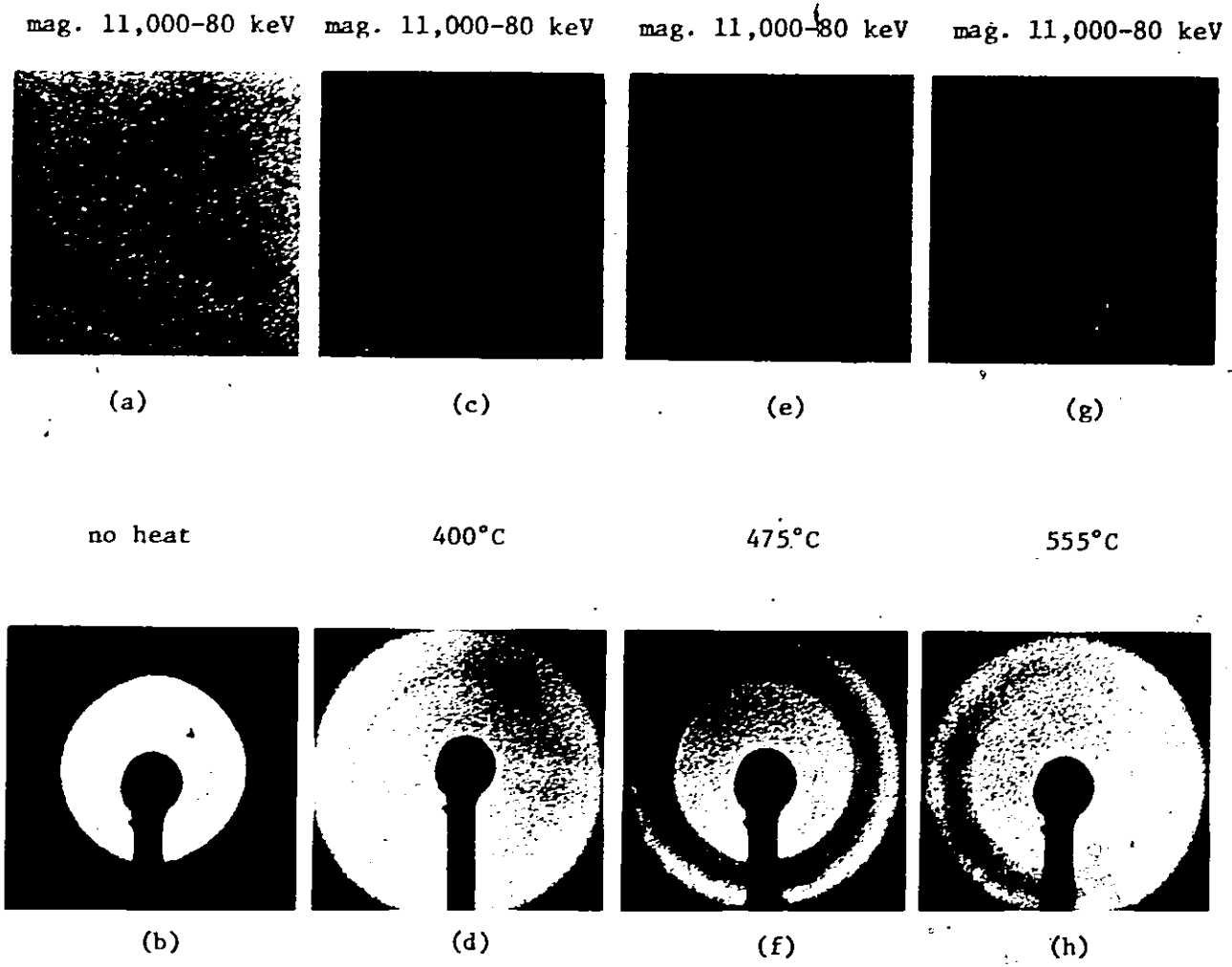

Fig. 2.6. Effect of heat treatment in air on crystallization of SnO_2 films prepared by ion-beam sputtering of anodized tin. Separate specimens were used for each treatment (6 min hold times in furnace). The crystallization temperature is shown to be ~550°C. Crystallized films show as usual very fine grain size.

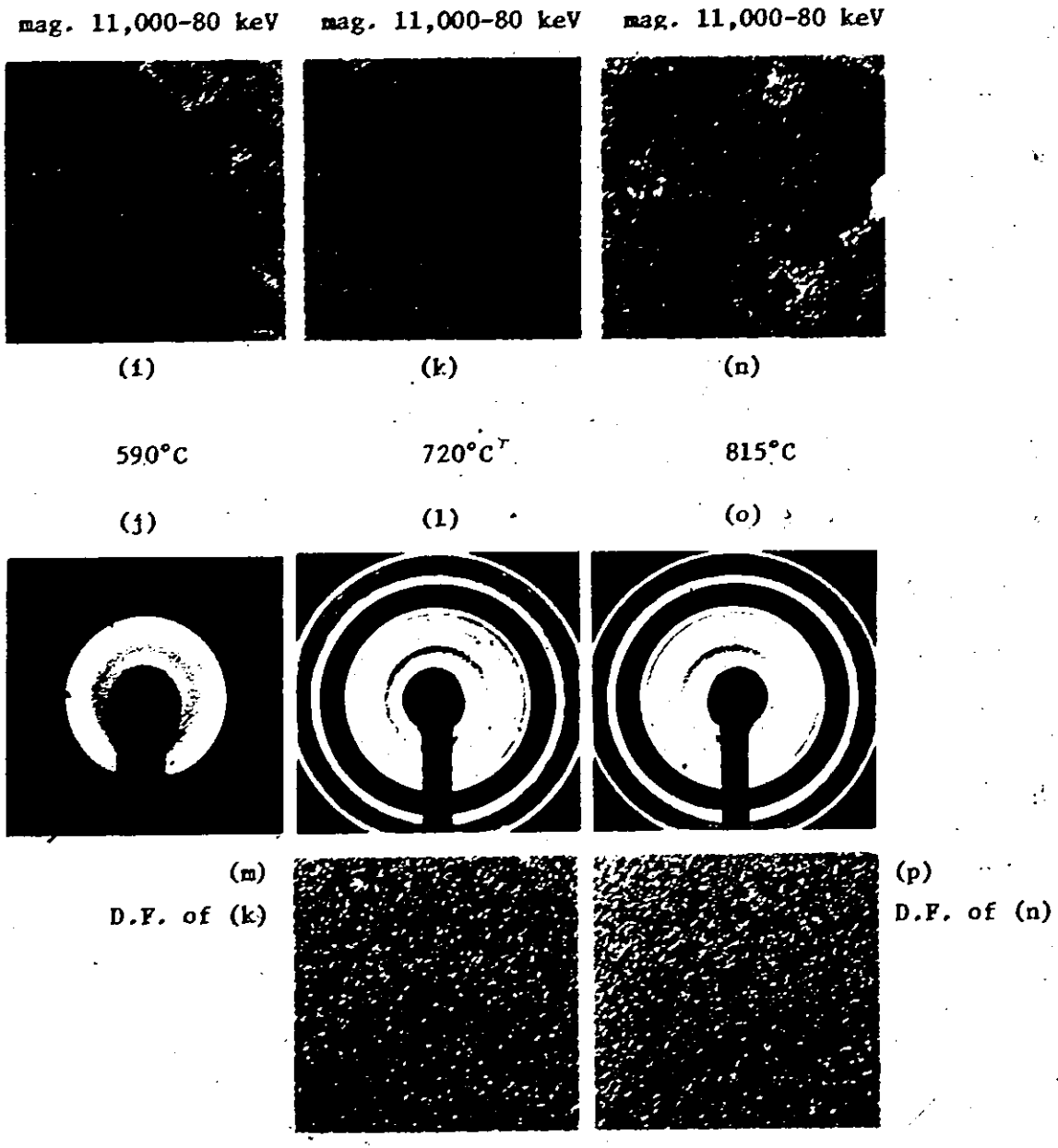

Fig. 2.6 (continued)

complete at 675°C (Fig. 2.4(h)) and higher, i.e. 800° and 900°C (Fig. 2.4(j),(l)). At 1000°C (Fig. 2.4(o)) the diffraction pattern retains rings of the polycrystalline phase together with a spotty pattern. Thus, the effect of heating was to initiate the amorphous-crystalline transition at about 550°C, while no appreciable crystal growth occurred up to 1000°C. As a matter of fact, dark field images (Fig. 2.4(m), (p)) reveal a grain size not higher than 400 Å at 1000°C, showing the polycrystallinity of SnO_2 to be on a fairly fine scale.

A similar evolution is shown in Fig. 2.5, where the starting material is a continuous (as distinct from island structure) film of SnO_2 prepared by reactive sputtering on heated (∿200°C) substrates. Films were stripped from KCl and heated in air with hold times of 6 min. A grain size ∢100 Å will be noted in a film crystallized at 600°C (Fig. 2.5(j),(k),(l)).

Fig. 2.6, where SnO_2 films were prepared by ion-beam sputtering of anodized tin, is similar. SnO_2 prepared by ion-beam sputtering has, therefore, the same crystallization temperature as SnO_2 prepared by reactive sputtering, which, in the light of Hecq and Portier's paper (2) (to be discussed in Section 2.4), is a remarkable result.

A somewhat lower crystallization temperature was obtained for heating in vacuum (10^{-5} torr)(Fig. 2.7). Heating was here carried on using the heating stage of the electron microscope, so that the structure change versus temperature

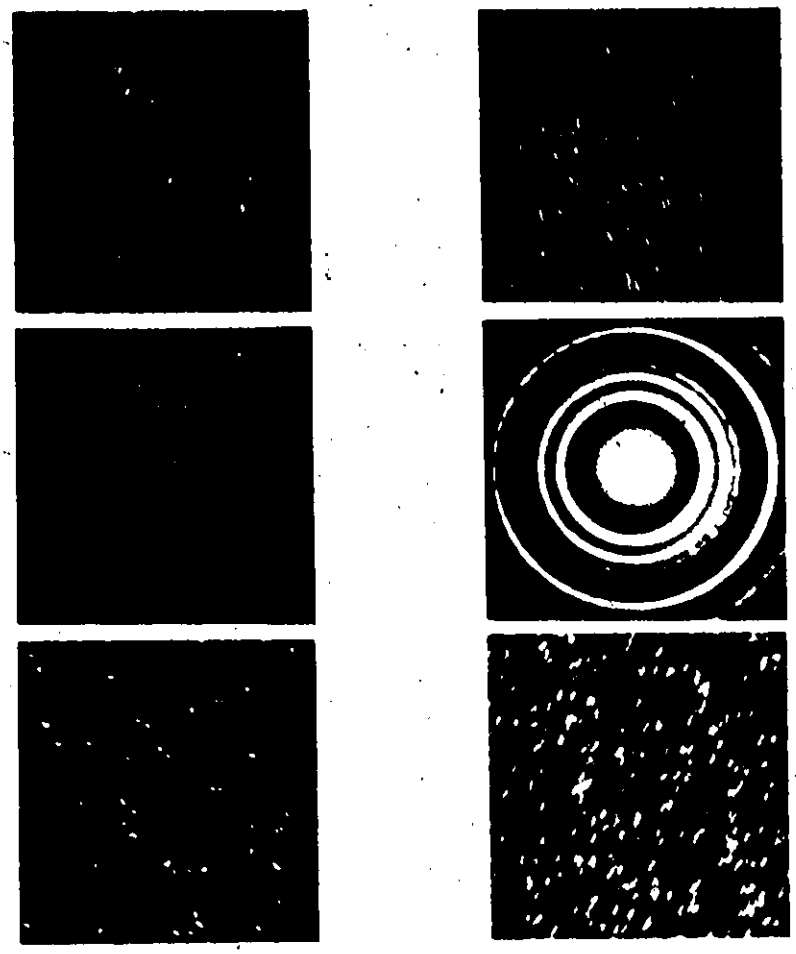

420°C 600°C

Fig. 2.7. Same sample which gives transmission and diffraction pattern of Fig. 2.2(a) (hence deposited by reactive sputtering on heated substrates) heat treated inside the microscope. Transmission, diffraction and dark field images at 420° and 600°C respectively. Results at 500° and 550°C were very similar.

was directly observed from the diffraction pattern evolution on the screen of the microscope. Structure changes corresponding to known values of the temperature could thus be recorded.

(ii) Supported films showed a still greater reduction in crystallization temperature, with a value of about 400°-450°C, when in contact with Ta (Fig. 2.8). Here the abrupt splitting of the second halo has been taken as signalling the onset of crystallization. The crystallization temperature was 250°-300°C for films in contact with KCl (Fig. 2.9), and <200°C (thence crystalline as deposited) when in contact with crystalline SnO_2 (Fig. 2.3).

(iii) A grain size <600 Å is obtained after heating in air on KCl substrate at 550°-600°C (Fig. 2.10). A lower grain size was obtained at all temperatures up to ~1000°C when samples were unsupported during heating (Fig. 2.4-2.7). The grains formed were, therefore, larger in supported films. The various results are summarized in Table 2.I. The differences in crystallization temperature and grain size suggest that nucleation rather than growth is the rate-controlling step in the crystallization of SnO_2 and, while perhaps not fully rate-controlling, at least plays a role in grain growth.

2.3.3 Abruptness of crystallization - A consistent result, clearly shown in Fig. 2.4-2.6 and summarized in Table 2.II, is that the crystallization of SnO_2 occurs in a fairly narrow temperature interval. Following the discussion of Mader (6), this will be taken as suggesting that the films consisted of a true amorphous phase as distinct from a microcrystalline material such

(a) (b)

Fig. 2.8. Reactive sputtering on Ta at ∿50°C. (a) 5 min at 410°C in air. (b) 5 min at 440°C in air.

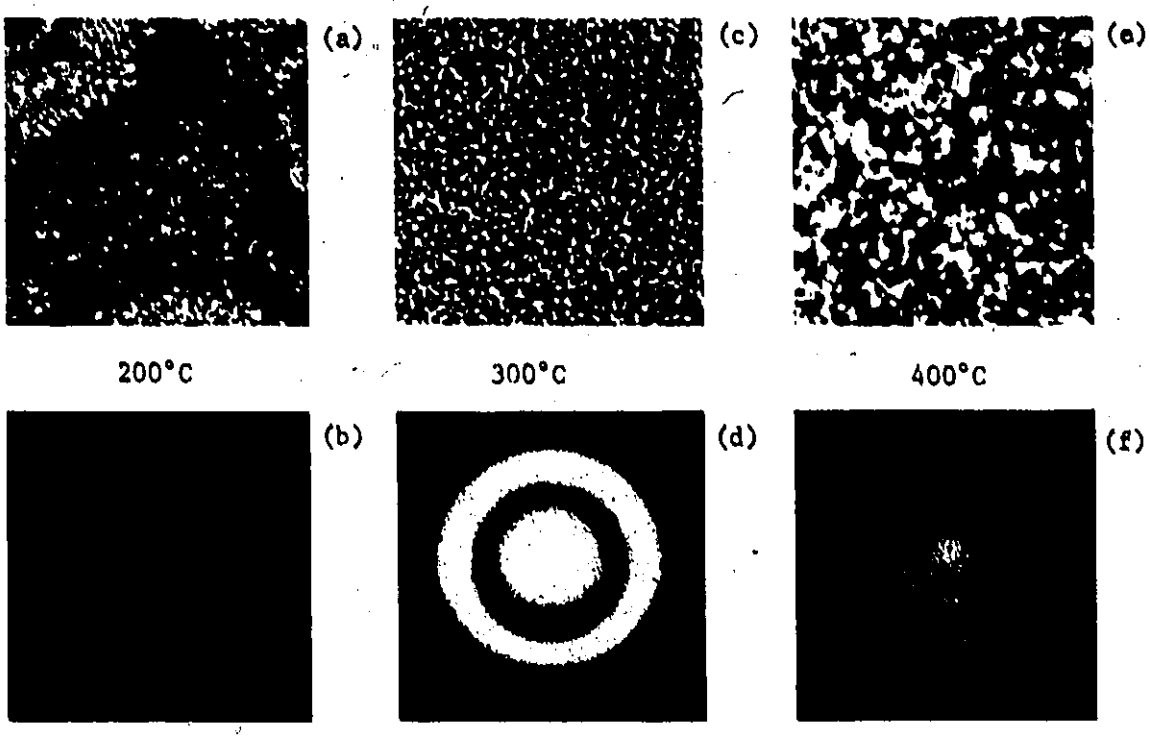

Fig. 2.9. The effect on progressive crystallization of heating the films directly on KCl substrates. Air heating with hold times of 6 min. (b), (d) and (f) are diffraction micrographs of (a), (c) and (e) respectively. (a) mag. 17,000-100 keV, (c) mag. 22,000-80 keV, (e) mag. 22,000-80 keV.

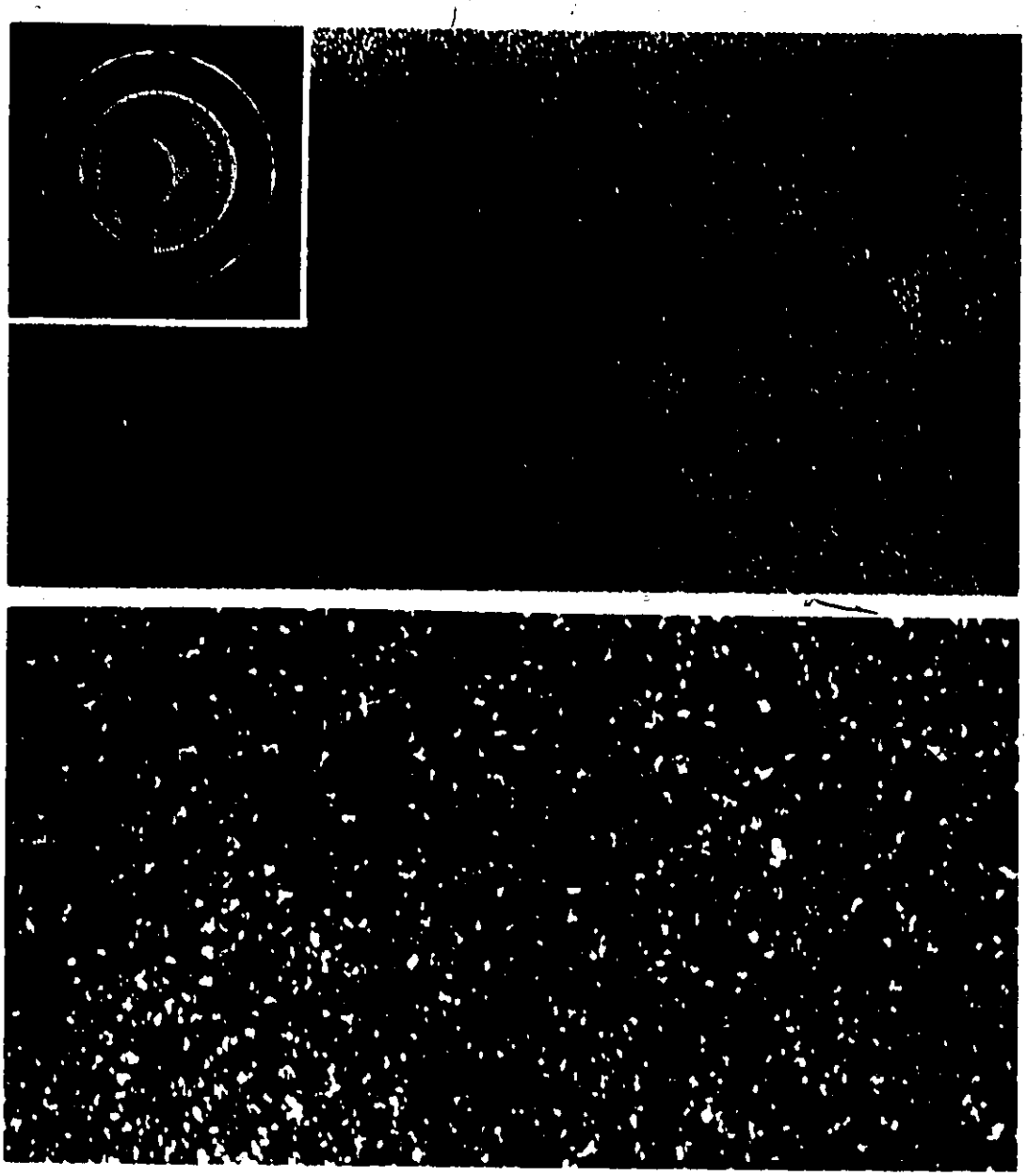

Fig. 2.10. Transmission, diffraction and dark field micrographs of SnO_2 film deposited by reactive sputtering on KCl substrate. Then heated, on KCl itself, for 6 min at 550°-600°C in air. Showing a grain size as high as 600 Å.

TABLE 2.I

Grain size in heat treated SnO_2 films

Temperature (°C)	Grain size (Å)	Figure
Air annealing - Unsupported films		
600	<100	2.5
720	<100	
815	<100	2.4
900	<400	
1000	<400	2.4
Vacuum annealing - Unsupported films		
420	< 50	2.7
600	<100	2.7
Air annealing - Supported films		
550-600	≤600	2.10

TABLE 2.II

Temperature interval for crystallization of unsupported SnO_2 films

Figure	Highest temperature with no evidence of crystallization	Temperature with partial crystallization	Lowest temperature with full crystallization
2.4	450	550	675
2.5	450	475	500
2.6	475	550	590

as that demonstrated in Chapter 3 to occur in anodic films.

2.3.4 Thickness of reactively sputtered films - In order to determine the thicknesses of the reactively sputtered films, substrates of Al, Sn, Ta, and V were included among the KCl cleavings on the anode table. It was hoped that well-defined interference colours would develop, and indeed satisfactory results were obtained with Ta, while we did not obtain any clearly detectable interference colours on Al, Sn, and V. The colours for SnO_2 on Ta were then described in terms of a voltage such that when Ta was anodized to this voltage the same colour was obtained. It was then assumed that the films had a similar "optical thickness", i.e.

$$n_{SnO_2} d_{SnO_2} = n_{Ta_2O_5} d_{Ta_2O_5}$$

where n, the index of refraction, was taken as 1.95 for SnO_2 (7) and 2.20 for Ta_2O_5 (8). Since the thickness of anodic Ta_2O_5 is given by 16.7 Å/V (9), we finally have

$$d_{SnO_2} = 19 \text{ Å/V} \qquad (2.1)$$

where the voltage refers to that to which Ta is anodized. The results are summarized in Table 2.III.

2.4 Discussion

The preparation of SnO_2 by reactive sputtering has a long precedent in the literature and we have little to add, at least from the point of view of preparation as an end in itself. The structural characteristics of SnO_2 films have, on the other hand, been largely neglected. Even such basic concepts as whether the films are amorphous or microcrystalline, and, if the former, the value of the crystallization temperature, have not been previously settled in a satisfactory way. The work has in all cases applied to

TABLE 2.III

Thicknesses of reactively sputtered SnO_2 films

Interference colour of SnO_2 on Ta	Voltage to which Ta must be anodized to show same colour (a)	Thickness of SnO_2 film from Eq. (2.1) (Å)
Dark blue	24	470
Intermediate blue	40	760
Light blue	48	910
Blue with bit of yellow	54	1030
Yellow with bit of red	80	1520
Purple	85	1620
Yellowish green	120	2280

(a) The Ta was anodized for 3 minutes in 0.2% KF.

supported films (where nucleation problems enter) and, considering just the problem of the crystallization temperature, the temperature was normally given as a limit (e.g., >280°C (10), <400°C (11), <500°C (12)). The present work suggests that the crystallization temperature depends strongly on the nucleation conditions as governed by the substrate, varying from <200°C for crystalline SnO_2 substrates, to 250°-300°C for KCl substrates, to 400°-450°C for Ta substrates, to 475°-550°C for unsupported films. We would propose that 475°-550°C is the upper limit to the crystallization temperature. A similar effect has been noted in the crystallization of amorphous Nb_2O_5 and Ta_2O_5 (13), depending on whether the films were unsupported or in contact with the metal. The unsupported films had the higher crystallization temperature. The temperature "<200°C" here specified for crystallization on an SnO_2 substrate needs qualification. It applies to crystallization <u>during deposition</u> and is therefore distinct from crystallization of a fully formed amorphous layer such as that formed by ion-impact on SnO_2 (Chapter 8). A similar distinction is known with Si and Ge (14) and remains to this day of uncertain origin.

As far as agreement with other work on SnO_2 is concerned, the range 250°-450°C for crystallization on KCl or Ta substrates is compatible with virtually all previous work (1,5,10-12,15) except that of Hecq and Portier (2) and of Yamanaka and Oohashi (16). The former authors obtained crystalline SnO_2 films at 90°C for sufficiently large anode-cathode separations. The argument was made that the density of nucleation sites should be low (leading to a crystalline film) for low sputtered-particle energies such as would result with large anode-cathode separations. A similar effect may have occurred also with Ref. (16), as the product (pressure) x (separation) was here as large as with Ref. (2) (Table 2.IV).

TABLE 2.IV

The product separation x pressure

for reactive sputtering of SnO_2

Reference	Separation x pressure (mm torr)	State of SnO_2 film
Vainshtein (1)	2.4	crystalline
Yamanaka and Oohashi (16)	1.8	crystalline
Hocq and Portier (2)	1.5	crystalline
Sinclair and Peters (11)	0.95	amorphous
Hocq and Portier (2)	0.75	amorphous
Lieberman and Medrud (5)	0.7	amorphous
present work (a)	0.3	amorphous
present work (b)	0.00	amorphous

(a) reactive sputtering

(b) ion-beam sputtering

By way of comparison with substances other than SnO_2, we would first of all point out that certain other amorphous oxides also show a substrate effect. They include the following examples:

oxide	Al_2O_3(17)	SiO_2(18,19)	Nb_2O_5(20)	Ta_2O_5(20)	TeO_2(21)
cryst. temp. in contact with metal (°C) or crystalline oxide	500	700	475	550	260
cryst. temp. when unsupported (°C)	680	>1300	590	715	400

SiO_2, GeO_2, and SnO_2 constitute a homologous series and here the main feature to emphasize is that the crystallization temperatures decrease along the series. For example, we have >1300°C for SiO_2 (19), ~630°C for GeO_2 (22), and 475°-550°C for SnO_2 (present work), in all cases for unsupported material.

A consistent result in this work has been that amorphous SnO_2, formed by either reactive or ion-beam sputtering, crystallized to cassiterite. Likewise SnO_2 films formed anodically (see next chapter) were cassiterite as formed. In view of the fact that other amorphous oxides often yield metastable or high-temperature phases when crystallized (Table 2.V), a possible conclusion is that SnO_2 lacks metastable or high-temperature phases. Whether or not this conclusion is warranted will be shown in part when the phase relations of SnO_2 in the still unstudied region above about 1600°C are determined. (We would point out that an argument of this type is valid with MoO_3, TeO_2, UO_2, and V_2O_5, all of which crystallize to the normal crystal type and, furthermore, have only one known phase.)

TABLE 2.V

The crystallization products of amorphous oxides

Oxide	Crystallization product	Stability	Reference
Al_2O_3	Gamma	Always metastable	(23)
Nb_2O_5	Low temp. form	Always metastable	(24)
Ta_2O_5	Low temp. form	Always metastable	(20)
TiO_2	Anatase	Always metastable	(25)
Bi_2O_3	Cubic	Stable above 717°C	(5)
GeO_2	Hexagonal	Stable above 1033°C	(22)
HfO_2	Cubic	Stable above ~2700°C	(26)
WO_3	Orthorhombic	Stable above 330°C	(5)
ZrO_2	Cubic	Stable above 2285°C	(3)

REFERENCES

1. V. M. Vainshtein, Simp. Protsessy Sin. Rosta Kriat. Plenok Poluprov. Mater., Tezisy Dokl., p. 296, Novosibirsk (1965).
2. M. Hecq and E. Portier, Thin Sol. Films 9, 341 (1972).
3. H. M. Naguib and R. Kelly, J. Nucl. Mater. 35, 293 (1970).
4. B. W. Farmery and M. W. Thompson, Phil. Mag. 18, 415 (1968).
5. H. L. Lieberman and R. C. Medrud, J. Electrochem. Soc. 116, 242 (1969).
6. S. Mader, Recrystallization, Grain Growth and Texture, ASM, Metals Park, Ohio, Oct. 16-17, 1965.
7. R. Groth, E. Kauer and P. C. v.d. Linden, Z. Naturforschung 17a, 789 (1962).
8. L. Young, Proc. Roy. Soc. A244, 41 (1958).
9. R. E. Pawel, Rev. Sci. Inst. 35, 1066 (1964).
10. F. v.d. Maesen and C. H. M. Witmer, Proc. 7th Intern. Conf. on the Phys. of Semiconductors, p. 1211, Paris (1964).
11. W. R. Sinclair and F. G. Peters, J. Am. Ceram. Soc. 46, 20 (1963).
12. K. Ishiguro, T. Sasaki, T. Arai, and I. Imai, J. Phys. Soc. Japan 13, 296 (1958).
13. P. H. G. Draper and J. Harvey, Acta Metallurgica 11, 873 (1963).
14. J. W. Mayer, L. Eriksson, S. T. Picraux, and J. A. Davies, Can. J. Phys. 46, 663 (1968).
15. V. Caslavska and R. Roy, J. Appl. Phys. 40, 3414 (1969).
16. S. Yamanaka and T. Oohashi, Jap. J. Appl. Phys. 8, 1058 (1969).
17. G. Haas, Optik 1, 134 (1946).
18. Jh. Matzke, Phys. Status Solidi. 18, 285 (1966).
19. F. W. Ainger, J. Mater. Sci. 1, 1 (1966).
20. P. H. G. Draper and J. Harvey, Acta Met. 11, 873 (1963).

21. M. L. Lieberman and R. C. Medrud, J. Electrochem. Soc. 116, 242 (1969).

22. J. Drowart, F. Degreve, G. Verhaegen, and R. Colin, Trans. Faraday Soc., 61, 1072 (1965).

23. R. G. Frieser, J. Electrochem. Soc. 113, 357 (1966).

24. F. Holtzberg, A. Reisman, M. Berry, and M. Berkenblit, J. Am. Chem. Soc., 79, 2039 (1957).

25. M. Shiojiri, J. Phys. Soc. Japan, 21, 335, (1966).

26. I. A. El Shanshoury, V. A. Rudenko, and J. A. Ibrahim, J. Am. Ceram. Soc., 53, 264 (1970).

CHAPTER 3

ANODIC FILMS

3.1 Introduction

Anodic oxidation is a film preparation technique by which oxides are prepared on substrates of the parent metal (though not necessarily*). As the name implies, the film is made to grow on the anode in an electrolytic cell, the basic equations that govern the process being similar in spirit, though not in detail, to what follows:

at anode

$$M + nH_2O \rightarrow MO_n + 2nH^+ + 2ne^- \qquad (3.1)$$

at cathode

$$H_2O + e^- \rightarrow OH^- + \tfrac{1}{2}H_2 \qquad (3.2)$$

Thus an oxide grows on the metal anode surface and hydrogen is evolved at the cathode. With some materials and/or electrolytes this may not be the anodizing reaction, with the metal of the anode instead going into solution or oxygen being evolved or species other than H^+ and OH^- being formed.

3.1.1 The electrolyte - The choice of the electrolyte is particularly

---

* For example, using Na_2WO_3 as the electrolyte, one can deposit WO_3 on an Mg anode.

broad, being determined in principle by the following requirements: the electrolyte (a) must not be able to dissolve the anodic oxide, (b) must be electrically conducting and (c) must contain oxygen.

The total current within the electrolyte is the sum of the ionic current leading to film growth, the ionic current leading to dissolution, and the electronic current. At the cathode, by choosing a platinum electrode, one insures that this current is purely electronic. At the anode, both ionic and electronic currents may pass through the oxide layer being formed. The presence of ionic current leading to dissolution will result, as a sufficient but not necessary condition, in a low anodizing efficiency, and if the dissolution rate is comparable to the growth rate, the film will never grow to large thicknesses.

The main source of oxygen in the oxide is the water contained in the electrolyte, as shown by Crobet et al. (1), while only a minor percentage of it comes from the salt. A possible role of an organic liquid as the electrolyte, in those instances where one is used, is again the production of water. It has been, in fact, observed (1) that the production of water per Faraday is double when using ethylene glycol, which contains two oxygens per molecule, than in the case of N-methylacetamide, which contains only one.

3.1.2 <u>The growth of the film</u> - Anodic oxide films are commonly prepared under one of three different conditions. The first method consists of growing under constant-voltage conditions until the current is conveniently small. Its disadvantage is that the current is initially uncontrollably high so that the structure of the anodic film may be unpredictable. In the second, a constant current is passed through the cell so that the total

amount of film is proportional to the time for which the current is passed. Again there is a disadvantage: while the amount of film is largely proportional to time, the film is not normally of uniform thickness. The third method involves a constant current followed by constant voltage. It is generally regarded as giving the best films as regards predictability of structure and uniformity of thickness.

If the oxide is a poor electronic conductor and the electrolyte does not attack the oxide, the applied voltage sets up an electrostatic field in the oxide (or increases the already existing field) and produces a continued growth of the film by causing metal and/or oxygen ions to migrate through the film. There is, however, a limit to the thickness that can be obtained, the limiting factors being variously (a) chemical, (b) electrochemical, (c) electrical, and (d) structural. As an example, we would note the work of Yahalom and Zahavi (2) whose films on Al, Ta and Ti were found to grow in a normal manner as long as they were amorphous. At a certain thickness they were found to crystallise and the voltage thereafter rose only reluctantly. This is shown in Fig. 3.1 for Al.

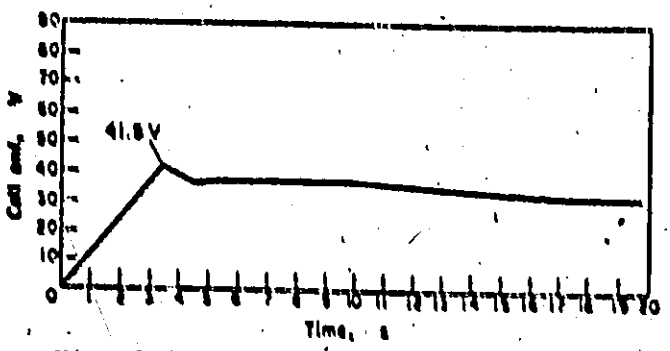

Fig. 3.1. Cell-voltage transient of aluminium anodising in 0.1 M Na_2SO_4 at 50 mA/cm^2, (from Ref. 2)

Thus, the growth of anodic films is basically a problem in the ionic conductivity of oxides at high fields combined with complications due to the processes occurring at the metal/oxide interface, at the oxide/electrolyte interface as well as within the film. Many of the phenomena were first established semi-quantitatively by Günthersschulze and Betz (3) in 1937. Reviews on the subject can be found in Ref. 4-7, while the classical theories on anodic oxidation are the work of Verwey (8), Mott and Cabrera (9) and Young (10).

3.2 Experimental

The anode was a chemically degreased 20 x 30 mm Sn sheet, while the cathode was either a 20 x 30 mm Al sheet or a 23 mm I.D. Pt cylinder. Previous work (Chapter 1, 55-60) has shown that water-based electrolytes, whether acidic or basic, do not permit Sn to be anodized to high voltages, and an organic-based one was therefore chosen. It consisted of 330 g/liter of ammonium pentaborate in ethylene glycol which was varied by adding water (subsequently indicated in units of ml/liter). Most films were formed using a preset voltage of 50 and a preset current of 10 mA/cm^2 as obtained with a Hewlett-Packard Model 6186B constant-current power supply.

The difference between electrolytes with different additions of water is brought out in Fig. 3.2. Electrolyte (a) (0 ml/liter) yields opaque, white films, though the time variation of current and voltage is sometimes unpredictable. Electrolyte (b) (150 ml/liter) gives opaque, gray films. Electrolyte (c) (300 ml/liter) leads to a voltage rise of 50-65 and the films show interference colours over approximately six orders, in agreement with the behaviour of most other substances which permit anodizing to high voltages.

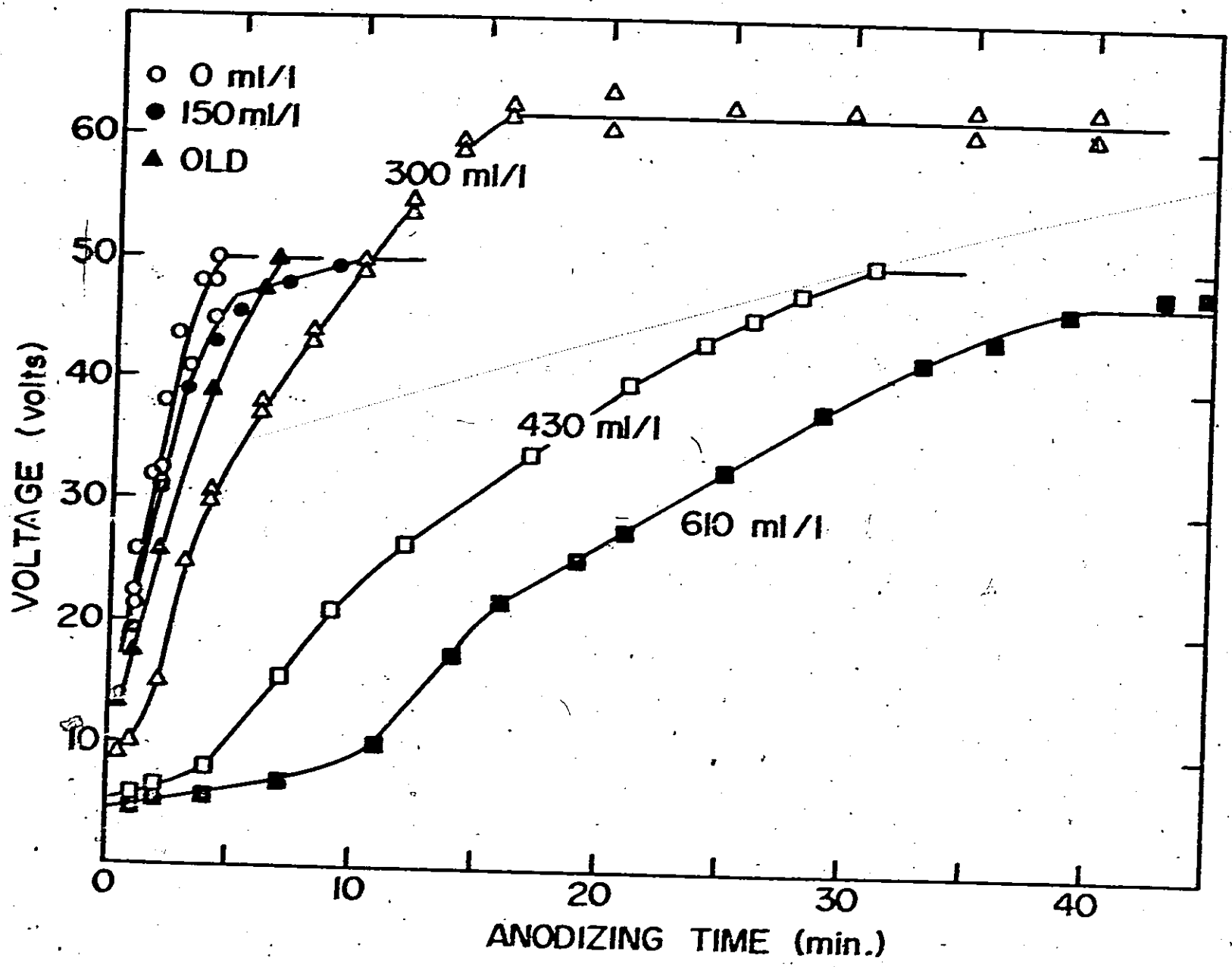

Fig. 3.2. Voltage-time curves for anodizing Sn at 10 ma/cm^2 in electrolytes consisting of ethylene glycol, 330 g/liter of ammonium pentaborate, and varying amounts (indicated in ml/liter) of water. "Old" refers to an electrolyte containing 300 ml/liter water which had aged owing to use. The upper voltage limit is due to presetting in all cases except "△" and "■", where it is a true upper limit.

Electrolyte (c) is subject to aging, through use or storage. This gives rise to electrolyte (c'), yielding opaque, white films. Electrolyte (d) (430 ml/liter) gives films which show slight interference effects, though are better described as opaque, yellowish brown. Finally, electrolyte (e) (610 ml/liter) gives opaque, grayish brown films.

Contrary to previous work, Sn can evidently be anodized in a "normal" manner provided a correct electrolyte is chosen. The normalcy is further shown by the existence of a well-defined fall in current when the preset voltage is reached (Fig. 3.3).

We have centred our attention on films obtained using electrolytes (c) and (c'), subsequently referred to as "coloured" and "white". When necessary, the films were stripped by placing the specimens in 1% HCl for several hours. We would note in hindsight, however, that the stripping process involving mercury, as discussed in Section 1.2.5, would have been greatly preferable.

3.3 Results

3.3.1 Crystal form - The state of the films that were obtained was determined using transmission electron microscopy as well as diffraction.

Coloured anodic films, as formed with electrolyte (c), were continuous and showed a characteristic cellular structure with mean dimensions of 200-700 Å (Fig. 3.4). The diffraction pattern was borderline between showing halos and rings, though was judged to be more nearly of a ring type with d spacings corresponding to cassiterite. Note that the grains are much smaller than the cells.

White anodic films, as formed with electrolyte (c'), were polycrystalline with the structure of cassiterite (Fig. 3.5). Though continuous

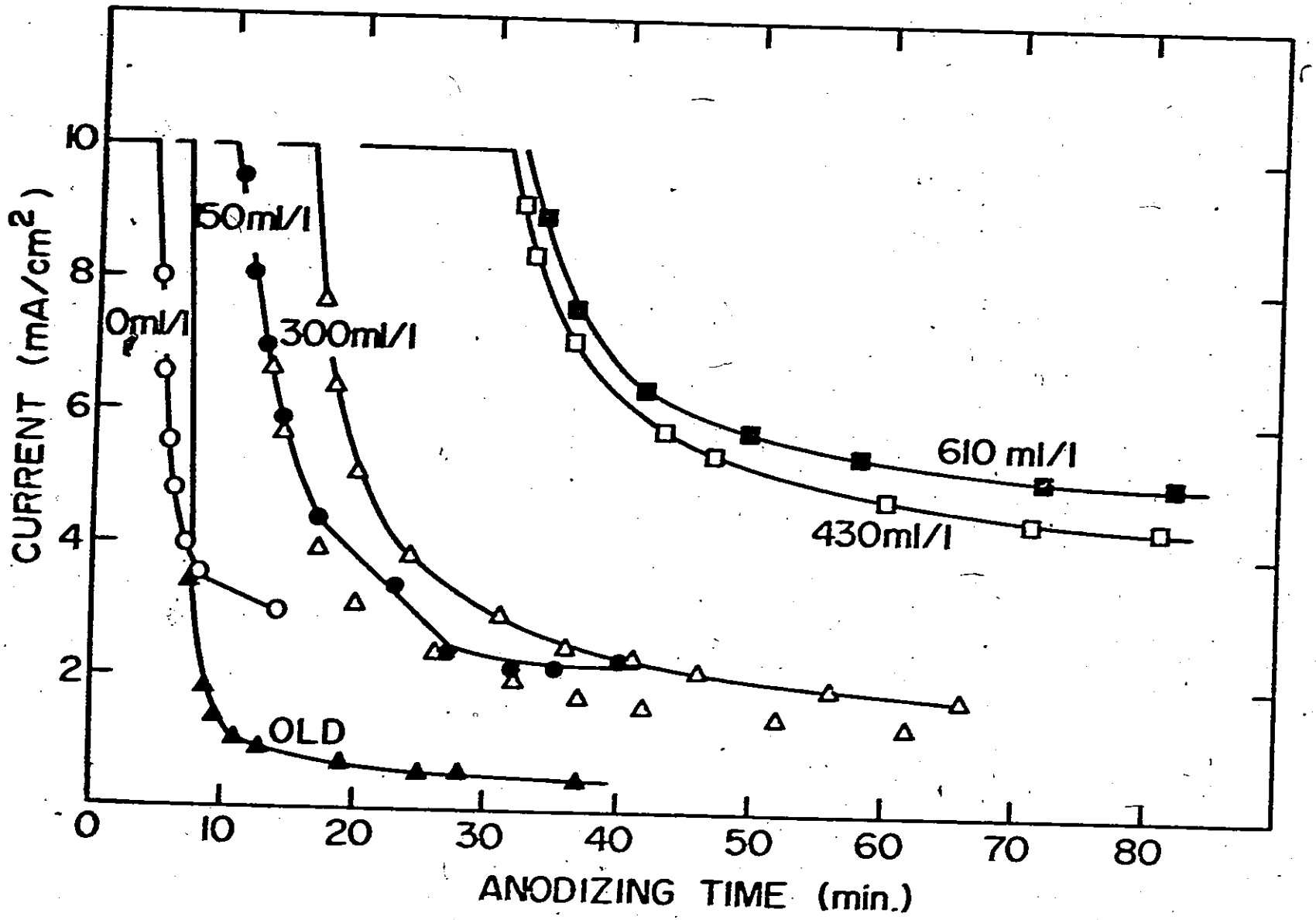

Fig. 3.3. Current-time curves for anodizing Sn when both current and voltage are preset. The anodizings are the same as in Fig. 3.2 in all cases except "Δ" and "■", where the preset voltages are 50 and 40. Note that, to avoid crowding, only one set of points "Δ" has been joined.

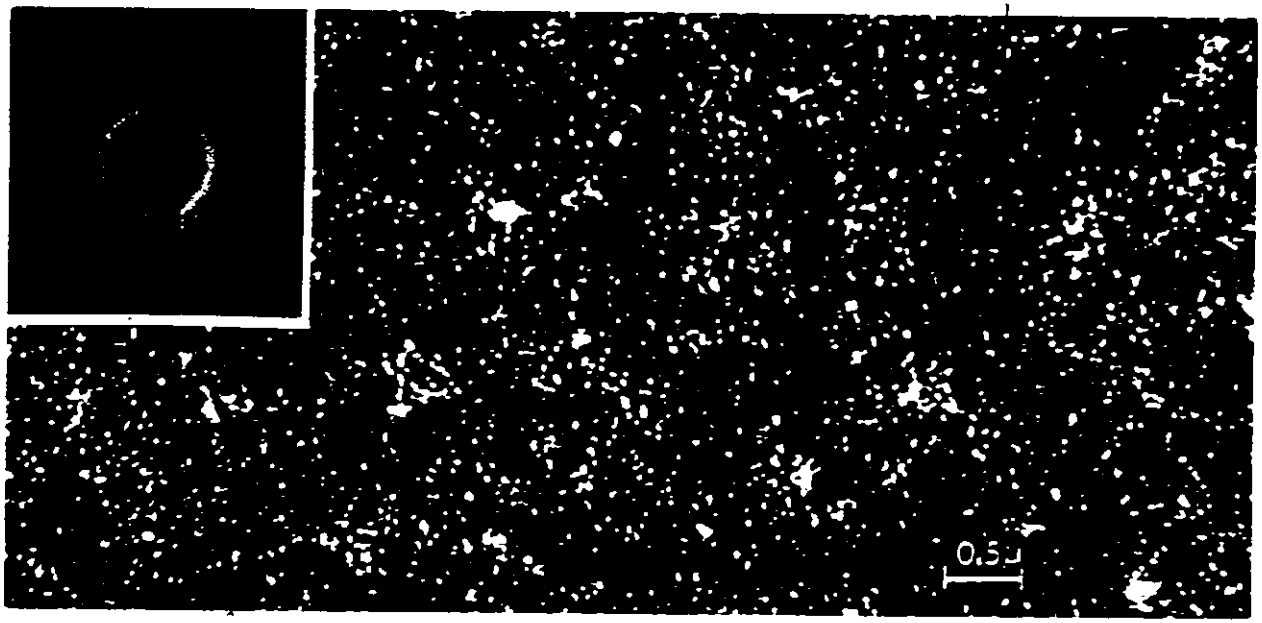

Fig. 3.4. Micrograph with mag. 22,000 of SnO_2 film formed by anodizing Sn using electrolyte (c). The film has a cellular structure on a scale of ~500 Å but consists of crystallites on a much smaller scale. The diffraction pattern was judged to be more nearly indicative of crystallinity than amorphousness.

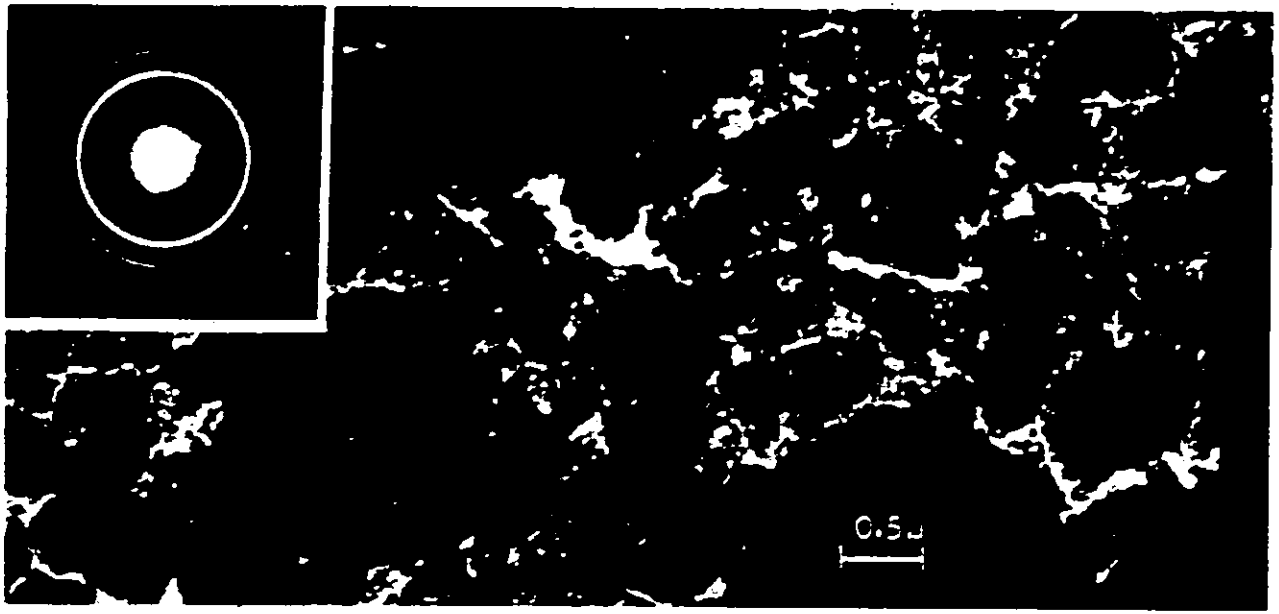

Fig. 3.5. Micrograph with mag. 22,000 of SnO_2 film formed by anodizing Sn using electrolyte (c'). The film consists in part of thin regions and in part of thick regions, the latter appearing as large black areas. Such films had better defined crystallinity than those of Fig. 3.4 and the diffraction pattern could be readily shown to be that of cassiterite.

they were characterized by a variation in thickness as if random crystal growth had occurred. One can speculate that it is the existence of such random crystals that causes the scattering of light, thence the white appearance.

3.3.2 Crystallization behaviour - Coloured anodic films which had been stripped were found to undergo virtually no increase in the sharpness of the rings with increasing temperature until ~1100°C (Fig. 3.6). In view of the fact that 1100°C is much greater than the crystallization temperature (Chapter 2: 475°-550°C), this can be taken as confirming their polycrystalline nature in the sense that an amorphous film would have shown an abrupt increase in ring sharpness at the crystallization temperature.

Besides undergoing no significant change in the sharpness of the rings, the films retained their continuous form and the grain remained small (e.g., 100-400 Å in Fig. 3.7(a)). Only once a temperature of 1100°C was reached was there evidence for major grain growth. The diffraction patterns became spotty and dark-field photographs revealed larger grains (e.g., 500-1000 Å in Fig. 3.7(b)).

3.3.3 Thickness - The film thicknesses on anodized Sn were estimated in several ways. (i) They were judged in the first place to be nearly independent of voltage between 6 and 50 V on the grounds that the interference colours changed only slightly with voltage for specimens anodized as in Fig. 3.3. (ii) Explicit thicknesses were obtained by measuring the weight increases due to anodizing and interpreting them in the light of the result (Section 3.3.4) that dissolution during anodizing is normally unimportant (column 2 of Table 3.I). (iii) Explicit thicknesses were also deduced by a sputtering technique in which anodized specimens are bombarded with 20-keV

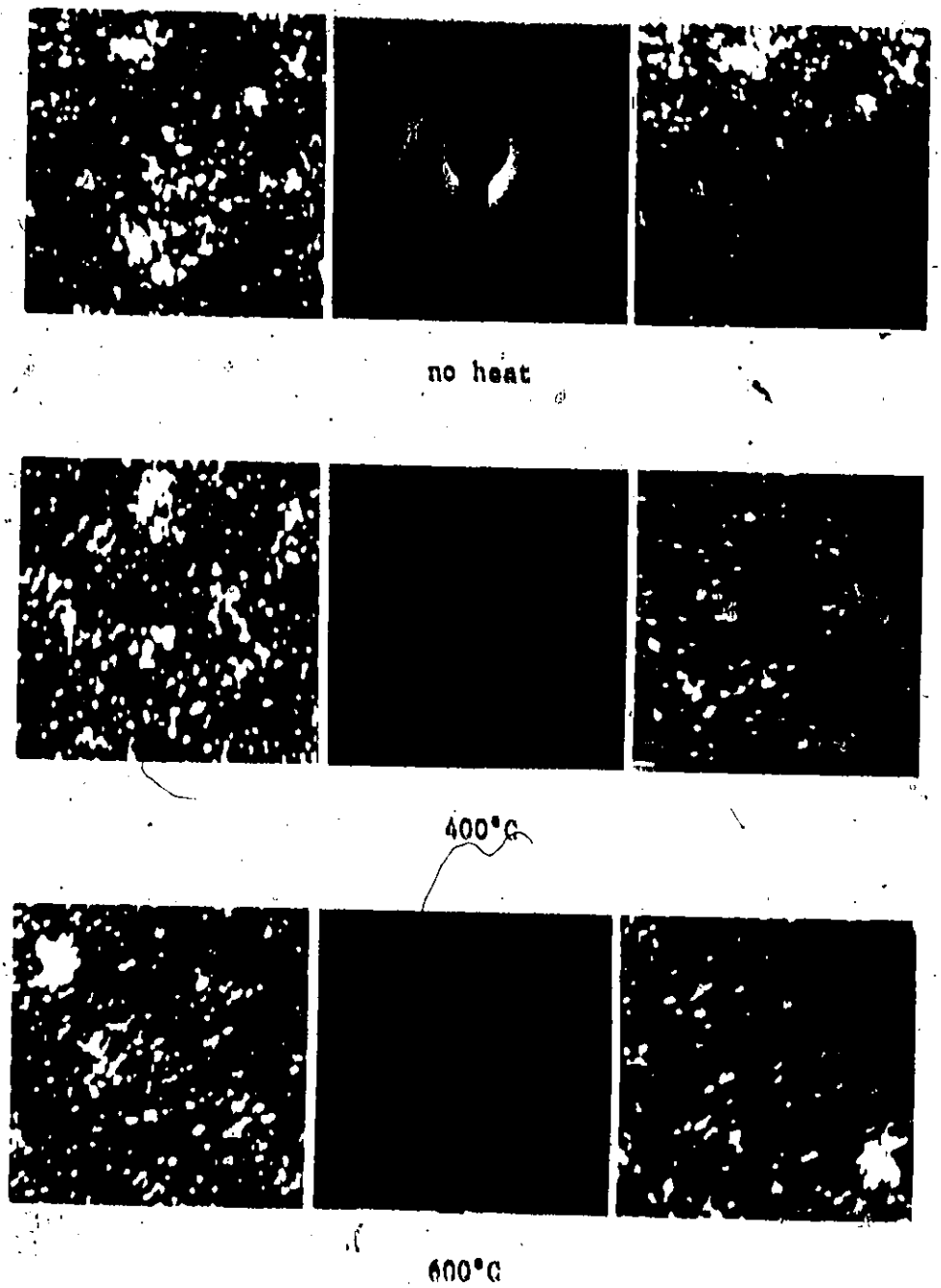

Fig. 3.6. Coloured anodic film which has been stripped and heat treated in air, using a series of hold times in furnace of 6 min each, at increasing temperatures. Each row of pictures shows, from left to right, transmission, diffraction and dark field micrographs. Mag. 27,000-80 keV.

(d)

700°C

(e)

800°C

(f)

900°C

Fig. 3.6 (continued)

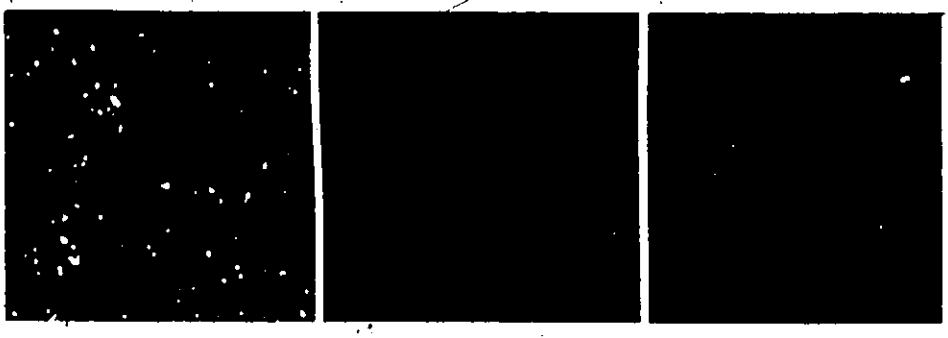

(g)

1000°C

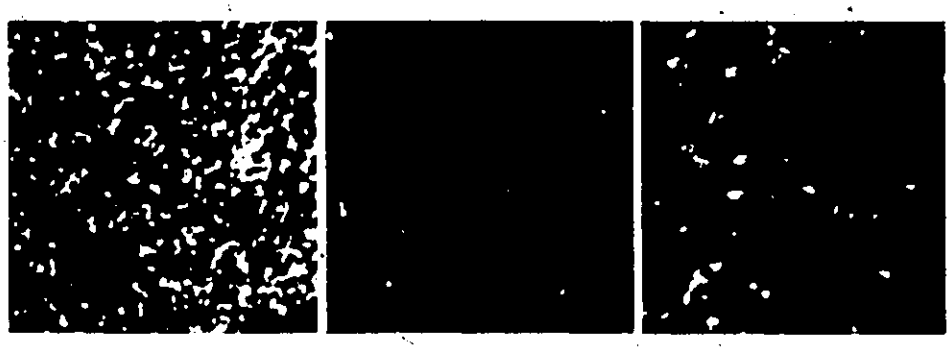

(h)

1100°C

Fig. 3.6 (continued)

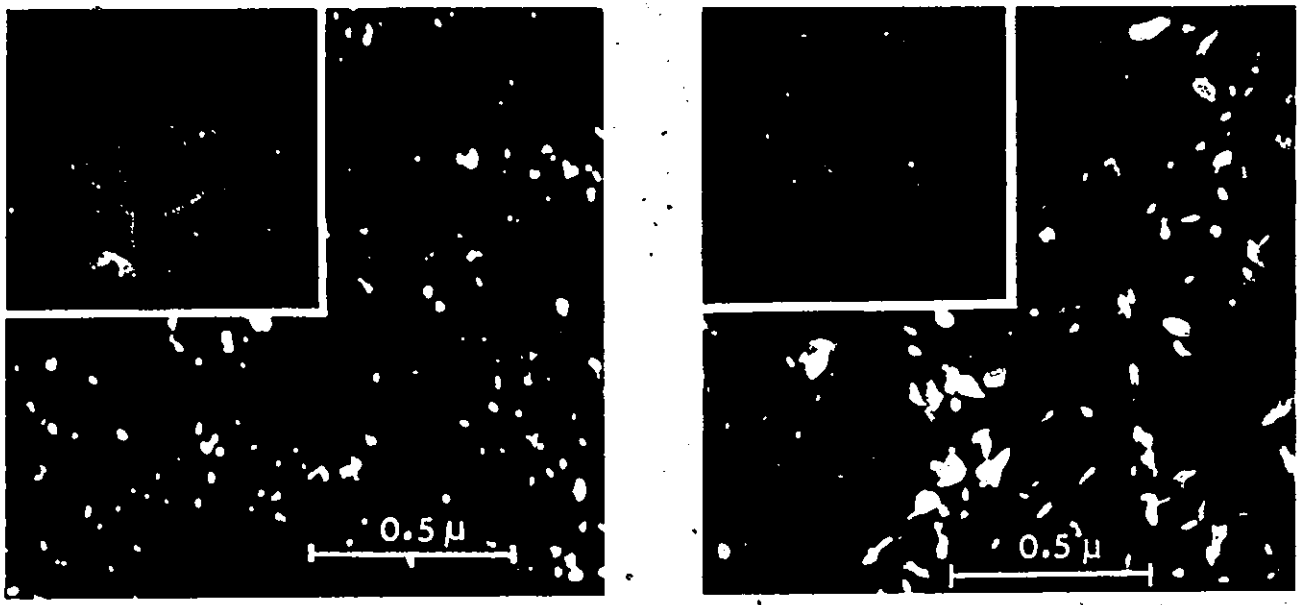

Fig. 3.7. (a,left) Bright-field micrograph with mag. 54,000 of SnO_2 film formed by anodizing Sn using electrolyte(c). The film was stripped and then heated for 6 min in air at 1000°C in an unsupported state. The diffraction pattern is still best described as consisting of rings. (b,right) As in (a) but dark-field and heated at 1100°C. The diffraction pattern now shows a tendency to be spotty.

TABLE 3.I

Thicknesses of anodic SnO_2 films[(a)]

Anodizing voltage (V)	Thickness as inferred from weight increase due to anodizing (Å)	Thickness as inferred from weight loss due to sputtering (Å)
6	3700 ± 300	3100 ± 300
8	6900 ± 100	6200 ± 600
15	4300 ± 700	4400 ± 400
25	2800 ± 500	3000 ± 300
35	2500 ± 500	4200 ± 400
50	2600 ± 300	4700 ± 500

(a) The current density was initially 6.5 or 10 and finally 2 mA/cm^2. The conversion from $\mu g/cm^2$ to angstroms was made using the assumed value 6.95 g/cm^2 for the density of SnO_2; the real density would be somewhat lower.

Kr until the metal is exposed. The thicknesses follow gravimetrically (column 3 of Table 3.I), while one obtains as an extra benefit values for the sputtering coefficient (Chapter 5).

The inferred independence of thickness and voltage is seen to be fairly well, though not completely, borne out. In fact, the films are thickest for a voltage in the vicinity of 8-15, an effect which will have to be left to future work for clarification.

3.3.4 Anodizing efficiency - The anodic film thicknesses are of additional interest in that they enable the anodizing efficiency to be deduced, even if only roughly. To this end it is sufficient to compare the film weights as obtained by integrating current-time curves as in Fig. 3.3 with observed weights. The results are summarized in Table 3.II (columns 2 and 3). The efficiency is 20% for a 6 V film but decreases with increasing voltage.

A low efficiency can arise either from electronic conduction or from film dissolution. These can be distinguished firstly from the fact that anodized specimens tended to gain weight approximately as required from the explicit film weights (columns 2 and 3 of Table 3.I). Evidently electronic conduction is occurring, for had dissolution been important there would have been pronounced weight losses as in column 4 of Table 3.II.

The origin of the low efficiency can be shown secondly from an experiment in which a specimen is first labeled with 30-keV Kr^{85} and is then anodized to 50 V as in Fig. 3.3 During the anodizing about 30 ± 10% of the activity is lost from coloured films and about 90 ± 6% is lost from white films. Such losses can be expressed in terms of Sn dissolution provided the integral depth distribution of the 30-keV Kr is known. The relevant relation is (11)

TABLE 3.II

Anodizing efficiency

Anodizing voltage (V)	Charged passed (coulombs/cm^2)	Anodizing efficiency (%)	Hypothetical weight loss if low efficiency is due to dissolution (μ g/cm^2)
6	2.7	20 ± 2	600
8	5.25	21 ± 2	1200
15	7.92	10 ± 1	2100
25	8.64	6 ± 1	2500
35	11.8	6 ± 1	3400
50	21.2	4 ± 0.5	6200

(a) The current density was initially 6.5 and finally 2 mA/cm^2.

$$C^{int.} \approx \frac{1}{2} \operatorname{erfc} \frac{x-\langle x \rangle}{2^{\frac{1}{2}}\Delta x} \qquad (3.3)$$

where $\langle x \rangle$ is the mean projected ion range [10.1 $\mu g/cm^2$ as for CdTe(12).] and Δx is the mean projected ion straggling [5.8 $\mu g/cm^2$ (12)]. This relation is shown graphically in Fig. 3.8 curve (a), from which we conclude that the amount of Sn dissolving is 7-21 $\mu g/cm^2$. Such an amount is small compared with the 350 $\mu g/cm^2$ of Sn contained in a 5000 Å film and we again conclude that the low efficiencies are due mainly to electronic conduction.

We would emphasize that the argument based on eq. (3.3) and Fig. 3.8 is weakened by the fact that it gives a lower limit to the amount of dissolution. This follows firstly since equation (3.3) is strictly valid only if channeling is minimal. Nothing is known about channeling in Sn and in so far as it occurs it will lead to deeper penetration of the Kr^{85} as in Fig. 3.8, curve (b). It follows secondly since the Kr^{85} will serve as a true marker only in so far as oxygen is mobile. In the contrary case (mobile Sn) the Kr^{85} is buried to some extent and less is lost due to a given amount of dissolution.

3.4 Discussion

While SnO_2 is frequently prepared by reactive sputtering (as discussed in Section 1.2.3), there is as far as we know no precedent for films being formed by high-voltage anodizing except for the instance in which a "thick black crust" was obtained (as discussed in Sections 1.2.4 and 1.4). This lack of success is not really surprising when it is remembered that Be, Mo, Ti and V, for example, were long regarded as being incapable of supporting high anodizing voltages yet have been recently found to yield uniform, protective films with thicknesses of ∿1200 Å at 100 V. The key

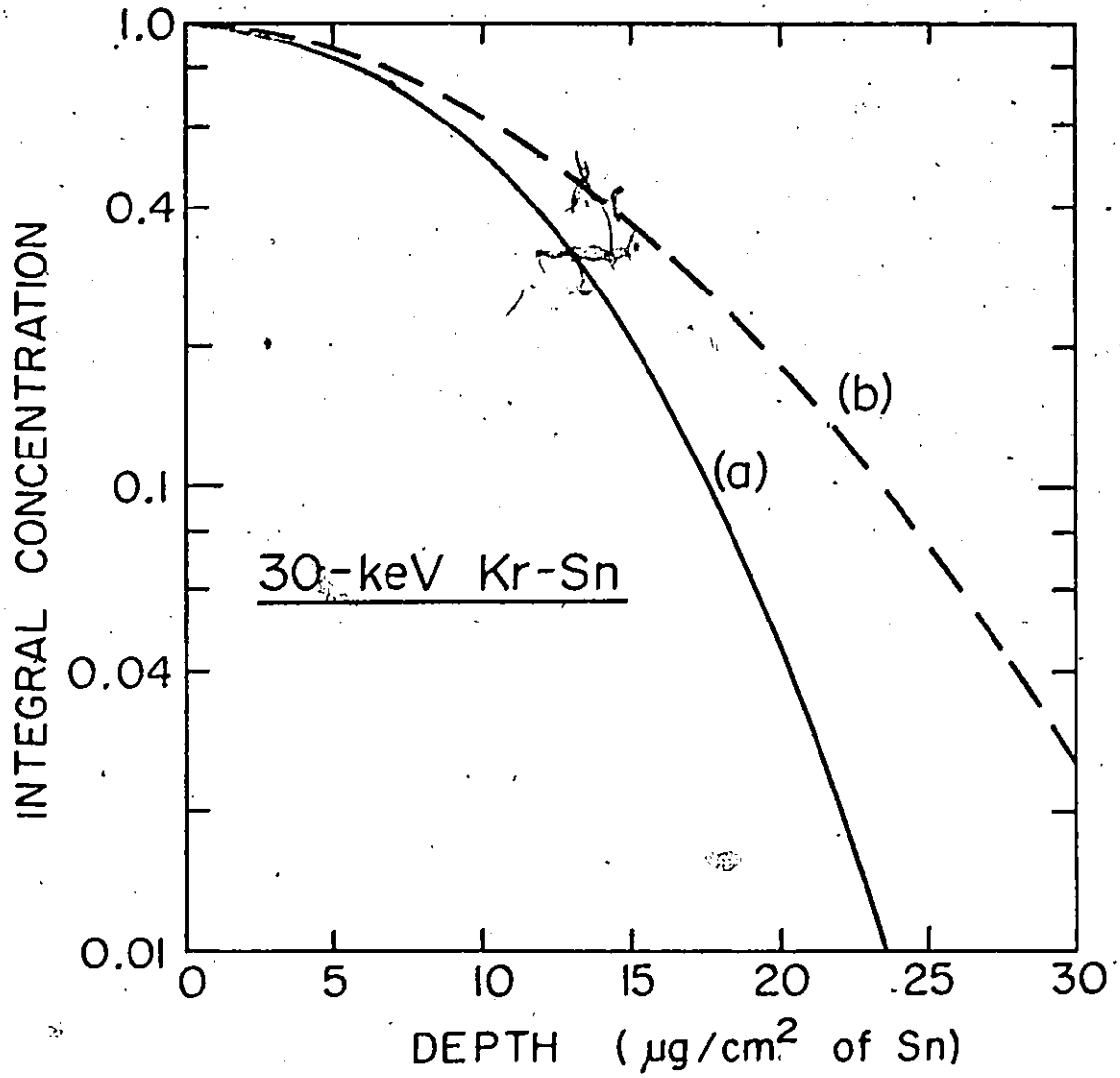

Fig. 3.8. Integral depth distribution of 30-keV Kr in Sn according to Eq. (3.3). The range parameters <x> and Δx in Eq. (3.3) were assigned values as for CdTe (12), which has a mean mass similar to that of Sn.

lay in choosing an appropriate nonaqueous electrolyte (13-16). The present work makes it clear that, though the process is far from being perfect, high voltage film growth is readily achieved with Sn. The main problem still to overcome is probably that of exploring alternative electrolytes or anodizing cycles until one is found which yields films which, due either to their structure or to doping, show the expected linearity between thickness and voltage.

Unexpected was the result that anodic SnO_2 is crystalline as formed, for anodic films are nearly invariably amorphous. HfO_2 and ZrO_2 appear to be exceptions in that they form in the monoclinic and cubic modification (17,18), while anodic BeO (19) and TiO_2 (20) are sometimes crystalline. Perhaps there is precedent in the work of Lakhiani and Shreir (21), where normally amorphous anodic Nb_2O_5 was shown to crystallize at high voltages due to voltage breakdown. Alternatively, it is a simple temperature effect governed by the current (19,20). However, a more systematic explanation follows from recent work by Arora and Kelly (22). They noted a marked parallel between the structure of anodic oxides and oxides subject to ion bombardment. As seen in Table 3.III we find in both cases a similar state of crystallinity and, furthermore, in both cases a correlation with the ratio (crystallization temperature)/(melting temperature). The argument is briefly as follows. A criterion to predict amorphization due to ion-impact states that the ratio (crystallization temperature)/(melting temperature) must exceed $\sim$0.30 for amorphization to occur (Section 1.2.7). The criterion is based on a physical model involving thermal-spikes, and is dealt with again in Section 6.2.1. It considers the fact that the displacement cascade created by a heavy ion hitting a target consists of a

TABLE 3.III

Structure of anodic oxides and of oxides subject to ion-bombardment (from Ref. 22)

Oxide	Structure when formed anodically	Structure when ion-bombarded	Tc/Tm
V_2O_5	am	am	0.61
Nb_2O_5	am	am	0.42-0.49
MoO_3	am	am	0.49
ZnO	cr	cr	0.17
BeO	cr	cr	0.21
Al_2O_3	am	am	0.43
SiO_2	am	am	0.61
GeO_2	am	am	0.65
ZrO_2	cr	cr	0.27
HfO_2	cr	cr	~0.25
UO_2	cr	cr	0.30

Similar parallels for VO_2, MoO_2, WO_2, WO_3 while Ta_2O_5, TiO_2 and SnO_2 constitute exceptions

compact region in which the target material is actually made to melt. During the subsequent rapid cooling, the melted region will solidify to either a crystalline or an amorphous phase. Now, according to Arora and Kelly (22), the same model can be used to explain the as-prepared state of an oxide formed by anodizing, namely its amorphicity or crystallinity. The argument hinges on an assumed equivalence between the energy deposited by an incident ion and the field-imparted energy. Namely the ions (oxygen and metal) which migrate to form a growing oxide, are subject to a field, and hence acquire an energy of a few eV after each jump, this being comparable to the energy dissipated by a bombarding ion provided the latter is properly distributed amongst the atoms affected. The same authors note that, though the model itself can be disputed, the remarkable parallel between anodically formed and bombarded oxides (as summarized in Table 3.III) still remains.

The low anodizing efficiency found here for Sn (4-21%) finds a parallel in the behaviour of Si and Ge. Thus the value 2% has been quoted for Si (23) and 10-17% for Ge (24). It is nevertheless highly unusual considering anodic oxides in general (Table 3.IV). We are not prepared to offer an explanation, as too little is known about anodizing efficiency. An argument based on the electronic band structure of the anodic film is, for example, meaningless when it is not known to what extent incorporation of components from the electrolyte ("doping") alters the band structure.

TABLE 3.IV

Comparison of fields and efficiencies for anodizing various metals (from Ref. 13)

Metal	Electrolyte	Field to form a 50-V film (10^8 V/m)	Efficiency at constant current of 2 or 3 mA/cm^2
V	mainly acetic acid	2.8	0.95
Mo	mainly acetic acid	2.9	0.95
Nb	aqueous	3.4	$\sim$1.0[a]
Zr	aqueous	4-6	0.50
W	mainly acetic acid	4.6	0.96
Ta	aqueous	6.2-6.6	0.99
Al	aqueous	8.7-9.1	0.90
Be	ethylen glycol saturated with both Na_2HPO_4 and Na_2SO_4	19.0	0.95

[a] Not for constant current.

REFERENCES

1. M. Croset, E. Petreaner, D. Samuel, G. Amsel and J. P. Nadai, J. Electrochem. Soc. 118, 717 (1971).

2. J. Yahalom and J. Zahavi, Electrochim. Acta 15, 1429 (1970).

3. A. Güntherschulze and H. Betz, "Electrolytkondensatoren", Krayn, Berlin (1937).

4. T. P. Hoar, "Modern Aspects of Electrochemistry", vol. 2, p. 262, Academic Press, New York (1959).

5. L. Young, "Anodic Oxide Films", Academic Press, New York (1961).

6. D. A. Vermilyea, "Advances in Electrochemistry", vol. 3, p. 211, Ed. P. Delahay, Interscience Publishers Inc., New York (1963).

7. M. J. Dignam, "Oxides and Oxide Films", p. 91, Ed. John Diggle, Marcel-Dekker Inc., New York (1972).

8. E. J. W. Verwey, Physica 2, 1059 (1935).

9. N. F. Mott, Trans. Faraday Soc. 43, 429 (1947).

10. L. Young, Can. J. Chem. 37, 276 (1959).

11. I. Reid and R. Kelly, Can. J. Phys. 50, 1887 (1972).

12. W. S. Johnson and J. F. Gibbons, "Projected Range Statistics in Semiconductors", Stanford University Bookstore, Stanford, Calif., (1969).

13. M. T. Shehata and R. Kelly, J. Electrochem. Soc. 122, 1359 (1975).

14. M. R. Arora and R. Kelly, J. Electrochem. Soc. 119, 270 (1972).

15. R. G. Keil and R. E. Salomon, J. Electrochem. Soc. 115, 628 (1968).

16. M. R. Arora and R. Kelly, J. Electrochem. Soc. 120, 128 (1973).

17. M. T. Thomas, J. Electrochem. Soc. 117, 396 (1970).

18. P. H. G. Draper and J. Harvey, Acta Met. 11, 873 (1963).

19. M. L. Levin, Trans. Faraday Soc. 54, 935 (1958).

20. D. G. Brandon, J. Zahavi, A. Aladjem, and J. Yahalom, J. Vacuum Sci. Technol. 6, 783 (1969).

21. D. M. Lakhiani and L. L. Shreir, Nature 188, 49 (1960).

22. M. R. Arora and R. Kelly, to be published.

23. M. A. Wilkins, Harwell (U.K.) Report AERER5875 (1968).

24. S. Zwerdling and S. Sheff, J. Electrochem. Soc. 107, 338 (1960).

CHAPTER 4

OXYGEN BOMBARDMENT OF Sn

4.1 General

We have seen that SnO_2 can be prepared in a number of ways (evaporation, chemical deposition, reactive sputtering, ion-beam sputtering, anodizing). We want to explore now the feasibility of preparing SnO_2 by oxygen implantation, i.e. by bombarding metallic tin with an oxygen ion-beam. There is an obvious practical application, namely being able to fabricate complicated patterns of SnO_2 for microcircuitry. It will be concluded that the desired goal is not easily reached due to the tendency for Sn to convert to SnO.

4.2 Sn metal thin films

4.2.1 Preparation and thin-film analysis - Sn metal films were prepared by evaporating Sn onto KCl and Ta substrates at room temperature in a standard evaporator* at 2×10^{-5} torr. Film thickness was controlled by varying the substrate exposure time to the molten Sn in a W boat. Times of 15 to 30 s were used for films intended for transmission electron microscopy, while the exposure time was longer when the film did not need to be detached from the substrate, i.e. when it was to be used for RED†. Films deposited on KCl were floated off in distilled water and mounted on grids. Worth mentioning is the fact that such films, once picked up on a

---

* Model VE-10, Varian

† Reflection electron diffraction

microscope grid, always collapsed through the holes in the grid, no matter how high the number of meshes or how thick the film. Hence the films were mounted on carbon-coated grids with Fig. 4.1(a) showing a typical film. The as-deposited films exhibited the diffraction pattern of Fig. 4.1(b), which, as shown in Table 4.I, is β-Sn, the expected structure. Films were also analyzed in RED (Fig. 4.2) and again showed the β-Sn structure.

4.2.2 Oxygen-ion bombardment of Sn - Oxygen-ion bombardment was performed at 35 keV, using doses ranging between 1×10^{15} and 3×10^{17} ions/cm^2. Some 15 different samples were implanted. Fig. 4.3 shows the diffraction pattern of a sample implanted to 3×10^{15} ions/cm^2. To begin with, one can notice, from the general appearance of the diffraction pattern as compared to Fig. 4.1(b), that some physical change has taken place: a new structure has appeared and it is not fully random. ASTM-cards relative to α-SnO (tetragonal), high pressure SnO (orthorhombic), β-SnO, a further orthorhombic form, SnO_2, β-Sn and α-Sn were considered (Table 4.II) and Fig. 4.3 was analyzed as follows. The first complete ring has a radius such that the planes it arises from have a spacing of approximately d = 2.94 Å. (Our camera constant was 3.21 Å cm, as determined using a gold sample.) Comparing with the ASTM-card for α-SnO, we see that the ring which is by far the brightest (I = 100 compared to values of I ≤ 37 for the rest of the rings) corresponds to d = 2.984 Å. Normalizing our experimental d-values to this (i.e. multiplying by $\frac{2.984}{2.94}$) one obtains the values as in Table 4.III, which match α-SnO very well. Such a normalization (which is needed due to a possible and likely error in the value of the camera constant) cannot reasonably be applied when comparing with the ASTM-cards relative to the other forms of SnO or to SnO_2. Thus the closest value of SnO_2

(a)

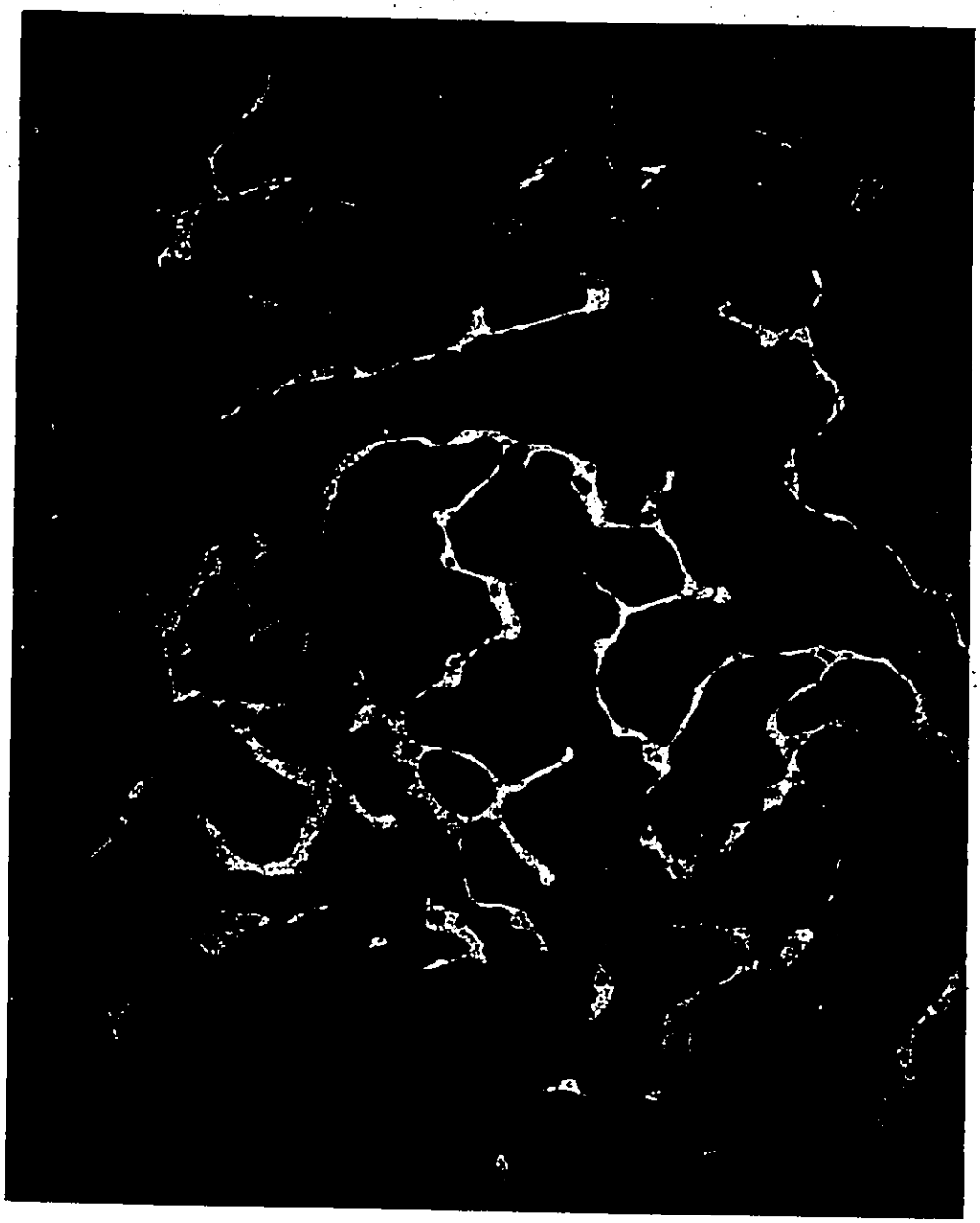

Fig. 4.1(a). Transmission micrograph (mag. 54,000) of Sn film.

(b)

Fig. 4.1(b). Diffraction micrograph of Sn film.

TABLE 4.I

Analysis of as-deposited evaporated Sn thin film.

Diffraction Pattern (Fig. 4.1(b))	β-Sn (ASTM-card 4-0669)
d(Å)	d(Å)
2.92	2.915
2.80	2.793
2.08	2.062
2.02	2.017
1.65	1.659
1.48	1.484
1.45	1.458
1.40	1.442
1.28	1.309

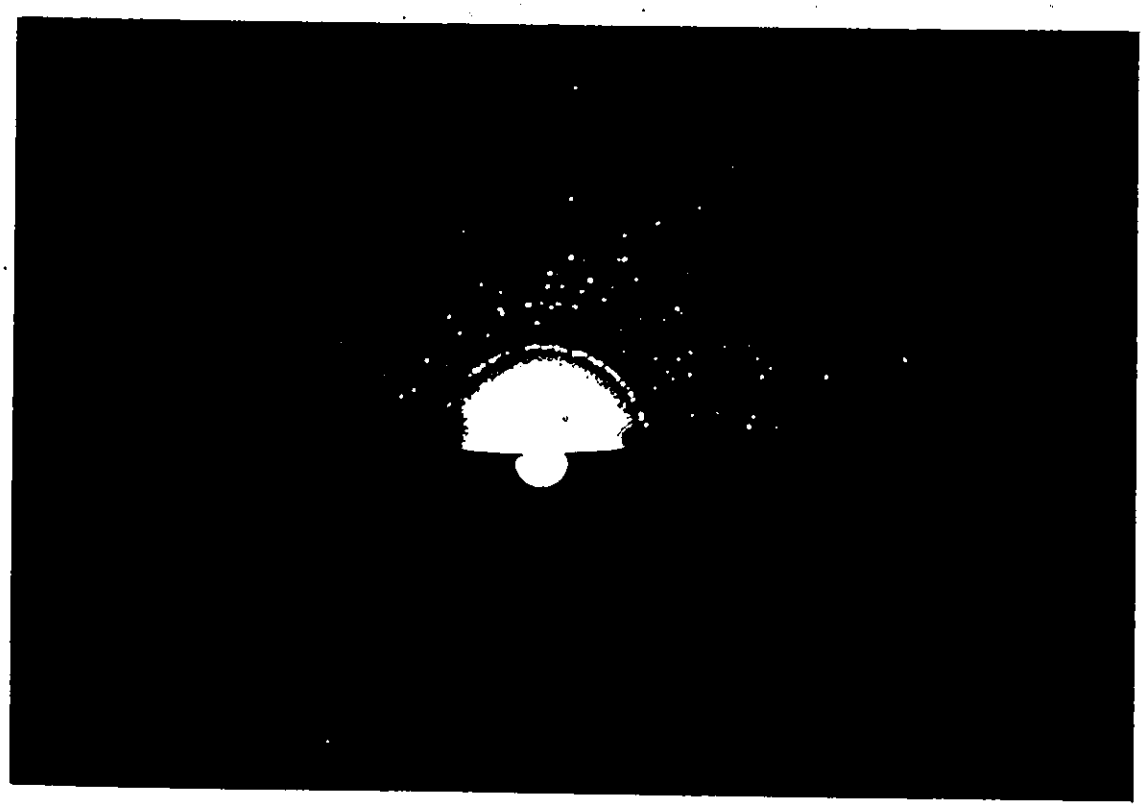

Fig. 4.2. RED of evaporated metallic tin.

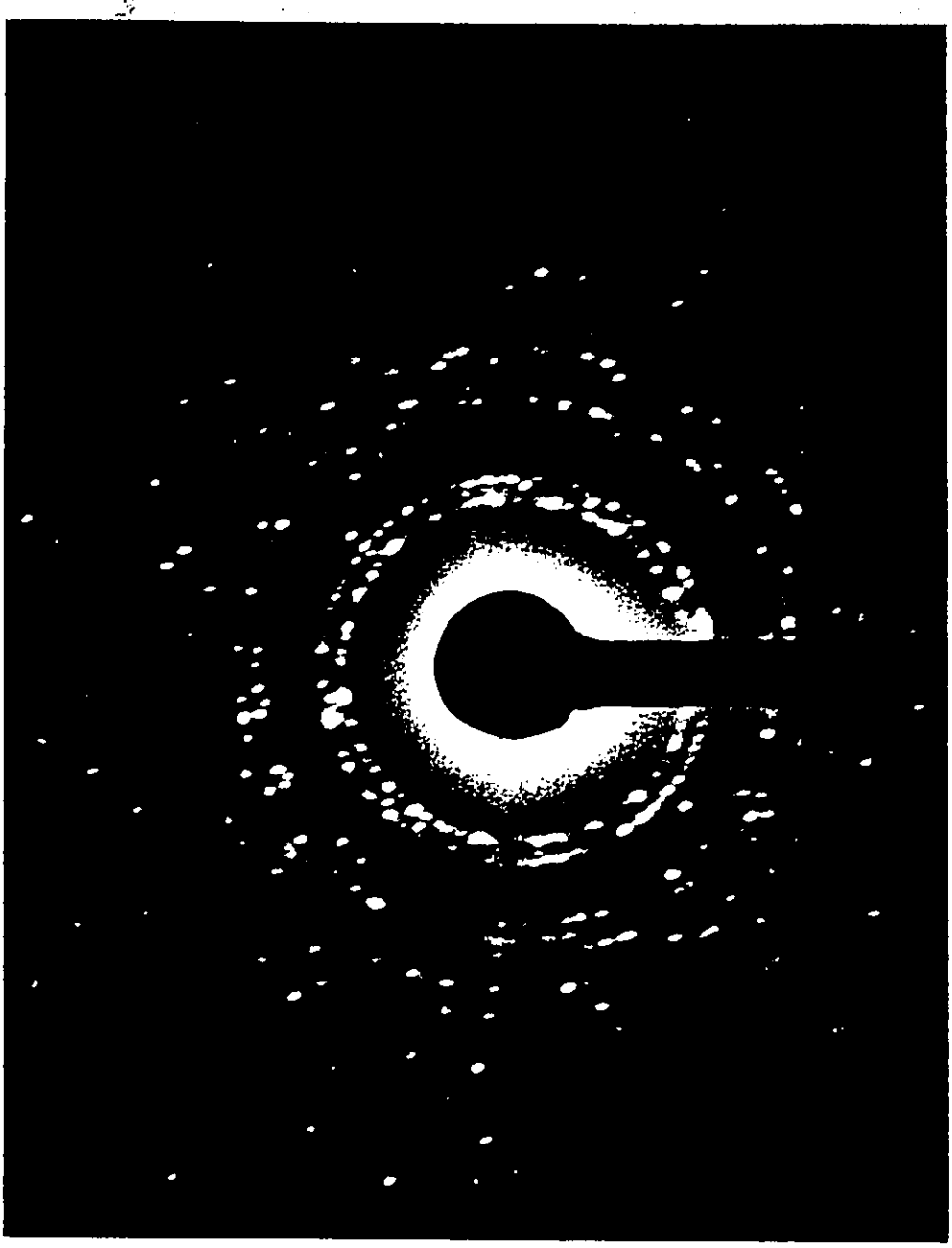

Fig. 4.3. Diffraction pattern of oxygen-implanted metallic tin-Dose: 3×10^{15} ions/cm^2 - 35 keV.

TABLE 4.II

Diffraction data for the Sn-O system

α-SnO(tetragonal)		SnO(high pressure)		β-SnO	
d(Å)	I	d(Å)	I	d(Å)	I
4.85	10	2.90	80	3.39	100
2.989	100	2.78	80	3.00	50
2.688	35	2.63	100	2.93	50
2.418	14	2.24	10	2.89	90
2.039	<1	2.12	10	2.67	90
1.901	14	1.95	30	2.08	10
1.797	25	1.80	10	2.02	40
1.604	25	1.75	20	1.773	80
1.494	12	1.66	50	1.678	20
1.484	12	1.572	50	1.598	20

Diffraction data for the Sn-O system (continued)

SnO(orthorhombic)		SnO_2		β-Sn	
d(Å)	I	d(Å)	I	d(Å)	I
5.56	10	3.351	100	2.915	100
3.71	10	2.644	81	2.793	90
3.58	30	2.369	24	2.062	34
3.12	100	2.309	5	2.017	74
2.86	20	2.120	2	1.659	17
2.78	40	1.765	63	1.484	23
2.50	30	1.675	63	1.458	13
2.25	20	1.593	8	1.442	20
1.994	10	1.498	13	1.304	15
1.888	20	1.439	17	1.292	15

α-Sn

d(Å)	I
3.751	100
2.294	83
1.956	53
1.622	12
1.489	20
1.325	21
1.249	11
1.470	6
1.0968	10

TABLE 4.III

Analysis of oxygen implanted metallic tin

Diffraction Pattern (Fig. 4.3) (normalized values)	α-SnO (ASTM-card 6-0395)
d(Å)	d(Å)
4.83(spots)	4.85
2.989	2.989
2.68	2.688
2.42(spots)	2.418
2.02	2.039
1.90	1.901
1.79	1.797
1.61	1.604
1.50	1.494,1.484

to our d = 2.94 Å and which is at the same time relatively intense is d = 3.35 Å. Comparing the experimental values with the ASTM-cards relative to β-Sn and α-Sn, we exclude the possibility of these structures due to two considerations: (a) our d-spacings mostly do not match the d-spacings of the ASTM-cards and (b) the ones which do match them are supposed (according to the ASTM-cards) to have such weak intensities that it would have been almost impossible for us to see them.

It is important to note, from Fig. 4.4 and Table 4.IV, that all the O_2-implanted samples showed the same pattern as in Fig. 4.3. This occurred even at the lowest dose used, i.e. 1×10^{15} ions/cm^2, where (cfr. Fig. 4.4(a),(b) and (c)) no lines are left from the β-Sn initial structure. Such a similarity over a wide range of oxygen doses (1×10^{15} to 3×10^{17} ions/cm^2) would be unlikely if two or more phases were present. We conclude that a layer of α-SnO is the end product of the bombardment of metallic tin with 35-keV O_2^+.

4.2.3 Sputtering coefficient of Sn due to O_2^+ impact - We have determined the sputtering coefficient of Sn due to 35-keV O_2^+, S, to be 1.88 atoms/ion. This is based on the average value of five experiments in which tin was bombarded with 35-keV O_2^+ at doses between 2×10^{17} and 5×10^{17} ions/cm^2 and the weight loss was measured. It will be shown in the next section that the formation of SnO rather than SnO_2 is closely related to the sputtering coefficient.

4.3 Discussion

Following the reasoning of Parker and Kelly (1), the expected phase for an oxygen-bombarded metal depends critically on S, the relevant sputtering coefficient. In particular, bombardment of metallic tin with O_2^+

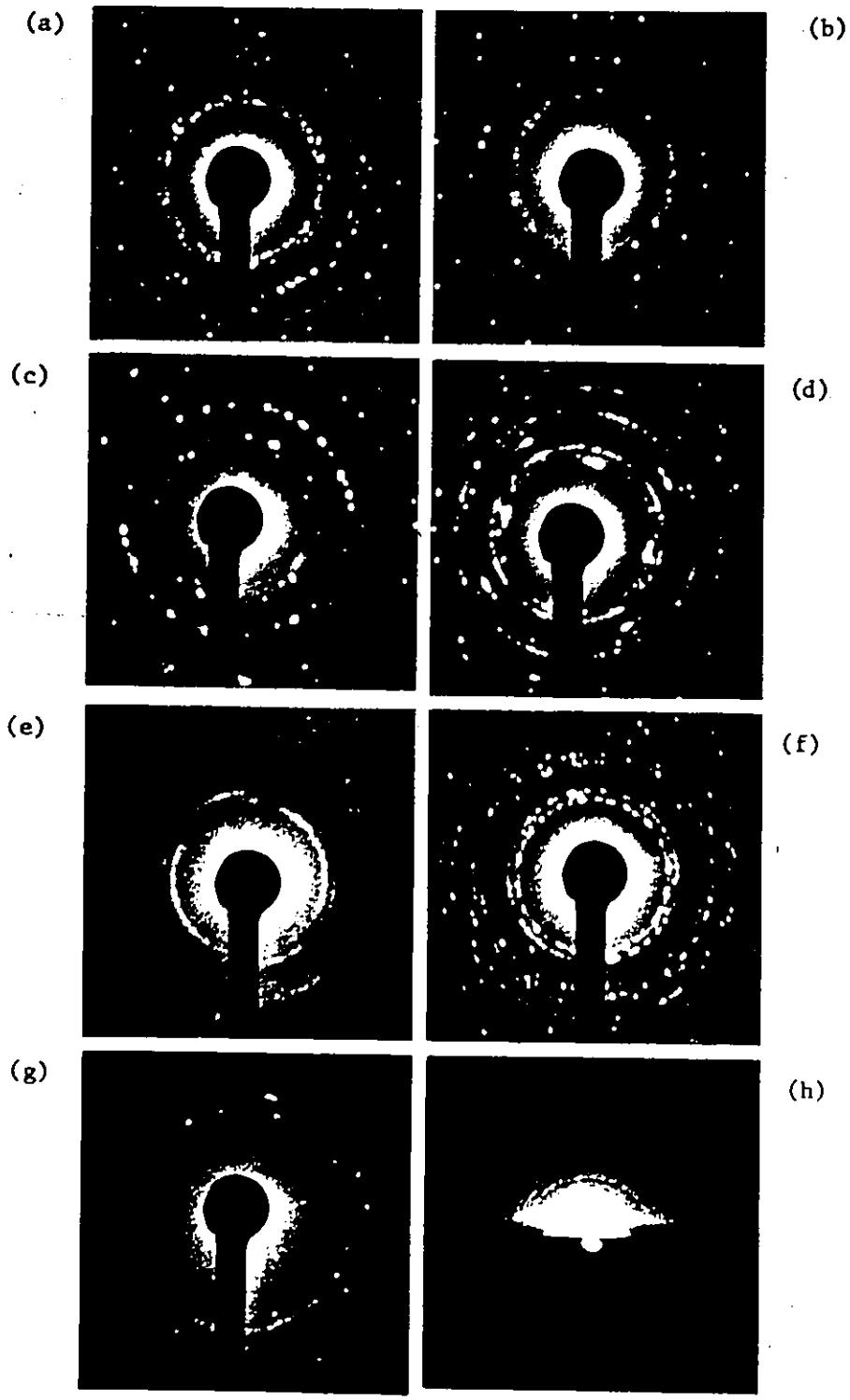

Fig. 4.4. Diffraction patterns of eight O_2-implanted Sn samples - 35 keV-Doses: (a) 1×10^{15} (b) 1×10^{15} (c) 1×10^{15} (d) 3×10^{15} (e) 3×10^{15} (f) 3×10^{15} (g) 3×10^{17} (h) 3×10^{17} ions/cm^2.

TABLE 4.IV

Comparing the ASTM d-spacings for α-SnO

with experimental (normalized) d-spacings obtained from Fig. 4.4

ASTM-card #6-0395 d(Å)	Sample #1 (Fig_{15} 4.4(a)) 1 x 10^{15} ions/cm^2	Sample #2 (Fig_{15} 4.4(b)) 1 x 10^{15} ions/cm^2	Sample #3 (Fig_{15} 4.4(c)) 1 x 10^{15} ions/cm^2	Sample #4 (Fig_{15} 4.4(d)) 3 x 10^{15} ions/cm^2
4.85				4.80
2.99	2.99	2.99	2.99	2.99
2.69	2.68	2.77	2.63	2.67
2.42				2.23
2.04	2.01	2.01	2.09	2.03
1.90	1.89	1.89	1.91	1.90
1.80	1.78			
1.60	1.59			1.60
1.49		1.49		
1.48				
1.38				
1.34			1.35	
1.23				

Comparing the ASTM d-spacings for α-SnO

with experimental (normalized) d-spacings obtained from Fig. 4.4

(continued)

ASTM-card #6-0395 d(Å)	Sample #5 (Fig_{15} 4.4(e)) 3 x 10^{15} ions/cm^2	Sample #6 (Fig_{15} 4.4(f)) 3 x 10^{15} ions/cm^2	Sample #7 (Fig_{17} 4.4(g)) 3 x 10^{17} ions/cm^2	Sample #8 (Fig_{17} 4.4(h)) 3 x 10^{17} ions/cm^2
4.85		4.83		
2.99	2.99	2.99	2.99	2.99
2.69	2.66	2.68	2.68	
2.42		2.42		
2.04		2.02	2.02	2.14
1.90	1.87	1.90	1.90	
1.80	1.78	1.79	1.79	1.76
1.60	1.57	1.61	1.61	1.57
1.49		1.50		1.54
1.48				1.47
1.38				1.38
1.34				
1.23				1.27

ions may be expected to lead to SnO_b, where b = 2/S. The argument was briefly as follows. Given an oxide whose initial stoichiometry is MO_a, the volume associated with an M atom, i.e. the volume of the "MO_a unit", is $\lambda^3 = (1 + a)/N$, where N is the number density of MO_a. When bombarding with O_2^+, the additional number of oxygen atoms per "MO_a unit" (i.e. per M atom) is given by Eq. (7) of Ref. 1:

$$\text{oxygen per } MO_a = (\lambda^3 N/S)\ \text{erfc}\ \frac{x-\langle x\rangle}{(2\mu_2)^{1/2}}$$

where $\langle x\rangle$ is the mean projected ion range, μ_2 is the mean square projected ion straggling, and a factor of 2 has been included to take into account that O_2^+ is diatomic. The maximum additional oxygen clearly occurs at the surface (x = 0), being given approximately by

$$\text{maximum oxygen per } MO_a = 2\ \lambda^3 N/S$$
$$= 2(1 + a)/S$$

and the resulting new stoichiometry is therefore MO_b, where b is given by

$$b = a + 2(1 + a)/S$$

Since in our case a = 0 (bombardment of a metal), we obtain b = 2/S = 1.06. Our experimental result (Section 4.2.3) thus matches the theoretically expected one rather well, and in fact constitutes the only instance known to the writer in which this was so. (Parker and Kelly (1) did not have access to the necessary S values.)

We would predict that Sn would be converted to SnO for all O_2^+ energies in the keV range, but that, due to S decreasing, SnO_2 would arise at very low or very high energies.

4.4 Conclusions

We have shown that Sn can be oxidized up to, but not beyond, the level SnO by oxygen implantation at keV energies. A sputtering argument was advanced and showed that formation of SnO is reasonable and understandable.

We will, in Chapter 6, treat the "mirror-image" problem, namely that of bombardment-induced oxygen removal from SnO_2. Work has been described in which oxygen bombardment of Cu led to Cu_2O (2,3), of Fe or FeS_2 led to Fe_3O_4 (2,4-6) and of U led to UO_2 (7). On the other hand, when bombarding CuO, Fe_2O_3 or U_3O_8 with inert gas or Hg ions, the following occurred:

$$CuO + 30\text{-keV Kr ions} \rightarrow Cu_2O \text{ and/or } Cu \quad (8)$$

$$U_3O_8 + 30\text{-keV Kr ions} \rightarrow UO_2 \quad (8,9)$$

$$CuO + \sim 0.5\text{-keV Hg ions} \rightarrow Cu_2O \text{ and } Cu \quad (10)$$

$$Fe_2O_3 + \sim 0.5\text{-keV Hg ions} \rightarrow Fe_3O_4 \text{ and } FeO \quad (10)$$

If the above results can be generalized, then we would expect Kr bombardment of SnO_2 to cause a loss of oxygen with resultant formation of α-SnO. On the other hand, a criterion to predict in each case whether oxygen loss should occur (Chapter 1, 6-9) can be applied to SnO_2 and, as will be discussed in Chapter 6, shown to predict no loss. The criterion is not infallible, however, so we do not regard the question of oxygen loss as being settled without explicit experiments.

REFERENCES

1. T. E. Parker and R. Kelly, J. Phys. Chem Solids, 36, 377 (1975).
2. A. Ladage, Z. Phys., 144, 354 (1956).
3. M. Meyer, C. Marelle and P. Haymann, C. R. Acad. Sci.(Paris), 268B, 1145 (1969).
4. J-J. Trillat, Cahiers de Physique, 83, (1957).
5. J-J. Trillat, Le Bombardament Ionique, Theories et Applications, Editions du C.N.R.S., Paris (1962).
6. J-J. Trillat and K.Mihama, C.R. Acad. Sci. (Paris), 248, 2827 (1959).
7. C. Sella and J-J. Trillat, Rév. Métallurg., 56, 105 (1959).
8. E. Kuczma, McMaster University, Canada, private communication (1973).
9. R. Kelly, Proc. Int. Conf. on Phys. Met. of Reactor Fuel Elements, Berkeley, U.S. (1973) in press.
10. G. K. Wehner, C. F. Kenknight and D. Rosenberg, Planet. Space Sci., 11, 1257 (1963).

CHAPTER 5

ION-IMPACT EFFECTS WITH SnO_2 FILMS

5.1 Introduction

We have given in Section 1.2.7 and 1.3 a comprehensive list of materials whose response to ion-impact is to undergo (a) a crystalline-amorphous transition, (b) an amorphous-crystalline transition, and (c) a stoichiometry change. We have also given the criteria which researchers have worked out in order to predict the occurrence of the above transformations. While we have noticed the lack of any published result as far as SnO_2 is concerned, we have pointed out, were the bombardment-induced amorphization of SnO_2 to occur, the possible technological implications of such an event.

The value of the crystallization temperature (Tc) for SnO_2 has been shown in Chapter 2 to be ∿773 K while Barczak and Insley (1) estimated the melting temperature (Tm) to be 1900 K. It follows that Tc/Tm ≈ 0.41, a value which is well above the cut off for a crystalline to amorphous transition to occur (cfr. Section 1.2.7). Likewise the ionicity, 0.43 (Ref. 74 of Chapter 1), also suggests ready amorphizability.

We will report now our findings on bombardment-induced phase transformations in SnO_2. We will start, in this chapter, with work on thin films, while in Part 2 (Chapters 6-9) we will treat the bulk material.

5.2 Sputtering coefficient of SnO_2

5.2.1 General - As far as obtaining the value of a sputtering coefficient

is concerned, the most satisfactory way of working with oxides is probably that in which an anodized metal is used as the target: such specimens are conductive by virtue of the extremely small oxide thicknesses, can be made as large as possible, and reveal in the interference colour changes the beam profile. The resulting films allow sputtering coefficient to be determined using, for example, the conventional weight-loss procedure. This method is based on the loss of weight of a target, the specimen having been weighted with a microbalance before and after prolonged bombardment. Thus one can calculate S (atoms/ion) using the general relation $x = BtS/N$ where Bt is the bombardment dose (ions/cm^2) and N is the number density (atoms/cm^2). This can also be written as

$$x(\text{in } \mu g/cm^2) = (Bt'S\bar{M})(6.21 \times 10^{-4}) \qquad (5.1a)$$

or

$$x(\text{in } Å) = (Bt'S\bar{M}/\rho)(0.0621) \qquad (5.1b)$$

where $\bar{M}$ is the mean atomic mass of the target, Bt' is the bombardment dose (μA min/cm^2), and ρ is the density of the target (g/cm^2). The interference colour changes, when sufficiently distinct, permit a somewhat simpler and more reliable determination of S (2). This approach could not be used with SnO_2, owing to the nature of the interference colours.

5.2.2 Experimental and Results - The sputtering coefficient, S, due to Kr bombardment of crystalline anodic films of SnO_2 has been determined for ion energies of 10, 20 and 30 keV. The method employed was based on the loss of weight of the target.

Table 5.I gives the complete data for the sputtering yield (S) for

TABLE 5.I

Sputtering yield at room temperature

for Kr-impact on SnO_2

Energy (keV)	Current (μA)	Dose (ions/cm^2)	S (atoms/ion)
10	5	1.42×10^{16}	10
10	5	2.81×10^{16}	32
10	5	4.23×10^{16}	20
10	5	5.61×10^{16}	23
20	2.5	7.11×10^{15}	60
20	5	7.11×10^{15}	49
20	5	8.60×10^{15}	30
20	5	1.27×10^{16}	29
20	2.5	1.42×10^{16}	53
20	5	1.42×10^{16}	28
20	5	1.42×10^{16}	26
20	5	1.42×10^{16}	37
20	2.5	1.76×10^{16}	45
20	5	2.10×10^{16}	16
20	5	2.10×10^{16}	51
20	2.5	2.81×10^{16}	35
20	5	2.81×10^{16}	24
20	5	2.81×10^{16}	18
20	5	2.81×10^{16}	34
20	15	2.96×10^{16}	14
20	5	3.52×10^{16}	29
20	15	3.96×10^{16}	17
20	15	4.23×10^{16}	12
20	15	4.23×10^{16}	16
20	5	4.86×10^{16}	15

Sputtering yield at room temperature

for Kr-impact on SnO_2 (continued)

20	5	4.94×10^{16}	29
20	15	4.97×10^{16}	16
20	15	4.97×10^{16}	18
20	5	5.61×10^{16}	26
20	15	5.95×10^{16}	7
20	15	5.95×10^{16}	15
20	9	6.32×10^{16}	11
20	15	6.32×10^{16}	10
20	15	6.32×10^{16}	14
20	22.5	7.59×10^{16}	9
20	5	8.42×10^{16}	18
20	5	8.42×10^{16}	24
20	15	8.42×10^{16}	13
20	15	9.95×10^{16}	13
20	9	1.14×10^{17}	15
20	15	1.35×10^{17}	13
20	15	1.52×10^{17}	14
20	15	1.68×10^{17}	14
20	7	1.74×10^{17}	15 (pellet)
20	15	2.11×10^{17}	15
20	15	2.18×10^{17}	16
20	15	3.08×10^{17}	17
20	7	3.18×10^{17}	20 (pellet)
20	15	3.37×10^{17}	12
30	5	7.11×10^{15}	62 (pellet)
30	5	1.42×10^{16}	22 (pellet)
30	5	1.42×10^{16}	14 (pellet)
30	5	2.09×10^{16}	25 (pellet)

Sputtering yield at room temperature

for Kr-impact on SnO_2 (continued)

30	5	2.81×10^{16}	30 (pellet)
30	5	2.81×10^{16}	23 (pellet)
30	5	2.81×10^{16}	21 (pellet)

Kr impact on SnO_2 as a function of the krypton energy and dose. Fig. 5.1 shows the average value of S for each energy, each point representing an average of four to 45 measurements made with various doses.

Fig. 5.2 shows that the sputtering coefficient is, for doses $\geq 3 \times 10^{16}$ ions/cm^2, dose independent; for lower doses, however, it appears to increase.

The first general characteristic of S for this oxide is that the dependence on energy is, between 10- and 30-keV, very small. This is, in fact, exactly the same behaviour as what one observes in sputtering of metals (3-5) and oxides (6). The second characteristic is the unusually high value of the sputtering coefficient. SnO_2 in this respect resembles MoO_3, V_2O_5, WO_3, and possibly SiO_2, but, to the writer's knowledge, no other oxide (7).

In view of the unexpected result that S for SnO_2 was unusually large, our next step has been to measure the sputtering coefficient as a function of the target temperature, with results as summarized in Table 5.II and Fig. 5.3. In this case, specimens were pellets made from sintered SnO_2 powder. Note that we have taken for S at room temperature the average of the values obtained at 20-keV for doses $\geq 3 \times 10^{16}$ ions/cm^2 (Table 5.I), namely 17 ± 1 atoms/ion (practically the same value is obtained, for all doses (Table 5.I) at 20-keV, if one calculates the "weighted mean").

The result of these experiments is seen to be a tendency for S to be even higher at elevated temperatures. This suggests that the unusually large values are associated with thermal (as distinct from collisional) effects.

5.2.3 Discussion - This section is concerned with a possible explanation for the unusually high value of S for the Kr-SnO_2 system.

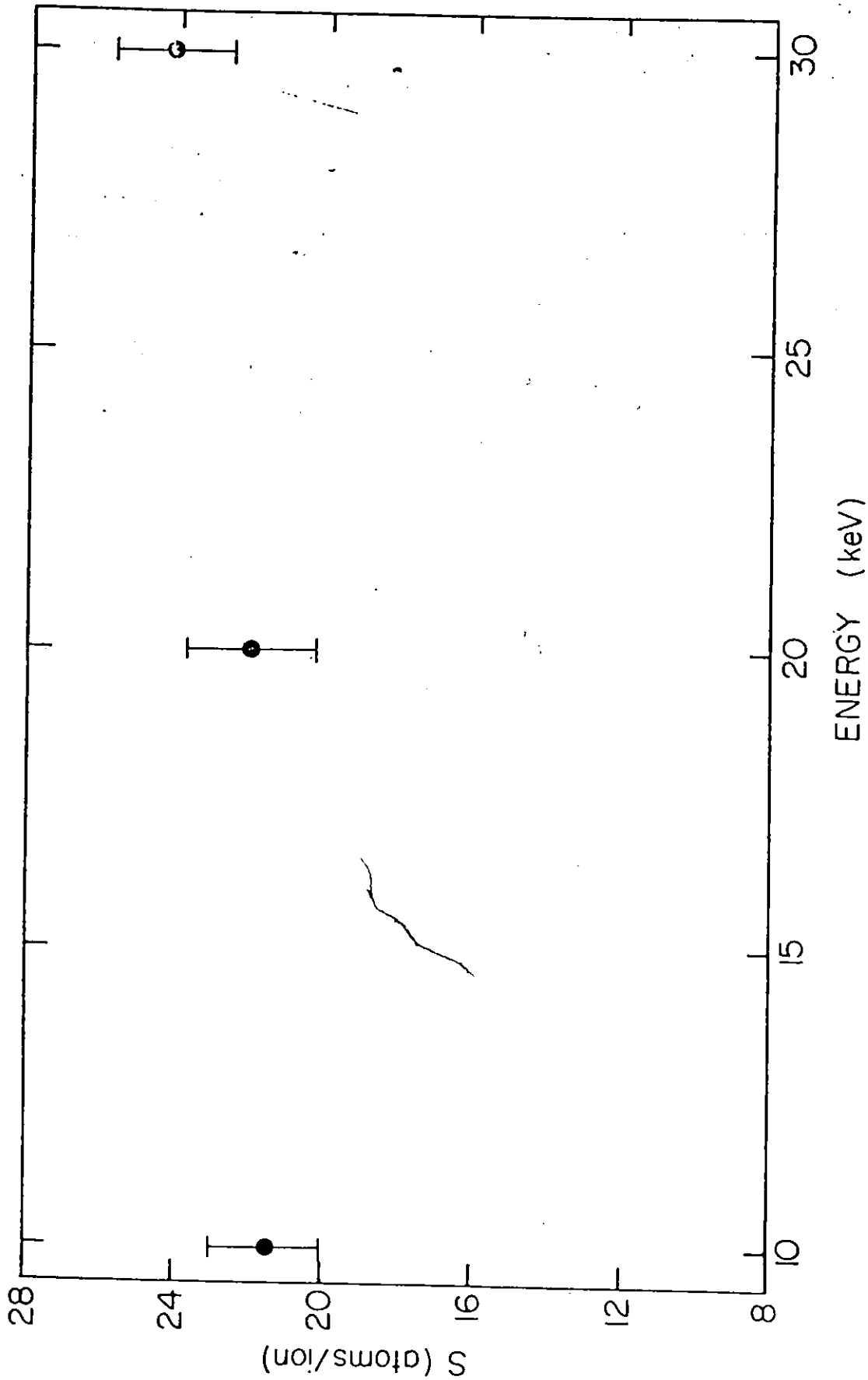

Fig. 5.1. The sputtering yield for Kr-impact on SnO_2 as a function of the krypton energy. Vertical bars represent the standard deviation of the arithmetic mean. The arithmetic mean is obtained from Table 5.I, where, for each energy, the highest and the lowest value of the sputtering coefficient are neglected.

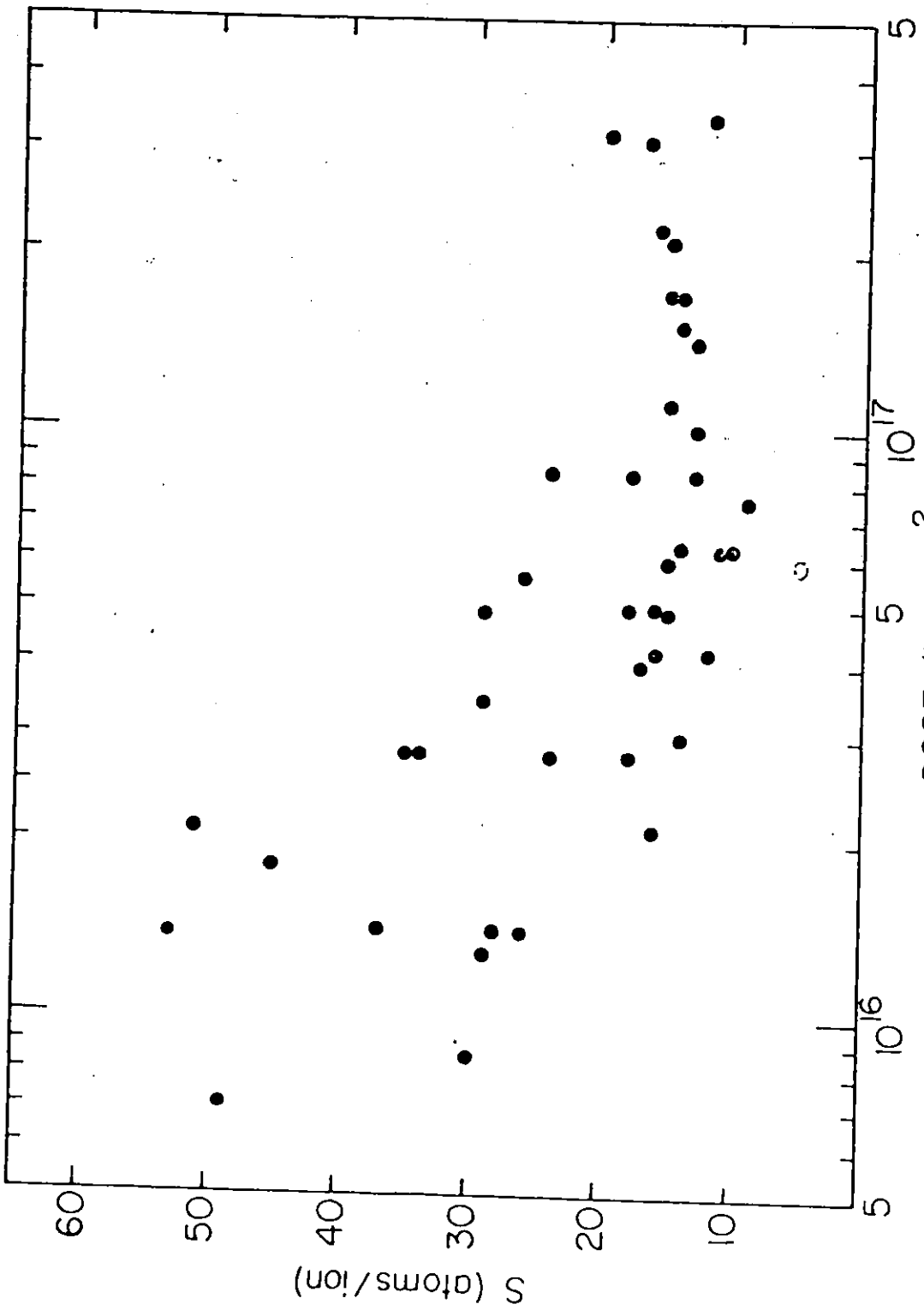

Fig. 5.2. Variation of sputtering coefficient with dose for 20 keV bombardment of SnO_2. Data are taken from Table 5.I, where, again, the highest and the lowest value of the sputtering coefficient are neglected.

TABLE 5.II

S at 20-keV for Kr-impact on SnO_2

as a function of temperature

Current (μA)	Dose (ions/cm^2)	T (°C)	S (atoms/ion)
8	2.96×10^{16}	300	28
8	2.96×10^{16}	300	37
25	5.35×10^{16}	300	30
25	5.35×10^{16}	300	11
8	5.95×10^{16}	300	26
10	5.95×10^{16}	300	24
18	9.35×10^{16}	300	27
18	9.35×10^{16}	300	23
17	9.50×10^{16}	300	24
18	1.04×10^{17}	300	22
40	1.28×10^{17}	400	16
40	1.28×10^{17}	400	19
40	2.55×10^{17}	400	17
40	2.55×10^{17}	400	22
38	4.35×10^{16}	520	15
42	5.98×10^{16}	520	10
60	1.07×10^{17}	520	26
60	1.07×10^{17}	520	22
47	1.17×10^{17}	520	25
50	1.64×10^{17}	520	30
50	1.78×10^{17}	520	38
60	2.14×10^{17}	520	22
60	4.28×10^{17}	520	28

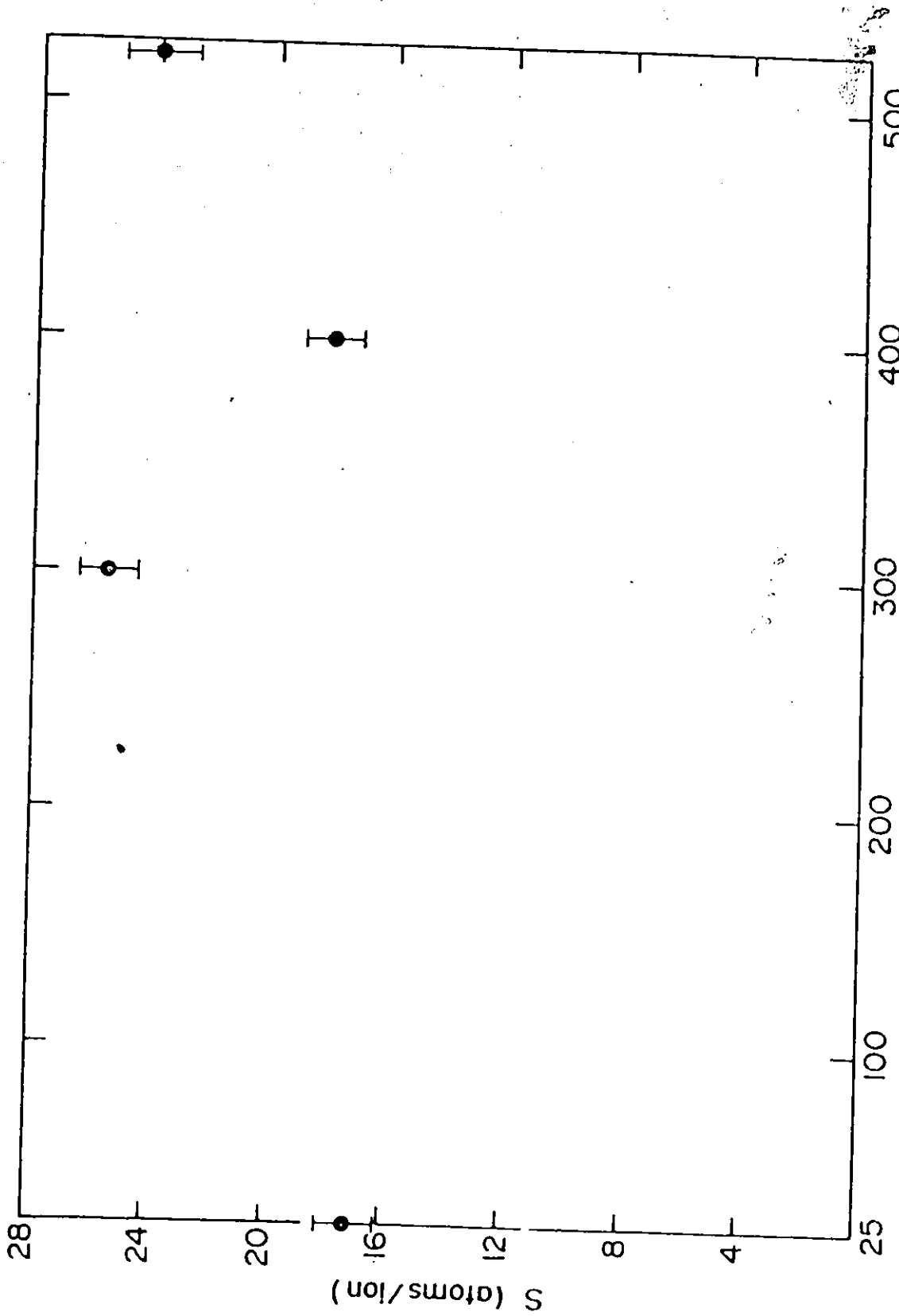

Fig. 5.3. S at 20 keV for Kr-impact on SnO_2, as a function of temperature. Vertical bars represent the standard deviation of the arithmetic mean. The arithmetic mean is obtained from Table 5.I and 5.II, where, for each temperature, the highest and the lowest value of the sputtering coefficient are neglected.

It is apparent from Table 5.III that some oxides (MoO_3, V_2O_5, WO_3, SnO_2; possibly also SiO_2) show very high sputtering coefficients. According to Sigmund's theory of collisional sputtering, S is given by

$$S = \frac{\alpha M_2 k_\rho s_n(\varepsilon)}{1.42 k_\varepsilon E_b} \qquad (5.2)$$

where M_1 and M_2 are the mass numbers of the ion and target, α is a quantity which depends only on M_2/M_1 (Fig. 13 of Ref. 17), k_ρ is defined by $\rho = k_\rho R$ where ρ is Lindhard's reduced distance variable and R is the total range in μ g/cm^2 (tabulated by Winterbon (18)), $s_n(\varepsilon)$ is the nuclear stopping cross-section in ε-ρ units (Table I of Ref. 17), and k_ε is defined by $\varepsilon = k_\varepsilon E$ where ε is Linhard's reduced energy variable and E is the incident energy in keV (tabulated in Ref. 18). Finally, E_b is the surface binding energy in units of eV/atom, which Jackson (19) has shown to be similar to (though, in fact, slightly less than) the heat of atomization.

We regard the correlation between S and E_b as the basic argument to be used when data such as the present on SnO_2 are considered.

Thus the seven oxides, Al_2O_3, MgO, Nb_2O_5, Ta_2O_5, TiO_2, UO_2 and ZrO_2, have sputtering coefficients equal or smaller than those expected from Sigmund's theory of collisional sputtering. This follows from the experimental values of E_b being equal or larger than those expected from thermodynamics (Table 5.IV). Here the experimental E_b is the quantity obtained by substituting the experimental S value into the analytical expression for S deduced by Sigmund and retrieving E_b. The thermodynamic E_b has been taken as the heat of atomization, as in the following example, this being equivalent to the use of the heat of vaporization with metals:

TABLE 5.III

Comparison of sputtering behaviour of oxides

for 10-keV Kr impact

Oxide	S for oxide (atoms/ion)	Ref.
Al_2O_3	1.6; 1.4 ± 0.2[a]	2, 8-10
MgO	1.8 ± 0.5[a]	10, 11
MoO_3	9.6 ± 0.4	12
Nb_2O_5	3.4 ± 0.5	13
SiO_2	4.2; 3.0 ± 1.5[a]	8, 12, 14, 15
Ta_2O_5	2.5 ± 0.5	13
TiO_2	1.9; 1.4[a]	2, 10
UO_2	3.8 ± 0.5[a]	16
V_2O_5	12.7 ± 1.7	12
WO_3	9.2 ± 1.2	13
ZrO_2	2.8 ± 0.1	12
SnO_2	21.5 ± 1.5	present work

[a]Data other than for 10-keV Kr; extrapolated as if for 10-keV Kr using Eq. (5.2).

TABLE 5.IV

Comparison of surface binding energies

Oxide	Experimental (from eq. (5.2)) (eV/atom)	Thermodynamic E_b (eV/atom)
Al_2O_3	9.4	6.4
MgO	7.8	5.2
TiO_2	11.3	6.6
Ta_2O_5	13.3	7.2
ZrO_2	8.3	7.6
UO_2	10.6	7.2
Nb_2O_5	6.8	6.8
SiO_2	3.9	6.4
WO_3	3.3	6.3
MoO_3	2.4	5.6
V_2O_5	1.5	5.7
SnO_2	1.8	4.8

$$SnO_2(s) = Sn(g) + 2.0(g)$$

$$\Delta H = \beta \times \Delta H_{atomization}$$

The necessary heats are tabulated by Kubaschewski et al. (20).

On the other hand, the five oxides showing high S have experimental E_b's which are significantly lower than the thermodynamic values. A further process, such as thermal sputtering, is evidently occurring; i.e. the sputtering is no longer a purely collisional phenomenon. The most direct information is of the type shown in Fig. 5.3, i.e. measurement of S as a function of temperature. Very little such work can be found in the literature, with results on oxides to date being confined to those shown in Table 5.V and Fig. 5.4. In all cases, except for Al_2O_3 and Nb_2O_5, but including SnO_2, S increases markedly with temperature. The occurrence of thermal sputtering, i.e. sputtering involving vaporization, is inferred.

Thermal sputtering is the name given to vaporization at a solid surface due to the heat (as distinct from momentum) which is dissipated by an ion. A criterion for thermal sputtering has been worked out by Parker and Kelly (22), based on evaluating the gas-kinetic relation

$$\text{atoms evaporating} = (1/4)N\langle v\rangle t_s \pi y_s^2 \qquad (5.3)$$

where N is the density of the equilibrium vapour in molecules/cm^3, $\langle v\rangle$ is the mean gas velocity, t_s is the lifetime of a thermal spike, and πy_s^2 is the spike area at the surface. Equation (5.3) can be re-expressed as follows:

$$\text{atoms evaporating} = 8.4 \times 10^{25} P_{atm} t_s y_s^2 M^{-(1/2)} T^{-(1/2)} \qquad (5.4)$$

TABLE 5.V

Effect of temperature on S

for oxides (10-keV Kr impact)

Oxide	S at room temperature (atoms/ion)	S at 200°C (atoms/ion)	Ref.
Al_2O_3[b]	1.25[a]	1.1	9
Nb_2O_5	3.4 ± 0.5	3.9 ± 0.4	12
WO_3	9.2 ± 1.2	13.2 ± 1.0	12
MoO_3	9.6 ± 0.4	15.1 ± 1.0	12
V_2O_5	12.7 ± 1.7	17.2 ± 1.1	12
SnO_2[c]	17.1 ± 1.0	25.5[d] ± 1.0	here

[a]Liquid-nitrogen temperature

[b]10-keV Cs impact

[c]20-keV Kr impact

[d]300°C

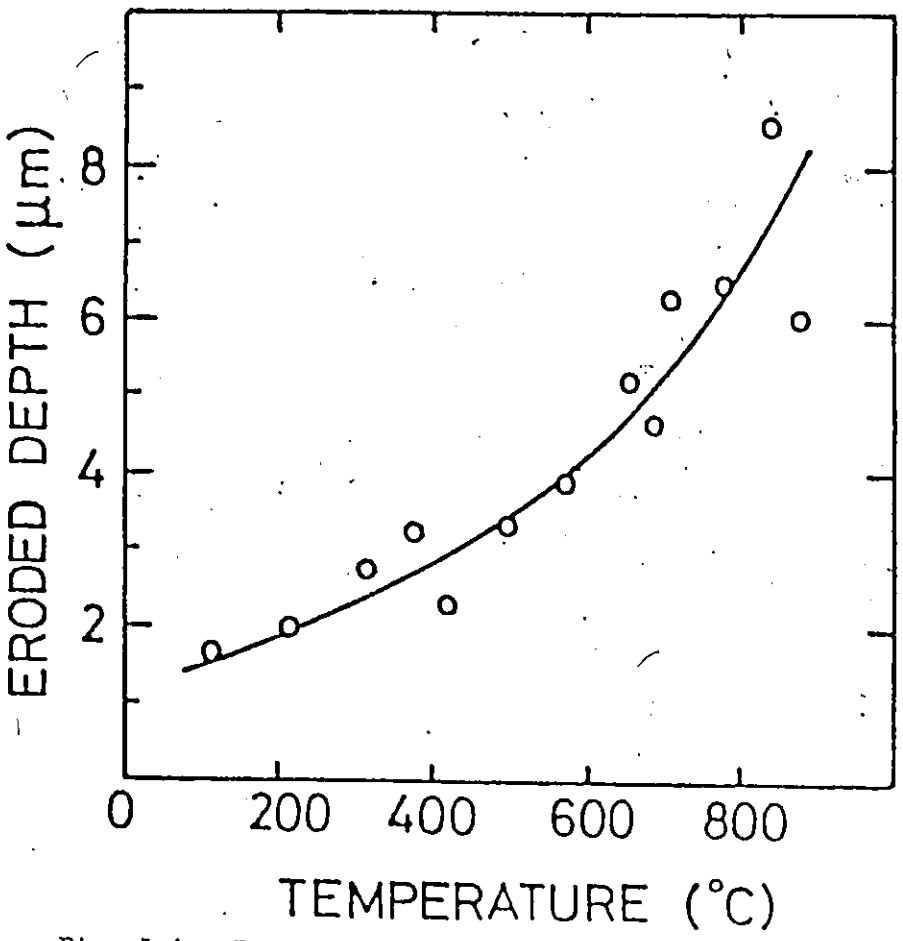

Fig. 5.4. Erosion depth of SiO_2 as caused by the impact of 12-keV Ar ions as a function of temperature. (from Ref. 21)

where P_{atm} is the equilibrium vapour pressure in atmospheres. "t_s" in eq. 5.3 or 5.4 is an ill defined quantity lying in the vicinity of 10^{-11} to 10^{-12} s (23,24) while y_s is a quantity which for keV-energy ions can be identified fairly safely with the product

$$(\langle y_d^2 \rangle)^{1/2} (\delta_y^{1/2})$$

Here $\langle y_d^2 \rangle$ is the mean square projected damage range perpendicular to the ion trajectory (25) and δ_y is a correction so that $\langle y_d^2 \rangle$ will be correlated to a particular trajectory (26). For example, for 30 keV Kr-TiO_2, δ_y is 0.74 and $(\langle y_d^2 \rangle)^{1/2}$ is 41 Å, whence y_s is 35 Å.

The criterion for thermal sputtering is then the following

$$\text{atoms evaporating} \geq 1,$$

that is,

$$P_{atm} \geq 5 \text{ to } 50 \qquad (5.5)$$

the latter inequality applying at the spike temperature, T_s. The main weakness of this approach is that the spike temperature is still undefined, though the following indirect approach for estimating it has been proposed (22).

Fig. 5.5 shows the vapour-pressure of ten oxides for which both sputtering and vapour-pressure data are available. Neglecting SnO_2 for the moment, we note that MoO_3, V_2O_5 (simulated by VO_2) and WO_3 are believed to show thermal sputtering in room-temperature bombardments, SiO_2 is uncertain as to its behaviour, while the remaining five apparently do not show thermal sputtering. This fixes T_s at a value near 3000 K or possibly higher, and

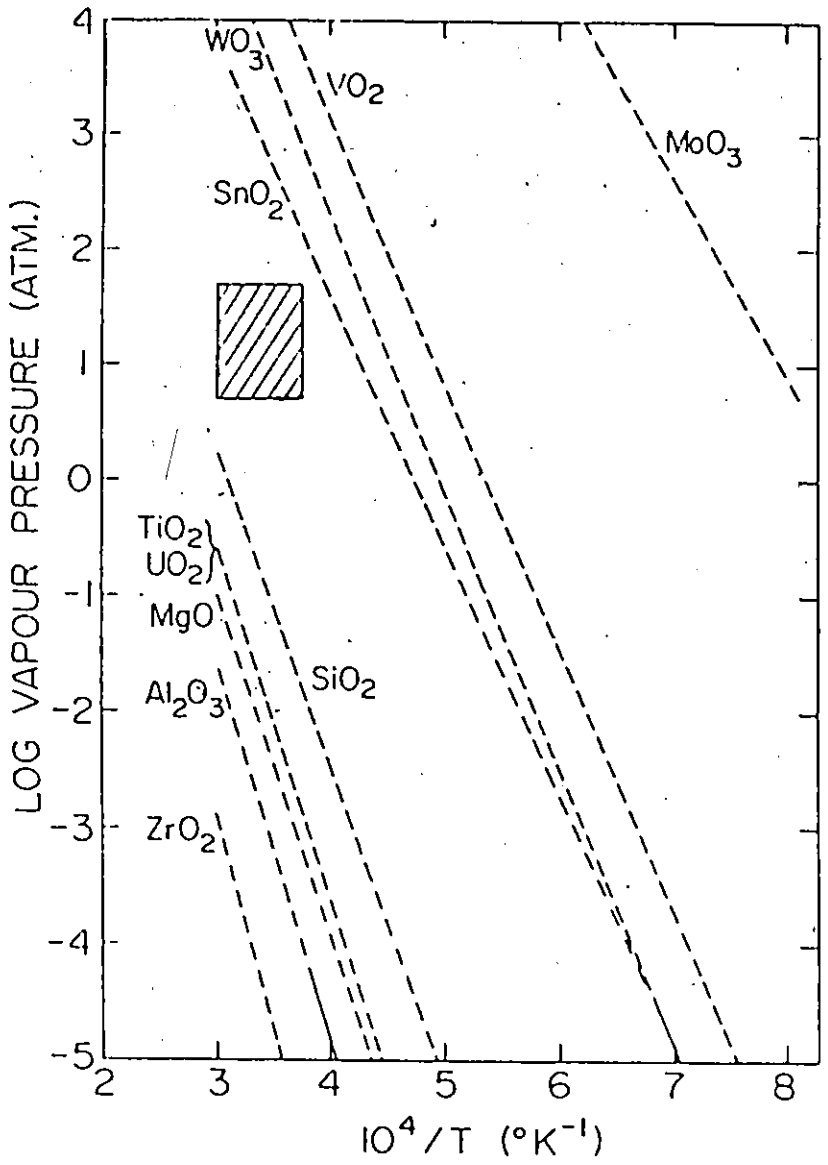

Fig. 5.5. Arrhenius plot of vapour pressure of dominant species for the oxides as indicated. The cross-hatched box encloses the pressures and temperatures which are argued to be the critical values for thermal-spike vaporization. The references are: ZrO_2(27), Al_2O_3(28), MgO(29), TiO_2(30), UO_2(31), SiO_2(20), WO_3(32), VO_2(33,34), MoO_3(35), and SnO_2(36). Dashed lines constitute extrapolations.

thus (together with eq. 5.5) defines the cross-hatched box.

To apply the criterion of eq. 5.5 to SnO_2 it is sufficient to note whether the vapour-pressure line of SnO_2 lies to the right of the cross-hatched box in Fig. 5.5. The line, in fact, does lie to the right, showing that thermal sputtering has a high likelihood.

There is thus no difficulty in understanding the unusually high values of S found with SnO_2.

5.3 Bombardment-induced structure changes of SnO_2

The next step in exploring the response of SnO_2 to ion-impact was to investigate the structure of the target material after bombardment.

Fig. 5.6(a) shows the diffraction pattern of anodized tin, showing the usual microcrystalline structure (Chapter 3). Amorphization due to ion-impact is evident from Fig. 5.6(b) and (c), which are the diffraction patterns of two samples bombarded to 2.81×10^{16} and 5.61×10^{16} ions/cm^2 respectively.

Given this preliminary result, namely that crystalline SnO_2 does indeed amorphize under ion-impact, in the remaining chapters we will look in more detail into this phenomenon, supplementing electron microscopy with techniques based on solubility changes, marker release and electrical conductivity. The last two techniques require the use of bulk material, and since this constitutes a major departure from the thin-film techniques characterizing Chapters 2-5, we have designated Chapters 6-9 as constituting Part 2.

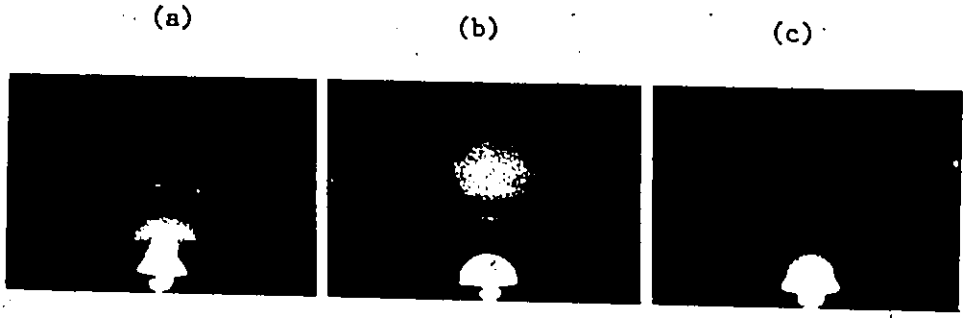

Fig. 5.6. RED of anodized tin

(a) before bombardment

(b) amorphization due to ion-impact in sample bombarded with 20 keV Kr-ions. Dose: 2.8×10^{16} ions/cm^2

(c) amorphization due to ion-impact in sample bombarded with 20 keV Kr-ions. Dose: 5.6×10^{16} ions/cm^2

REFERENCES

1. V. J. Barczak and R. H. Insley, J. Am. Ceram. Soc. 45 (3), 144 (1962).

2. R. Kelly, Can. J. Phys. 46, 473 (1968).

3. G. K. Wehner and D. Rosenberg, J. Appl. Phys. 32, 887 (1961).

4. O. Almén and G. Bruce, Nucl. Instr. Methods 11, 257 (1961).

5. P. K. Rol, J. M. Fluit and J. Kistemaker, Physica 26, 1000 (1960).

6. N. Q. Lam (or L. Q. Nghi) and R. Kelly, Can. J. Phys. 48, 137 (1970).

7. R. Kelly and Nghi Q. Lam, Radiation Effects 19, 39 (1973).

8. P. D. Davidse and L. I. Maissel, J. Vac. Sci. Technol. 4, 33 (1967).

9. E. H. Hasseltine, F. C. Hurlbut, N. T. Olson and H. P. Smith, J. Appl. Phys. 38, 4313 (1967).

10. H. Bach, Nucl. Instr. Methods 84, 4 (1970).

11. H. Schirrwitz, Beitrage zur Plasmaphysik 2, 188 (1962).

12. N. Q. Lam, Ph.D. thesis, McMaster University, Canada (1971).

13. N. Q. Lam (or L. Q. Nghi) and R. Kelly, Can. J. Phys. 48, 137 (1970).

14. A. I. Akishin, S. S. Vasil'ev and L. N. Isaev, Acad. Sci. USSR Bull. Phys. Sci. 26, 1379 (1962).

15. H. Bach, A. Naturforsch. 27a, 333 (1972).

16. O. Gautsch, C. Mustacchi and H. Wahl, EURATOM Report EUR 2515.e (1965).

17. P. Sigmund, Phys. Rev. 184, 383 (1969).

18. K. B. Winterbon, Chalk River Report AECL-3194 (1968).

19. D. P. Jackson, Rad. Effects 18, 185 (1973).

20. O. Kubaschewski, E. L. Evans and C. B. Alcock, Metallurgical Thermochemistry (Pergamon Press, Oxford, 1967), p. 303.

21. R. A. Dugdale and S. D. Ford, Trans. Brit. Ceram. Soc. 65, 165 (1966).

22. T. Parker and R. Kelly, Proc. 3rd Intern. Conf. on Ion Implantation in Semiconductors and Other Materials, Yorktown Heights, N.Y. (1973).

23. M. W. Thompson and R. S. Nelson, Phil. Mag. 7, 2015 (1962).

24. R. Kelly and H. M. Naguib, Proc. Intern. Conf. on Atomic Collision Phenomena in Solids, Brighton, U.K., 179 (1969).

25. K. B. Winterbon, P. Sigmund and J. B. Sanders, Kgl. Danske Vid. Selsk. Mat. Fys. Medd. 37, No. 14 (1970).

26. P. Sigmund. G. P. Scheidler and G. Roth, Proc. Conf. on Solid-State Research with Accelerators, Brookhaven Nat. Lab., Upton, N.Y. (1967).

27. W. A. Chupka, J. Berkowitz, and M. G. Inghram, J. Chem. Phys. 26, 1207 (1957).

28. J. Drowart, G. DeMaria, R. P. Burns, and M. G. Inghram, J. Chem. Phys. 32, 1366 (1960).

29. C. A. Alexander, J. S. Ogden, and A. Levy, J. Chem. Phys. 39, 3057 (1963).

30. J. Berkowitz, W. A. Chupka, and M. G. Inghram, J. Phys. Chem. 61, 1569 (1957).

31. R. J. Ackermann, P. W. Gilles, and R. J. Thorn, J. Chem. Phys. 25, 1089 (1956).

32. R. J. Ackermann and E. G. Rauh, J. Phys. Chem. 67, 2596 (1963).

33. S. A. Shchukarev, G. A. Semenov, and K. E. Frantseva, Russ. J. Inorg. Chem. 4, 1217 (1959).

34. N. Kimizuka, M. Saeki, and M. Nakahira, Mat. Res. Bull. 5, 403 (1970).

35. P. E. Blackburn, M. Hoch, and H. L. Johnston, J. Phys. Chem. 62 769 (1958).

36. R. Colin, J. Drowart, and G. Verhaegen, Trans. Faraday Soc. 61, 1364 (1965).

PART 2

ION-IMPACT EFFECTS

IN BULK SnO_2

CHAPTER 6

INTRODUCTION AND THEORETICAL

6.1 Introduction

A thorough study on the effects of ion-bombardment of oxides cannot be carried out using solely thin-film samples.

While thin films can be used when the material is to be analyzed by electron microscopy (Section 5.3) or when solubility measurements are performed (Section 8.3), only bulk material (and not anodic films) can be used when we study our material employing such techniques as gas-release spectrometry or resistivity measurements. The former requires bulk material due to the difference in melting point between the oxide and its parent metal substrate, the latter due to the metallic nature of the substrate and the film being, by definition, "thin". It is in principle possible to use films which have been detached from their substrate, but the practical handling of such specimens is very awkward.

We will, in the following chapters, report our findings on bulk samples (described in Section 7.1) which have been ion-bombarded and then analyzed using the following techniques: marker-release spectrometry (Sections 6.3 and 7.2), electrical conductivity measurements (Sections 6.4 and 7.2), dissolution measurements (Sections 6.5 and 7.2), and reflection electron diffraction (Section 7.2). The present chapter (Chapter 6) will give a brief indication of the theoretical background of our work, while Chapter 9 will be devoted to discussing the results. A summary of the whole thesis will be given in Chapter 10, together with some suggestions

for future work.

6.2 Criteria to predict the structural stability of solids under ion-impact

Before proceeding with the treatment of the individual criteria, we refer the reader to Section 1.2.7, where we have given a survey of experimental results concerning the ion-bombardment of oxides, and where it is also shown that these results are not random, but fit into predictable categories, depending (a) on the ratio Tc/Tm, (b) on the degree of ionicity of the atomic bond and (c) on the feasibility of oxygen loss to occur due to ion-bombardment. We will now show how this dependence was borne out.

6.2.1 Criterion based on a physical model involving thermal spikes - The formulation of the "thermal spike model" given in Ref. 1 is briefly as follows.

An ion hitting the surface of a material which is being bombarded will create, in a localized microscopic region, a temperature excursion such that the material will actually melt. During the subsequent cooling process, the target material may or may not go back to its original structure. This will depend on the distance (x_c) moved by the solid-liquid (amorphous-crystalline) interface, namely on the ability of the "host" material to sweep away the bombardment-induced alteration, and to restore the original structure. In mathematical terms this translates to:

$$x_c = \frac{1}{\lambda} \int_{t_1}^{t_2} D_c \, dt > \Gamma \qquad (6.1)$$

where D_c is the diffusion coefficient for the process under consideration (crystallization), λ is the distance between adjacent atomic planes in a

crystal (~0.25 nm), Γ is a quantitatively unspecified distance, and t_1 and t_2 are times corresponding to the beginning and the end of the thermal spike. The result of the integration

$$\int_{t_1}^{t_2} D_c dt = \int_{t_1}^{t_2} D_c^\circ (\exp[-\frac{\Delta H_c}{RT}])dt$$

is a series whose leading term is

$$D_c^\circ t_{eff} \exp[-\frac{\Delta H_c}{RTm}]$$

where Tm is the melting temperature, t_{eff} is the effective duration of the thermal spike and can be calculated for each material, and ΔH_c can be shown to equal (69±9)Tc.

Substituting in equation 6.1 (where we put $\Gamma = \lambda$), and rearranging, one concludes that, for the crystallinity of a material to be preserved under ion-impact, the following must hold:

$$(Tc/Tm) < (Tc/Tm)^* \approx 0.24$$

Inspection of Table 1.III and 1.IV shows that this relation is reasonable although better agreement with experiment is obtained with $(Tc/Tm)^* \approx 0.30$.

6.2.2 Criterion based on ionicity - We have already pointed out (Section 1.2.7) that the bond-type criterion to predict bombardment-induced structure changes in non-metallic solids is a basically empirical one, and it is shown in Ref. 1 that it accounts for the behaviour of a large number of ion-bombarded substances. The criterion can be formulated that if the ionicity is greater than 0.59 a solid will retain its crystalline structure while if the ionicity is less than 0.47 it will amorphize.

We will just mention here that the two approaches to predict bombardment induced phase transformations, namely the "thermal spike" model and the "bond-type" criterion, can perhaps be regarded as different aspects of a single, more inclusive model, in that a large value of Tc/Tm is characteristic of a covalent substance.

6.2.3 Criterion for oxygen loss - Bombardment-induced oxygen loss is currently discussed on the basis of two models (1-5): (a) vaporization due to thermal spikes (governed by the vapour pressure) and (b) preferential oxygen sputtering (governed by the surface binding energy). A third model, based on internal precipitation, can apparently be excluded according to work by Murti on Nb_2O_5 (5).

The "preferential oxygen sputtering" model is based on the theoretical result that $S \propto 1/E_b$ (6,7). E_b in turn is approximated by the heat of atomization (ΔHa) for the process of interest. In our case we consider two processes:

$$SnO_2(s) = Sn(g) + 2.0(g) \qquad (6.2)$$

$$SnO_2(s) = SnO(s) + O(g) \qquad (6.3)$$

Since $\Delta Ha = 4.8$ eV/(gas atom) for the first process, while $\Delta Ha = 5.7$ eV/(gas atom) for the second one, the first process will be favoured. That is, a high-dose bombardment of SnO_2 will leave the stoichiometry unchanged while the SnO_2 sputters congruently. This, of course, is the observed result as will be shown in Sections 8.2 and 8.4.*

---

* The heats were evaluated for 298 K (as in the absence of thermal spikes) rather than for 3000 K on the grounds that we are dealing with a collisional process and therefore one which occurs before the lattice is heated (4).

It has been argued that processes such as equations 6.2 and 6.3 will proceed due to thermal spikes provided the relevant vapour pressures exceed 5 to 50 atm at roughly 3000 K (Section 5.2.3). Let us consider the following processes:

$$SnO_2(l) = Sn(l) + O_2(g) \qquad I$$

$$SnO_2(l) = Sn(l) + 2.0(g) \qquad II$$

$$SnO_2(l) = SnO(l) + \tfrac{1}{2}\,O_2(g) \qquad III$$

$$SnO_2(l) = SnO(l) + O(g) \qquad IV$$

$$SnO_2(l) = Sn(g) + O_2(g) \qquad V$$

$$SnO_2(l) = Sn(g) + 2.0(g) \qquad VI$$

$$SnO_2(l) = SnO(g) + \tfrac{1}{2}\,O_2(g) \qquad VII$$

$$SnO_2(l) = SnO(g) + O(g) \qquad VIII$$

Here all solid phases should be taken as liquids, the initial phase due to amorphization and the final phase due to its formation at high temperature. Kubaschewski (8) gives the oxygen pressure for a process similar to I:

$$SnO_2(s) \rightarrow Sn(l) + O_2(g)$$

over the temperature range 770-980 K. Curve (a) of Fig. 6.1 shows an extrapolation to the temperature of interest, i.e. 3000 K, while the point marked + is our own calculated result when 2.0 appears instead of O_2 (similar to II):

$$SnO_2(s) \rightarrow Sn(l) + 2.0(g)$$

Colin et al. (9) report the oxygen pressure for a process similar to VII:

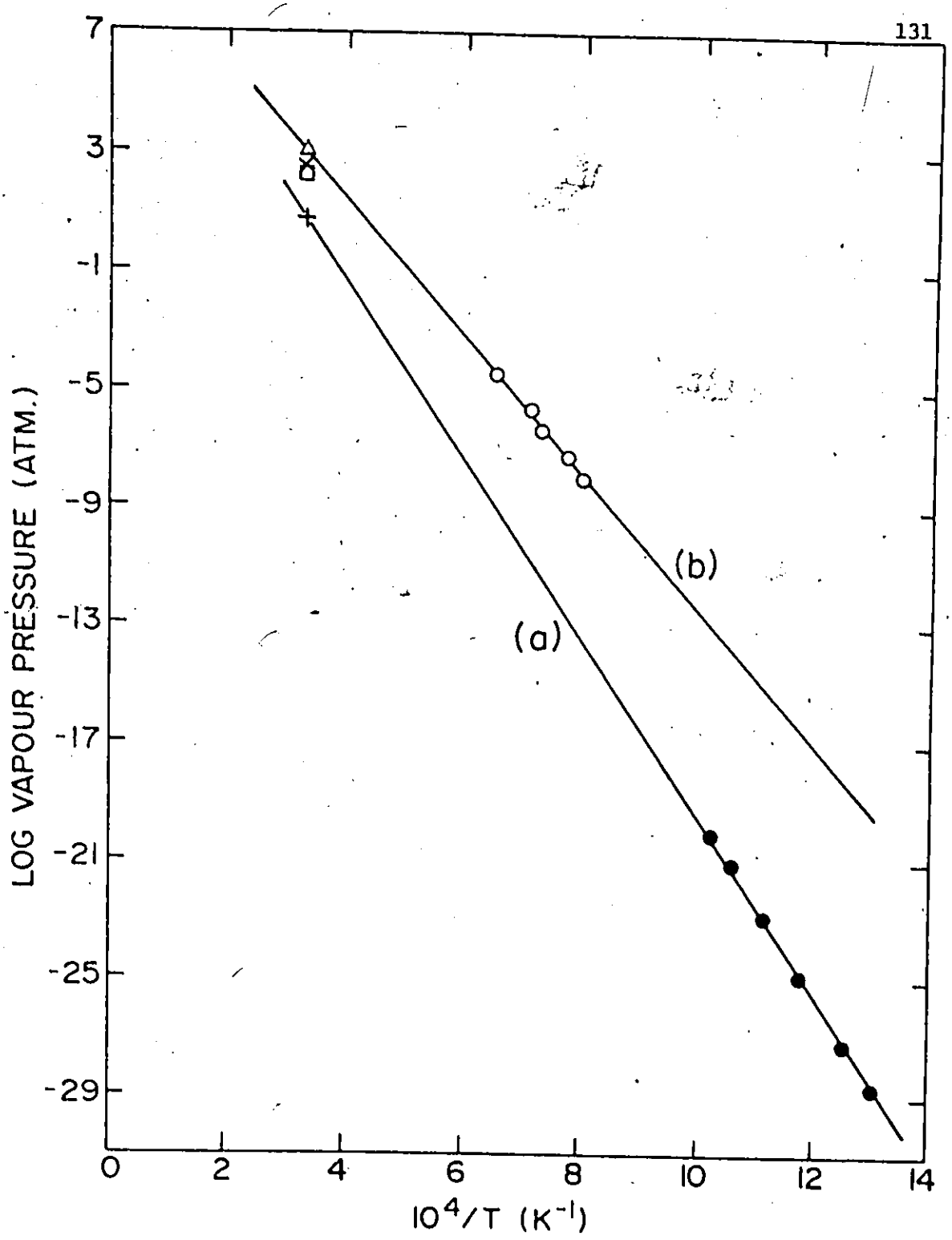

Fig. 6.1. Arrhenius plot of vapour pressure for the reactions:

- • $SnO_2(s) \rightarrow Sn(\ell) + O_2(g)$
- \+ $SnO_2(s) \rightarrow Sn(\ell) + 2.O(g)$
- o $SnO_2(s) \rightarrow SnO(g) + \frac{1}{2} O_2(g)$
- x $SnO_2(s) \rightarrow SnO(g) + O(g)$
- Δ $SnO_2(s) \rightarrow Sn(g) + O_2(g)$
- ▫ $SnO_2(s) \rightarrow Sn(g) + 2.O(g)$

$$SnO_2(s) \rightarrow SnO(g) + \frac{1}{2} O_2(g)$$

in the temperature range 1254-1538 K. Again, curve (b) of Fig. 6.1 shows an extrapolation to 3000 K, while the point marked X is our own calculated result when O appears instead of $\frac{1}{2} O_2$ (similar to VIII):

$$SnO_2(s) \rightarrow SnO(g) + O(g)$$

The points marked □ and Δ in Fig. 6.1 are the vapour pressures for relations V and VI, which we have obtained using the same calculations as for relations I and II and taking into consideration the heat of vaporization of Sn, which is 71 kcal/mole at 2956 K (8). There is a major omission here in that processes III and IV possibly have a higher pressure than I and II, but no information is available. We conclude firstly that processes I and II are barely able to satisfy the criterion of having a vapour pressure in excess of 5-50 atm at roughly 3000 K. These processes are of such a kind that they would have led to preferential oxygen loss from SnO_2.

A second conclusion is that processes V to VIII appear to satisfy the vapour-pressure criterion, the pressures here being a factor of about 20 higher than required. While they do not lead to preferential oxygen loss they could still cause the rate of congruent sputtering to be in excess of what is expected using Sigmund's theory. This, of course, is precisely the result of the sputtering experiments of Chapter 5.

6.2.4 Other criteria - (a) The time needed to form a stable nucleus, namely (10) the time that atoms in the liquid phase take to jump from the liquid into the nucleus until a certain "critical size" is exceeded (11), is inversely proportional to the diffusion coefficient for self-diffusion in the liquid which is related to the viscosity (η) by the following

relation (12):

$$D = \frac{1}{\eta} T \frac{k}{3\pi a_o}$$

where k is Boltzmann's constant and a_o, the molecular diameter. Hence the higher is the viscosity, the higher is the time needed to form a stable nucleus, the lower is the minimum cooling rate sufficient to by-pass crystallization (13). The law by which "thermal spikes" (Section 6.2.1) dissipate heat is shown in Fig. 6.2. If the cooling rate (namely the slope in Fig. 6.2) happens to be higher than the rate needed to by-pass crystallization for a particular material, then we will have bombardment-induced amorphization. Since the cooling rate needed to by-pass crystallization is dictated by the viscosity of the material (as discussed above), we anticipate that materials with high viscosity are the most prone to show bombardment-induced amorphization. This model suffers mainly from a severe lack of knowledge of η, it being born in mind that what is required is values for liquids in the temperature range 2000-3500 K.

(b) Essentially equivalent to the ionicity criterion is Stanworth's (14) use of electronegativity values to predict the glass-forming ability of a substance. He showed that the oxides which were known at the time (1952) to form glasses (B_2O_3, SiO_2, P_2O_5, GeO_2, As_2O_3, Sb_2O_3) all had an amount of ionic character ≤ 0.6. The main qualification to make is that Stanworth had access to exceedingly limited information.

(c) Another criterion for predicting glass formation is Sun's (15), based on "bond strength".

We would point out that these early examples, besides being based on limited information (as already emphasized) describe amorphization

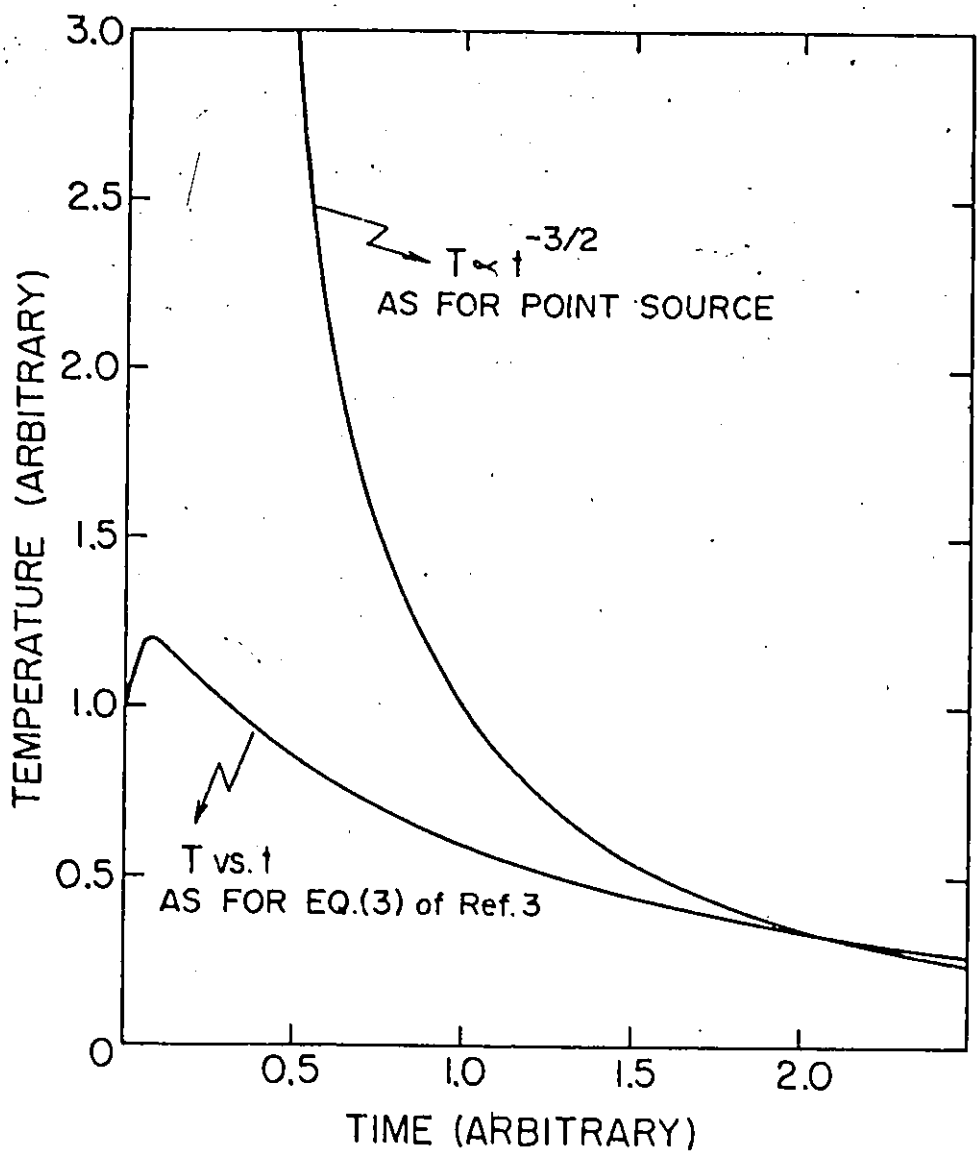

Fig. 6.2. The temperature-versus-time relations to be expected for an initial energy distribution which is concentrated either just beneath the surface ($\dot{T}$ versus t appropriate to the use of Eq. (3) of Ref. 3) or else at the surface ($T \propto t^{-3/2}$ as for a point source). (from Ref. 3)

which has a fundamentally different origin. It arises from the relatively slow supercooling of liquids in the absence of nuclei, whereas we are interested in very fast supercooling in the presence of nuclei.

We finally notice that oxides like SiO_2, GeO_2, Al_2O_3, TiO_2, V_2O_5, Bi_2O_3, MoO_3, WO_3, TeO_2, which are readily amorphized under ion-impact (Table 1.III), are also known to be glass formers or "conditional" glass formers (16) (namely they form glasses when melted alone or, if "conditional", when melted with a suitable quantity of a second oxide or mixture of oxides). In other words, insofar as information is available, glass formers show bombardment-induced amorphization. On the other hand, SnO_2, which according to the previously mentioned criterion of Stanworth and more recent electronegativity values given by Pauling (17), should behave like SiO_2 and GeO_2 (i.e. be a glass former), "cannot be made as a glass by normal methods" (16). Since SnO_2 is subject to bombardment-induced amorphization (Sections 5.3 and 8.2), this would suggest that the experimental glass forming ability of SnO_2 should be reinvestigated.

6.3 Gas-release spectrometry as a means of studying ion-implanted specimens

During the past few years much work has been done on rare gas-release and diffusion in nonmetallic systems (for an early survey see Ref. 18). Kelly and Matzke (19) and Kelly and Jech (20) have proposed that diffusion in inert-gas bombarded solids can be described in terms of five basic processes or Stages. Fig. 6.3 shows a systematic sketch, for an annealing schedule with a linear increase of temperature with time; with such a heating schedule, a clear separation of the Stages is achieved since one Stage goes to completion before the next starts. Frequently,

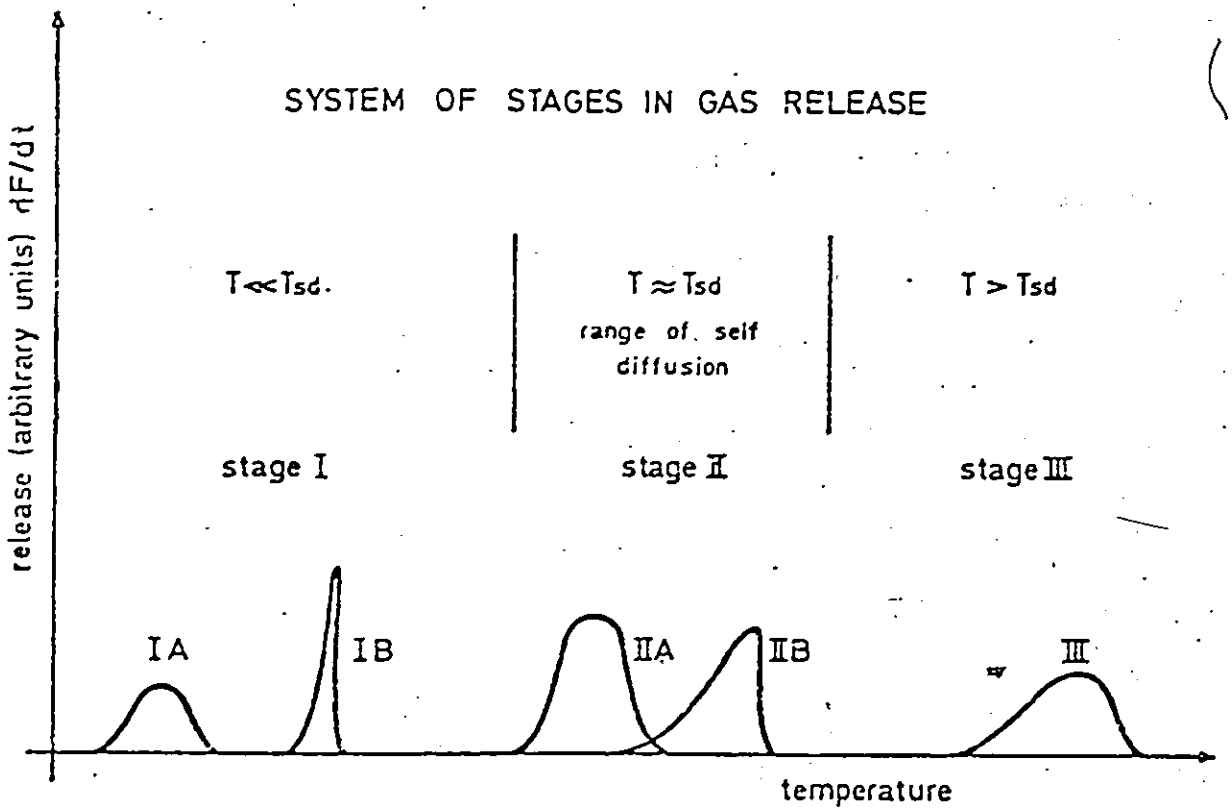

Fig. 6.3. Systematic representation of the System of Stages in gas release studies for the case of a linear temperature increase (dF/dt vs temperature). T_{sd} refers to the temperatures of self-diffusion for the geometrical conditions of ion bombardment. In compound materials, the temperature range for self-diffusion of the less mobile lattice species is relevant. (from Ref. 21)

however, other experimental heating schedules are employed, e.g. isochronal annealing with fixed arrests at different temperatures. The release curves obtained in these studies (F-vs-T) represent the integral of the dF/dt-vs-T curves of Fig. 6.3. A separation of Stages is still normally possible. Finally, isothermal annealing is often used, and here, an overlapping of release due to all Stages occurring below and at the experimental temperature will be observed.

In any practical case, some Stage or Stages will dominate depending on the system being studied. The main parameters affecting the release are gas concentration, damage concentration, the physical form taken by the radiation damage or defects, and the distance of the gas atoms to a free surface. On the basis of how the various Stages respond to these variables it has been possible to infer their origin as follows:

Stage I involves gas mobility at unusually low temperatures, namely, it designates release processes at temperatures significantly below those of normal volume diffusion. The latter starts to be the dominant process between 0.4 to 0.5 of the melting point on the absolute temperature scale. Stage IA is probably due to gas fortuitously located in high mobility sites, e.g. in interstitial positions; Stage IB is now well-established to be due to annealing of structural radiation damage, the most common form of which is radiation induced amorphousness.

Stage II involves gas mobility at normal temperatures, i.e. temperatures similar to those of self-diffusion of the lattice atoms. Stage IIA is due to unperturbed mobility of single gas atoms probably involving vacancies, though perhaps vacancy clusters; Stage IIB

is due to temporary trapping of the gas, i.e. to weak interactions of gas atoms with radiation damage, with pre-existing defects, or with other gas atoms. In order to discriminate between the two processes, we will recall that Kelly et al. (22) propose that low-dose release involves gas motion without an implied gas-gas or gas-damage interaction. High-dose release seems, by contrast, to be affected by transient gas-gas or gas-damage interaction. The probability that a gas atom at depth p will escape without getting trapped is exp(-p/L) where L is the diffusion length for trapping (23,24). L is in turn proportional to (volume of trapping zone)$^{1/2}$/(number of trapping centres)$^{1/2}$, i.e. approximately to (p/dose)$^{1/2}$ for gas-gas trapping and 1/(dose)$^{1/2}$ for gas-damage trapping. It finally follows that p/L is proportional to either (p x dose)$^{1/2}$ or p(dose)$^{1/2}$ for the two kinds of trapping, so that the escape probability should be higher for low doses or low energies.

Stage III involves gas mobility at unusually high temperature and is due to strong trapping of the gas at pre-existing defects or in gas-filled bubbles.

The theory behind marker-release spectrometry has been dealt with in a series of publications (18,19,20). The relations of interest in the present context are those for $\Delta T_{1/2}/T_{max}$ and $\Delta H/T_{max}$ valid under conditions of linearly increasing temperature. Here ΔH stands for activation enthalpy in J/mol, T_{max} is the temperature in kelvins at which a release process maximizes, and $\Delta T_{1/2}$ is the peak width in kelvins at half-height.

Specifically, let the initial distribution of the inert gas beneath the surface be of a type appropriate to an amorphous solid, namely, as can be seen from curve A of Fig. 6.4, "xe^{-x}". This distribution appears as

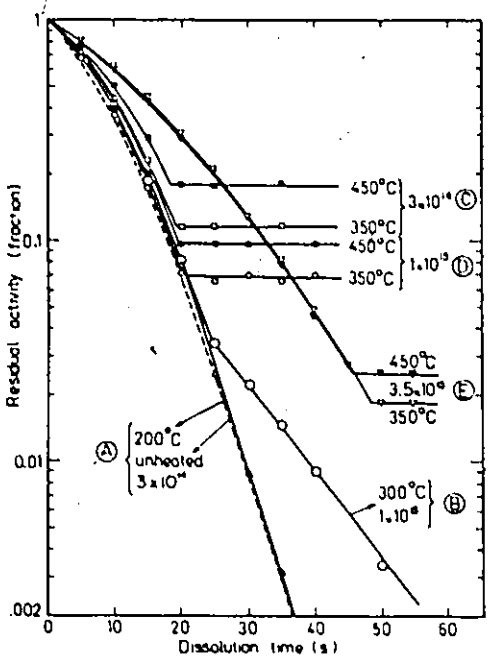

Fig. 6.4. Activity-verus-time curves for 65 V WO_3 films which had been heated as indicated, bombarded with 10 keV Kr to doses as indicated, and then exposed to 0.1 g/l KOH. (from Ref. 25)

follows when written in full:

$$\text{differential concentration} = [xdx/(R_m/1.68)^2]\exp[-x/(R_m/1.68)] \qquad (6.4)$$

where R_m is the median or 50% range. Then it can be shown by solving the diffusion equation $\partial C/\partial t = D\partial^2 C/\partial x^2$ with equation (6.4) as the initial condition that the following is true (26):

$$\frac{\Delta H}{T_{max}} = 311 + 19.1 \log_{10}\frac{T_{max} D_o}{R_m^2 \beta \min} \qquad (6.5a)$$

and

$$\frac{\Delta T_{1/2}}{T_{max}} = 0.126 - 0.0092 \log_{10} \frac{T_{max} D_o}{R_m^2 \beta min} \qquad (6.5b)$$

where βmin is the linear heating rate in K/min, D_o is the pre-exponential part of the diffusion coefficient in cm^2/s, and R_m is in angstroms.

In some cases the distribution of the inert gas is better treated as "e^{-x}" type. Such a distribution is most generally found with targets which remain crystalline during bombardment and, in addition, permit extensive channeling. The corresponding diffusion solutions in this case are:

$$\frac{\Delta H}{T_{max}} = 308 + 19.1 \log_{10} \frac{T_{max} D_o}{R_m^2 \beta min} \qquad (6.6a)$$

$$\frac{\Delta T_{1/2}}{T_{max}} = 0.160 - 0.0117 \log_{10} \frac{T_{max} D_o}{R_m^2 \beta min} \qquad (6.6b)$$

Formulae (6.5a) to (6.6b) apply to so-called "Stage IIA", namely marker-release due to normal homogeneous volume diffusion.

Let us assume now the release process to be due to crystallization of bombardment-induced amorphousness by the motion of a planar amorphous-crystalline interface, i.e. so-called "Stage IB". This type of process will typically have a small temperature width, for it involves not random motion but rather the unidirectional motion of an interface. Such unidirectional motion can be described in similar terms to crystal growth into an undercooled liquid, i.e. a series of R jumps all in the same direction. This motion was shown to lead to the relation (27):

$$\frac{\Delta H}{T_{max}} = 284 + 19.1 \log_{10} \frac{10\ T_{max} D_o}{R\ \beta min} \qquad (6.7a)$$

In addition the same authors have suggested that a temperature width for marker-release due to crystallization can be deduced by assuming the release to start owing to remnant crystallinity near the surface and to be completed with the unidirectional motion of the amorphous-crystalline interface over distance R. In this case the temperature width should be:

$$\frac{\Delta T}{T_{max}} < 0.063 \log_{10}(R/\lambda) \qquad (6.7b)$$

where λ ($\sim$0.25 nm) is the mean atomic spacing. This estimate is an upper limit because remnant crystallinity at depth λ would, because of the depth profile of the implanted ions, not cause measurable out-diffusion.

The disordered layer thickness R in Eqs. (6.7a) and (6.7b) can also be written as

$$R = \alpha R_m$$

where α is found experimentally with Al_2O_3 (28), Si (29) and WO_3 (25) to lie between 1 and 2.7.

A hint of the way the formalism of marker-release spectrometry is used is given in a review by Kelly et al. (30). Let us consider, for example, Eq. (6.5a) and take a material, for example Bi_2O_3, of which we know ΔH and D_o for cation self-diffusion (values derived from experiments other than marker-release). Now, Eqs. (6.5a) and (6.5b) are based on the assumption of Fick's second law just as are the self-diffusion data, and this means that one can deduce T_{max} as well as $\Delta T_{1/2}$ of a hypothetical release peak related to self-diffusion. Making at this point a marker-release experiment in Bi_2O_3, if one observes a process which shows T_{max} and $\Delta T_{1/2}$ satisfying Eqs. (6.5a) and (6.5b), then that peak is said to be

related to self-diffusion and is called "Stage IIA". The second process in Fig. 6.5 was in this was identified as Stage IIA.

On the other hand, it is known that the crystallization temperature for amorphous Bi_2O_3 films is 250°C (31), a value similar to the maximum of the first process in Fig. 6.5. Eq. (6.7b) is based on the assumption of release due to crystallization and this means that one can deduce $\Delta T_{1/2}$ of a hypothetical release peak. As a matter of fact, $\Delta T_{1/2}$ was found in this way to be twice as large as expected and the crystallization was concluded to be abnormal. A later study (27) revealed that the abnormality lay in the fact that crystallization occurred homogeneously rather than by interface motion (cfr. Mador (32)). This means that instead of the marker being swept out in a single step, it escapes in a more complicated manner, which, though difficult to treat analytically, will by necessity involve a greater temperature width.

Eq. (6.7b) is on the other hand in good agreement with what is observed for gas release associated with disorder annealing for at least 10 substances: Si, Ge, α- Al_2O_3, TiO_2, Cr_2O_3, α- Fe_2O_3 (28), TeO_2 MoO_3, V_2O_5 (27)(Fig. 6.6), and SiO_2 (33). Thus, as summarized in Table 6.I, the values observed experimentally for the width at half-height during the crystallization lay between 0.056 and 0.096. This implied crystallization by interface motion, a result which has been verified for 7 of the 10 substances. TiO_2 probably crystallizes homogeneously (34), while Cr_2O_3 and Fe_2O_3 have yet to be studied. SiO_2 crystallizes in one step by interface motion after low-dose bombardment and homogeneously (to yield α-cristobalite) after high doses.

Summarizing, the relations we will be interested in, while analyzing

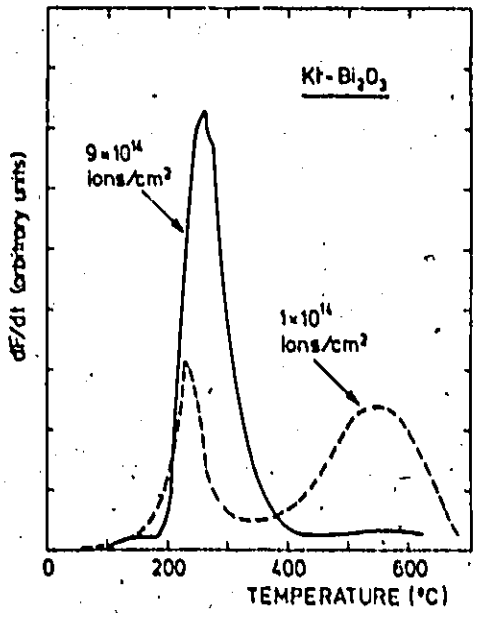

Fig. 6.5. Typical differential gas-release spectra for Bi_2O_3 specimens which have been bombardment-labeled with 10 keV Kr^{85} and then heated at 25 K/min in flowing oxygen. Two processes are clearly resolved. (from Ref. 27)

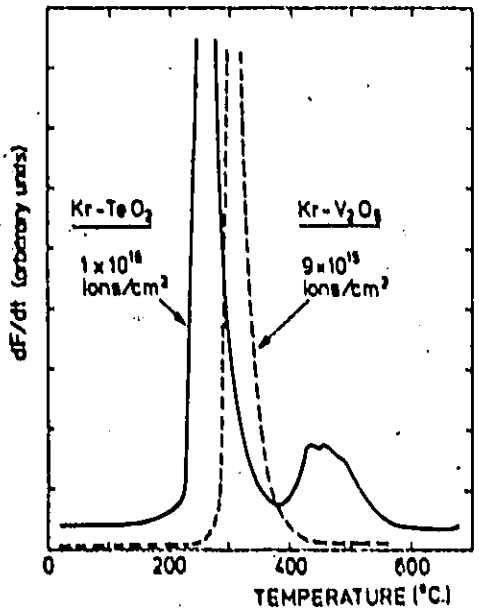

Fig. 6.6. Typical differential gas-release spectra for TeO_2 and V_2O_5 specimens which have been bombardment-labeled with 10 keV Kr^{85} and then heated at 25 K/min in flowing oxygen. Two processes are clearly resolved with TeO_2 but only one, owing to the volatility, with V_2O_5. (from Ref. 27)

TABLE 6.I

Experimental values for the width at half-height during crystallization

Substance	ΔT/T	Interface motion?
Si	0.071	yes
Ge	0.061	yes
Al_2O_3	0.060	yes
TiO_2	0.093	no
Cr_2O_3	0.091	-
Fe_2O_3	0.074	-
TeO_2	0.056	yes
MoO_3	0.096	yes
V_2O_5	0.084	yes
SiO_2	$\leq$0.10	yes (low-dose bombardment)

marker-release spectra in SnO_2, are Eq. (6.5b) and Eq. (6.7b). Eq. (6.6b) assumes an "e^{-x}" distribution, and this is not a good approximation for a substance subject to bombardment-induced amorphization.

Comparing experimental spectra with the predictions from Eqs. (6.5)-(6.7) is not the only information which is available for understanding the spectra. In fact, an important step in interpreting spectra is to note that release due to a true diffusion of the implanted Kr ions in the undamaged lattice of the host crystal will diminish in relative importance as the dose increases due to the onset of processes correlating with radiation damage.

Another phenomenon to keep in mind when analyzing marker-release spectra is the possible volatility of the substance. In the Sn-O system the main decomposition process is the following:

$$SnO_2(s) \rightarrow SnO(g) + \frac{1}{2} O_2$$

for which the O_2 pressure at 1000 K is $10^{-12} - 10^{-13}$ atm (Section 6.2.3). When oxygen at 1 atm is used as the carrier gas as in the present work, such a process is completely blocked.

At this point one may wonder why we are placing such an exaggerated importance on an indirect technique such as marker-release spectrometry The fact is that though high-energy reflection electron diffraction is the only truly direct way for categorizing how bulk materials respond to high doses, it fails to provide detailed information on the amount of disorder as a function of dose, dose rate, energy, temperature of bombardment, etc. In addition, the diffraction technique could fail to detect structural changes induced by low-energy ions as in such cases the electron beam would

penetrate to a depth which is large with respect to the damage mean range and within which the damage would be a negligible component. Finally, electron diffraction is too slow to enable a detailed study. We have therefore adopted the policy of seeking indirect evidence to as great an extent as possible in such experiments as marker-release spectroscopy as well as dissolution-curve analysis or a measurement of electrical conductivity. In this way we have obtained much information on the doses, energies, and temperatures of interest and have had to perform only a minimal number of diffraction measurements.

6.4 Electrical conductivity measurements as a means of studying bombardment-induced stoichiometry changes

We have seen in Section 1.2.7 that bombardment-induced oxygen loss in an oxide can be detected by the remarkable increase in the electrical conductivity that normally accompanies it.

As far as SnO_2 is concerned, it should be noticed that while the prepondering weight of evidence shows SnO_2 to be an n-type semiconductor (35-40), it seems that such a property was not measured on pure SnO_2. In fact, recently Vincent (41), investigating the nature of semiconductivity in SnO_2 films produced by pyrolytic decomposition of tin chlorides (42-44), concluded that the conducting tin oxide films "probably owe their conductivity almost entirely to the inclusion of chlorine ions in the lattice". Likewise, Aboaf et al. (45) have carried out work in which X-ray diffraction and electron-microprobe measurements showed that changes of electrical conductivity in polycrystalline vapour deposited SnO_2 films were due to the combined effect of O deficiency and the incorporation of Cl in the film.

We would note also that investigators have not had consistent

results for the extent of semiconductivity even in supposedly pure, crystalline tin oxide: vastly different values were in fact noted, e.g. less than 10^{-9} ohm^{-1} cm^{-1} (46) versus 0.2 ohm^{-1} cm^{-1} (47).

Only when the possible effects of chemical impurities have been eliminated, can arguments based on the stoichiometry of the compound be considered (48-51). As to the stoichiometry being of an excess or deficient character, and of which ion species, Peterson (52) concludes that SnO_2 is an n-type semiconductor in which non-stoichiometry is due to oxygen vacancies. In ref. 53 it is shown as well that "the dominant native defect in SnO_2 is a doubly ionizable oxygen vacancy".

We have in the present work measured conductivity using a 4-point probe.

Consider a rectangularly-shaped thin film of thickness w, length ℓ, and width b (Fig. 6.7). The resistance of the thin film, R, is given by

$$R = \frac{\rho \ell}{wb} = R_s \left(\frac{\ell}{b}\right)$$

where R_s is called <u>sheet resistivity</u>. The ratio ℓ/b is called the number of squares, and R_s is given in units of "ohm per square". The <u>sheet conductivity</u>, σ_s, is the reciprocal of the sheet resistivity, and is given in units of "$ohm^{-1}.\square$".

The relevant expression for deducing σ appropriate for a thin layer with a non-conducting bottom surface is (54):

$$\sigma_s = \sigma w = (I/V) \frac{\ell n 2}{\pi} \quad ohm^{-1}. \square \qquad (6.8a)$$

The expression for a semi-infinite specimen is

$$\sigma = (I/V) \frac{1}{2\pi s} \quad ohm^{-1}.cm^{-1} \qquad (6.8b)$$

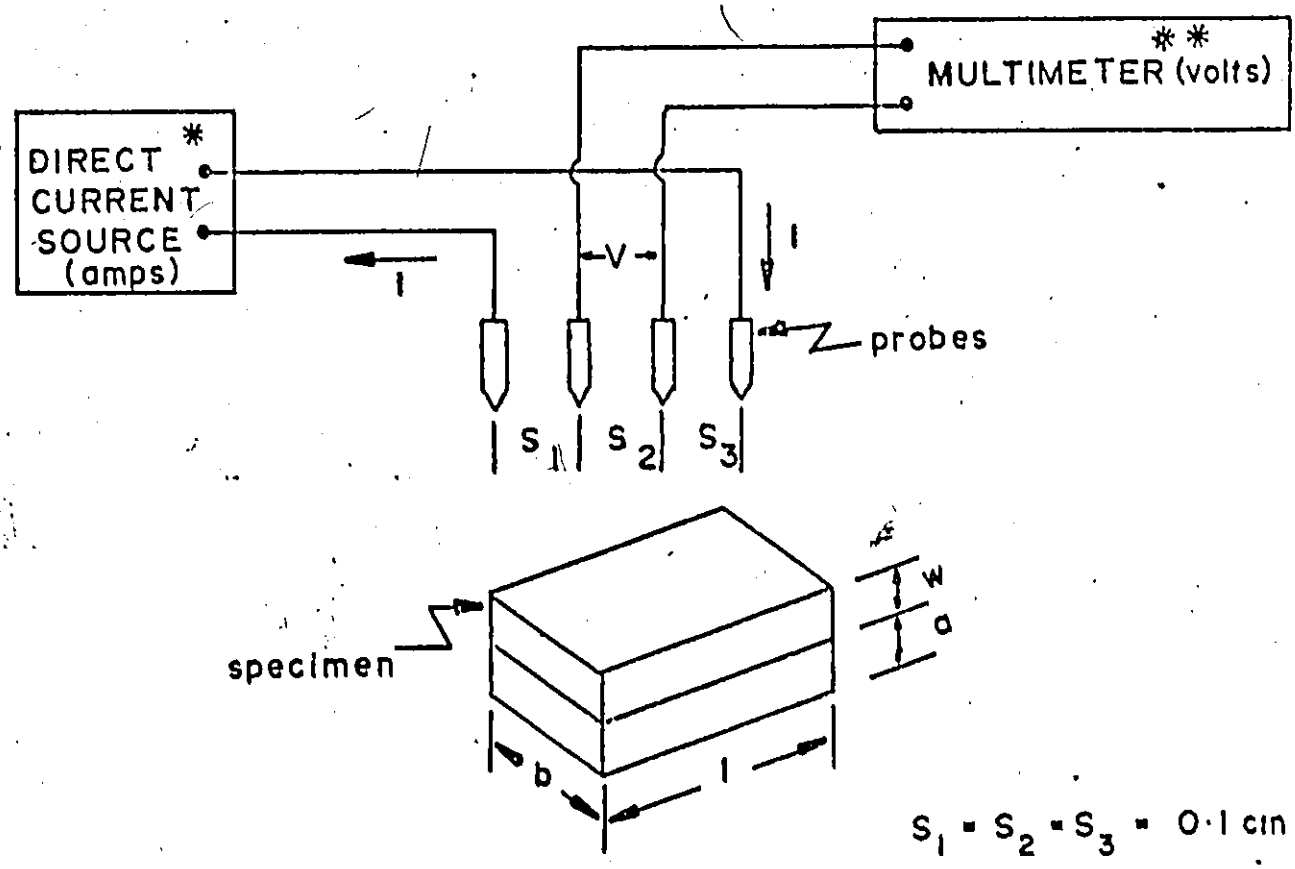

Figure 6.7. Schematic of conductivity measurement method; S_1, S_2, S_3 are the inter-probe spacings; W is the conducting thickness; a, b, and l are the specimen dimensions where generally W << S. (after Valdes, Ref. 54)

* Keithley Model 225

** Keithley Model 160

where s is the spacing of the points (0.1 cm)(Fig. 6.7). This last expression is for a truly semi-infinite medium, and the correction for the finite width and thickness of the specimens can be inferred from Figs. 6 and 11 of ref. 54 to be unimportant.

6.5 Dissolution experiments as a means of determining the thickness of altered layers

As pointed out by Jech (55), solubility changes can be used as an important supplement to methods such as electron diffraction or marker-release as a sensitive indicator of lattice disorder produced in solids by ion-bombardment.

The depth of the alteration can be estimated if the integral ion concentration profile is known. Since SnO_2 has a mean atomic weight of 50, we will simulate it with ZnS, mean mass 49, for which depth distribution parameters are available (56). This means that an integral profile can be plotted using the relation

$$C^{int} = \frac{1}{2} \operatorname{erfc} \frac{x-\langle x \rangle}{\sqrt{2}\Delta x} \qquad (6.9)$$

where $\langle x \rangle$ is the mean projected ion range (7.0 μ g/cm^2 for 35-keV Kr as deduced by interpolation of data in ref. 56) and Δx is the mean projected ion struggling (3.0 μ g/cm^2(56)). The result is given in Fig. 6.8.

In particular one would inject a radioactive tracer (e.g. 35-keV Kr), dissolve the disordered surface layer of the solid, and note the fractional retention of activity. Reference to Fig. 6.8 immediately enables a depth to be inferred.

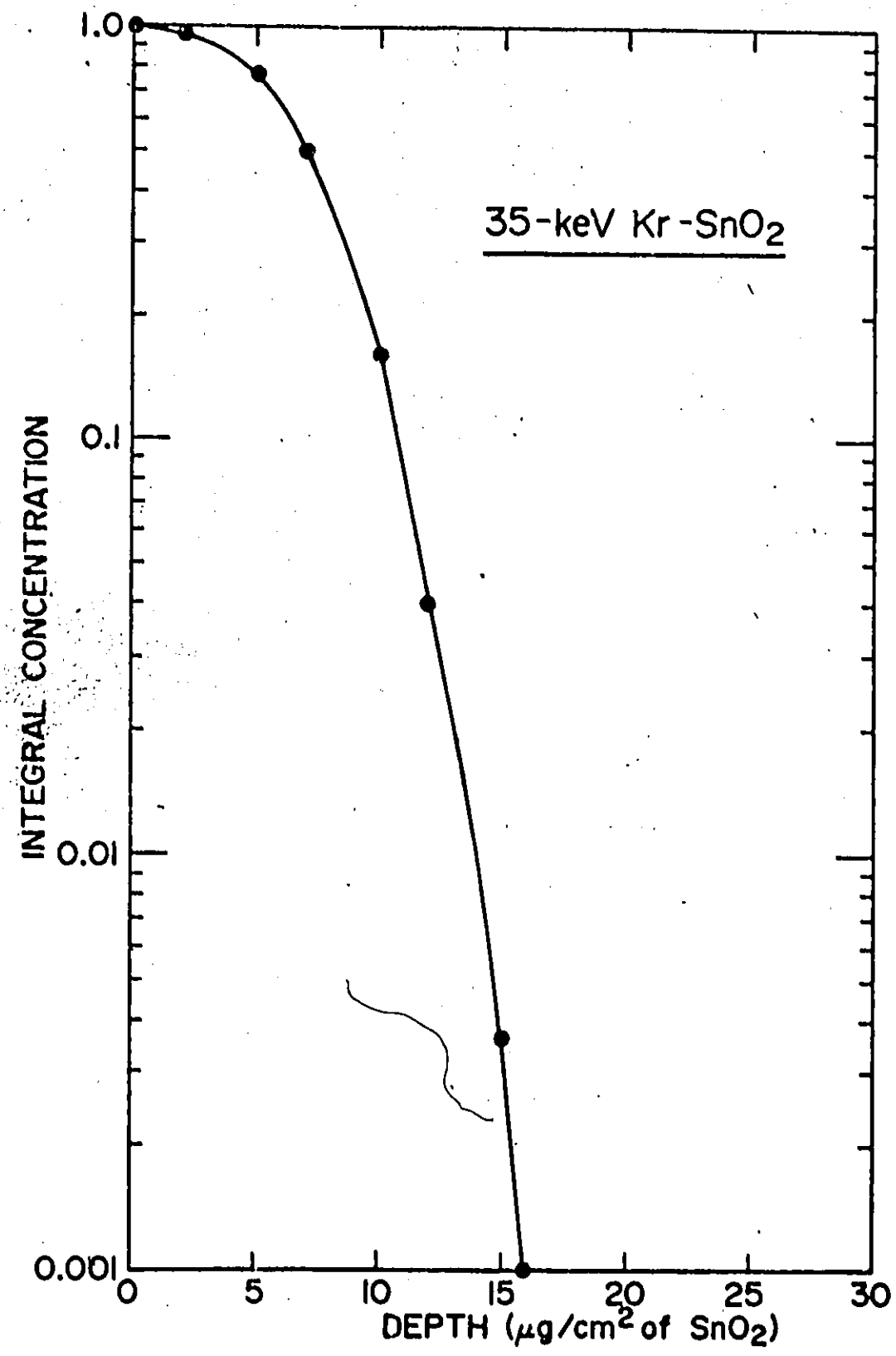

Fig. 6.8. Integral depth distribution of 35 keV Kr in SnO_2 according to Eq. (6.9). The range parameters <x> and Δx in Eq. (6.9) were assigned values as for ZnS, which has a mean mass similar to that of SnO_2.

REFERENCES

1. H. M. Naguib and R. Kelly, Radiation Effects 25, 1 (1975).

2. H. M. Naguib and R. Kelly, J. Phys. Chem. Solids 33, 1751 (1972).

3. T. Parker and R. Kelly, Ion Implantation in Semiconductors and Other Materials, ed. Billy L. Crowder, 551.

4. T. E. Parker and R. Kelly, J. Phys. Chem. Solids 36, 377 (1975).

5. D. K. Murti and R. Kelly, Surface Science 47, 282 (1975).

6. N. Andersen and P. Sigmund, Kgl. Danske Vid. Selsk. Mat. Fys. Medd. 39, no. 3 (1974).

7. P. Sigmund, Phys. Rev. 184, 383 (1969).

8. O. Kubaschewski, E. L. Evans and C. B. Alcock, Metallurgical Thermochemistry, Pergamon Press, Oxford, 1967, p. 303.

9. R. Colin, J. Drowart and G. Verhaegen, Trans. Faraday Soc. 61, 1364 (1965).

10. D. Turnbull, Contemp. Phys. 10, 473 (1969).

11. J. Burke, The Kinetics of Phase Transformations in Metals, Pergamon Press, 1975.

12. D. Turnbull, Trans. Metallurgical Society of AIME 221, 422 (1961).

13. H. Rawson, Inorganic Glass-Forming Systems, Academic Press, 1967.

14. J. E. Stanworth, J. Soc. Glass Technol. 36, 217 (1952).

15. K. H. Sun, J. Am. Ceram. Soc. 30, 277 (1947).

16. H. Rawson, Inorganic Glass-Forming Systems, Academic Press, 1967.

17. L. Pauling, The Nature of the Chemical Bond, Cornell University Press, 1960.

18. Hj. Matzke and R. Lindner, Atomkernenergie 9, 2 (1964).

19. R. Kelly and Hj. Matzke, J. Nucl. Mat. 17, 179 (1965).

20. R. Kelly and C. Jech, J. Nucl. Mat. 30, 122 (1969).

21. Hj. Matzke, Lecture at the Summer School on the Physics of Ionized Gases, Herceg-Novi, Yugoslavia, 1970.

22. R. Kelly, C. Jech and Hj. Matzke, phys. stat. sol. 25, 641 (1968).

23. R. Kelly and Hj. Matzke, J. Nucl. Mat. 20, 171 (1966).

24. D. G. Hurst, Chalk River (Canada) Rep. CRRP-1124, 1962.

25. N. Q. Lam and R. Kelly, Canad. J. Phys. 50, 1887 (1972).

26. R. Kelly et al., Proc. VI Yugoslav Symp. Phys. Ionized Gases, 1972, p. 349.

27. H. M. Naguib and R. Kelly, Radiation Effects 25, 79 (1975).

28. C. Jech and R. Kelly, J. Phys. Chem. Solids 30, 465 (1969).

29. I. Reid and R. Kelly, Radiation Effects 17, 253 (1973).

30. R. Kelly, N. Q. Lam, D. K. Murti, H. M. Naguib and T. E. Parker, VI Yugoslav Symposium and Summer School on the Physics of Ionized Gases, July 16-21, 1972, p. 349.

31. M. L. Lieberman and R. C. Medrud, J. Electrochem. Soc. 116, 242 (1969).

32. S. Mader, "Recrystallization, Grain Growth and Texture" (ASM, Metal Park, Ohio, 1966), p. 523.

33. Hj. Matzke, phys. stat. sol. 18, 285 (1966).

34. Hj. Matzke and J. L. Whitton, Can. J. Phys. 44, 995 (1966).

35. K. Ishiguro, T. Sasaki, T. Arai and I. Imai, J. Phys. Soc. Japan 13, 296 (1958).

36. S. Namba, Rikagaku Kenkyusho Hokoku 35, (1959).

37. V. K. Miloslavskii and S. P. Lyashenko, Optics and Spectroscopy 8, 455 (1960).

38. R. Groth, E. Kauer and P. C. v.d. Linden, Z. Naturforschung 17A, 789 (1962).

39. A. I. Sholykh and V. Z. Chukanov, Poroshkovaya Met., Akad. Nauk. Ukr. SSR 2, 96 (1962).

40. H. Koch, Phys. Status Solidi 3, 1059 (1963).

41. C. A. Vincent, J. Electrochem. Soc. 119, 515 (1972).

42. V. K. Miloslavskii, Opt. Spectr. (USSR)(English Transl.) 7, 154 (1959).

43. R. F. Bartholomew and H. M. Garfinkel, J. Electrochem. Soc. 116, 1205 (1969).

44. T. Arai, K. Ishiguro, T. Sasaki and I. Imai, J. Phys. Soc. Japan 13, 296 (1958).

45. J. A. Aboaf, V. C. Marcotte and N. J. Chou, J. Electrochem Soc. 120(5), 701 (1973).

46. H. F. Kunkle and E. E. Kohnke, J. Appl. Phys. 36, 1498 (1965).

47. G. Bauer, Ann. Der Physik. 30, 433 (1937).

48. J. A. Marley and R. C. Dockerty, Phys. Rev. 140, 304 (1965).

49. F. P. Koffyberg, J. Appl. Phys. 36, 844 (1965).

50. W. R. Sinclair, F. G. Peters, O. W. Stillinger and S. E. Koonce, J. Electrochem. Soc. 112, 1096 (1965).

51. A. Ya. Kuznetsov. Soviet Physics, Solid State 2, 35 (1960).

52. A. F. Peterson, Ph.D. Thesis, 1968--University Microfilms, Inc., Ann Arbor, Michigan.

53. S. Samson and C. G. Fonstad, J. Appl. Phys. 44(10), 4618 (1973).

54. L. B. Valdes, Proc. I.R.E. 42, 420 (1954).

55. C. Jech, phys. stat. sol. 21, 481 (1967).

56. W. S. Johnson and J. F. Gibbons, "Projected Range Statistics in Semiconductors", Stanford University Bookstore, Stanford, Calif. (1969).

CHAPTER 7

EXPERIMENTAL

7.1 Specimens

The specimens were in some instances pellets prepared by cold-pressing high purity tin-oxide powder* without the use of a binder. The pellets were sintered overnight in air at ∿1350°C and furnace cooled; they were then polished on fine sandpaper, washed with CCl_4 and acetone, and refired to ∿1150°C for two hours followed by furnace cooling. Since the second heating exceeds the temperature for grain growth established in Chapters 2 and 3, it can be assumed that surface damage introduced by the mechanical treatment was annealed.

A second set of experiments was carried out using the mineral cassiterite, i.e. naturally occurring SnO_2 (Mount Chorolque, S. W. Bolivia). About the matter of chemical composition of these samples, Kohnke (1) studied cassiterite from Bolivia; he writes that his "results imply that O-H groups are also present in natural stannic oxide, presumably having been introduced during a natural hydrothermal growth process, and that they are oriented in a plane perpendicular to the C-axis of the crystal"; no other information concerning the purity or stoichiometry of the specimens was given. On the other hand, the impurity content of cassiterite crystals from Schlaggenwald (Germany) was reported by Liebisch (2): SnO_2-99.33; TiO_2-0.44; SiO_2-0.13; $(Fe,Al)_2O_3$-0.17; rare earths-0.10; total-100.17 as the

---

* Merck and Co.

ore analysis. A spectrophotographic study by Eberhard, also reported in Ref. 2, showed Al, Ca, Cr, Cu, Fe, Ga, In, K, Mg, Mn, Mo, Cb, Sc, Sr, Si, Ta, Ti, V, W and Zr to be present in the cassiterite. More recent investigations (3) show that "the Sn in cassiterite is replaced by Fe^{3+}(≤8%), Ta(≤5%), Nb(≤2.5%), Sc(≤0.2%), and In(≤0.2%)". Before use, the specimens were either annealed or both polished and annealed. The polishing was necessary if reflection electron diffraction was to be used.

A third set of experiments was carried out using tin anodized to 30V and already reported in Chapter 5.

7.2. Techniques

Since the clearest and most direct means of characterizing the changes in solids due to ion-impact is probably high-energy electron-diffraction, samples were examined before and after bombardment, as well as following various annealing treatments, with the electron-diffraction unit of a Philips EM-300 electron microscope operated at 40, 60 and 80 kV. Because the materials are non-conductors the charges produced on them by the electron beam had to be neutralized by means of silver paint running from the sample holder up to the sides of the sample.

An alternative and somewhat indirect method of determining structure changes due to ion-impact is marker-release spectrometry. The typical experimental arrangement has been already reported in previous publications (Ref. 26 and 28 of Chapter 6). The basis is to label the specimen with a radioactive inert gas and then determine, with a linear temperature increase, the temperatures for the release of the gas, the gas serving as an inert marker for phase changes, stoichiometry changes, defect annealing, or diffusion. The approach is formally very similar to DTA, even to the

extent that similar equipment can be used. In our case the gas flowing over the sample was either oxygen or helium, and bombardments were made in the McMaster 0-50 keV accelerator. Radioactive Kr^{85} was injected into the specimens at an energy of 35 keV using fluences between 1.5×10^{14} ions/cm^2 and 2×10^{16} ions/cm^2 and fluxes up to 25 μA/cm^2. The most commonly used flux, 5 μA/cm^2, was shown previously to give negligible heating of a specimen (4).

The third technique employed was one based on solubility changes (Ref. 55 of Chapter 6). The first step in obtaining so-called dissolution curves was to label specimens with radioactive Kr^{85}, or, more economically, to inject trace amounts of Kr^{85} into specimens which previously had been exposed to a high-fluence bombardment of normal Kr. The specimens were then exposed to a suitable solvent and the fraction of retained activity noted as a function of time. Provided the depth distribution of the injected ions can be estimated (Section 6.5), the fraction of retained activity enables one to deduce the thickness of the layer removed. Sensitivities down to as little as 2 nm are easily obtained. This is illustrated in Fig. 7.1, where a retained fractional activity of 0.32 is shown to correspond to the removal of 8.5 μg/cm^2. A solvent such as 10% HF proved to work very satisfactorily and, as will be shown in Section 8.3, it was possible to resolve the rapid release of Kr^{85} due to dissolution of the disordered phase from a negligible or much slower release due to attack on the underlying less damaged lattice. The specimens used included both SnO_2 pellets and natural cassiterite.

The fourth technique involved the measurement of electrical conductivity. The electrical conductivities of the specimens (pellets and

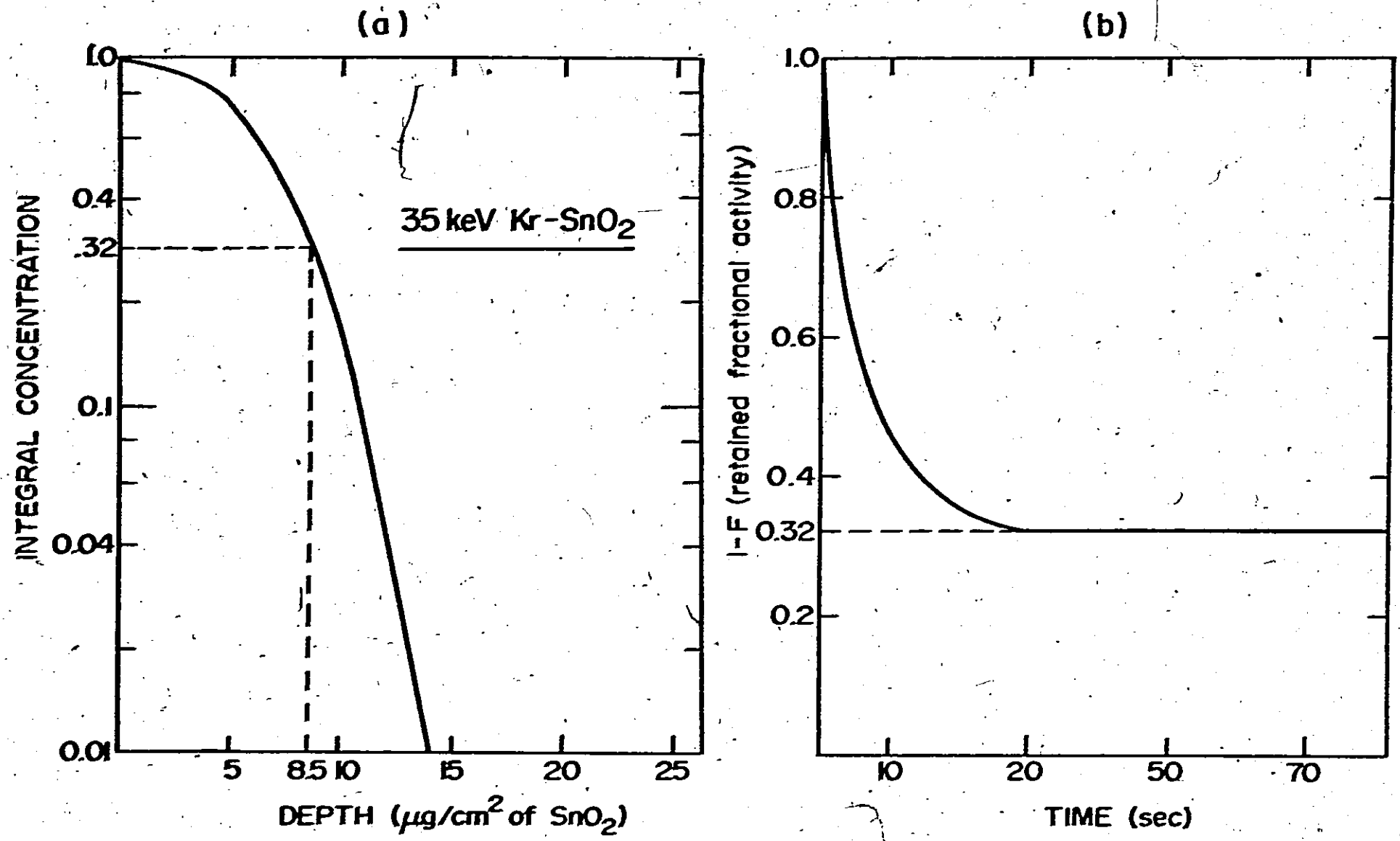

Fig. 7.1. (a) from Section 6.5. (b) from Fig. 8.5. A retained fractional activity of (e.g.) 32% corresponds to a dissolved layer of 8.5 μ g/cm^2 of SnO_2. 8.5 μ g/cm^2 is about 13 nm.

natural cassiterite) were measured using a linear four-point D.C. probe* technique similar to Ref. 5, 6, and 7, for which the experimental arrangement was schematically shown in Fig. 6.7. Measurements consisted in passing a known direct current (I) through the outer pair of probes and measuring the potential (V) across the inner pair of probes. Thus, the conductivity (I/V) in units of ohm^{-1} was evaluated and could be substituted into Eq. 6.8a or 6.8b. An average value of (I/V) was established from several separate measurements by changing the polarity, magnitude of I and probe-head position on the pellet. Varying I also served as a verification of the ohmic behaviour of the specimens.

---

* A. M. Fell (Mfg) Ltd., Sussex, England.

REFERENCES

1. E. E. Kohnke, J. Phys. Chem. Solids 23, 1557 (1962).

2. I. Th. Liebisch, Sitzb. Kgl. Preuss. Akad. Wiss., 414 (1911).

3. A. S. Povarennykh, Crystal Chemical Classification of Minerals, Vol. 1, Plenum Press, 1972.

4. R. Kelly and H. M. Naguib, Atomic collision phenomena in solids, eds. D. W. Palmer, M. W. Thompson and P. D. Townsend, North-Holland, 172 (1971).

5. L. B. Valdes, Proc. I.R.E. 42, 420 (1954).

6. F. M. Smuts, Bell Systems Technical Journal 37, (1958).

7. A. Uhlir, Jr., Bell Systems Technical Journal 34, 105 (1955).

CHAPTER 8

RESULTS

8.1 Marker-release measurements

The first set of marker-release experiments was carried out on SnO_2 pellets using He as a carrier gas. As shown in Fig. 8.1, the main feature of the release spectrum is the clear resolution of two processes. On the other hand, in a second series of experiments using O_2 as the carrier, we notice that the low temperature release process tends to be less prominent though still normally present (Fig. 8.2). Fig. 8.3 shows a release spectrum for an experiment carried out on natural cassiterite.

Tables 8.Ia, 8.Ib and 8.Ic summarize the results for 35 keV Kr bombardment of SnO_2.

In Table 8.II the experimental values of the temperature widths are compared with those expected for (a) out-diffusion related to crystallization (Stage IB) and (b) a release process related to self-diffusion (Stage IIA).

8.2 Reflection electron diffraction

In view of the evidence from the marker-release experiments that at least two release processes occurred; it looked logical to check by electron diffraction the structure of samples after heat treatments at temperature T_A and T_B (Fig. 8.3). Fig. 8.4 shows the patterns of a sample of natural cassiterite (a) before bombardment, (b) after bombardment to $\sim 10^{17}$ ions/cm^2 with 35 keV Kr, (c) after annealing in air to $\sim$650°C, (d)

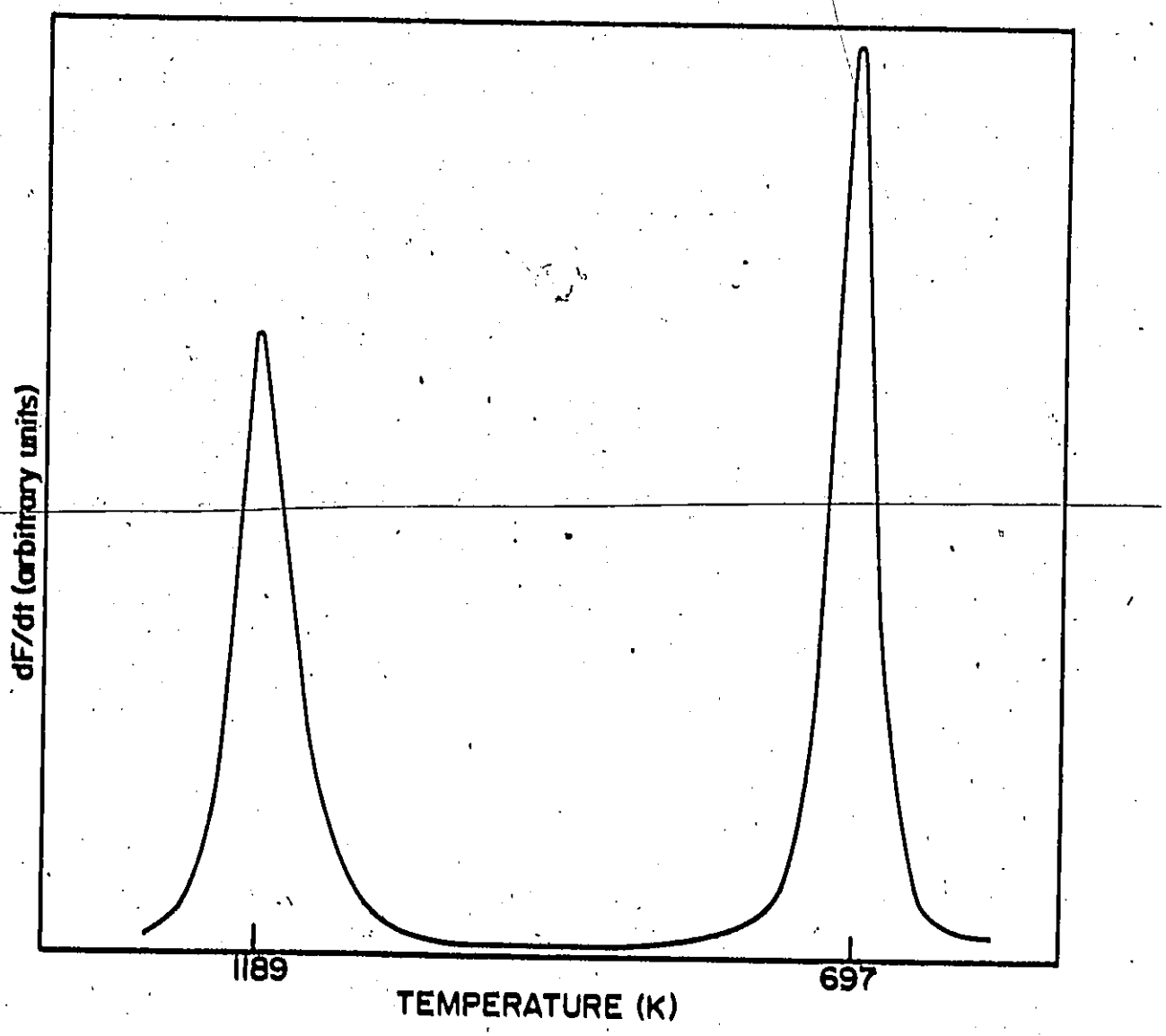

Fig. 8.1. Typical differential gas-release spectrum for SnO_2 pellets which have been bombardment-labeled with 35-keV Kr^{85} and then heated at 25 K/min in flowing helium. In this specific example the dose used was 4.7×10^{15} ions/cm^2; the release processes maximize at temperatures as indicated.

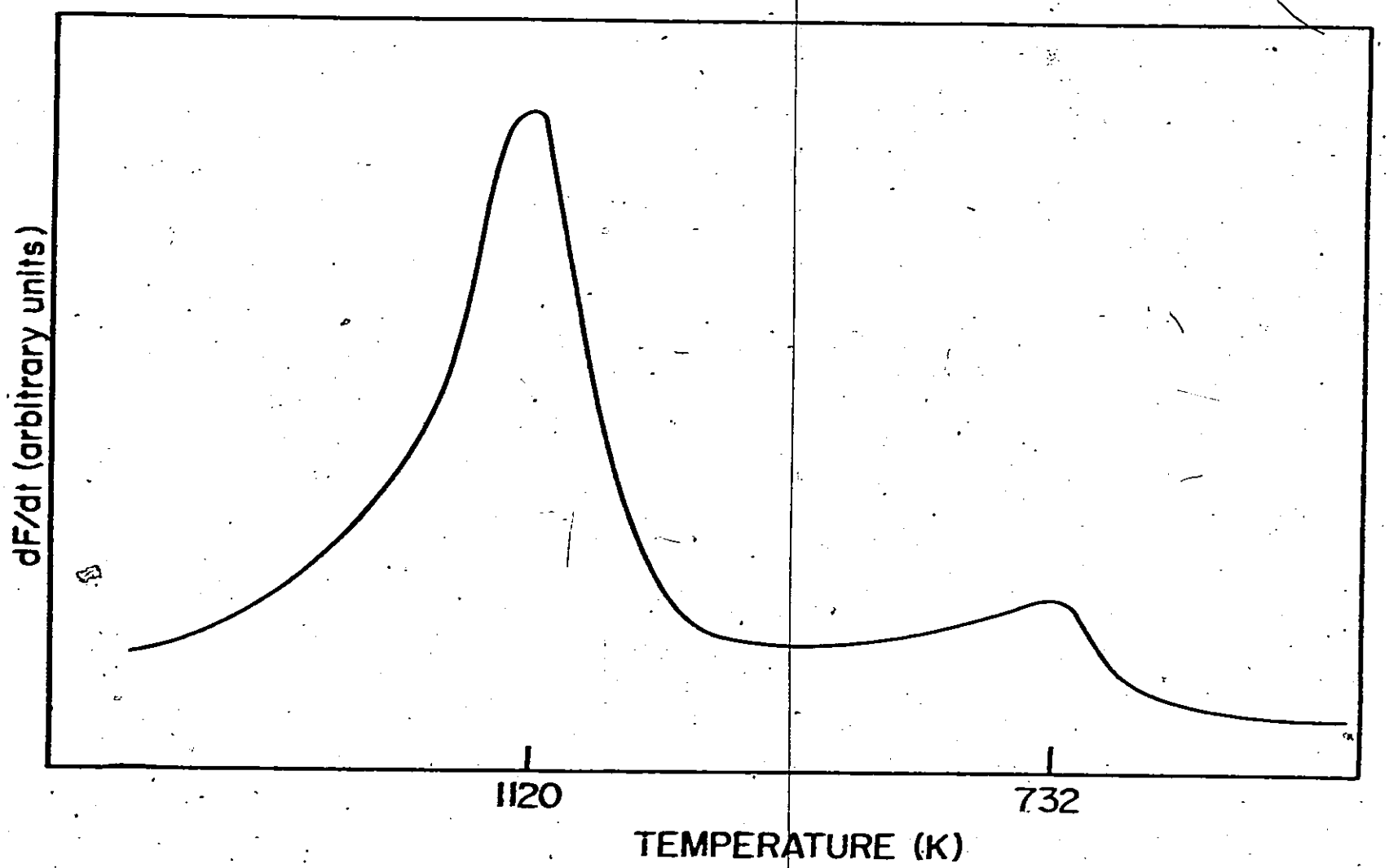

Fig. 8.2. Typical differential gas-release spectrum for SnO_2 pellets which have been bombardment-labeled with 35-keV Kr^{85} and then heated at 25 K/min in flowing oxygen. In this specific example the dose used was 4.6×10^{15} ions/cm^2; the release processes maximize at temperatures as indicated.

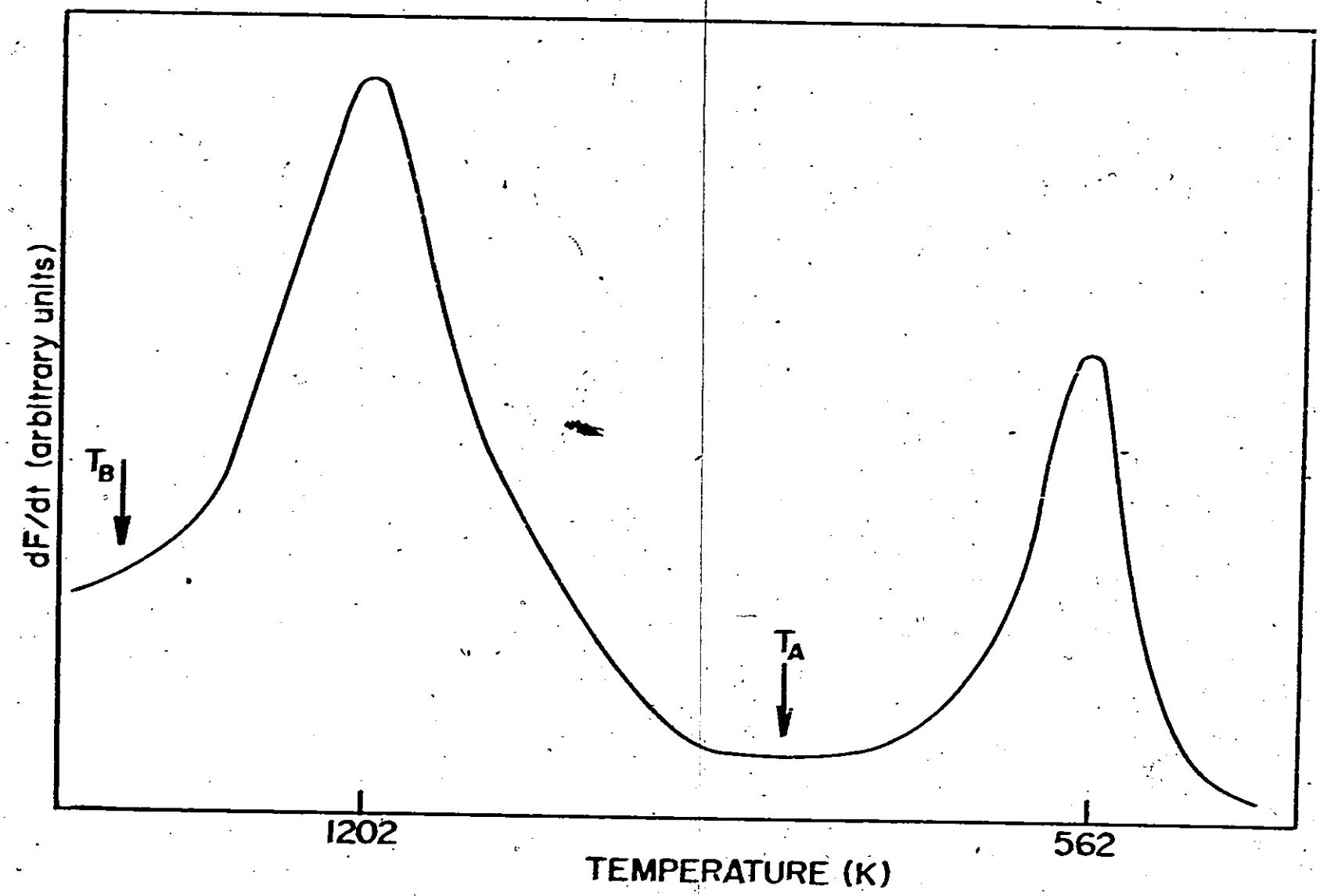

Fig. 8.3. Typical differential gas-release spectrum for natural cassiterite specimens which have been bombardment-labeled with 35-keV Kr^{85} and then heated at 25 K/min in flowing oxygen. In this specific example the dose used was 4.6×10^{15} ions/cm^2; the release processes maximize at temperatures as indicated.

TABLE 8.Ia

Analysis of marker-release spectra (He-flow) in SnO_2 pellets bombarded with 35 keV Kr

Number of spectra	T_{max} for low-temp. process(K)	T_{max} for high-temp. process(K)	$\Delta T/T$ for low-temp. process	$\Delta T/T$ for high-temp. process
14	700 ± 12	1191 ± 4	.123 ± .017	.045 ± .000

TABLE 8.Ib

Analysis of marker-release spectra (O_2-flow) in SnO_2 pellets bombarded with 35 keV Kr

Number of spectra	T_{max} for low-temp. process(K)	T_{max} for high-temp. process(K)	$\Delta T/T$ for low-temp. process	$\Delta T/T$ for high-temp. process
15	747 ± 19	1172 ± 8	.222 ± .033	.069 ± .017

TABLE 8.Ic

Analysis of marker-release spectra (O_2-flow) in natural cassiterite bombarded with 35 keV Kr

Number of spectra	T_{max} for low-temp. process(K)	T_{max} for high-temp. process(K)	$\Delta T/T$ for low-temp. process	$\Delta T/T$ for high-temp. process
11	592 ± 13	1200 ± 7	.225 ± .026	.094 ± .010

TABLE 8.II

Comparison of experimental $\Delta T/T$ with expected values

Low-temperature process	pellets, O_2-flow	pellets, He-flow	natural cassiterite, O_2-flow
Observed $\Delta T_{1/2}/T_{max}$ (K/K)	.222	.123	.225
Calculated $\Delta T_{1/2}/T_{max}$ (K/K):			
(a) for out-diffusion due to crystallization due to interface motion (Stage IB)*	<.101	<.101	<.101
(b) assuming normal volume diffusion with an "x exp(-x)" type initial distribution (Stage IIA)†	.147-.165	.147-.166	.148-.166
High-temperature process			
Observed $\Delta T_{1/2}/T_{max}$ (K/K)	.069	.045	.094
Calculated $\Delta T_{1/2}/T_{max}$ (K/K):			
(a) for out-diffusion due to crystallization due to interface motion (Stage IB)*	<.101	<.101	<.101
(b) assuming normal volume diffusion with an "x exp(-x)" type initial distribution (Stage IIA)†	.144-.162	.144-.162	.143-.162

* R was taken as 10 nm, as measured in Section 9.4. Eq. 6.7b then gave an upper limit to $\Delta T_{1/2}/T_{max}$.

† R_m was taken as 13 nm, as from Ref. 1 and D_o as $3 \times 10^{-1\pm1}$ cm^2/sec (2). Eq. 6.5b then gave $\Delta T_{1/2}/T_{max}$. The range of values comes from the assumed range for D_o.

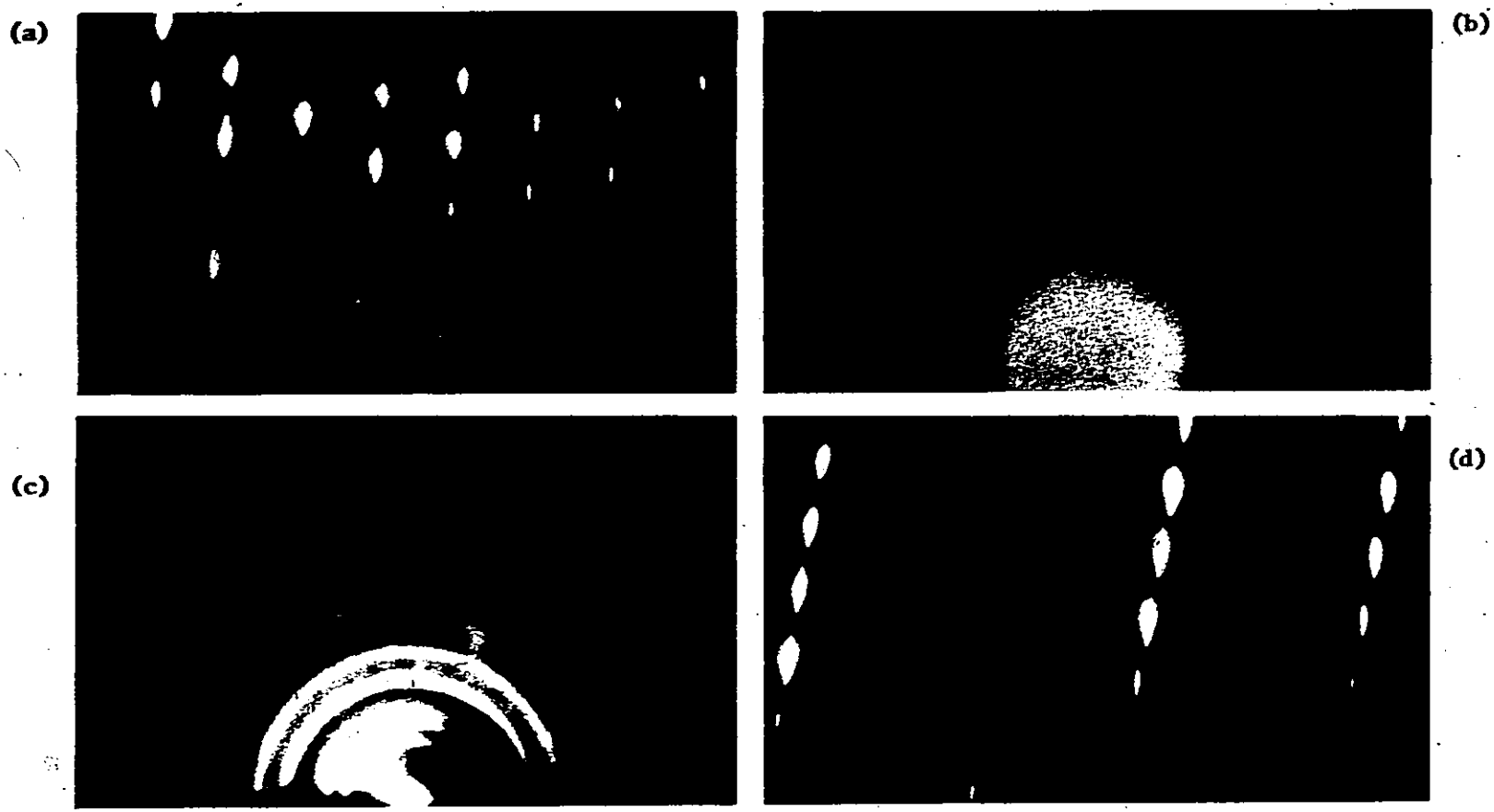

Fig. 8.4. RED at 80 keV of natural cassiterite. (a) before bombardment, (b) after bombardment to $\sim 10^{17}$ ionc/cm^2 with 35 keV Kr, (c) after annealing in air to 650°C, (d) after annealing in air to 1100°C.

after annealing in air to 1100°C. We thus confirm the bombardment-induced amorphization of SnO_2. We show further that crystallization takes place at 600-750 K and occurs homogeneously rather than by interface motion. Finally, we establish that epitaxial recrystallization takes place over a comparatively narrow temperature range centering at 1170-1200 K.

8.3 Dissolution and F-vs-dose curves

Figs. 8.5 and 8.6 show the fractional activity released as a function of the time an SnO_2 pellet or cassiterite single crystal is exposed to 10% HF. Dissolution periods as short as two seconds have been used. Such curves were obtained with about forty specimens bombarded with 35 keV Kr at doses ranging between 1.6×10^{14} and 5.0×10^{16} ions/cm^2.

The curves are interpreted as showing that the surface layer of an implanted pellet is readily dissolved away, but the underlying material is not attacked at a measurable rate. As a matter of fact, once F has reached its plateau, it remains constant even after hours of exposure to 10% HF. From Figs. 8.5 and 8.6 it can also be seen that the amount of activity retained decreases with increasing dose, being 18% at the highest dose used, i.e. 5×10^{16} ions/cm^2. Explicit figures are given in Table 8.III.

Tables 8.IV and 8.V show the fractional activity retained after thermal annealing to >1100°C or <1100°C respectively. It can be seen that when annealing is carried on up to at least ~1100°C, thermal annealing (Table 8.IV) and dissolution (Table 8.III) are equivalent in that the activity retained after dissolution is similar to that retained after thermal annealing. This equivalence does not hold for lower annealing temperatures.

The information in Tables 8.III, 8.IV and 8.V is plotted in

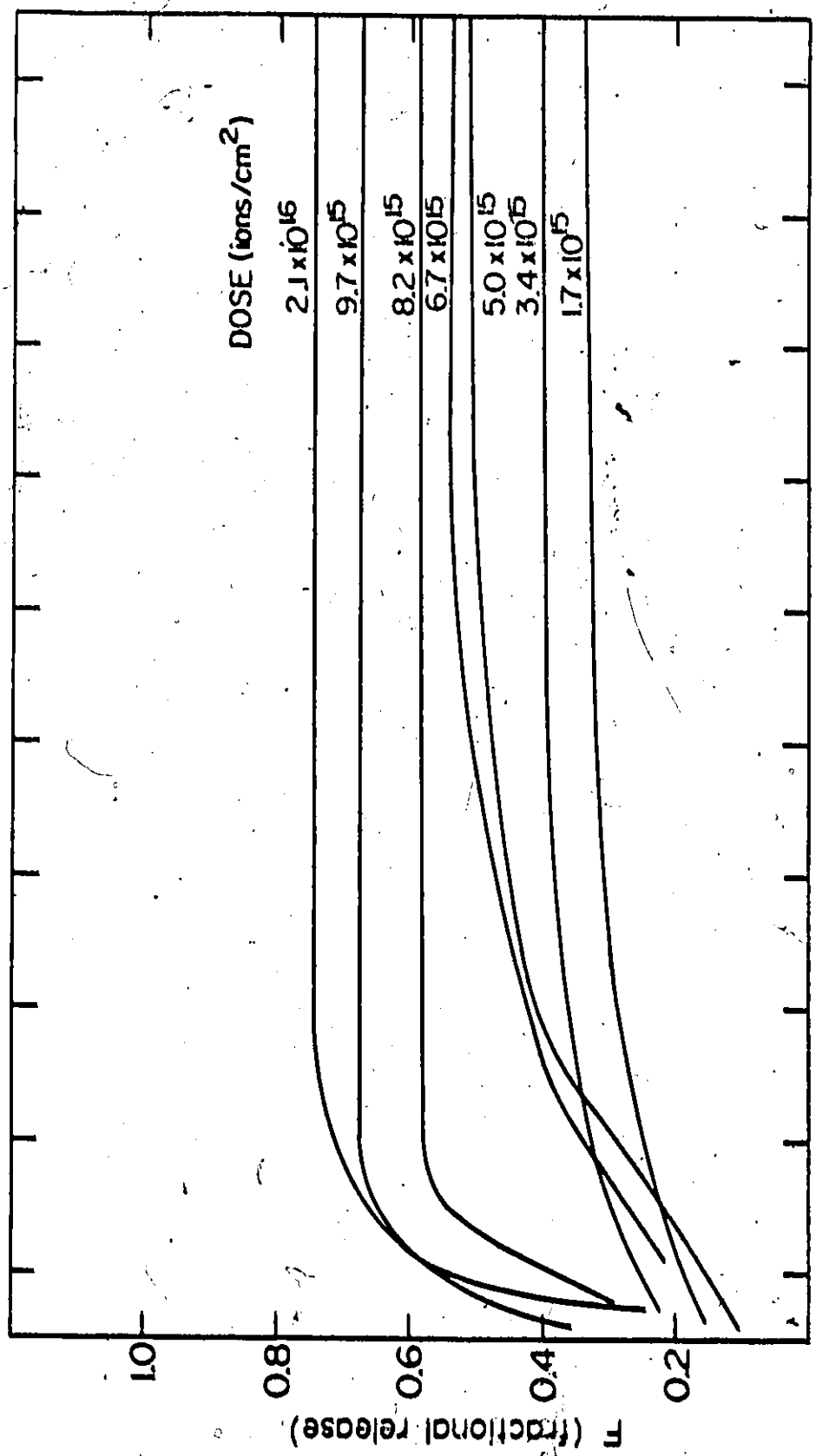

Fig. 8.5. Dissolution curves for Kr-implanted (35-keV) SnO_2 pellets. Doses as indicated on curves. Solvent: 10% HF.

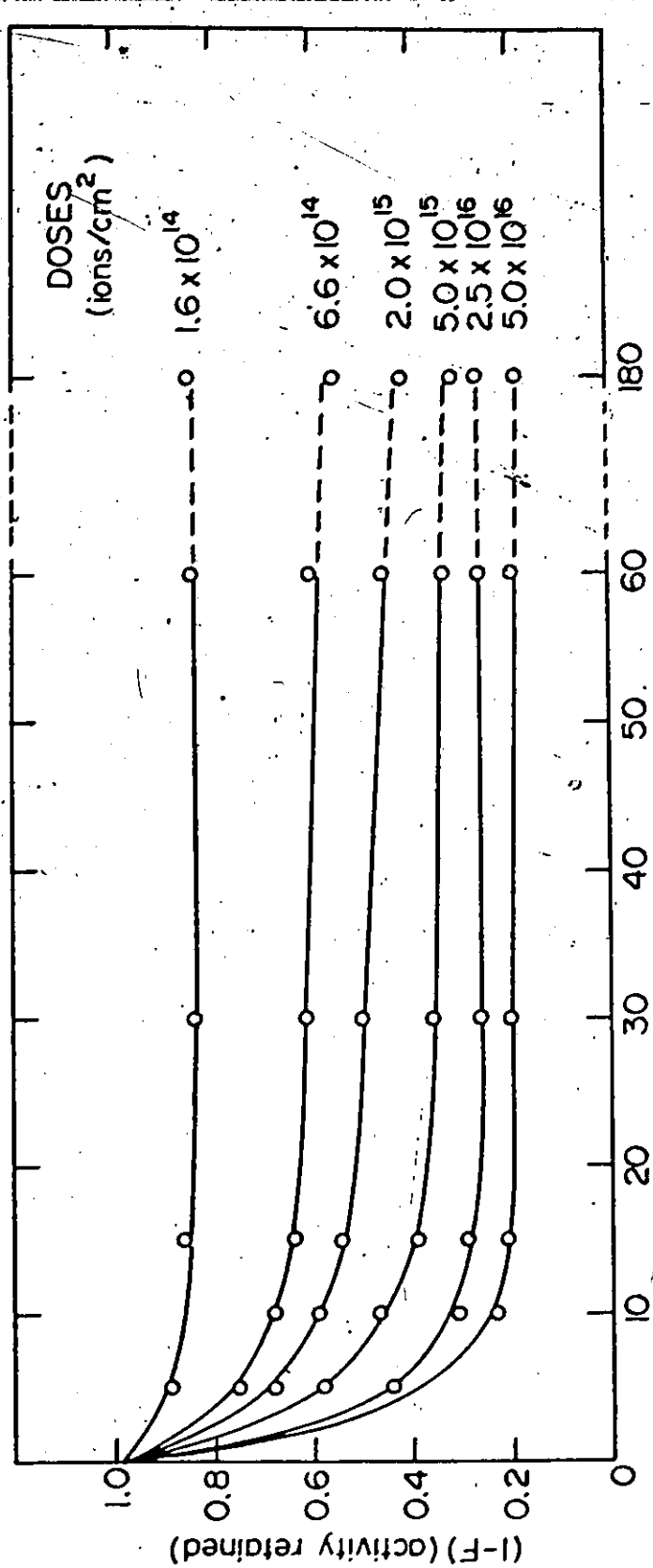

Fig. 8.6. Dissolution curves for Kr-implanted (35-keV) natural cassiterite. Doses as indicated on curves.

TABLE 8.III

Activity retained after dissolution of SnO_2 samples (pellets and natural cassiterite) has gone to completion

Dose (ions/cm^2)	Fractional activity retained (1-F)
1.6×10^{14} (nat. cass.)	.84
6.6×10^{14} (nat. cass.)	.55
1.7×10^{15} (pellet)	.65
2.0×10^{15} (nat. cass.)	.41
3.4×10^{15} (pellet)	.59
5.0×10^{15} (pellet)	.47
5.0×10^{15} (nat. cass.)	.31
6.7×10^{15} (pellet)	.45
8.2×10^{15} (pellet)	.41
9.7×10^{15} (pellet)	.32
2.1×10^{16} (pellet)	.25
2.5×10^{16} (nat. cass.)	.26
5.0×10^{16} (nat. cass.)	.18

TABLE 8.IV

Activity retained after heating to T ≳ 1100°C

(heating rate 25 K/min)

Dose (ions/cm^2)	Activity retained (1-F)	Maximum temperature (°C)
1.6×10^{14} (nat. cass.)	.54	1,109 (oxygen flow)
4.7×10^{14} (pellet)	.53	1,117 (helium flow)
4.7×10^{14} (pellet)	.66	∿1,100 (helium flow)
3.7×10^{14} (pellet)	.82	∿1,100 (oxygen flow)
4.7×10^{14} (nat. cass.)	.35	1,123 (oxygen flow)
8.3×10^{14} (pellet)	.84	∿1,100 (oxygen flow)
9.4×10^{14} (pellet)	.59	1,117 (helium flow)
9.4×10^{14} (pellet)	.54	∿1,100 (helium flow)
1.9×10^{15} (pellet)	.46	∿1,100 (helium flow)
1.9×10^{15} (pellet)	.61	∿1,100 (oxygen flow)
1.9×10^{15} (nat. cass.)	.29	1,104 (oxygen flow)
1.9×10^{15} (nat. cass.)	.33	1,116 (oxygen flow)
2.8×10^{15} (pellet)	.43	1,190 (oxygen flow)
2.8×10^{15} (pellet)	.54	1,190 (oxygen flow)
4.6×10^{15} (pellet)	.48	∿1,100 (oxygen flow)
4.6×10^{15} (pellet)	.53	1,117 (oxygen flow)
4.6×10^{15} (pellet)	.58	1,109 (oxygen flow)
5.4×10^{15} (pellet)	.26	1,244 (helium flow)
5.4×10^{15} (pellet)	.31	1,230 (helium flow)
6.0×10^{15} (pellet)	.48	1,210 (oxygen flow)
6.0×10^{15} (pellet)	.44	1,245 (oxygen flow)
7.0×10^{15} (pellet)	.48	∿1,100 (oxygen flow)
7.0×10^{15} (pellet)	.46	∿1,100 (oxygen flow)
7.0×10^{15} (pellet)	.49	∿1,100 (oxygen flow)
9.4×10^{15} (pellet)	.30	∿1,100 (helium flow)

TABLE 8.IV (continued)

9.4×10^{15} (pellet)	.42	1,135 (oxygen flow)
9.4×10^{15} (nat. cass.)	.14	1,112 (oxygen flow)
9.4×10^{15} (nat. cass.)	.17	1,100 (oxygen flow)
2.1×10^{16} (pellet)	.39	1,156 (oxygen flow)

TABLE 8.V

Activity retained after heating to T < 1100°C

(heating rate 25 K/min)

Dose (ions/cm^2)	Activity retained (1-F)	Maximum temperature (°C)
8.2×10^{14} (pellet)	.96	768 (oxygen flow)
4.7×10^{14} (pellet)	.91	666 (helium flow)
9.4×10^{14} (pellet)	.85	666 (helium flow)
1.5×10^{15} (pellet)	.92	745 (helium flow)
1.9×10^{15} (pellet)	.69	704 (helium flow)
2.5×10^{15} (pellet)	.86	768 (oxygen flow)
4.9×10^{15} (pellet)	.85	745 (helium flow)
5.0×10^{15} (pellet)	.86	768 (oxygen flow)
8.3×10^{15} (pellet)	.91	768 (oxygen flow)
9.4×10^{15} (pellet)	.68	666 (helium flow)
9.7×10^{15} (pellet)	.60	745 (helium flow)
9.7×10^{15} (pellet)	.57	745 (helium flow)
9.7×10^{15} (pellet)	.66	745 (helium flow)
9.7×10^{15} (pellet)	.51	745 (helium flow)
9.7×10^{15} (pellet)	.84	745 (air)
1.2×10^{16} (pellet)	.93	768 (oxygen flow)
1.7×10^{16} (pellet)	.73	768 (oxygen flow)
1.7×10^{16} (pellet)	.55	745 (helium flow)

Fig. 8.7. We have seen that the low temperature release, corresponding to the amorphous-polycrystalline transition (Fig. 8.4c and 8.1-8.3), maximizes at 600-750 K (Table 8.I). Likewise the high-temperature release, corresponding to the polycrystalline-single crystal transition in the case of cassiterite (Fig. 8.4d and 8.1-8.3), maximizes at 1170-1200 K (Table 8.I). Curve 1 of Fig. 8.7, therefore, confirms the observation mentioned above that the total release due to both crystallization and recrystallization is equivalent, as far as the amount of activity retained in the sample is concerned, to a chemical process in which the disordered surface layers of the sample are dissolved away. Curve 2 shows that the amount of activity retained if the sample is heated in He through, but not beyond the first release process, is rather greater than otherwise. Moreover, it can be seen from curve 3 that the fractional activity retained is still higher if the annealing atmosphere is oxygen. This in agreement with the already noted fact (cfr. Section 8.1) that the first process is less pronounced when marker-release in an O_2-atmosphere is used.

The identification of the dissolution curve with the annealing curve is particularly important. It is an indication that all marker atoms imbedded in the amorphized layers, and finally removed by dissolution, are driven out during the overall crystallization and recrystallization process.

In other experiments, dissolution and annealing were combined. When dissolution experiments were performed on samples annealed at a high temperature ($\geq$1350 K, which is past the high-temperature release process) the result was that no further dissolution took place, namely the retained activity remained as shown in curve 1 of Fig. 8.7. This is expected.

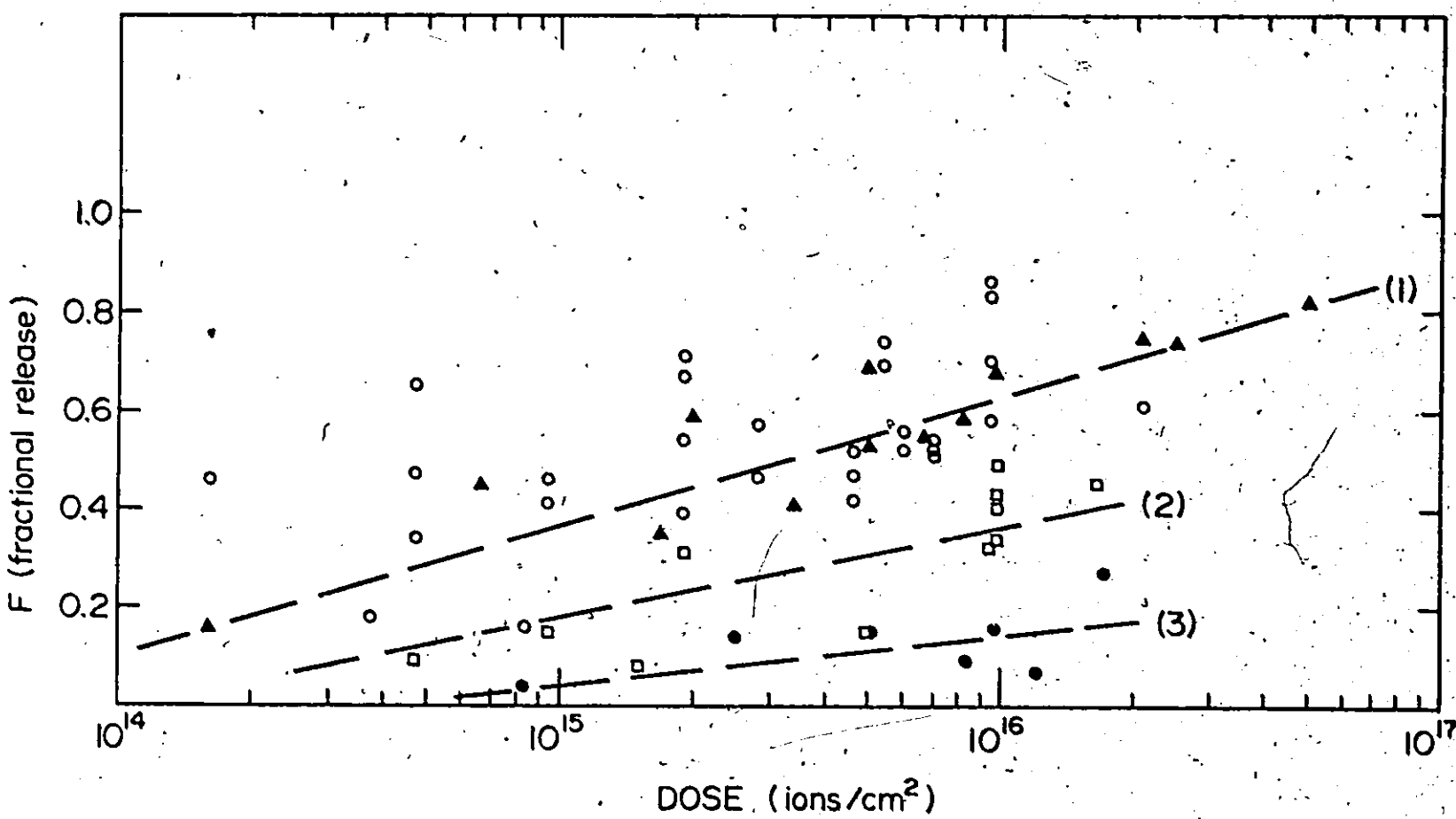

Fig. 8.7. Fractional release of implanted ions in SnO_2, due to dissolution and annealing, ▲ dissolution, o annealing to T ≥ 1100°C, □ annealing to T < 1100°C(helium flow), ● annealing to T < 1100°C(oxygen flow).

When dissolution experiments were performed on samples annealed at ∿1030 K (i.e. a temperature which is above the first release process, but below the second), the result was that there was still dissolution taking place (Table 8.VI), though the total amount of activity retained after combined annealing (∿1030 K) and dissolution was higher than that shown in curve 1 of Fig. 8.7 (Table 8.VII).

Taken together these results are understandable if it is assumed that the rate of dissolution in HF is higher for amorphous SnO_2 than for polycrystalline or single crystal SnO_2 respectively.

An alternative view is that some amorphous material is still present in the polycrystalline layer. Perhaps the crystalline material can be thought of as being "in suspension in an amorphous solvent". The existence of amorphous material between the grains is more likely in a homogeneous transformation (Section 6.3), as the amorphous-polycrystalline transition in SnO_2, than when the transformation is by interface motion.

8.4 Electrical conductivity measurements

The specimens used were SnO_2 pellets (sintered in air) and natural cassiterite (annealed in air), while the DC currents were 10^{-2}, 10^{-3} and 10^{-4} amp. In spite of the decreasing values of the current used, the DC current source* always showed the "voltage compliance limit" to be functioning, indicating that the load conductivity was less than $10^{-4}/100 = 10^{-6}$ ohm^{-1}.

Samples were subsequently bombarded with Kr at 20 keV using fluences between 9.4×10^{15} ions/cm^2 and 3.2×10^{17} ions/cm^2 and fluxes ≤ 7 μA/cm^2. Again I/V resulted to be $< 10^{-6}$ ohm^{-1}. Then the conductivity

* Model 225 Keithley

TABLE 8.VI

Released fractional activity after annealing (∿1030 K) and subsequent dissolution

Dose (ions/cm^2)	F due to annealing to T ≈ 1030 K		F due to: annealing to T ≈ 1030 K + dissolution	
	O_2-atmosphere	He-atmosphere	O_2-atmosphere	He-atmosphere
8.2×10^{14}	.04		.14	
2.5×10^{15}	.14		.28	
5×10^{15}	.15		.36	
8.3×10^{15}	.09		.19	
9.7×10^{15}	.16		.30	
1.2×10^{16}	.07		.21	
1.7×10^{16}	.27		.48	
1.5×10^{15}		.08		.15
4.9×10^{15}		.15		.19
9.7×10^{15}		.34		.38
9.7×10^{15}		.40		.55
9.7×10^{15}		.43		.53
9.7×10^{15}		.49		.50
1.7×10^{16}		.45		.67

TABLE 8.VII

Retained fractional activity after annealing to T $\geq$ 1350 K and after combined annealing ($\sim$1030 K) and dissolution

Dose (ions/cm^2)	1-F, as from curve 1 of Fig. 8.7	1-F, as from samples annealed at $\sim$1030 K and then dissolved; annealing atmosphere: O_2	He
8.2×10^{14}	.66	.86	
1.5×10^{15}	.59		.85
2.5×10^{15}	.53	.72	
4.9×10^{15}	.46		.81
5×10^{15}	.45	.64	
8.3×10^{15}	.40	.81	
9.7×10^{15}	.38	.70	.62, .45, .47, .50
1.2×10^{16}	.35	.79	
1.7×10^{16}	.31	.52	.33

was measured after Kr-bombardment, but this time while the SnO_2 sample (pellet) was still in the accclerator chamber, i.e. under vacuum. The Kr ion energy was 35 keV, fluences were 1.4×10^{17} to 1.2×10^{18} ions/cm^2, and fluxes were $\leq 8\,\mu A/cm^2$. Again no conductivity change occurred.

REFERENCES

1. E. Giani, M.Sc. thesis (1971), McMaster University, Canada.

2. D. Lazarus, Solid State Physics 10, 71 (1960).

CHAPTER 9

DISCUSSION

9.1 Low-temperature process

As we have already pointed out, the low-temperature marker-release is more prominent in the case of He-flow than O_2-flow (Section 8.1). Thus, it might at first sight be thought to be related to an annealing stage associated with a partial reduction of the specimens which persists to a higher temperature due to the He atmosphere (1).

The above point of view is supported (erroneously, of course) by the experimental $\Delta T_{1/2}/T_{max}$ values (Table 8.II) suggesting the release not to be related to crystallization by interface motion. On the other hand, the $\Delta T_{1/2}/T_{max}$ values are fairly close to what is calculated for normal volume diffusion (diffusion in a damage-free lattice).

Both the correlation of the low-temperature process with a He carrier and the $\Delta T_{1/2}/T_{max}$ values are evidently misleading. Thus the diffraction evidence is completely clear in showing that the low-temperature process is due to an amorphous-crystalline transition with formation, not of a phase epitaxial with the original phase, but rather of a polycrystalline phase. We are thus dealing with one of the few known cases where the model of crystallization by interface motion used to derive eqn. (6.7b) was incorrect, as the crystallization had occurred homogeneously. The low-temperature process can be correctly designated as Stage IB.

Another example is Bi_2O_3 (2). Here the experimental $\Delta T_{1/2}/T_{max}$

for the low-temperature release does not match the calculated $\Delta T_{1/2}/T_{max}$ for Stage IB, and at the same time the diffraction patterns confirm the formation, not of the original single-crystal, but of a polycrystalline phase of untypical crystal form. SiO_2 is intermediate. It crystallizes in one step by interface motion after low-dose bombardments and homogeneously (to yield α-cristobalite) after high doses (3). Al_2O_3 and TiO_2 resemble SnO_2, Bi_2O_3 and SiO_2 by virtue of crystallizing homogeneously (to what in the case of TiO_2 is possibly anatase) and of showing epitaxial recrystallization only at higher temperature (1). It is more usual, however, that a substance shows interface motion insofar as this is possible: MoO_3, TeO_2, V_2O_5 (2), SiO_2 (low-dose bombardment)(3), Ge (4), Si (4,5), GaAs (6), GaP (7). The distinction between what is essentially interface motion and homogeneous crystallization is discussed further by Mader (8), as both processes are found with the amorphous alloys with which he works. (In fact, Mader uses the term "heterogeneous crystallization" for what is equivalent to our "interface motion".)

In a process where there is an evolution of the type amorphous→polycrystalline→epitaxial, the intermediate phase could in principle (though not by necessity) have a different structure than the starting material. Crystallization by interface motion, on the other hand, by necessity leads to an epitaxial phase. Known examples relating to oxides are summarized in Table 9.I.

We were able to establish that bombardment-induced amorphousness in SnO_2 anneals to a polycrystalline phase showing the normal cassiterite structure. We have in fact analyzed Fig. (8.4c) both in terms of calculating the d-spacings corresponding to the diffraction rings, and also, which is probably a more reliable means, comparing by eye these micro-

TABLE 9.I

The intermediate and stable phase

in the crystallization of amorphous oxides

Oxide	Product of homogeneous crystallization	Stable crystal form	Reference
Al_2O_3	γ-Al_2O_3 (cubic)	corundum (α-Al_2O_3)	1
Bi_2O_3	δ-Bi_2O_3 (cubic)	α-Bi_2O_3(monoclinic)	2,8,9
GeO_2	hexagonal	tetragonal	10
HfO_2	cubic	monoclinic	11
Nb_2O_5	low temperature form	α-Nb_2O_5(monoclinic)	12
SiO_2	α-cristobalite(tetragonal)	α-quartz(hexagonal)	3
Ta_2O_5	low temperature form	orthorhombic	13
TiO_2	probably anatase	rutile	1
WO_3	orthorhombic	monoclinic	9
ZrO_2	cubic	monoclinic	11,14

graphs to a standard reflection electron diffraction pattern of polycrystalline SnO_2. (The visual comparison is to be preferred in that it takes intensities better into account.) We have thus convinced ourselves that the structure shown in Fig. (8.4c) is indeed normal cassiterite.

In conclusion, crystallization by homogeneous transformation is a necessary but not sufficient condition for a material to crystallize to a phase different from the original. Nevertheless, most amorphous oxides do yield a different phase, with SnO_2 being exceptional in not doing so. One can speculate that this result is due to the structure of amorphous SnO_2 being "cassiterite"-like just as the structure of different kinds of carbon are described variously as graphite-like or diamond-like (15). Similar comments have been made of amorphous ZrO_2 (14).

9.2 High-temperature process

Considering now the high-temperature marker-release, we have proved by electron microscopy that it is related to epitaxial recrystallization. In the case of cassiterite this involved the evolution of our SnO_2 sample from a polycrystalline to a single-crystal structure. With pellets, the sequence would probably have been amorphous→finely polycrystalline→coarsely polycrystalline, though the necessary experiments were not done.

This does not, however, establish the release process as being caused by epitaxial grain growth per se. The temperature range in question (1170–1200 K) could in principle be that for normal volume diffusion, with the marker-release and the grain growth being results

and not causes. The experimental $\Delta T_{1/2}/T_{max}$ values are therefore of prime importance, as they are found to be distinctly smaller than what would be expected for normal volume diffusion. In fact, they agree well with interface motion (Table 8.III). From this we conclude that the high-temperature process is both related to and caused by the epitaxial recrystallization.

Other materials showing well-defined epitaxial recrystallization as a second step after crystallization include Bi_2O_3, SiO_2 and TiO_2 as already discussed in the preceding section. Al_2O_3 also shows epitaxial grain but not as a well-defined process (1). In addition, Cr_2O_3 (16) and MgO (1) possibly belong to this group, as can be inferred from the existence of intermediate-temperature marker-release processes as marked by arrows in Fig. 9.1. Ge does not belong to this group. Although Krikorian and Sneed (17) did indeed find a well-defined polycrystalline-crystalline transition in the annealing of amorphous Ge, this result applies to a thin film which has no crystalline substrate. An amorphous surface layer on Ge crystallizes epitaxially in one step (18).

We would point out that in the case of bombardment-induced amorphization in Al_2O_3 and Bi_2O_3, marker-release spectroscopy of the thermally annealed samples (1,2) records the whole evolution (amorphous-polycrystalline-epitaxial) by <u>one</u> release process only. These are therefore examples where one technique is not sufficient to unravel all the details. The reason for the single release peak is probably that release went to such a degree of completion that no marker remained to signal the epitaxial recrystallization. Two processes are, however, resolved (or assumed to be resolved) with Cr_2O_3, MgO, SiO_2, SnO_2 and TiO_2.

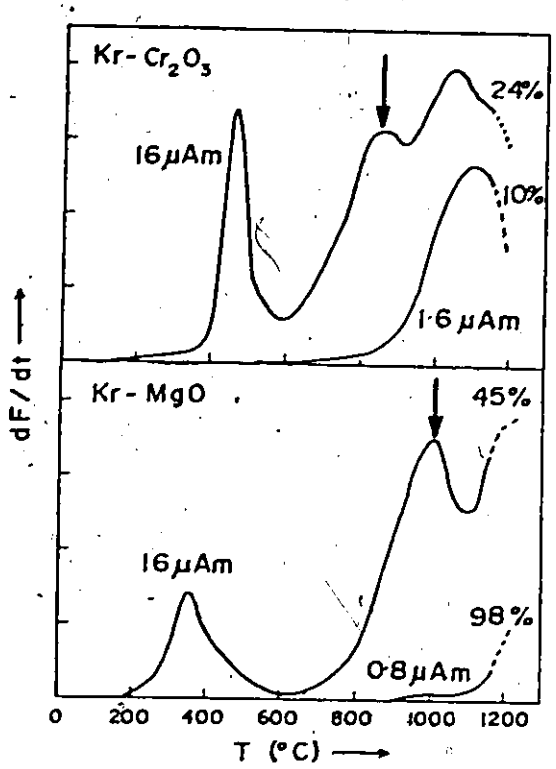

Fig. 9.1. dF/dt vs. T curves for Cr_2O_3 and MgO which have been ion-bombardment labeled with 10 keV Kr. The doses are given in units of μ Amin/cm^2, written "μ Am". The percentage refers to the amount of gas remaining at the highest temperature reached (from Ref. 16).

9.3 Marker-release stages

We have seen that in certain instances marker-release spectrometry reveals one peak for an amorphous-polycrystalline transition (Stage IB) and one for a polycrystalline-epitaxial transition.

The question is now how these two release processes are to be designated with the formalism of marker-release spectrometry (19,20). The current practice is that diffusion in inert-gas implanted solids is described in terms of five basic processes or stages of increasing temperature (Section 6.3). Specifically, if the low-temperature release with SnO_2 is identified with Stage IB, then to which of the remaining three stages (IIA, IIB and III) can the release due to epitaxial recrystallization be attributed? Let us consider MgO, quartz, Cr_2O_3, SnO_2 and TiO_2, bearing in mind that, as already said, in all these cases recovery from the amorphous (or otherwise disordered) to the original crystalline phase occurs through an intermediate stage where the material is not epitaxial and where gas-release spectroscopy clearly resolves the two transitions in question.

With MgO the temperature required for marker-release due to the assumed epitaxial crystallization was 780°-965°C (1,16), while the temperature for Stage IIA was ≥1175°C (16)(Table 9.II). Similar comments hold for Cr_2O_3, TiO_2 and SiO_2 (Table 9.II), in the sense that the stage for known or assumed crystallization lies between the stage for crystallization of amorphicity (Stage IB) and that for normal diffusion (Stage IIA).

Another basic feature is that epitaxial crystallization does not involve random diffusion, like Stage IIA and IIB, but rather motion which

TABLE 9.II

The annealing of bombardment-induced amorphousness in oxides, as monitored using marker-release spectrometry and diffraction

Substance	T(°C) of first release process	State of target during this process as shown by diffraction	T(°C) of second release process	State of target during this process as shown by diffraction	T(°C) of third release process	Diffusion stage of third release process as shown by dose dependence	Ref.
MgO	300-325	cryst.	780-965	recryst.	1200; >1175	IIA	1,15
Cr_2O_3	445	-	875	-	∿1090	IIA	15
SiO_2 (high-doses)	400	cryst.	650	recryst.	800	IIA	3
TiO_2	480	cryst.	775	recryst.	∿1200	IIA	1,15
SnO_2	320-475	cryst.	910	recryst.	-	-	present work

is directional. Directionality is a common feature also to Stage IA and IB.

These two features suggest that, very simply, the spirit of the system of gas-release stages is preserved by designating epitaxial crystallization as Stage IC.

9.4 Dissolution and F-vs-dose data

Dissolution and F-vs-dose experiments such as are described in Section 8.3 are valuable in determining the depth of alteration induced by ion-bombardment. From Figs. 8.5 and 8.6, rapid dissolution stops, for the highest dose, while about 18-25% of the original activity remains. The corresponding depths, as deduced from Fig. 6.8, are about 130-140 Å. The thicknesses of the amorphized layer as a function of bombardment dose are summarized in Table 9.III.

Table 9.IV serves to compare SnO_2 with the other systems for which extensive information is available, namely Nb_2O_5, Si, and WO_3.

9.5 Electrical conductivity measurements

The conclusion from what we have shown in Section 8.4 is that SnO_2 shows high values of the resistance both before and after Kr-bombardment. This implies that the original stoichiometry was retained (Section 1.3).

It had been assumed (and even hoped) that SnO_2 would resemble materials such as CuO, Fe_2O_3, MoO_3, Nb_2O_5, TiO_2, U_3O_8, V_2O_5, WO_3 (Section 1.2.7). It does not, however, due to the tendency of this oxide to resist oxygen removal, but the result turns out to be consistent both with a model of preferential sputtering and with one of thermal spike induced vaporization (Section 6.2.3).

TABLE 9.III

Thicknesses of amorphized layer as a function of bombardment dose

Dose (ions/cm^2)	Activity retained (from Figs. 8.5 and 8.6)	Thickness (Å) (from Fig. 6.8) (*)
1.6×10^{14}	.84	58
6.6×10^{14}	.55	96
1.7×10^{15}	.66	83
2.0×10^{15}	.41	111
3.4×10^{15}	.59	92
5.0×10^{15}	.48	102
5.0×10^{15}	.31	121
6.7×10^{15}	.46	104
8.2×10^{15}	.41	111
9.7×10^{15}	.32	119
2.1×10^{16}	.25	131
2.5×10^{16}	.26	128
5.0×10^{16}	.18	141

(*) Thicknesses so obtained are in principle as reliable as LSS range parameters, namely ±20%.

TABLE 9.IV

Thickness of amorphized layer

in various substances

Substance	Ion and Energy	Dose ($ions/cm^2$)	Thickness amorphized (Å)	Ref.
SnO_2	Kr; 35-keV	3.4×10^{15}	92	present work
Nb_2O_5	Kr; 35-keV	4×10^{15}	270	21
Si	Kr; 35-keV	3.8×10^{15}	450*	22
WO_3	Kr; 35-keV	3.5×10^{15}	390	23

* obtained by interpolation from data for 2-, 10-, and 40-keV (ref. 22)

The failure of SnO_2 to lose oxygen under ion-bombardment shows, moreover, that it is not correct to use the results of experiments involving oxygen bombardment of metals (cfr. Chapter 4 and in particular Section 4.4) to predict the bombardment of oxides. Oxygen bombardment of a metal is governed by completely different principles from oxygen loss for an oxide. In particular, we must not argue that the two experiments constitute a bombardment analog to approaching an equilibrium state from two directions.

9.6 Other observations

The temperature 592 K for the first release process, in the case of marker-release spectrometry in the mineral cassiterite, is somewhat lower than those obtained when SnO_2 pellets are used (700-747 K)(Table 8.I). We regard this tentatively as an example of impurity effect (cfr. Table 2 of Ref. 14).

A further discrepancy is between the crystallization temperature for bombardment-induced amorphousness in SnO_2 (592, 700, 747 K) and those for unsupported SnO_2 thin films (750, 825 K)(Section 2.3.2). Similar discrepancies occurred also with MoO_3, TeO_2, V_2O_5(2), Si_3N_4(24), and SiO_2(3,25), as summarized in part on p. 58. We regard this as an example of a nucleation effect.

REFERENCES

1. Hj. Matzke and J. L. Whitton, Can. J. Phys. 44, 995 (1966).

2. H. M. Naguib and R. Kelly, Radiation Effects 25, 79 (1975).

3. Hj. Matzke, phys. stat. sol. 18, 285 (1966).

4. J. W. Mayer, L. Eriksson, S. T. Picraux and J. A. Davies, Can. J. Phys. 46, 663 (1968).

5. D. J. Mazey, R. S. Nelson and R. S. Barnes, Phil. Mag. 17, 1145 (1968).

6. D. J. Mazey and R. S. Nelson, Rad. Effects 1, 229 (1969).

7. H. M. Naguib, W. A. Grant and G. Carter, Rad. Effects 18, 279 (1973).

8. S. Mader, Recrystallization, Grain Growth and Textures, ASM, Metals Park, Ohio, October 16-17, 1965.

9. M. L. Lieberman and R. C. Medrud, J. Electrochem. Soc. 116, 242 (1969).

10. J. Drowart, F. Degrève, G. Verhaegen and R. Colin, Trans. Faraday Soc. 61, 1072 (1965).

11. I. A. El Shanshoury, V. A. Rudenko and J. A. Ibrahim, J. Am. Ceram. Soc. 53, 264 (1970).

12. F. Holtzberg, A. Reisman, M. Berry and M. Berkenblit, J. Am. Chem. Soc. 79, 2039 (1957).

13. P. H. G. Draper and J. Harvey, Acta Met. 11, 873 (1963).

14. H. M. Naguib and R. Kelly, J. Nucl. Mater. 35, 293 (1970).

15. J. Kakinoki, K. Katada, T. Hanawa and T. Ino, Acta Cryst. 13, 171 (1960).

16. C. Jech and R. Kelly, J. Phys. Chem. Solids 30, 465 (1969).

17. E. Krikorian and R. J. Sneed, Trans. Nat. Symp. Vacuum Technol. 10, 368 (1963).

18. J. W. Mayer, L. Eriksson, S. T. Picraux and J. A. Davies, Can. J. Phys. 46, 663 (1968).

19. R. Kelly and C. Jech, J. Nucl. Mat. 30, 122 (1969).

20. Hj. Matzke, Lecture at the Summer School on the Physics of Ionized Gases, Herceg-Novi, Yugoslavia, 1970.

21. D. K. Murti, Thin Solid Films, in press.

22. J. Reid and R. Kelly, Radiation Effects,17, 253 (1973).

23. N. Q. Lam and R. Kelly, Can. J. Phys. 50, 1887 (1972).

24. P. V. Pavlov, E. V. Shitova, E. I. Zorin and N. A. Genkina, Sov. Phys. Crystallogr. 18, No. 3, 381 (1973).

25. F. W. Ainger, J. Mat. Sci. 1, 1 (1966).

CHAPTER 10

SUGGESTIONS FOR FUTURE WORK AND SUMMARY

10.1 Suggestions for future work

10.1.1 A possible thickness effect - Fig. 10.1 shows RED micrographs of SnO_2 films deposited by reactive sputtering on Ta substrates. It can be noticed that diffraction patterns of films whose thickness was estimated to be ~3600 Å or higher, show well defined rings rather than halos. Thus films appear to change spontaneously from an amorphous to a crystalline state with increasing thickness. A systematic investigation could be undertaken to probe deeper into this phenomenon. Precedents can be found in work by Krikorian and Sneed (1) on sputtered films of Ge, Behrndt (2) on Bi, Ga, Fe and V, Piercy (3) on anodic WO_x, and Arora (4) on anodic VO_x, WO_x, MoO_x, NbO_x, and TaO_x.

10.1.2 Thickness-vs-anodizing voltage - As already noticed in Section 3.3.3 anodized films are thicker for a voltage in the vicinity of 8-15 than for higher values (Table 3.I). We have no explanation at all for this result, though consider it to justify future work for its clarification. We would in particular recall that the present work constitutes the first instance in which thick protective oxide films were grown on Sn by anodizing.

10.1.3 Preparation of SnO_2 by oxygen-bombardment of metallic tin - As already mentioned in Section 4.3, we would predict that, due to S (sputtering coefficient) decreasing, SnO_2, rather than SnO, would be formed at very low ($E << 35$-keV) or at very high ($E >> 35$-keV) O_2^+ energies.

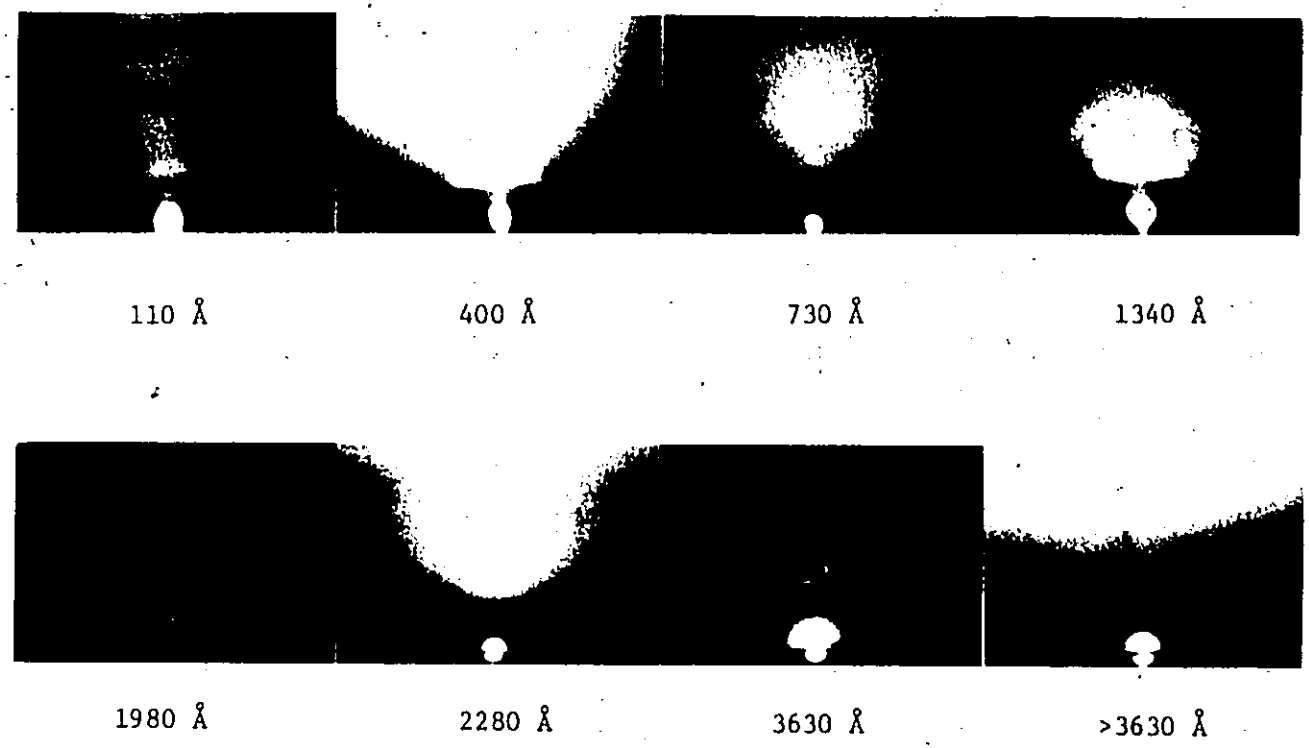

Fig. 10.1. SnO_2 reactively sputtered on Ta substrate. All thicknesses deduced gravimetrically, i.e. weighing Ta before and after deposition.

Were one able to obtain SnO_2 in this way, the possibility would exist to form films with all possible thicknesses from zero to the range of thicknesses represented by anodic films. The latter cannot be obtained (see Chapter 3) with thicknesses less than ~3000 Å.

10.1.4 Formation of oxygen-bubbles in O_2-implanted metallic tin - Looking at Fig. 10.2, which is the transmission electron micrograph of a metallic tin film implanted with oxygen, it will be noticed that black spots appear on a uniform background. This feature always appeared in transmission electron micrographs of oxygen-implanted samples, as distinguished from unbombarded samples (cfr. Fig. 4.1(a)). Noticing that bubbles are detected in electron microscope studies as having the appearance either of white or black dots (see, e.g., Ref. 5), the possibility was considered that oxygen bubbles had formed. Consider the gas law:

$$pV = nRT$$

If $p = 2\gamma/r$, γ = surface tension, N = number of atoms, L = Avogadro's number, then it can be rewritten as

$$\frac{2\gamma}{r}\frac{4}{3}\pi r^3 = \frac{N}{L}RT$$

Assuming a surface tension $\gamma = 200$ erg/cm^2, and an average radius of 1000 Å for the black spots in Fig. 10.2, one obtains

$$N = 4 \times 10^6 \text{ atoms/black dot}$$

Multiplying the oxygen dose used (3×10^{15} ions/cm^2) by the average area of a black dot, one obtains 2×10^5 ions/black dot. Clearly, the black dots are not bubbles. Presumably the formation of SnO (Section 4.2.2)

Fig. 10.2. Sn film on carbon coated grid--
Bombarded with oxygen:
3×10^{15} ions/cm^2 - 35 keV
mag. 53,000 - 100 keV

during O_2^+ bombardment hinders the possibility of the simultaneous existence of oxygen bubbles.

To decide about the real origin of such features, one should undertake a quantitative electron optical investigation, inclusive of dark field, underfocus and overfocus imaging, as well as heat treatment of the specimen. The reason for the latter is that in many cases bubbles migrate at a temperature which, though above the self-diffusion temperature, is below the melting point; that is, there is a possibility of bubbles being made to move and therefore identified as bubbles, by pulse heating or by using the heating stage.

10.1.5 Stage IIA and melting point - Release due to a true (Stage IIA) diffusion of the implanted inert-gas ions in the undamaged lattice of the host crystal will diminish in relative importance as the dose increases due to the onset of processes caused by the radiation damage. It is therefore possible that the reason our release spectra do not record Stage IIA somewhere in the region >1200 K is that we have been using too high a dose.

The identification of Stage IIA would have enabled one to estimate, even if crudely, the melting temperature for SnO_2. In fact, Matzke (6), has found that an empirical relation exists between Stage IIA release temperatures and melting points. This relation is obtained from data for a great number of different materials, namely halides, oxides and metals:

$$T_{IIA(10\%)} = 0.4\text{-}0.5\ T_{melting}$$

We would point out that the melting point for SnO_2 is variously reported to lie between 1400 and 2200 K. One of the low values, namely 1673 K, has

been checked by Sinclair et al. (7) and is certainly wrong. What probably happens is that when SnO_2 is heated in vacuum the relevant process is $SnO_2 \rightarrow SnO + \frac{1}{2} O_2$ and what has actually been observed is the melting (1353 K) of tin monoxide. The higher values are probably wrong too, for they correlate better with the sublimation temperature (2073-2173 K).

We anticipate the melting temperature of SnO_2 may be in the vicinity of 3000 K, corresponding to Stage IIA occurring at >1200 K.

10.2 Summary

(a) A thorough review of the literature has shown that many different approaches have been attempted, with varying degrees of success, in order to prepare SnO_2 films.

Films have been formed (i) by chemical vapour deposition, (ii) by reactive evaporation of Sn, (iii) by sputtering, and (iv) by gas oxidation of metallic tin (which has produced contradicting results). Concerning the possibility of obtaining SnO_2 films by anodizing Sn at high voltages, work with both acidic and basic electrolytes has invariably involved low voltages (<5) and never values (>>5) characteristic of the growth of thick, uniform films.

There has been an enormous amount of electronic and optical characterization in previous work. This is attributable to the fact that SnO_2 is a high potentiality material for device fabrication, due to its unique property of combining, when oxygen deficient, electrical conductivity with a high degree of transparency to visible light.

As far as structural characterization is concerned, knowledge is largely confined, until now, to two results: chemically deposited layers are invariably crystalline, while evaporated or reactively sputtered layers

are normally, though not always, amorphous. Such basic concepts as whether the films are amorphous or crystalline, and, if the former, the value of the crystallization temperature, have not been so far settled in a satisfactory way, the crystallization temperature, for example, being given as a limit, e.g. >280°C, <400°C, <500°C. Non-existent is also any information about crystallization mode, the crystallization product, and the grain size of crystallization product.

We regard structural characterization to be as important as other properties if SnO_2 is to find use in device fabrication, in view of the fact that, for example, both the magnitude of conductivity, as well as its temperature stability, are effected by crystallinity. (cfr. V_2O_3 and VO_2, as shown in Fig. 1.1.)

As far as ion-impact effects are concerned, there is no published study at all in which SnO_2 is considered explicitly.

On the basis of these considerations, we have defined an area of lack of knowledge, a space in which to operate by means of our choice of techniques, experimental apparatus, materials preparation and treatment, materials analysis.

(b) The first experiments involved the preparation of SnO_2 films by reactive as well as ion-beam sputtering. While the preparation of SnO_2 films by these techniques has a long precedent in the literature, at least from the point of view of preparation as an end in itself, our work gives explicit information on the crystallization temperature. The latter depends strongly on the nucleation conditions as governed by the substrate, varying from <200°C for crystalline SnO_2 substrates, to 250°-300°C for KCl substrates, to 400°-450°C for Ta substrates, to 475°-550°C for unsup-

ported films. We would propose that 475°-550°C is the upper limit to the crystallization temperature (for a 1000 Å thick amorphous film and an annealing time of 6 min; which are typical values, to within a factor of 2).

While the crystallization process occurred homogeneously, a consistent result in this work has been that amorphous SnO_2, formed by either reactive or ion-beam sputtering, crystallized to cassiterite. Likewise SnO_2 films formed anodically (see (c)) were cassiterite as formed. We therefore tentatively suggest that SnO_2 lacks metastable or high temperature phases.

Once crystallization was attained, the grain size remained in the vicinity of 400 Å to temperatures as high as 1000°C, in the case of unsupported films, while a grain size of 600 Å is reached after heating supported films to 550°-600°C. The difference in crystallization temperature between supported and unsupported films suggests that nucleation rather than growth is the rate-controlling step in the crystallization of SnO_2. Similarly, the difference in grain size obtained in annealing experiments suggests that nucleation, while perhaps not fully rate-controlling, at least plays a role in grain growth.

The thickness (d) of the reactively sputtered films was estimated by noting the interference colours when using a Ta substrate and assuming the validity of the relation $n_{SnO_2} d_{SnO_2} = n_{Ta_2O_5} d_{Ta_2O_5}$ where n is the index of refraction.

(c) While SnO_2 is frequently prepared by sputtering, there is as far as we know no precedent for films being formed by high-voltage anodizing. We have found it possible (apparently for the first time) to anodize Sn up to 65 V and the growing films showed 6 orders of interference colours. The present work makes it clear that, though the process is far from being per-

fect, high voltage film growth can be achieved with Sn. Anodic SnO_2 was found to be crystalline as formed, which was an unexpected result in view of the fact that anodic films are almost invariably amorphous.

The thicknesses of the anodic films were estimated, among other ways, by sputtering the films with 20-keV Kr ions until the metal was exposed and noting the weight loss. This confirmed the thicknesses to be nearly independent of voltage between 6 and 50 V; which is what was anticipated on the grounds that the interference colours changed only slightly with voltage. The anodization of Sn has a rather low efficiency (4-21%) and this could be shown to be due to electronic conduction rather than dissolution.

Efforts to characterize the anodic films structurally have led to further information on grain growth of SnO_2. Specifically the films retained their microcrystalline structure in heat treatment, until a temperature of about 1000°C was reached, this being in good agreement with the behaviour of sputtered films.

(d) A completely novel approach to forming SnO_2 films has here been attempted, by bombarding metallic tin with oxygen ions. The nominal objective failed in that the films turned out to be crystalline α-SnO. Still, this work has led us to indicate that SnO_2 films can, in principle, be formed by oxygen-implantation, thus providing a very controllable technique to form "very thin" thin films. The key is anticipated to lie in the choice of the oxygen-ion energy, as dictated by considerations on the sputtering coefficient for the system O_2-Sn.

(e) Having so far explored the properties of 500-5000 Å SnO_2 films as formed by reactive sputtering, ion-beam sputtering and high-

voltage anodizing, we have at this point undertaken to investigate, using the result of this work as a guide, Kr-ion-impact effects with SnO_2 thin films.

We have first of all made a survey of materials whose response to ion-impact is known. Included are materials which undergo (i) a crystalline-amorphous transition, (ii) an amorphous-crystalline transition, and (iii) a stoichiometry change. We have also given the criteria which researchers have worked out in order to predict the occurrence of the above transformations. While we have noticed the lack of any published result as far as SnO_2 is concerned, we have pointed out that, were a bombardment-induced amorphization or change of stoichiometry to occur with SnO_2, there would be significant technological implications for device fabrication. Furthermore, we want to point out that bombarding a material with inert-gas ions in the keV range is both a way to dope a material with what is one of the primary causes for swelling of fuel materials for nuclear reactors, as well as a way to simulate neutron irradiation in the MeV range. In addition, these experiments may be regarded as pointing the way to important effects, such as, for example, preferential sputtering. The sputtering process will play an obvious role with nuclear and thermonuclear materials due to their continuing exposure to fission fragments, fast neutrons, or helium ions. Preferential sputtering can alter the surface of binary alloys, with possible consequences such that external surfaces may in general have unexpected corrosion, electrical or transport properties.

(f) Our first experimental finding has been that SnO_2 shows an unusually high value of the sputtering coefficient. SnO_2 in this respect resembles MoO_3, V_2O_5, WO_3 and possibly SiO_2, but, to the writer's knowledge,

no other oxide. S was then measured as a function of temperature, the result of these experiments being that it was even higher at elevated temperatures. Taken together these experiments suggest that SnO_2 undergoes thermal sputtering, i.e. sputtering involving vaporization. This unusual behaviour is also shown to be predictable, when a general criterion which takes the vapour pressure into consideration, is applied to SnO_2. Pursuing the criterion further, it was argued that both a model based on "vaporization due to thermal spikes" (governed by vapour pressure) and one based on "preferential oxygen sputtering" (governed by the surface binding energy) predict that high-dose bombardment of SnO_2 will leave the stoichiometry unchanged, while the SnO_2 sputters congruently (as distinct from preferential sputtering).

(g) The next step in exploring the response of SnO_2 to ion-impact was to investigate the structure of the target material after bombardment. The experimental evidence was that SnO_2 amorphizes under ion-impact, in agreement with both a criterion based on a physical model involving thermal spikes and one of empirical nature based on ionicity.

(h) Given this preliminary result, namely that crystalline SnO_2 does indeed amorphize under ion-impact, we started at this point to look in more detail into this phenomenon.

Bulk samples (either sintered SnO_2 powder or natural cassiterite) were ion-bombarded and then analyzed using the following techniques: (i) reflection electron diffraction, (ii) dissolution measurements, (iii) resistivity measurements, and (iv) marker-release spectrometry.

(i) Monitoring, by electron diffraction, the annealing of bombardment-induced amorphousness at increasing values of the annealing

temperature, could only be done using bulk samples, and not anodized tin, due, if not to any other reason, to the difference in melting temperature between SnO_2 and the metallic Sn substrate. Such experiments have established that the annealing to the original single crystalline phase occurs (i) by a homogeneous transformation rather than by interface motion ("heterogeneous" transformation in the terminology of Mader). Moreover, it goes (ii) through an intermediate polycrystalline phase showing the normal cassiterite structure. Though most substances show crystallization by interface motion and by necessity therefore return to the original structure, in a process where there is an evolution of the type amorphous→polycrystalline→epitaxial, the intermediate phase could in principle have a different structure than the starting material. In fact most amorphous oxides do yield a different phase, with SnO_2 being an exception in not doing so.

(j) Dissolution measurements have been performed in order to establish the depth of alteration due to ion-bombardment. The first step in obtaining so-called dissolution curves was to label specimens with radioactive Kr^{85}. The specimens were then exposed to a suitable solvent and the fraction of retained activity noted as a function of time. Provided the depth distribution of the injected ions can be estimated, the fraction of retained activity enables one to deduce the thickness of the layer removed. Results for SnO_2 have been compared with other systems for which information is available. It turned out that the thickness of the amorphized layer is rather smaller in the case of SnO_2. Namely, SnO_2 shows high "resistance" to amorphization.

We have also carried out experiments in which dissolution and

thermal annealing were compared. Thermal annealing and dissolution resulted to be equivalent (when annealing is carried on up to at least ~1100°C) in that the activity retained after dissolution is similar to that retained after thermal annealing. This equivalence, though, does not hold for lower annealing temperatures. In other experiments, dissolution and annealing were combined. Taken together the results of the above experiments are understandable if it is assumed that amorphous SnO_2 is fully soluble in HF, polycrystalline SnO_2 is partly soluble, and single-crystal SnO_2 is not soluble at all.

(k) Oxygen loss normally causes the conductivity of an oxide to increase, at times by many orders of magnitude. If oxygen loss were to occur with SnO_2, the result would have been of fundamental importance in device fabrication, owing to its conductivity varying, apparently, as much as 5 orders of magnitude due to stoichiometry changes.

Again, bulk material had to be used in order to carry out conductivity measurements. (Anodic films could not be used due to the metallic nature of the substrate.)

The conclusion from the experiments was that SnO_2 shows high values of resistance both before and after high-dose Kr-bombardment. This implies that the original stoichiometry was retained. The result is consistent both with a model of preferential sputtering and with one of thermal-spike induced vaporization and its implication is that SnO_2 insulators or resistors should be particularly suited to be used in a radioactive environment (as distinct, for example, from devices based on TiO_2).

(l) Marker-release spectrometry was finally used. The basic idea behind this technique is to label the specimen with a radioactive inert-

gas and then determine, with a linear temperature increase, the temperatures for the release of the gas, the gas serving as an inert marker which signals phase changes, stoichiometry changes, defect annealing, or diffusion. Once more bulk SnO_2 had to be used, rather than anodized SnO_2, owing to the latter lying on a substrate (metallic tin) which has an unsuitable melting behaviour. Two reproducible release processes, at definite temperatures, were in this way promptly identified. Electron diffraction investigation of the specimen at these temperatures revealed the two release processes to be due to an amorphous-crystalline and a crystalline-epitaxial phase transformation, while the release spectrum provided a simple yet accurate means for locating the temperatures at which these processes occurred.

The present results allow us to expand the formalism on which marker-release spectrometry is based. Three characteristic release processes had been so far identified when a material implanted with a radioactive inert-gas is thermally treated: release due to recovery of bombardment-induced disorder, release due to self-diffusion and release due to bubble motion. We have identified a somewhat different release process, namely one due to epitaxial crystallization. This process has been clearly identified in the case of SnO_2, while a search of the literature has shown that precedents for such a phenomenon could be found with MgO, Cr_2O_3, SiO_2 and TiO_2. We have then pointed out that the known or suspected examples always lie above the temperature of Stage IB (crystallization) yet below the temperature of Stage IIA (unhindered diffusion). Also they share in common with Stages IA and IB motion which is directional rather than random. We therefore propose the designation "Stage IC" for epitaxial

crystallization.

A deeper knowledge of the marker-release technique will be valuable in better understanding the diffusion behaviour of inert-gas atoms in a host lattice, which, as already mentioned, is of primary importance, for example, in understanding, and eventually solving, the problem of swelling in fuel materials used in nuclear reactors. Besides, marker-release can be used as an important supplement to electron optics as an indicator of lattice disorder due to low energy ions. Or it can be used, again as a supplement to electron optics, to infer the presence of bubbles in a material, especially when the material is not in a form (thin film) suitable for electron optics. Finally, it yields valuable insight into self-diffusion and melting behaviour.

REFERENCES

1. E. Krikorian and R. J. Sneed, Trans. Nat. Symp. Vacuum Technol. 10, 368 (1963).

2. K. H. Behrndt, J. Vac. Sci. Tech. 7, 385 (1969).

3. G. R. Piercy, AECL Annual Report, Apr. 1 - June 30, 1964.

4. M. R. Arora, Ph.D. thesis, McMaster University, Canada, 1974.

5. E. Ruedl and R. Kelly, J. Nucl. Mat. 16, 89 (1965).

6. Hj. Matzke, Can. J. of Phys. 46, 621 (1968).

7. W. R. Sinclair, R. G. Peters, D. W. Stillinger and S. E. Koonce, J. Electrochem. Soc. 112, 1096 (1965).

ERRATA

p. 124: Ref. 6 and Ref. 13 refer to the same publication

p. 152: Ref. 26 and Ref. 30 refer to the same publication

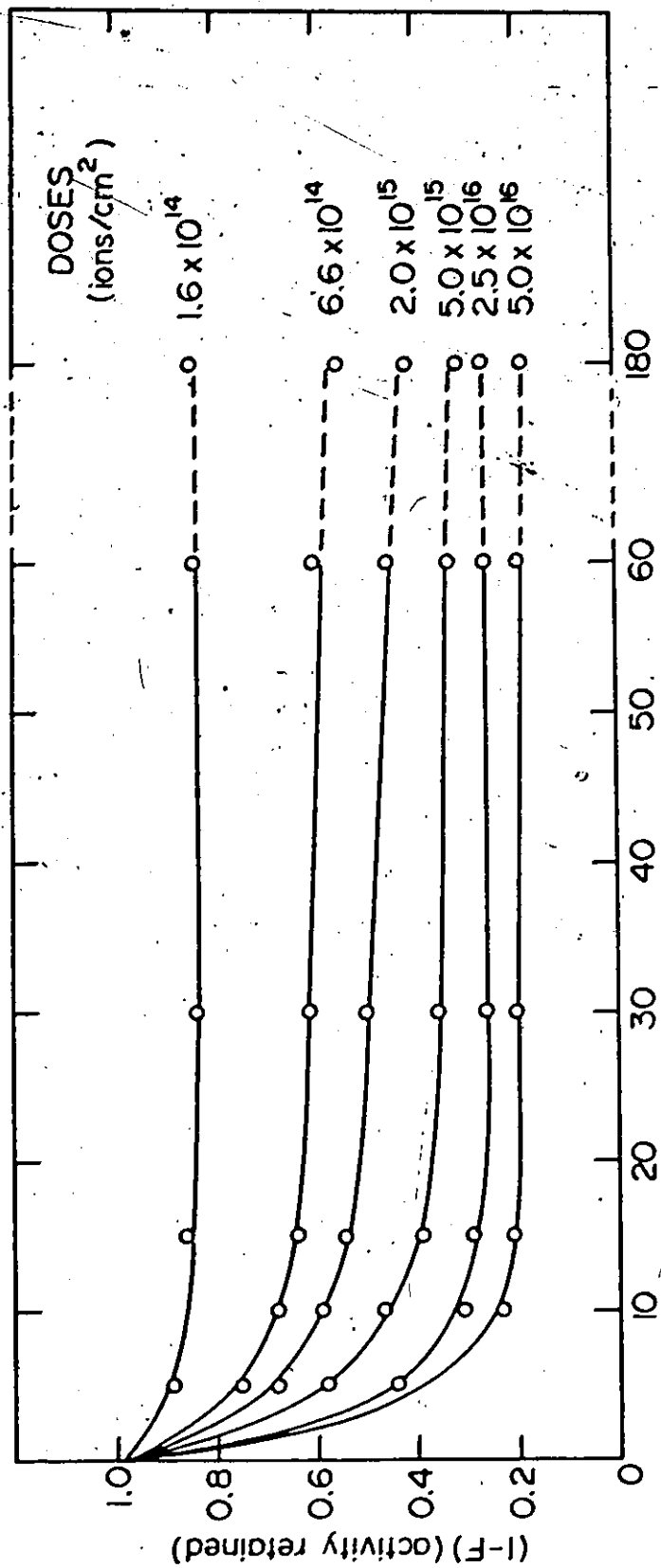

Fig. 8.6. Dissolution curves for Kr-implanted (35-keV) natural cassiterite. Doses as indicated on curves.

TABLE 8.III

Activity retained after dissolution of SnO_2 samples (pellets and natural cassiterite) has gone to completion

Dose (ions/cm^2)	Fractional activity retained (1-F)
1.6×10^{14} (nat. cass.)	.84
6.6×10^{14} (nat. cass.)	.55
1.7×10^{15} (pellet)	.65
2.0×10^{15} (nat. cass.)	.41
3.4×10^{15} (pellet)	.59
5.0×10^{15} (pellet)	.47
5.0×10^{15} (nat. cass.)	.31
6.7×10^{15} (pellet)	.45
8.2×10^{15} (pellet)	.41
9.7×10^{15} (pellet)	.32
2.1×10^{16} (pellet)	.25
2.5×10^{16} (nat. cass.)	.26
5.0×10^{16} (nat. cass.)	.18

TABLE 8.IV

Activity retained after heating to T ≥ 1100°C

(heating rate 25 K/min)

Dose (ions/cm^2)	Activity retained (1-F)	Maximum temperature (°C)
1.6×10^{14} (nat. cass.)	.54	1,109 (oxygen flow)
4.7×10^{14} (pellet)	.53	1,117 (helium flow)
4.7×10^{14} (pellet)	.66	∿1,100 (helium flow)
3.7×10^{14} (pellet)	.82	∿1,100 (oxygen flow)
4.7×10^{14} (nat. cass.)	.35	1,123 (oxygen flow)
8.3×10^{14} (pellet)	.84	∿1,100 (oxygen flow)
9.4×10^{14} (pellet)	.59	1,117 (helium flow)
9.4×10^{14} (pellet)	.54	∿1,100 (helium flow)
1.9×10^{15} (pellet)	.46	∿1,100 (helium flow)
1.9×10^{15} (pellet)	.61	∿1,100 (oxygen flow)
1.9×10^{15} (nat. cass.)	.29	1,104 (oxygen flow)
1.9×10^{15} (nat. cass.)	.33	1,116 (oxygen flow)
2.8×10^{15} (pellet)	.43	1,190 (oxygen flow)
2.8×10^{15} (pellet)	.54	1,190 (oxygen flow)
4.6×10^{15} (pellet)	.48	∿1,100 (oxygen flow)
4.6×10^{15} (pellet)	.53	1,117 (oxygen flow)
4.6×10^{15} (pellet)	.58	1,109 (oxygen flow)
5.4×10^{15} (pellet)	.26	1,244 (helium flow)
5.4×10^{15} (pellet)	.31	1,230 (helium flow)
6.0×10^{15} (pellet)	.48	1,210 (oxygen flow)
6.0×10^{15} (pellet)	.44	1,245 (oxygen flow)
7.0×10^{15} (pellet)	.48	∿1,100 (oxygen flow)
7.0×10^{15} (pellet)	.46	∿1,100 (oxygen flow)
7.0×10^{15} (pellet)	.49	∿1,100 (oxygen flow)
9.4×10^{15} (pellet)	.30	∿1,100 (helium flow)

TABLE 8.IV (continued)

9.4×10^{15} (pellet)	.42	1,135 (oxygen flow)
9.4×10^{15} (nat. cass.)	.14	1,112 (oxygen flow)
9.4×10^{15} (nat. cass.)	.17	1,100 (oxygen flow)
2.1×10^{16} (pellet)	.39	1,156 (oxygen flow)

TABLE 8.V

Activity retained after heating to T < 1100°C

(heating rate 25 K/min)

Dose (ions/cm^2)	Activity retained (1-F)	Maximum temperature (°C)
8.2×10^{14} (pellet)	.96	768 (oxygen flow)
4.7×10^{14} (pellet)	.91	666 (helium flow)
9.4×10^{14} (pellet)	.85	666 (helium flow)
1.5×10^{15} (pellet)	.92	745 (helium flow)
1.9×10^{15} (pellet)	.69	704 (helium flow)
2.5×10^{15} (pellet)	.86	768 (oxygen flow)
4.9×10^{15} (pellet)	.85	745 (helium flow)
5.0×10^{15} (pellet)	.86	768 (oxygen flow)
8.3×10^{15} (pellet)	.91	768 (oxygen flow)
9.4×10^{15} (pellet)	.68	666 (helium flow)
9.7×10^{15} (pellet)	.60	745 (helium flow)
9.7×10^{15} (pellet)	.57	745 (helium flow)
9.7×10^{15} (pellet)	.66	745 (helium flow)
9.7×10^{15} (pellet)	.51	745 (helium flow)
9.7×10^{15} (pellet)	.84	745 (air)
1.2×10^{16} (pellet)	.93	768 (oxygen flow)
1.7×10^{16} (pellet)	.73	768 (oxygen flow)
1.7×10^{16} (pellet)	.55	745 (helium flow)

Fig. 8.7. We have seen that the low temperature release, corresponding to the amorphous-polycrystalline transition (Fig. 8.4c and 8.1-8.3), maximizes at 600-750 K (Table 8.I). Likewise the high-temperature release, corresponding to the polycrystalline-single crystal transition in the case of cassiterite (Fig. 8.4d and 8.1-8.3), maximizes at 1170-1200 K (Table 8.I). Curve 1 of Fig. 8.7, therefore, confirms the observation mentioned above that the total release due to both crystallization and recrystallization is equivalent, as far as the amount of activity retained in the sample is concerned, to a chemical process in which the disordered surface layers of the sample are dissolved away. Curve 2 shows that the amount of activity retained if the sample is heated in He through, but not beyond the first release process, is rather greater than otherwise. Moreover, it can be seen from curve 3 that the fractional activity retained is still higher if the annealing atmosphere is oxygen. This in agreement with the already noted fact (cfr. Section 8.1) that the first process is less pronounced when marker-release in an O_2-atmosphere is used.

The identification of the dissolution curve with the annealing curve is particularly important. It is an indication that all marker atoms imbedded in the amorphized layers, and finally removed by dissolution, are driven out during the overall crystallization and recrystallization process.

In other experiments, dissolution and annealing were combined. When dissolution experiments were performed on samples annealed at a high temperature ($\geq$1350 K, which is past the high-temperature release process) the result was that no further dissolution took place, namely the retained activity remained as shown in curve 1 of Fig. 8.7. This is expected.

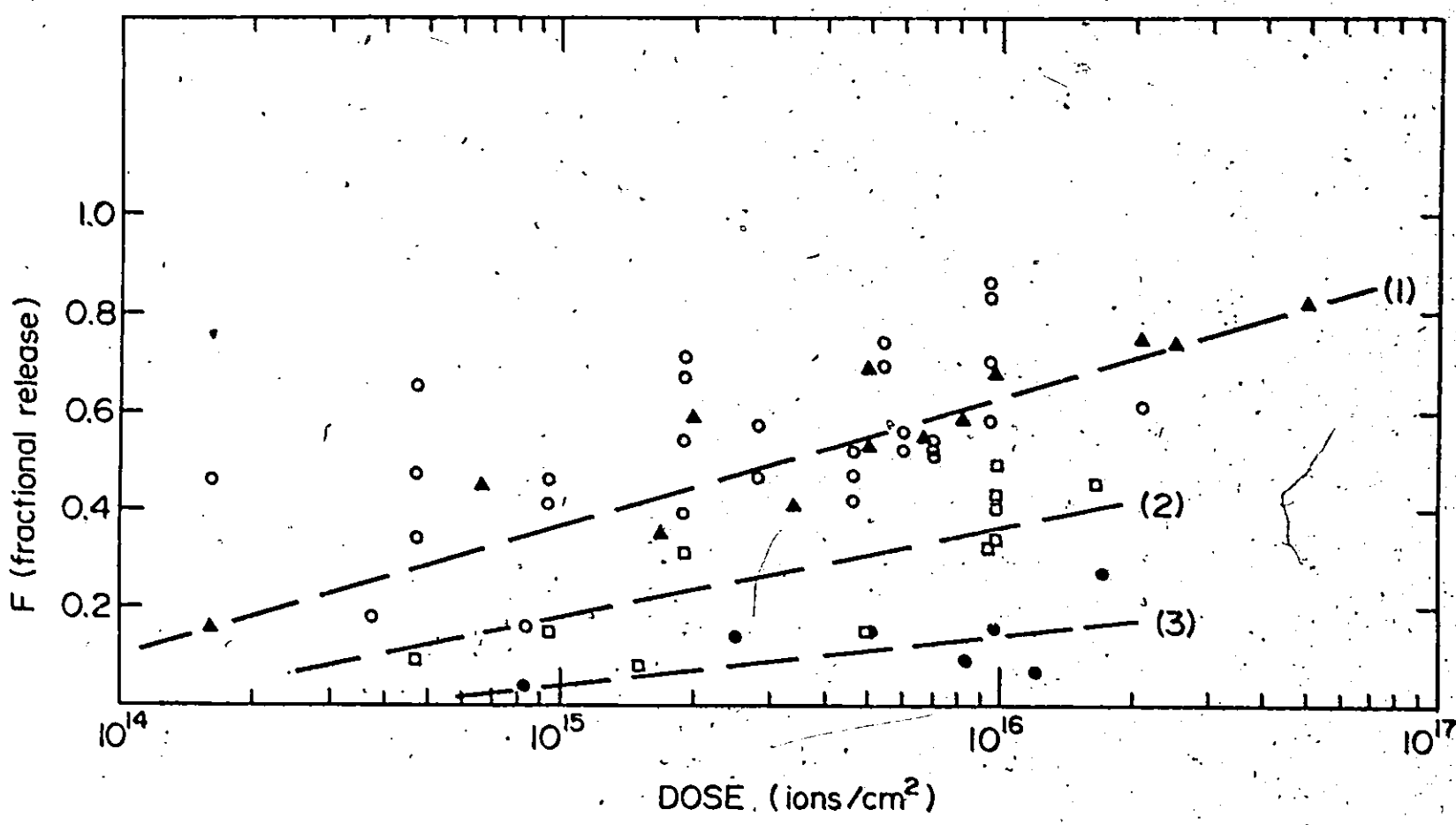

Fig. 8.7. Fractional release of implanted ions in SnO_2, due to dissolution and annealing, ▲ dissolution, o annealing to T ≥ 1100°C, □ annealing to T < 1100°C(helium flow), ● annealing to T < 1100°C(oxygen flow).

When dissolution experiments were performed on samples annealed at ~1030 K (i.e. a temperature which is above the first release process, but below the second), the result was that there was still dissolution taking place (Table 8.VI), though the total amount of activity retained after combined annealing (~1030 K) and dissolution was higher than that shown in curve 1 of Fig. 8.7 (Table 8.VII).

Taken together these results are understandable if it is assumed that the rate of dissolution in HF is higher for amorphous SnO_2 than for polycrystalline or single crystal SnO_2 respectively.

An alternative view is that some amorphous material is still present in the polycrystalline layer. Perhaps the crystalline material can be thought of as being "in suspension in an amorphous solvent". The existence of amorphous material between the grains is more likely in a homogeneous transformation (Section 6.3), as the amorphous-polycrystalline transition in SnO_2, than when the transformation is by interface motion.

8.4 Electrical conductivity measurements

The specimens used were SnO_2 pellets (sintered in air) and natural cassiterite (annealed in air), while the DC currents were 10^{-2}, 10^{-3} and 10^{-4} amp. In spite of the decreasing values of the current used, the DC current source* always showed the "voltage compliance limit" to be functioning, indicating that the load conductivity was less than $10^{-4}/100 = 10^{-6}$ ohm^{-1}.

Samples were subsequently bombarded with Kr at 20 keV using fluences between 9.4×10^{15} ions/cm^2 and 3.2×10^{17} ions/cm^2 and fluxes ≤ 7 μA/cm^2. Again I/V resulted to be $< 10^{-6}$ ohm^{-1}. Then the conductivity

* Model 225 Keithley

TABLE 8.VI

Released fractional activity after annealing (~1030 K) and subsequent dissolution

Dose (ions/cm^2)	F due to annealing to T ≈ 1030 K		F due to: annealing to T ≈ 1030 K + dissolution	
	O_2-atmosphere	He-atmosphere	O_2-atmosphere	He-atmosphere
8.2×10^{14}	.04		.14	
2.5×10^{15}	.14		.28	
5×10^{15}	.15		.36	
8.3×10^{15}	.09		.19	
9.7×10^{15}	.16		.30	
1.2×10^{16}	.07		.21	
1.7×10^{16}	.27		.48	
1.5×10^{15}		.08		.15
4.9×10^{15}		.15		.19
9.7×10^{15}		.34		.38
9.7×10^{15}		.40		.55
9.7×10^{15}		.43		.53
9.7×10^{15}		.49		.50
1.7×10^{16}		.45		.67

TABLE 8.VII

Retained fractional activity after annealing to T $\geq$ 1350 K

and after combined annealing ($\sim$1030 K) and dissolution

Dose (ions/cm^2)	1-F, as from curve 1 of Fig. 8.7	1-F, as from samples annealed at $\sim$1030 K and then dissolved; annealing atmosphere: O_2	He
8.2×10^{14}	.66	.86	
1.5×10^{15}	.59		.85
2.5×10^{15}	.53	.72	
4.9×10^{15}	.46		.81
5×10^{15}	.45	.64	
8.3×10^{15}	.40	.81	
9.7×10^{15}	.38	.70	.62, .45, .47, .50
1.2×10^{16}	.35	.79	
1.7×10^{16}	.31	.52	.33

was measured after Kr-bombardment, but this time while the SnO_2 sample (pellet) was still in the accclerator chamber, i.e. under vacuum. The Kr ion energy was 35 keV, fluences were 1.4×10^{17} to 1.2×10^{18} ions/cm^2, and fluxes were $\leq 8\,\mu$A/cm^2. Again no conductivity change occurred.

REFERENCES

1. E. Giani, M.Sc. thesis (1971), McMaster University, Canada.

2. D. Lazarus, Solid State Physics 10, 71 (1960).

CHAPTER 9

DISCUSSION

9.1 Low-temperature process

As we have already pointed out, the low-temperature marker-release is more prominent in the case of He-flow than O_2-flow (Section 8.1). Thus, it might at first sight be thought to be related to an annealing stage associated with a partial reduction of the specimens which persists to a higher temperature due to the He atmosphere (1).

The above point of view is supported (erroneously, of course) by the experimental $\Delta T_{1/2}/T_{max}$ values (Table 8.II) suggesting the release not to be related to crystallization by interface motion. On the other hand, the $\Delta T_{1/2}/T_{max}$ values are fairly close to what is calculated for normal volume diffusion (diffusion in a damage-free lattice).

Both the correlation of the low-temperature process with a He carrier and the $\Delta T_{1/2}/T_{max}$ values are evidently misleading. Thus the diffraction evidence is completely clear in showing that the low-temperature process is due to an amorphous-crystalline transition with formation, not of a phase epitaxial with the original phase, but rather of a polycrystalline phase. We are thus dealing with one of the few known cases where the model of crystallization by interface motion used to derive eqn. (6.7b) was incorrect, as the crystallization had occurred homogeneously. The low-temperature process can be correctly designated as Stage IB.

Another example is Bi_2O_3 (2). Here the experimental $\Delta T_{1/2}/T_{max}$

for the low-temperature release does not match the calculated $\Delta T_{1/2}/T_{max}$ for Stage IB, and at the same time the diffraction patterns confirm the formation, not of the original single-crystal, but of a polycrystalline phase of untypical crystal form. SiO_2 is intermediate. It crystallizes in one step by interface motion after low-dose bombardments and homogeneously (to yield α-cristobalite) after high doses (3). Al_2O_3 and TiO_2 resemble SnO_2, Bi_2O_3 and SiO_2 by virtue of crystallizing homogeneously (to what in the case of TiO_2 is possibly anatase) and of showing epitaxial recrystallization only at higher temperature (1). It is more usual, however, that a substance shows interface motion insofar as this is possible: MoO_3, TeO_2, V_2O_5 (2), SiO_2 (low-dose bombardment)(3), Ge (4), Si (4,5), GaAs (6), GaP (7). The distinction between what is essentially interface motion and homogeneous crystallization is discussed further by Mader (8), as both processes are found with the amorphous alloys with which he works. (In fact, Mader uses the term "heterogeneous crystallization" for what is equivalent to our "interface motion".)

In a process where there is an evolution of the type amorphous→polycrystalline→epitaxial, the intermediate phase could in principle (though not by necessity) have a different structure than the starting material. Crystallization by interface motion, on the other hand, by necessity leads to an epitaxial phase. Known examples relating to oxides are summarized in Table 9.I.

We were able to establish that bombardment-induced amorphousness in SnO_2 anneals to a polycrystalline phase showing the normal cassiterite structure. We have in fact analyzed Fig. (8.4c) both in terms of calculating the d-spacings corresponding to the diffraction rings, and also, which is probably a more reliable means, comparing by eye these micro-

TABLE 9.I

The intermediate and stable phase

in the crystallization of amorphous oxides

Oxide	Product of homogeneous crystallization	Stable crystal form	Reference
Al_2O_3	γ-Al_2O_3 (cubic)	corundum (α-Al_2O_3)	1
Bi_2O_3	δ-Bi_2O_3 (cubic)	α-Bi_2O_3(monoclinic)	2,8,9
GeO_2	hexagonal	tetragonal	10
HfO_2	cubic	monoclinic	11
Nb_2O_5	low temperature form	α-Nb_2O_5(monoclinic)	12
SiO_2	α-cristobalite(tetragonal)	α-quartz(hexagonal)	3
Ta_2O_5	low temperature form	orthorhombic	13
TiO_2	probably anatase	rutile	1
WO_3	orthorhombic	monoclinic	9
ZrO_2	cubic	monoclinic	11,14

graphs to a standard reflection electron diffraction pattern of polycrystalline SnO_2. (The visual comparison is to be preferred in that it takes intensities better into account.) We have thus convinced ourselves that the structure shown in Fig. (8.4c) is indeed normal cassiterite.

In conclusion, crystallization by homogeneous transformation is a necessary but not sufficient condition for a material to crystallize to a phase different from the original. Nevertheless, most amorphous oxides do yield a different phase, with SnO_2 being exceptional in not doing so. One can speculate that this result is due to the structure of amorphous SnO_2 being "cassiterite"-like just as the structure of different kinds of carbon are described variously as graphite-like or diamond-like (15). Similar comments have been made of amorphous ZrO_2 (14).

9.2 High-temperature process

Considering now the high-temperature marker-release, we have proved by electron microscopy that it is related to epitaxial recrystallization. In the case of cassiterite this involved the evolution of our SnO_2 sample from a polycrystalline to a single-crystal structure. With pellets, the sequence would probably have been amorphous→finely polycrystalline→coarsely polycrystalline, though the necessary experiments were not done.

This does not, however, establish the release process as being caused by epitaxial grain growth per se. The temperature range in question (1170-1200 K) could in principle be that for normal volume diffusion, with the marker-release and the grain growth being results

and not causes. The experimental $\Delta T_{1/2}/T_{max}$ values are therefore of prime importance, as they are found to be distinctly smaller than what would be expected for normal volume diffusion. In fact, they agree well with interface motion (Table 8.III). From this we conclude that the high-temperature process is both related to and caused by the epitaxial recrystallization.

Other materials showing well-defined epitaxial recrystallization as a second step after crystallization include Bi_2O_3, SiO_2 and TiO_2 as already discussed in the preceding section. Al_2O_3 also shows epitaxial grain but not as a well-defined process (1). In addition, Cr_2O_3 (16) and MgO (1) possibly belong to this group, as can be inferred from the existence of intermediate-temperature marker-release processes as marked by arrows in Fig. 9.1. Ge does not belong to this group. Although Krikorian and Sneed (17) did indeed find a well-defined polycrystalline-crystalline transition in the annealing of amorphous Ge, this result applies to a thin film which has no crystalline substrate. An amorphous surface layer on Ge crystallizes epitaxially in one step (18).

We would point out that in the case of bombardment-induced amorphization in Al_2O_3 and Bi_2O_3, marker-release spectroscopy of the thermally annealed samples (1,2) records the whole evolution (amorphous-polycrystalline-epitaxial) by <u>one</u> release process only. These are therefore examples where one technique is not sufficient to unravel all the details. The reason for the single release peak is probably that release went to such a degree of completion that no marker remained to signal the epitaxial recrystallization. Two processes are, however, resolved (or assumed to be resolved) with Cr_2O_3, MgO, SiO_2, SnO_2 and TiO_2.

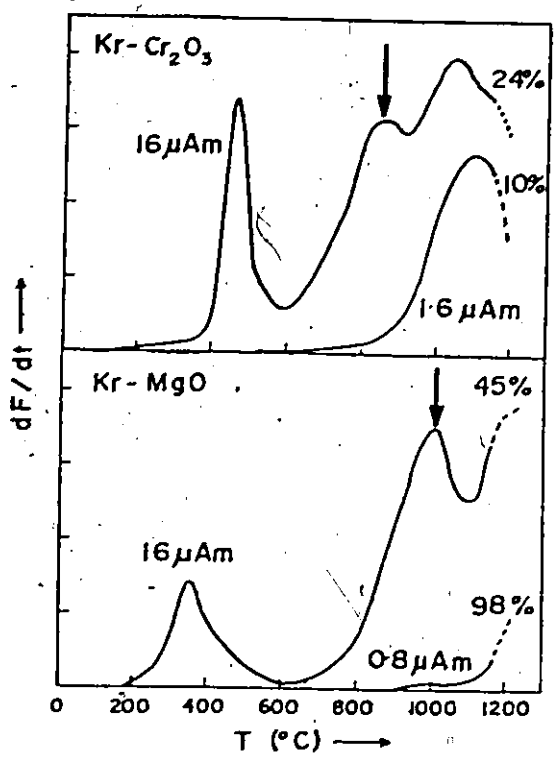

Fig. 9.1. dF/dt vs. T curves for Cr_2O_3 and MgO which have been ion-bombardment labeled with 10 keV Kr. The doses are given in units of μ Amin/cm^2, written "μ Am". The percentage refers to the amount of gas remaining at the highest temperature reached (from Ref. 16).

9.3 Marker-release stages

We have seen that in certain instances marker-release spectrometry reveals one peak for an amorphous-polycrystalline transition (Stage IB) and one for a polycrystalline-epitaxial transition.

The question is now how these two release processes are to be designated with the formalism of marker-release spectrometry (19,20). The current practice is that diffusion in inert-gas implanted solids is described in terms of five basic processes or stages of increasing temperature (Section 6.3). Specifically, if the low-temperature release with SnO_2 is identified with Stage IB, then to which of the remaining three stages (IIA, IIB and III) can the release due to epitaxial recrystallization be attributed? Let us consider MgO, quartz, Cr_2O_3, SnO_2 and TiO_2, bearing in mind that, as already said, in all these cases recovery from the amorphous (or otherwise disordered) to the original crystalline phase occurs through an intermediate stage where the material is not epitaxial and where gas-release spectroscopy clearly resolves the two transitions in question.

With MgO the temperature required for marker-release due to the assumed epitaxial crystallization was 780°-965°C (1,16), while the temperature for Stage IIA was ≥1175°C (16)(Table 9.II). Similar comments hold for Cr_2O_3, TiO_2 and SiO_2 (Table 9.II), in the sense that the stage for known or assumed crystallization lies between the stage for crystallization of amorphicity (Stage IB) and that for normal diffusion (Stage IIA).

Another basic feature is that epitaxial crystallization does not involve random diffusion, like Stage IIA and IIB, but rather motion which

TABLE 9.II

The annealing of bombardment-induced amorphousness in oxides, as monitored using marker-release spectrometry and diffraction

Substance	T(°C) of first release process	State of target during this process as shown by diffraction	T(°C) of second release process	State of target during this process as shown by diffraction	T(°C) of third release process	Diffusion stage of third release process as shown by dose dependence	Ref.
MgO	300-325	cryst.	780-965	recryst.	1200; >1175	IIA	1,15
Cr_2O_3	445	-	875	-	∿1090	IIA	15
SiO_2 (high-doses)	400	cryst.	650	recryst.	800	IIA	3
TiO_2	480	cryst.	775	recryst.	∿1200	IIA	1,15
SnO_2	320-475	cryst.	910	recryst.	-	-	present work

is directional. Directionality is a common feature also to Stage IA and IB.

These two features suggest that, very simply, the spirit of the system of gas-release stages is preserved by designating epitaxial crystallization as Stage IC.

9.4 Dissolution and F-vs-dose data

Dissolution and F-vs-dose experiments such as are described in Section 8.3 are valuable in determining the depth of alteration induced by ion-bombardment. From Figs. 8.5 and 8.6, rapid dissolution stops, for the highest dose, while about 18-25% of the original activity remains. The corresponding depths, as deduced from Fig. 6.8, are about 130-140 Å. The thicknesses of the amorphized layer as a function of bombardment dose are summarized in Table 9.III.

Table 9.IV serves to compare SnO_2 with the other systems for which extensive information is available, namely Nb_2O_5, Si, and WO_3.

9.5 Electrical conductivity measurements

The conclusion from what we have shown in Section 8.4 is that SnO_2 shows high values of the resistance both before and after Kr-bombardment. This implies that the original stoichiometry was retained (Section 1.3).

It had been assumed (and even hoped) that SnO_2 would resemble materials such as CuO, Fe_2O_3, MoO_3, Nb_2O_5, TiO_2, U_3O_8, V_2O_5, WO_3 (Section 1.2.7). It does not, however, due to the tendency of this oxide to resist oxygen removal, but the result turns out to be consistent both with a model of preferential sputtering and with one of thermal spike induced vaporization (Section 6.2.3).

TABLE 9.III

Thicknesses of amorphized layer as a function of bombardment dose

Dose (ions/cm^2)	Activity retained (from Figs. 8.5 and 8.6)	Thickness (Å) (from Fig. 6.8) (*)
1.6×10^{14}	.84	58
6.6×10^{14}	.55	96
1.7×10^{15}	.66	83
2.0×10^{15}	.41	111
3.4×10^{15}	.59	92
5.0×10^{15}	.48	102
5.0×10^{15}	.31	121
6.7×10^{15}	.46	104
8.2×10^{15}	.41	111
9.7×10^{15}	.32	119
2.1×10^{16}	.25	131
2.5×10^{16}	.26	128
5.0×10^{16}	.18	141

(*) Thicknesses so obtained are in principle as reliable as LSS range parameters, namely ±20%.

TABLE 9.IV

Thickness of amorphized layer

in various substances

Substance	Ion and Energy	Dose ($ions/cm^2$)	Thickness amorphized (Å)	Ref.
SnO_2	Kr; 35-keV	3.4×10^{15}	92	present work
Nb_2O_5	Kr; 35-keV	4×10^{15}	270	21
Si	Kr; 35-keV	3.8×10^{15}	450*	22
WO_3	Kr; 35-keV	3.5×10^{15}	390	23

* obtained by interpolation from data for 2-, 10-, and 40-keV (ref. 22)

The failure of SnO_2 to lose oxygen under ion-bombardment shows, moreover, that it is not correct to use the results of experiments involving oxygen bombardment of metals (cfr. Chapter 4 and in particular Section 4.4) to predict the bombardment of oxides. Oxygen bombardment of a metal is governed by completely different principles from oxygen loss for an oxide. In particular, we must not argue that the two experiments constitute a bombardment analog to approaching an equilibrium state from two directions.

9.6 Other observations

The temperature 592 K for the first release process, in the case of marker-release spectrometry in the mineral cassiterite, is somewhat lower than those obtained when SnO_2 pellets are used (700-747 K)(Table 8.I). We regard this tentatively as an example of impurity effect (cfr. Table 2 of Ref. 14).

A further discrepancy is between the crystallization temperature for bombardment-induced amorphousness in SnO_2 (592, 700, 747 K) and those for unsupported SnO_2 thin films (750, 825 K)(Section 2.3.2). Similar discrepancies occurred also with MoO_3, TeO_2, V_2O_5(2), Si_3N_4(24), and SiO_2(3,25), as summarized in part on p. 58. We regard this as an example of a nucleation effect.

REFERENCES

1. Hj. Matzke and J. L. Whitton, Can. J. Phys. 44, 995 (1966).

2. H. M. Naguib and R. Kelly, Radiation Effects 25, 79 (1975).

3. Hj. Matzke, phys. stat. sol. 18, 285 (1966).

4. J. W. Mayer, L. Eriksson, S. T. Picraux and J. A. Davies, Can. J. Phys. 46, 663 (1968).

5. D. J. Mazey, R. S. Nelson and R. S. Barnes, Phil. Mag. 17, 1145 (1968).

6. D. J. Mazey and R. S. Nelson, Rad. Effects 1, 229 (1969).

7. H. M. Naguib, W. A. Grant and G. Carter, Rad. Effects 18, 279 (1973).

8. S. Mader, Recrystallization, Grain Growth and Textures, ASM, Metals Park, Ohio, October 16-17, 1965.

9. M. L. Lieberman and R. C. Medrud, J. Electrochem. Soc. 116, 242 (1969).

10. J. Drowart, F. Degrève, G. Verhaegen and R. Colin, Trans. Faraday Soc. 61, 1072 (1965).

11. I. A. El Shanshoury, V. A. Rudenko and J. A. Ibrahim, J. Am. Ceram. Soc. 53, 264 (1970).

12. F. Holtzberg, A. Reisman, M. Berry and M. Berkenblit, J. Am. Chem. Soc. 79, 2039 (1957).

13. P. H. G. Draper and J. Harvey, Acta Met. 11, 873 (1963).

14. H. M. Naguib and R. Kelly, J. Nucl. Mater. 35, 293 (1970).

15. J. Kakinoki, K. Katada, T. Hanawa and T. Ino, Acta Cryst. 13, 171 (1960).

16. C. Jech and R. Kelly, J. Phys. Chem. Solids 30, 465 (1969).

17. E. Krikorian and R. J. Sneed, Trans. Nat. Symp. Vacuum Technol. 10, 368 (1963).

18. J. W. Mayer, L. Eriksson, S. T. Picraux and J. A. Davies, Can. J. Phys. 46, 663 (1968).

19. R. Kelly and C. Jech, J. Nucl. Mat. 30, 122 (1969).

20. Hj. Matzke, Lecture at the Summer School on the Physics of Ionized Gases, Herceg-Novi, Yugoslavia, 1970.

21. D. K. Murti, Thin Solid Films, in press.

22. J. Reid and R. Kelly, Radiation Effects,17, 253 (1973).

23. N. Q. Lam and R. Kelly, Can. J. Phys. 50, 1887 (1972).

24. P. V. Pavlov, E. V. Shitova, E. I. Zorin and N. A. Genkina, Sov. Phys. Crystallogr. 18, No. 3, 381 (1973).

25. F. W. Ainger, J. Mat. Sci. 1, 1 (1966).

CHAPTER 10

SUGGESTIONS FOR FUTURE WORK AND SUMMARY

10.1 Suggestions for future work

10.1.1 A possible thickness effect - Fig. 10.1 shows RED micrographs of SnO_2 films deposited by reactive sputtering on Ta substrates. It can be noticed that diffraction patterns of films whose thickness was estimated to be ~3600 Å or higher, show well defined rings rather than halos. Thus films appear to change spontaneously from an amorphous to a crystalline state with increasing thickness. A systematic investigation could be undertaken to probe deeper into this phenomenon. Precedents can be found in work by Krikorian and Sneed (1) on sputtered films of Ge, Behrndt (2) on Bi, Ga, Fe and V, Piercy (3) on anodic WO_x, and Arora (4) on anodic VO_x, WO_x, MoO_x, NbO_x, and TaO_x.

10.1.2 Thickness-vs-anodizing voltage - As already noticed in Section 3.3.3 anodized films are thicker for a voltage in the vicinity of 8-15 than for higher values (Table 3.I). We have no explanation at all for this result, though consider it to justify future work for its clarification. We would in particular recall that the present work constitutes the first instance in which thick protective oxide films were grown on Sn by anodizing.

10.1.3 Preparation of SnO_2 by oxygen-bombardment of metallic tin - As already mentioned in Section 4.3, we would predict that, due to S (sputtering coefficient) decreasing, SnO_2, rather than SnO, would be formed at very low (E << 35-keV) or at very high (E >> 35-keV) O_2^+ energies.

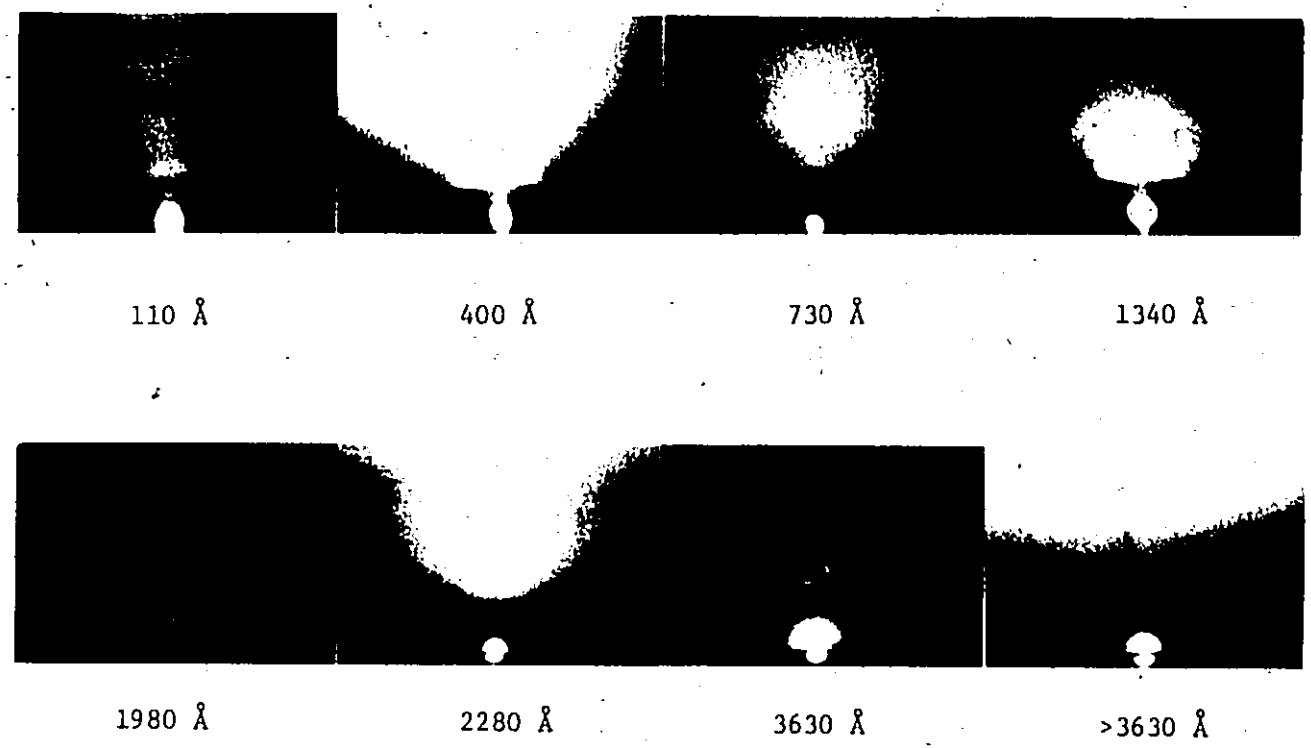

Fig. 10.1. SnO_2 reactively sputtered on Ta substrate. All thicknesses deduced gravimetrically, i.e. weighing Ta before and after deposition.

Were one able to obtain SnO_2 in this way, the possibility would exist to form films with all possible thicknesses from zero to the range of thicknesses represented by anodic films. The latter cannot be obtained (see Chapter 3) with thicknesses less than ∿3000 Å.

10.1.4 Formation of oxygen-bubbles in O_2-implanted metallic tin - Looking at Fig. 10.2, which is the transmission electron micrograph of a metallic tin film implanted with oxygen, it will be noticed that black spots appear on a uniform background. This feature always appeared in transmission electron micrographs of oxygen-implanted samples, as distinguished from unbombarded samples (cfr. Fig. 4.1(a)). Noticing that bubbles are detected in electron microscope studies as having the appearance either of white or black dots (see, e.g., Ref. 5), the possibility was considered that oxygen bubbles had formed. Consider the gas law:

$$pV = nRT$$

If $p = 2\gamma/r$, γ = surface tension, N = number of atoms, L = Avogadro's number, then it can be rewritten as

$$\frac{2\gamma}{r}\frac{4}{3}\pi r^3 = \frac{N}{L}RT$$

Assuming a surface tension $\gamma = 200$ erg/cm^2, and an average radius of 1000 Å for the black spots in Fig. 10.2, one obtains

$$N = 4 \times 10^6 \text{ atoms/black dot}$$

Multiplying the oxygen dose used (3×10^{15} ions/cm^2) by the average area of a black dot, one obtains 2×10^5 ions/black dot. Clearly, the black dots are not bubbles. Presumably the formation of SnO (Section 4.2.2)

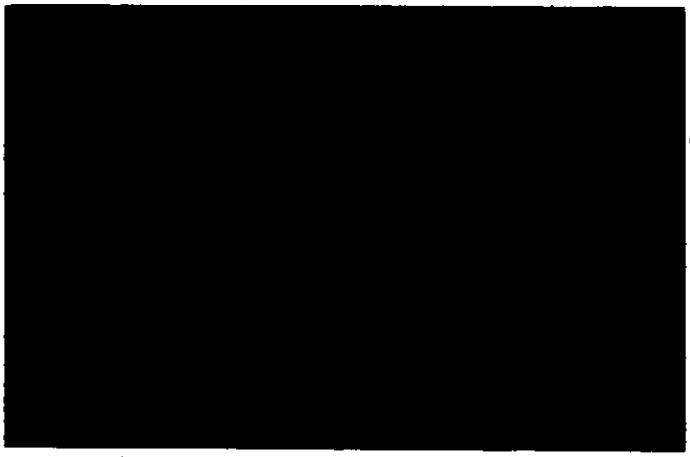

Fig. 10.2. Sn film on carbon coated grid--
Bombarded with oxygen:
3×10^{15} ions/cm^2 - 35 keV
mag. 53,000 - 100 keV

during O_2^+ bombardment hinders the possibility of the simultaneous existence of oxygen bubbles.

To decide about the real origin of such features, one should undertake a quantitative electron optical investigation, inclusive of dark field, underfocus and overfocus imaging, as well as heat treatment of the specimen. The reason for the latter is that in many cases bubbles migrate at a temperature which, though above the self-diffusion temperature, is below the melting point; that is, there is a possibility of bubbles being made to move and therefore identified as bubbles, by pulse heating or by using the heating stage.

10.1.5 Stage IIA and melting point - Release due to a true (Stage IIA) diffusion of the implanted inert-gas ions in the undamaged lattice of the host crystal will diminish in relative importance as the dose increases due to the onset of processes caused by the radiation damage. It is therefore possible that the reason our release spectra do not record Stage IIA somewhere in the region >1200 K is that we have been using too high a dose.

The identification of Stage IIA would have enabled one to estimate, even if crudely, the melting temperature for SnO_2. In fact, Matzke (6), has found that an empirical relation exists between Stage IIA release temperatures and melting points. This relation is obtained from data for a great number of different materials, namely halides, oxides and metals:

$$T_{IIA(10\%)} = 0.4\text{-}0.5\ T_{melting}$$

We would point out that the melting point for SnO_2 is variously reported to lie between 1400 and 2200 K. One of the low values, namely 1673 K, has

been checked by Sinclair et al. (7) and is certainly wrong. What probably happens is that when SnO_2 is heated in vacuum the relevant process is $SnO_2 \rightarrow SnO + \frac{1}{2} O_2$ and what has actually been observed is the melting (1353 K) of tin monoxide. The higher values are probably wrong too, for they correlate better with the sublimation temperature (2073-2173 K).

We anticipate the melting temperature of SnO_2 may be in the vicinity of 3000 K, corresponding to Stage IIA occurring at >1200 K.

10.2 Summary

(a) A thorough review of the literature has shown that many different approaches have been attempted, with varying degrees of success, in order to prepare SnO_2 films.

Films have been formed (i) by chemical vapour deposition, (ii) by reactive evaporation of Sn, (iii) by sputtering, and (iv) by gas oxidation of metallic tin (which has produced contradicting results). Concerning the possibility of obtaining SnO_2 films by anodizing Sn at high voltages, work with both acidic and basic electrolytes has invariably involved low voltages (<5) and never values (>>5) characteristic of the growth of thick, uniform films.

There has been an enormous amount of electronic and optical characterization in previous work. This is attributable to the fact that SnO_2 is a high potentiality material for device fabrication, due to its unique property of combining, when oxygen deficient, electrical conductivity with a high degree of transparency to visible light.

As far as structural characterization is concerned, knowledge is largely confined, until now, to two results: chemically deposited layers are invariably crystalline, while evaporated or reactively sputtered layers

are normally, though not always, amorphous. Such basic concepts as whether the films are amorphous or crystalline, and, if the former, the value of the crystallization temperature, have not been so far settled in a satisfactory way, the crystallization temperature, for example, being given as a limit, e.g. >280°C, <400°C, <500°C. Non-existent is also any information about crystallization mode, the crystallization product, and the grain size of crystallization product.

We regard structural characterization to be as important as other properties if SnO_2 is to find use in device fabrication, in view of the fact that, for example, both the magnitude of conductivity, as well as its temperature stability, are effected by crystallinity. (cfr. V_2O_3 and VO_2, as shown in Fig. 1.1.)

As far as ion-impact effects are concerned, there is no published study at all in which SnO_2 is considered explicitly.

On the basis of these considerations, we have defined an area of lack of knowledge, a space in which to operate by means of our choice of techniques, experimental apparatus, materials preparation and treatment, materials analysis.

(b) The first experiments involved the preparation of SnO_2 films by reactive as well as ion-beam sputtering. While the preparation of SnO_2 films by these techniques has a long precedent in the literature, at least from the point of view of preparation as an end in itself, our work gives explicit information on the crystallization temperature. The latter depends strongly on the nucleation conditions as governed by the substrate, varying from <200°C for crystalline SnO_2 substrates, to 250°-300°C for KCl substrates, to 400°-450°C for Ta substrates, to 475°-550°C for unsup-

ported films. We would propose that 475°-550°C is the upper limit to the crystallization temperature (for a 1000 Å thick amorphous film and an annealing time of 6 min; which are typical values, to within a factor of 2).

While the crystallization process occurred homogeneously, a consistent result in this work has been that amorphous SnO_2, formed by either reactive or ion-beam sputtering, crystallized to cassiterite. Likewise SnO_2 films formed anodically (see (c)) were cassiterite as formed. We therefore tentatively suggest that SnO_2 lacks metastable or high temperature phases.

Once crystallization was attained, the grain size remained in the vicinity of 400 Å to temperatures as high as 1000°C, in the case of unsupported films, while a grain size of 600 Å is reached after heating supported films to 550°-600°C. The difference in crystallization temperature between supported and unsupported films suggests that nucleation rather than growth is the rate-controlling step in the crystallization of SnO_2. Similarly, the difference in grain size obtained in annealing experiments suggests that nucleation, while perhaps not fully rate-controlling, at least plays a role in grain growth.

The thickness (d) of the reactively sputtered films was estimated by noting the interference colours when using a Ta substrate and assuming the validity of the relation $n_{SnO_2} d_{SnO_2} = n_{Ta_2O_5} d_{Ta_2O_5}$ where n is the index of refraction.

(c) While SnO_2 is frequently prepared by sputtering, there is as far as we know no precedent for films being formed by high-voltage anodizing. We have found it possible (apparently for the first time) to anodize Sn up to 65 V and the growing films showed 6 orders of interference colours. The present work makes it clear that, though the process is far from being per-

fect, high voltage film growth can be achieved with Sn. Anodic SnO_2 was found to be crystalline as formed, which was an unexpected result in view of the fact that anodic films are almost invariably amorphous.

The thicknesses of the anodic films were estimated, among other ways, by sputtering the films with 20-keV Kr ions until the metal was exposed and noting the weight loss. This confirmed the thicknesses to be nearly independent of voltage between 6 and 50 V; which is what was anticipated on the grounds that the interference colours changed only slightly with voltage. The anodization of Sn has a rather low efficiency (4-21%) and this could be shown to be due to electronic conduction rather than dissolution.

Efforts to characterize the anodic films structurally have led to further information on grain growth of SnO_2. Specifically the films retained their microcrystalline structure in heat treatment, until a temperature of about 1000°C was reached, this being in good agreement with the behaviour of sputtered films.

(d) A completely novel approach to forming SnO_2 films has here been attempted, by bombarding metallic tin with oxygen ions. The nominal objective failed in that the films turned out to be crystalline α-SnO. Still, this work has led us to indicate that SnO_2 films can, in principle, be formed by oxygen-implantation, thus providing a very controllable technique to form "very thin" thin films. The key is anticipated to lie in the choice of the oxygen-ion energy, as dictated by considerations on the sputtering coefficient for the system O_2-Sn.

(e) Having so far explored the properties of 500-5000 Å SnO_2 films as formed by reactive sputtering, ion-beam sputtering and high-

voltage anodizing, we have at this point undertaken to investigate, using the result of this work as a guide, Kr-ion-impact effects with SnO_2 thin films.

We have first of all made a survey of materials whose response to ion-impact is known. Included are materials which undergo (i) a crystalline-amorphous transition, (ii) an amorphous-crystalline transition, and (iii) a stoichiometry change. We have also given the criteria which researchers have worked out in order to predict the occurrence of the above transformations. While we have noticed the lack of any published result as far as SnO_2 is concerned, we have pointed out that, were a bombardment-induced amorphization or change of stoichiometry to occur with SnO_2, there would be significant technological implications for device fabrication. Furthermore, we want to point out that bombarding a material with inert-gas ions in the keV range is both a way to dope a material with what is one of the primary causes for swelling of fuel materials for nuclear reactors, as well as a way to simulate neutron irradiation in the MeV range. In addition, these experiments may be regarded as pointing the way to important effects, such as, for example, preferential sputtering. The sputtering process will play an obvious role with nuclear and thermonuclear materials due to their continuing exposure to fission fragments, fast neutrons, or helium ions. Preferential sputtering can alter the surface of binary alloys, with possible consequences such that external surfaces may in general have unexpected corrosion, electrical or transport properties.

(f) Our first experimental finding has been that SnO_2 shows an unusually high value of the sputtering coefficient. SnO_2 in this respect resembles MoO_3, V_2O_5, WO_3 and possibly SiO_2, but, to the writer's knowledge,

no other oxide. S was then measured as a function of temperature, the result of these experiments being that it was even higher at elevated temperatures. Taken together these experiments suggest that SnO_2 undergoes thermal sputtering, i.e. sputtering involving vaporization. This unusual behaviour is also shown to be predictable, when a general criterion which takes the vapour pressure into consideration, is applied to SnO_2. Pursuing the criterion further, it was argued that both a model based on "vaporization due to thermal spikes" (governed by vapour pressure) and one based on "preferential oxygen sputtering" (governed by the surface binding energy) predict that high-dose bombardment of SnO_2 will leave the stoichiometry unchanged, while the SnO_2 sputters congruently (as distinct from preferential sputtering).

(g) The next step in exploring the response of SnO_2 to ion-impact was to investigate the structure of the target material after bombardment. The experimental evidence was that SnO_2 amorphizes under ion-impact, in agreement with both a criterion based on a physical model involving thermal spikes and one of empirical nature based on ionicity.

(h) Given this preliminary result, namely that crystalline SnO_2 does indeed amorphize under ion-impact, we started at this point to look in more detail into this phenomenon.

Bulk samples (either sintered SnO_2 powder or natural cassiterite) were ion-bombarded and then analyzed using the following techniques: (i) reflection electron diffraction, (ii) dissolution measurements, (iii) resistivity measurements, and (iv) marker-release spectrometry.

(i) Monitoring, by electron diffraction, the annealing of bombardment-induced amorphousness at increasing values of the annealing

temperature, could only be done using bulk samples, and not anodized tin, due, if not to any other reason, to the difference in melting temperature between SnO_2 and the metallic Sn substrate. Such experiments have established that the annealing to the original single crystalline phase occurs (i) by a homogeneous transformation rather than by interface motion ("heterogeneous" transformation in the terminology of Mader). Moreover, it goes (ii) through an intermediate polycrystalline phase showing the normal cassiterite structure. Though most substances show crystallization by interface motion and by necessity therefore return to the original structure, in a process where there is an evolution of the type amorphous→polycrystalline→epitaxial, the intermediate phase could in principle have a different structure than the starting material. In fact most amorphous oxides do yield a different phase, with SnO_2 being an exception in not doing so.

(j) Dissolution measurements have been performed in order to establish the depth of alteration due to ion-bombardment. The first step in obtaining so-called dissolution curves was to label specimens with radioactive Kr^{85}. The specimens were then exposed to a suitable solvent and the fraction of retained activity noted as a function of time. Provided the depth distribution of the injected ions can be estimated, the fraction of retained activity enables one to deduce the thickness of the layer removed. Results for SnO_2 have been compared with other systems for which information is available. It turned out that the thickness of the amorphized layer is rather smaller in the case of SnO_2. Namely, SnO_2 shows high "resistance" to amorphization.

We have also carried out experiments in which dissolution and

thermal annealing were compared. Thermal annealing and dissolution resulted to be equivalent (when annealing is carried on up to at least ~1100°C) in that the activity retained after dissolution is similar to that retained after thermal annealing. This equivalence, though, does not hold for lower annealing temperatures. In other experiments, dissolution and annealing were combined. Taken together the results of the above experiments are understandable if it is assumed that amorphous SnO_2 is fully soluble in HF, polycrystalline SnO_2 is partly soluble, and single-crystal SnO_2 is not soluble at all.

(k) Oxygen loss normally causes the conductivity of an oxide to increase, at times by many orders of magnitude. If oxygen loss were to occur with SnO_2, the result would have been of fundamental importance in device fabrication, owing to its conductivity varying, apparently, as much as 5 orders of magnitude due to stoichiometry changes.

Again, bulk material had to be used in order to carry out conductivity measurements. (Anodic films could not be used due to the metallic nature of the substrate.)

The conclusion from the experiments was that SnO_2 shows high values of resistance both before and after high-dose Kr-bombardment. This implies that the original stoichiometry was retained. The result is consistent both with a model of preferential sputtering and with one of thermal-spike induced vaporization and its implication is that SnO_2 insulators or resistors should be particularly suited to be used in a radioactive environment (as distinct, for example, from devices based on TiO_2).

(l) Marker-release spectrometry was finally used. The basic idea behind this technique is to label the specimen with a radioactive inert-

gas and then determine, with a linear temperature increase, the temperatures for the release of the gas, the gas serving as an inert marker which signals phase changes, stoichiometry changes, defect annealing, or diffusion. Once more bulk SnO_2 had to be used, rather than anodized SnO_2, owing to the latter lying on a substrate (metallic tin) which has an unsuitable melting behaviour. Two reproducible release processes, at definite temperatures, were in this way promptly identified. Electron diffraction investigation of the specimen at these temperatures revealed the two release processes to be due to an amorphous-crystalline and a crystalline-epitaxial phase transformation, while the release spectrum provided a simple yet accurate means for locating the temperatures at which these processes occurred.

The present results allow us to expand the formalism on which marker-release spectrometry is based. Three characteristic release processes had been so far identified when a material implanted with a radioactive inert-gas is thermally treated: release due to recovery of bombardment-induced disorder, release due to self-diffusion and release due to bubble motion. We have identified a somewhat different release process, namely one due to epitaxial crystallization. This process has been clearly identified in the case of SnO_2, while a search of the literature has shown that precedents for such a phenomenon could be found with MgO, Cr_2O_3, SiO_2 and TiO_2. We have then pointed out that the known or suspected examples always lie above the temperature of Stage IB (crystallization) yet below the temperature of Stage IIA (unhindered diffusion). Also they share in common with Stages IA and IB motion which is directional rather than random. We therefore propose the designation "Stage IC" for epitaxial

crystallization.

A deeper knowledge of the marker-release technique will be valuable in better understanding the diffusion behaviour of inert-gas atoms in a host lattice, which, as already mentioned, is of primary importance, for example, in understanding, and eventually solving, the problem of swelling in fuel materials used in nuclear reactors. Besides, marker-release can be used as an important supplement to electron optics as an indicator of lattice disorder due to low energy ions. Or it can be used, again as a supplement to electron optics, to infer the presence of bubbles in a material, especially when the material is not in a form (thin film) suitable for electron optics. Finally, it yields valuable insight into self-diffusion and melting behaviour.

REFERENCES

1. E. Krikorian and R. J. Sneed, Trans. Nat. Symp. Vacuum Technol. 10, 368 (1963).

2. K. H. Behrndt, J. Vac. Sci. Tech. 7, 385 (1969).

3. G. R. Piercy, AECL Annual Report, Apr. 1 - June 30, 1964.

4. M. R. Arora, Ph.D. thesis, McMaster University, Canada, 1974.

5. E. Ruedl and R. Kelly, J. Nucl. Mat. 16, 89 (1965).

6. Hj. Matzke, Can. J. of Phys. 46, 621 (1968).

7. W. R. Sinclair, R. G. Peters, D. W. Stillinger and S. E. Koonce, J. Electrochem. Soc. 112, 1096 (1965).

ERRATA

p. 124: Ref. 6 and Ref. 13 refer to the same publication

p. 152: Ref. 26 and Ref. 30 refer to the same publication